Magnetooptical and Hole-Burning Studies of Matrix-Isolated Metallophthalocyanines

A thesis

submitted in partial fufillment

of the requirements for the Degree of

Doctor of Philosophy

in Chemistry

at the

University of Canterbury

by

Cara L. Dunford

University of Canterbury

1997

Abstract

In this thesis, absorption, magnetic circular dichroism (MCD) and hole burning spectroscopies have been used to investigate a range of metalloporphyrins derivatives, in particular, the metallophthalocyanines (MPcs). The aim of these investigations was the elucidation of a number of excited-state properties, such as spin-orbit splittings, orbital angular momenta and vibronic effects. Use has been made of quantum mechanics, group theory and moment analysis in relating theoretical expressions to the experimentally observed spectra. The main method of sample preparation was matrix isolation. The combination of this technique with the measurement of spectra at low, accurately known temperatures was achieved using a matrix-injection procedure, the refinement of which formed a significant part of the work in this thesis.

The Q band of MPcs and metalloporphyrins arises from the lowest ligand $\pi \rightarrow \pi^*$ transition. Weak MCD temperature dependence is observed for this band in CuPc, CoPc, and Cu tetrabenzoporphyrin. This effect can be attributed to a zero-field splitting of the excited-state levels, which has been shown to arise from interference between second-order exchange and spin-orbit coupling between the so-called singdoublet and tripdoublet excited states. The spin-orbit coupling is proposed to arise from a (small) metal contribution to the ligand π orbital.

MCD temperature dependence has also been observed for lutetium bisphthalocyanine ($LuPc_2$). For the Q band, this effect is weak. There are three transitions in the Q region, but it has been shown theoretically that the overall temperature dependence of two of these, as measured by moment analysis, will cancel. The red vibronic (RV) band shows much stronger temperature dependence, with the sign of the MCD changing from positive to negative between 65 and 1.4 K. The strength of this effect is ascribed to a greater metal contribution to the excited-state orbital.

Hole burning and MCD spectroscopies have been combined to measure the MCD of holes for ZnPc, CuPc and $LuPc_2$. This is the first time this combination of techniques has been used. A qualitative analysis of the resulting spectra is given, including a proposed hole-burning mechanism involving intermolecular charge transfer.

Acknowledgements

I would firstly like to thank my supervisor, Bryce Williamson for his help and support. His expertise in all aspects of experimental and theoretical work, enthusiasm, and willingness and ability to share his knowledge have been greatly appreciated. My thanks also to Elmars Krausz of the Australian National University, for making his laboratory facilities available, and for his valuable collaboration.

I am grateful to the staff of the mechanical and glassblowing workshops, for their assistance with the construction of some of the apparatus used in this work. The University of Canterbury provided three years of funding, in the form of a Doctoral Scholarship, for which I am appreciative. My heartfelt thanks go also to my husband, Adam, for his love, support and technical assistance. Finally, I acknowledge that without God I am nothing.

I will say of the Lord, "He is my refuge and my fortress,
my God in whom I trust" (Psalm 91:2)

Table of Contents

List of Figures

List of Tables

Glossary of Acronyms

ANU	Australian National University
BO	Born-Oppenheimer
CD	Circular dichroism
CF	Crystal field
CF1204	Oxford Instruments continuous-flow cryostat
ESBH	Electronic side-band hole
FC	Franck-Condon
FWHM	Full width at half maximum
He frig./emag	Helium refrigerator/electromagnet matrix-deposition system
HOMO	Highest occupied molecular orbital
JT	Jahn-Teller
LCAO	Linear combination of atomic orbitals
lcp	Left-circularly-polarised
lHe	Liquid helium
LIHF	Laser-induced hole filling
lN$_2$	Liquid nitrogen
LUMO	Lowest unoccupied molecular orbital
LuPc$_2$	Lutetium bisphthalocyanine
MCD	Magnetic circular dichroism
MI/SM4	Matrix-injection/cryomagnet system
MO	Molecular orbital
MOD3	One of two spectrometers used at the University of Canterbury
MOD4	One of two spectrometers used at the University of Canterbury (high resolution)
MPc	Metallophthalocyanine
MPc/Ar	Metallophthalocyanine in an argon matrix
MP	Metalloporphyrin
NPHB	Non-photochemical hole burning (also known as photophysical hole burning)
OEP	Octaethylporphyrin
P	Porphyrin

Pc	Phthalocyanine
PEM	Photoelastic modulator
PHB	Photochemical hole burning
PMMA	Polymethylmethacrylate
PMT	Photomultiplier tube
PSBH	phonon side-band hole
pseudo-PSBH	Pseudo phonon side-band hole
pseudo-VSBH	Pseudo-vibrational side-band hole
PVC	Polyvinylchloride
rcp	Right-circularly-polarised
RS	Rigid shift
SM4	Oxford Instruments super-conducting cryomagnet
SO	Spin orbit
TBP	Tetrabenzoporphryin
TLS	Two-level system
UOC	University of Canterbury
UV	Ultra violet
VSBH	Vibrational side-band hole
VTI	Variable-temperature insert
ZPH	Zero-phonon hole
ZPL	Zero-phonon line

Glossary of Symbols

This glossary covers symbols occuring frequently in one or more chapters.

A	Absorbance
δA	Hole-absorption (change in absorbance due to spectral hole burning)
ΔA	MCD
$\delta\Delta A$	Hole-MCD (change in MCD due to spectral hole burning)
$\mathbf{A}_0$	The first moment of the absorption
$\mathcal{A}$	A derivative-shaped MCD dispersion
$\mathcal{A}_1$	The MCD Faraday parameter describing the magnitude of an $\mathcal{A}$ term
$\mathcal{B}$	A single-signed, temperature-independent MCD dispersion
$\mathcal{B}_0$	The MCD Faraday parameter describing the magnitude of a $\mathcal{B}$ term
B	Magnetic field strength (inductance, in tesla)
$\mathcal{C}$	A single-signed, temperature-dependent MCD dispersion
$\mathcal{C}_0$	The MCD Faraday parameter describing the magnitude of a $\mathcal{C}$ term
c	Speed of light
c	Concentration
$\mathcal{D}_0$	Absorption dipole strength
Δ	The zero-field splitting of an excited state (except in Chapter 7, where Δ is the full-width at half-maximum of a band)
ΔQ	The zero-field splitting of the Q excited state (in Chapter 7)
E	Energy (in cm^{-1})
$\overline{E}$	Band barycentre (in cm^{-1})
E_{burn}	Hole-burning energy
g_{orb}	orbital g value
I	Intensity of light
I_0	Incident intensity of light
h	Planck's constant

$\hbar$	$h/2\pi$
$\mathcal{H}$	Hamiltonian operator
J_{ab}	Coulomb integral involving orbitals a and b
k	Boltzmann's constant
K_{ab}	Exchange integral involving orbitals a and b
l	Orbital angular-momentum operator
l	Pathlength
l_z	z-component of the one-electron orbital angular momentum operator
L_z	z-component of the many-electron orbital angular momentum operator
λ	Wavelength (in general), or one-electron orbital angular momentum of an axial molecule (Chapter 1)
m	Metal-orbital label in Chapter 4
m	Electric-dipole operator
m_x, m_y, m_z	Cartesian components of the electric-dipole operator
m_{+1}, m_{-1}, m_0	Complex components of the electric-dipole operator
$\mathcal{M}_{\pm}$	Electric-dipole transition moments for left and right circularly polarised light
$\mathbf{M}_0$	The zeroth MCD moment
$\mathbf{M}_1$	The first MCD moment
m_e	Mass of an electron
M_R	Relative molecular mass
μ_B	Bohr magneton
p	Linear momentum operator
Q_+, Q_-	Upper and lower components respectively, of a zero-field split Q excited state
r_{ij}	Separation radius between particles i and j
ρ	Mass density
s	spin angular-momentum operator
s_z	z-component of the one-electron spin angular-momentum operator
t	Time
ν	Frequency
Z	Spin-orbit coupling matrix element (or nuclear charge)

Chapter 1

Introduction

1.1 Porphyrins and Phthalocyanines

Phthalocyanines (Pcs) and porphyrins are molecules with a wide range of interesting and useful properties, which have important applications in many fields of science and technology. Synthetic porphyrins are of much interest in science,[1] primarily as models for biological molecules such as haemes, and the photosynthetic reaction centres of certain bacteria.[2] Phthalocyanines are extremely stable to acid, alkali, heat, and light, and are relatively insoluble in many solvents. Such properties, in combination with the intense colours of these compounds, make them ideal candidates for use as pigments. Indeed, their main industrial applications are as pigments in printing inks, dyes, coatings, paints, plastics and photocopying agents.[3] As an example of the volumes involved, about 7000 tonnes of pigment blue (β CuPc) were produced in the US in 1987. Phthalocyanines and their derivatives are also used as catalysts, as well as being under investigation for such applications as electrochromic display devices, photodynamic reagents for cancer therapy, materials for optical read-write disks and sensing elements in chemical sensors, to name but a few.

A number of excellent reviews of Pcs and porphyrins have been published, to which the reader is referred for further details. For information on Pcs, the exhaustive literature survey of the science and applications of Pcs from the time of their discovery up to 1987 presented by Thomas and Moser,[3–6] and the series edited by Leznoff and Lever[7–9] containing detailed accounts of a number of aspects of the science of these molecules are recommended. Particular mention must also be made of the series of volumes on porphyrin chemistry, edited by Dolphin.[1]

As shown in Figure 1.1, metalloporphyrins (of which MPcs are a subgroup) have large planar structures with extensive π delocalisation. The two lowest-energy absorption bands, historically labelled Q and B,[10] are shown in Figure 1.2 for a

number of the zinc analogues. The spectra have been normalised so that the areas under the curves are equal.

The relevance of the Pcs and porphyrins to each of the technologies mentioned above is due in some way to their electronic structure, and in particular to the intense colour arising from the strong $\pi \rightarrow \pi^*$ transitions in the visible region. Advancement in the application of these molecules thus benefits from a detailed knowledge of their electronic structure, and, in particular, the nature of the excited states. The primary tool used to achieve such information is spectroscopy. The work described in this thesis involves the application of three such techniques, namely absorption, magnetic circular dichroism (MCD) and hole-burning spectroscopies, to a variety of MPcs and metalloporphyrins. Information concerning a number of excited-state phenomena such as spin-orbit coupling, vibronic effects and orbital angular momenta has been obtained. A brief introduction to some aspects of these topics, along with a discussion of electronic models developed to explain the spectra, is given here; further details appear at the start of the relevant chapters.

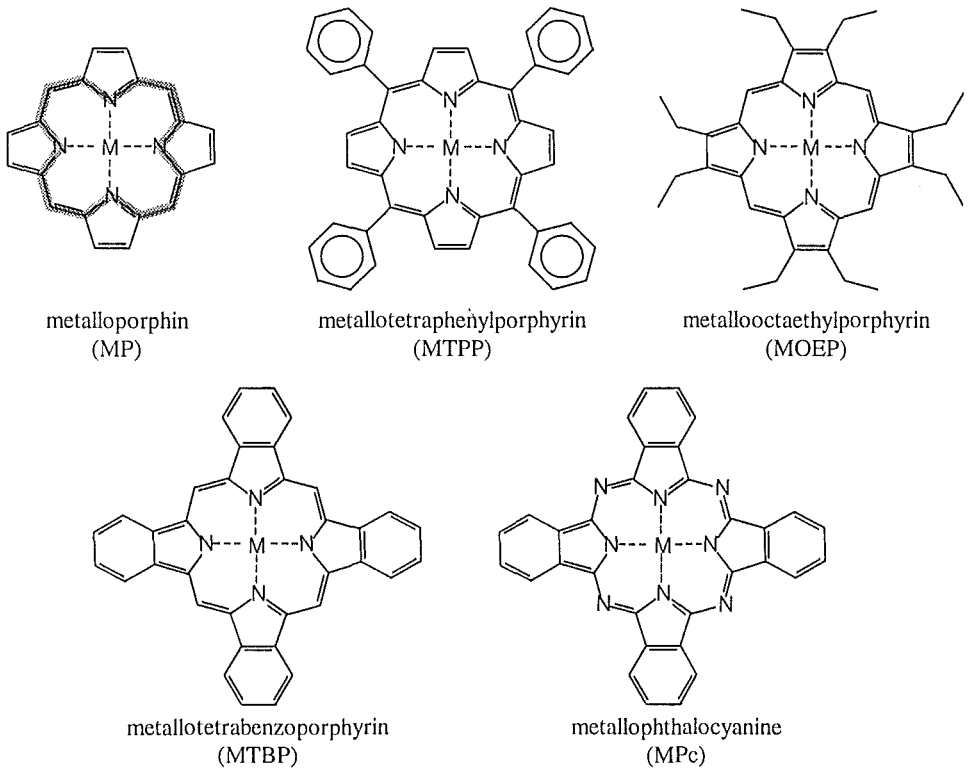

Figure 1.1. The molecular structures of a range of metalloporphyrins. The grey shading on the MP molecule indicates the delocalised π ring discussed in the text.

1.2 Electronic Models

Substantial efforts have been made to explain the spectral features of porphyrins and Pcs theoretically. An excellent review of the different approaches taken is presented by Gouterman.[11] A regular metalloporphyrin (for which the metal has only closed shells) has an electronic 'core' of 18 π electrons delocalised *via* the $2p_z$ orbitals of a 16-member ring of C and N atoms (shown in grey for MP in Figure 1.1). It is this core, perturbed to various degrees by the substituent groups and metal ions, which is responsible for the optical spectra. (Note that in the following discussion, the term 'metalloporphyrin' includes the MPcs.)

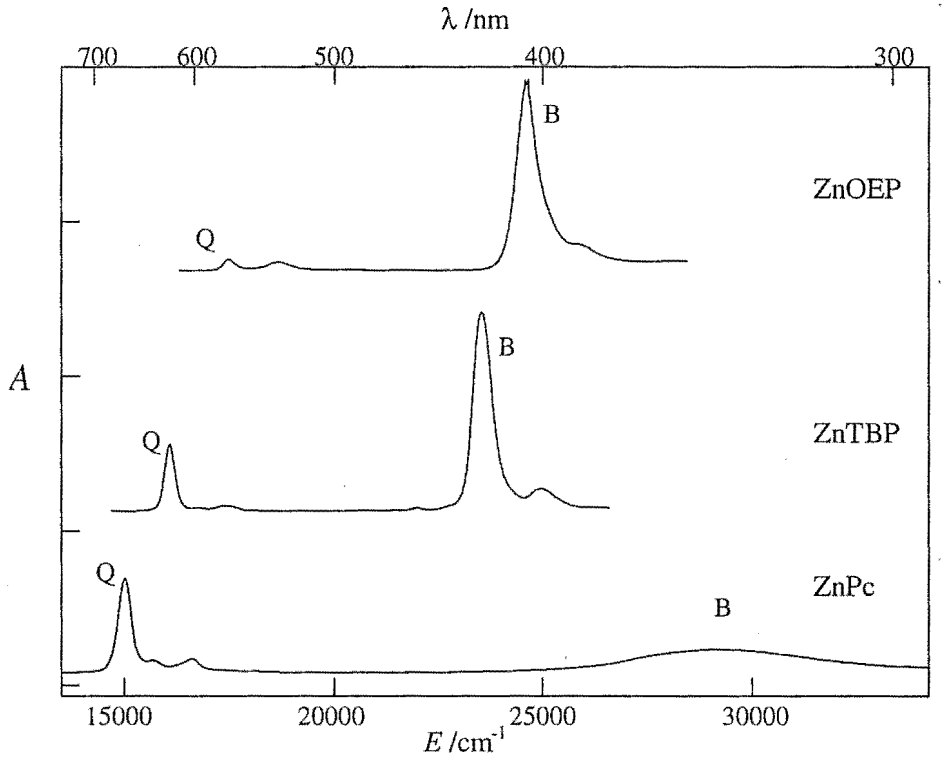

Figure 1.2. Absorption spectra of three zinc porphyrins, measured in a solution of tetrahydrofuran. The Q and B bands are labelled. Note the change in relative intensities and positions of these two bands. Spectra have been normalised so that the area under each curve is the same.

1.2.1 The Free-Electron Model

The simplest model used to describe the delocalised system is that of 18 free electrons 'threaded' on a circular loop, as first described by Simpson[12] and Platt.[10] The wavelength of the electrons must be an integral fraction of the length of the

loop, and hence from the de Broglie condition, the linear momentum of the electrons about the loop is

$$p = \frac{nh}{2\pi r} = \frac{n\hbar}{r} \tag{1.1}$$

where h is Plancks constant, r is the radius of the loop, and $n = 0, 1, 2, ...$ Denoting the axis perpendicular to the plane of the loop as z, the magnitude of the orbital angular momentum about this axis is

$$|l_z| = pr = n\hbar \tag{1.2}$$

and the corresponding kinetic energy is

$$E = \frac{l_z^2}{2m_e r^2} = \frac{n^2\hbar^2}{2m_e r^2} \tag{1.3}$$

where m_e is the mass of an electron. It is a common convention to express angular momenta in units of $\hbar$, and (for axial molecules) to denote its magnitude along z by λ. This gives

$$\lambda = n \tag{1.4}$$

and

$$E = \frac{\lambda^2\hbar^2}{2m_e r^2} \tag{1.5}$$

Since the angular momentum can be in either of two directions, the orbital angular momenta are quantised by

$$m_\lambda = \pm\lambda \tag{1.6}$$

From (1.6) it can be seen that an orbital corresponding to $\lambda = 0$ is non-degenerate, while all other orbitals have two-fold degeneracy. Hence, the 18 π electrons occupy the first 5 orbital levels ($\lambda = 0$ - 4) and the lowest-energy transitions are from $\lambda = 4$ to $\lambda = 5$, as shown on the left-hand side of Figure 1.3. Using a ring radius of 4 Å, the energy of these transitions (on a wavenumber scale, see Section 3.2) is predicted to be

$$\Delta E = \frac{(5^2 - 4^2)\,h}{8c\pi^2 m r^2} = 17300 \text{ cm}^{-1} \tag{1.7}$$

which is qualitatively correct (Figure 1.2).

Defining the *total* (many-electron) angular momentum by

$$\Lambda = \left| \sum m_\lambda \right| \tag{1.8}$$

the ground state corresponds to $\Lambda = 0$, and transitions with $\Delta\Lambda = 1$ (dark grey in Figure 1.3) and $\Delta\Lambda = 9$ (light grey in Figure 1.3) are possible. The former (assigned to the B transition) is formally allowed, while the latter (assigned to the Q transition) is formally forbidden. After inclusion of interaction between electrons, Hund's rule predicts that the excited state with the greater angular momentum ($\Lambda = 9$) should lie at lower energy, which agrees with the experimental observation of the Q band at longer wavelength than the B band.

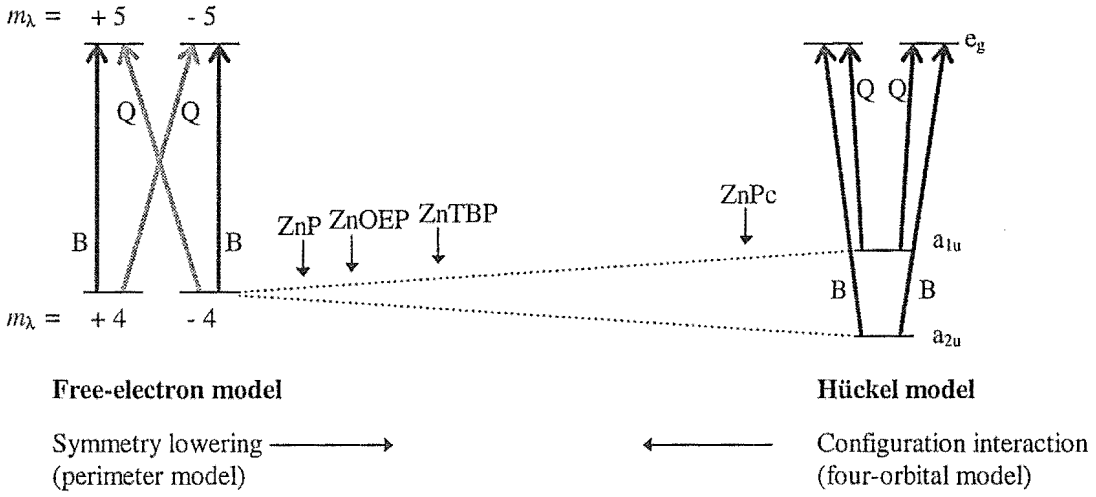

Figure 1.3. The HOMO and LUMO orbitals of metalloporphyrins, as determined by the free-electron model (left) and the Hückel model (right). Dark grey arrows indicate allowed transitions and light grey lines indicate forbidden transitions.

1.2.2 The Perimeter Model

Deviations from the free-electron model for real systems are considered in the perimeter model, developed by Michl.[13] As the symmetry is lowered from the $D_{\infty h}$ point group of the model to the D_{4h} symmetry of a metalloporphyrin, the two-fold degeneracy of orbitals with even λ is lowered (Figure 1.3) and the transitions become mixed. Thus the Q transition gains intensity at the expense of the B transition, and the Q state loses angular momentum to the B state. However, as long as these effects are not too great, the B transition will remain the stronger, and the Q

state will carry most of the angular momentum. The former is clearly the case for substituted metalloporphyrins (*e.g.* ZnOEP and ZnTBP of Figure 1.2), while the latter has been confirmed for such molecules by MCD and Zeeman experiments.[14–16] Along with these changes, the Q - B band energy separation should also increase slightly. From Figure 1.3 it is seen that an explanation of the spectra of the 'simpler' metalloporphyrins (ZnP, ZnOEP) requires relatively small deviation from the free-electron model, with larger deviations necessary for ZnTBP and ZnPc.

1.2.3 Hückel Calculations

A Hückel calculation carried out by Longett-Higgins *et al.*[17] was the first model to take account of the specific details of the porphyrin shape. In this case, the π molecular orbitals (MOs) are expanded as linear combinations of atomic orbitals (LCAO). Results of such calculations show that for metalloporphyrins of D_{4h} symmetry, the lowest two transitions are $a_{1u} \rightarrow e_g$ and $a_{2u} \rightarrow e_g$, and are assigned to the Q and B bands respectively (right-hand side of Figure 1.3). However, unlike the free-electron model, these two transitions are calculated to have approximately the same intensities, and the corresponding excited states have the same angular momentum. In effect, the transitions and states are complete admixtures of the free-electron entities. This fits the observed characteristics of MPcs quite well (Figure 1.3), but not so those of the simpler metalloporphyrins.

1.2.4 The Four-Orbital Model

In order to account for the differences in Q- and B-band transition intensities observed for many of the metalloporphyrins it is necessary to include the effects of configuration interaction. This has been done by Gouterman and co-workers[11,18] in what is known as the four-orbital model. This model considers the only the two highest-occupied and two lowest-occupied molecular orbitals (HOMOs and LUMOs), as obtained from a Hückel calculation, *i.e.* a_{1u}, a_{2u} e_{gx} and e_{gy} (in D_{4h}). Interaction between the four possible excited-state configurations produces wavefunctions which contain a mixture of these , *i.e.*

$$|B_\alpha\rangle = \frac{1}{\sqrt{2}}\left(|a_{1u}\, e_{gx}\rangle - |a_{2u}\, e_{gy}\rangle\right) \tag{1.9}$$

$$|B_\beta\rangle = \frac{1}{\sqrt{2}}\left(|a_{1u}\, e_{gy}\rangle - |a_{2u}\, e_{gx}\rangle\right) \tag{1.10}$$

$$|Q_\alpha\rangle = \frac{1}{\sqrt{2}}\left(|a_{1u}\, e_{gx}\rangle + |a_{2u}\, e_{gy}\rangle\right) \tag{1.11}$$

$$|Q_\beta\rangle = \frac{1}{\sqrt{2}}\left(|a_{1u}\, e_{gy}\rangle + |a_{2u}\, e_{gx}\rangle\right) \tag{1.12}$$

The electric-dipole moments for transitions to each of the $a_{1u}e_g$ and $a_{2u}e_g$ pairs appearing in the wavefunctions above are opposite in sign. Thus, for the B states, interference is constructive, giving a larger transition intensity, whereas for the Q states interference is destructive, and the transition intensity correspondingly smaller. The Q state also gains angular momentum at the expense of the B state. Huckel calculations[18] predict that the energy spacing between a_{1u} and a_{2u} decreases from MPc to MTBP to MP, and so the degree of configuration interaction should increase along this series. Thus, the four-orbital model correctly predicts the observed trends in intensity (Figure 1.2, ZnOEP has similar spectral features to ZnP) and angular-momentum distribution.[15,16,19]

Later calculations and experimental data have shown that the situation is not quite as simple as that predicted by this model, with the B band in particular containing additional contributions from a number of other excitations. Nonetheless, the four-orbital model gives a fairly accurate description of nature of the Q transition, as well as providing a useful starting point from which to consider more complicated effects.

In summary, the free-electron and Hückel models can be seen as lying at the extremes of a continuum, as shown in Figure 1.2. The perimeter model lowers the symmetry of the free-electron model, causing a shift to the right. The four-orbital model introduces configuration interaction between the Hückel states, equivalent to a shift to the left. The properties of the metalloporphyrins, as listed in Table 1.1, place

Table 1.1. Spectral parameters of various Zn porphyrins. The values listed are for samples in Ar matrices. $\mathcal{D}_0$ is the absorption dipole strength.

	$\frac{\mathcal{D}_0(Q)}{\mathcal{D}_0(B)}$	$\frac{A(Q)}{A(B)}$	ΔE_{max}(Q,B) (cm^{-1})
ZnOEP[20]	0.11	7.0	7700
ZnTBP[15]	0.17	4.8	8400
ZnPc[19]	0.63	1.0	14700

them in a progression along this continuum, with the 'simpler' metalloporphyrins to the left, and the MPcs to the right.

1.3 MCD Spectroscopy

The electronic information provided by absorption spectroscopy is largely limited to transition energies and intensities (and in some cases, vibrational frequencies). Magnetooptical techniques such as Zeeman and MCD spectroscopies, on the other hand, can be much more productive. The band widths of MPcs and metalloporphyrins are, in general, too broad for Zeeman studies, but MCD is very useful, and indeed is one of the main techniques applied in the work presented here.

In the 1960s, Buckingham and Stephens developed a theoretical formalism of the Faraday effect,[21–23] which made possible the use of magnetooptical spectroscopic data, particularly MCD, in the determination of molecular electronic structure. Among the earliest applications of this formalism, Stephens *et al.*[24] provided an interpretation of magnetooptical data (obtained earlier by Shashoua[25]) concerning porphyrin and Pc systems, and showed that analysis of the data could be used to determine information on excited-state angular momenta.

The substantial literature that has since accumulated on the MCD of porphyrins and Pcs has been the subject of several reviews.[26–31] Most of these studies involve the determination of electronic symmetries and angular momenta, and correlations of these properties against central metal ion or substituents. However, when used in conjunction with the method of moments and/or analysis of the spectral dispersion, the technique is capable of much more,[32] for example the elucidation of vibronic and crystal-field effects.[15,16,19,33]

For paramagnetic systems, information can also be obtained by following the magnetic-field and temperature dependencies of the MCD. The former has been used in investigations of haemoproteins,[30] but there are surprisingly few examples where the temperature dependence has been utilized. The most comprehensive spectroscopic temperature-dependence study of porphyrin-related species was conducted by Misener,[34] who surveyed a series of first-row transition-metal phthalocyanines (MPc, with M = Mn to Zn) isolated in Ar matrices. He measured MCD and

absorption spectra at nominal temperatures of 4.2 and 3.0 K and noted that all of the paramagnetic species showed MCD temperature dependence. For MnPc/Ar, this dependence was very strong, and was later ascribed to a large magnetic moment associated with a ^4E_g ground-state term.[35] However for CuPc/Ar and CoPc/Ar, the dependence was much weaker, and its origins proved elusive. In Chapter 4, results of temperature-dependence MCD studies are presented for CuPc and CoPc. The temperature dependence is quantified, and an explanation of its source is given. Similar temperature-dependence results were obtained for CuTBP; these, along with vibrational overtone frequencies are discussed in Chapter 5. $LuPc_2$, a sandwich-type bisphthalocyanine complex also shows MCD temperature dependence of both the Q and RV bands, as detailed in Chapter 6.

The MCD studies described above require low temperatures, and optically isotropic samples. These requirements are well met by the technique of matrix isolation (described in Chapter 2) in which the molecules to be studied are embedded in, and separated from each other by a host material, thus reducing intermolecular interactions. In the cases presented here the host is frozen Ar, a substance which is chemically inert, optically isotropic, and transparent down to vacuum-UV wavelengths. As well as conferring beneficial optical properties, matrix isolation also precludes axial solvent coordination (a significant complication in the investigation of MPcs in solution) and circumvents the acute insolubility of CuPc. Matrix isolation was the main sample-preparation technique used in the work presented here, with a number of materials also studied in polymer films.

1.4 Hole-Burning Spectroscopy

MCD facilitates investigation of weak perturbations even in the presence of very broad bands, allowing determination various excited-state phenomena, as discussed above. However, the parameters obtained by such a method are weighted averages over the entire inhomogeneous distribution of chromophores. Hole-burning spectroscopy overcomes the problem of broad bands in a different way, by probing them with a laser beam to selectively excite discrete (or a narrow distribution of) states. In such a way, it is theoretically possible to obtain information about individual shifts and splittings. In Chapter 7, experiments are described in which

a magnetic field was applied after holes had been burnt, allowing the measurement of MCD hole-burning spectra. The complexity of the spectra produced precluded quantification of the observed magnetic effects, however, the qualitative results presented for ZnPc/Ar, CuPc/Ar and $LuPc_2$/Ar are nonetheless very interesting. This is the first time MCD spectra of 'holes' have been reported.

Chapter 2

Experimental Techniques and Instrumentation

2.1 Introduction

This chapter describes the instrumentation and techniques used in the measurement of the absorption, MCD and hole-burning spectra produced for this thesis. The materials investigated were a range of MPcs and metalloporphyrins. These were generally prepared in the form of a matrix-isolated sample, although some polymer films were also analysed. The majority of this work was carried out in our laboratory, with the exception of the hole-burning studies, which were performed in the laboratory of Dr Elmars Krausz, at the Research School of Chemistry, Australian National University, Canberra.

Section 2.2 describes the two spectrometers used in the work conducted at the University of Canterbury (UOC). It is intended to give only an overview of these instruments, as details may be found elsewhere.[36,37] The photoelastic modulator (PEM) is described more fully, as this component is essential to the measurement of MCD. A brief outline of the method of derivation of absorbance and MCD from the detector signals is also given.

The materials under investigation, and the methods used for the preparation of samples of these are detailed in Section 2.3. Matrix isolation was the principal technique used, and full details of the procedures and apparatus involved are given. A brief description of the method of preparation of polymer films is also included.

In order to measure MCD spectra of a matrix-isolated sample, it is necessary to transfer the matrix from the deposition region, where it is under vacuum, into the magnetic field and optical path where it is bathed in liquid or gaseous helium. The technique used to accomplish this is known as matrix injection, and is described in Section 2.4. Refinement of this technique has formed an major part of the work

carried out for this thesis. Section 2.4 also details the apparatus used for matrix injection and temperature control.

Because the matrix-injection system is complex and expensive (due to the amount of liquid He required) to use, preliminary measurements of absorption and MCD spectra were made using the combination of a closed-cycle helium refrigerator and an electromagnet. A brief description of these instruments is given in Section 2.5 - for more details the reader is referred to Langford's thesis.[37]

Another important section of experimental work carried out in the course of this thesis was the measurement of absorption and MCD 'hole' spectra. This was carried out at the Australian National University (ANU), and the instrumentation used is described in Section 2.6.

2.2 Spectral Measurement

2.2.1 Overview

Absorption and MCD spectra were measured simultaneously on one of two double-beam spectrometers, known as MOD3 and MOD4. MOD3 is a substantially modified Jasco ORD/UV-5 spectrometer, the base of which has been shortened so that the injection system can be accommodated within the height of the laboratory.[36] MOD4 was built by Langford,[37] and uses a Jarrell Ash 78-463 Czerny-Turner monochromator. A generic outline of the components used in these spectrometers is given

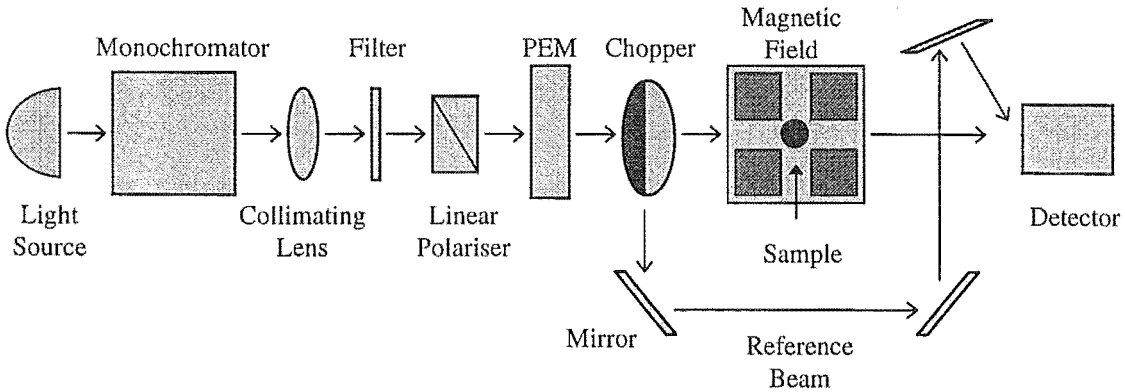

Figure 2.1. A schematic outline of a double-beam absorption and MCD spectrometer.

Table 2.1. Instrumental specifications for the MOD3 and MOD4 spectrometers.

Component	Specifications	
	MOD4	MOD3
Lamp	300 W Xe-arc	500 W Xe-arc
Monochromator	1-m Czerny-Turner grating	Czerny-Turner double prism
Polariser	Glan-Tayler polariser	Rochon prism
PEM	Hinds International Inc. PEM - IF4	Hinds International Inc. PEM-80 I/FS5
Chopper	11 Hz	186 Hz
PMT	Hamamatsu R-376 (UV-vis) 1-mm^2 Phillips BPX-65 Silicon Photodiode (near-IR)	Hamamatsu R-376
LIA	Stanford Research SR510	PAR 5101
Computer	PC 486SX with 14-bit Advantech PCL-814B interface card	PC-AT with 14-bit ADDA card
Reciprocal Dispersion	0.82 nm mm^{-1} at first order	44 nm mm^{-1} at 650 nm
Order-sorting Filters	Esco RG-395 for $395 < \lambda < 800$ nm, Corning 7-54 for < 395 nm, Esco RG-665 for < 665 nm	Not required for prism monochromator

in Figure 2.1. The instrument specifications relevant to the experiments reported in this work are listed in Table 2.1. In brief, MOD4 has higher spectral resolution and a wider spectral range than MOD3, but scans more slowly. Also, absorption baseline problems during the earlier period of operation of MOD4 made the use of MOD3 more attractive in some cases.

In both cases, light from a xenon-arc lamp is passed through a monochromator, and the resulting beam is collimated. The monochromatic light passes through a polariser (which aligns the electromagnetic vector of the beam in a plane at 45° to the vertical), and then through a photoelastic modulator (PEM, Section 2.2.2), which alternately creates left and right circularly polarised (lcp and rcp) light at 50 kHz. The beam is then mechanically chopped: the light either continues past the chopper and through the sample, hits a mirror and travels around the reference path, or is absorbed by a matt-black section of the chopper. Both the reference and sample beams are detected by a photomultiplier tube (PMT), and the dark signal

(principally due to the thermal noise of the PMT and electronics) is measured during the third portion of the chopper cycle.

MOD3 and MOD4 process the voltages produced by the PMT in quite different ways. In both spectrometers the signals are preamplified before passing to the electronics, and a lock-in amplifier is used to extract MCD data. On MOD3 the rest of the necessary signal processing is carried out using analogue electronics; the computer merely collects and displays the end data. On MOD4 all processing is done digitally by the 25 MHz 486SX CPU of the computer. The latter method significantly reduces the amount of noise introduced and allows the absorption to be calculated directly, avoiding the need for calibration. It also enables measurements to be integrated over longer sample periods, leading to a more favourable signal to noise ratio.

2.2.2 The Photoelastic Modulator (PEM)

The PEM consists of a rectangular bar of fused silica attached to a quartz piezoelectric transducer. A material with piezoelectric properties is one for which the application of an external electric field causes a change in the dimensions of the material (and *vice versa*). The piezoelectric transducer used in the PEM is tuned to the resonant frequency of the longitudinal vibration of the silica bar (~50 kHz), and is driven by an electronic circuit which controls the amplitude of the vibration. As the linearly polarised light beam with electric vector **E** passes through the (optically transparent) fused-silica bar at 45° to the vertical, the velocity of the E_x component, which is in the plane of the vibration, is increased if the bar is compressed and decreased if the bar is stretched. In other words, the E_x component alternately leads then lags the E_y component at the frequency of the vibration.

The phase difference between the two components is known as the retardation, the peak retardation being determined by the amplitude of the piezoelectrically induced vibration. For our purposes, the peak retardation is set at quarter of the wavelength ($\lambda/4$) of the light. The instantaneous state of the electric vector components at $\lambda/4$ retardation is shown in Figure 2.2. The net effect is that the polarisation vector of the light emerging from the PEM maps out a spiral about the optical axis, in other words, creating circularly polarised light. Note that lcp and

rcp light are being assigned according to the handedness of the helices formed in space by their electric vectors. Thus the light emerging from the PEM in Figure 2.2 is rcp.

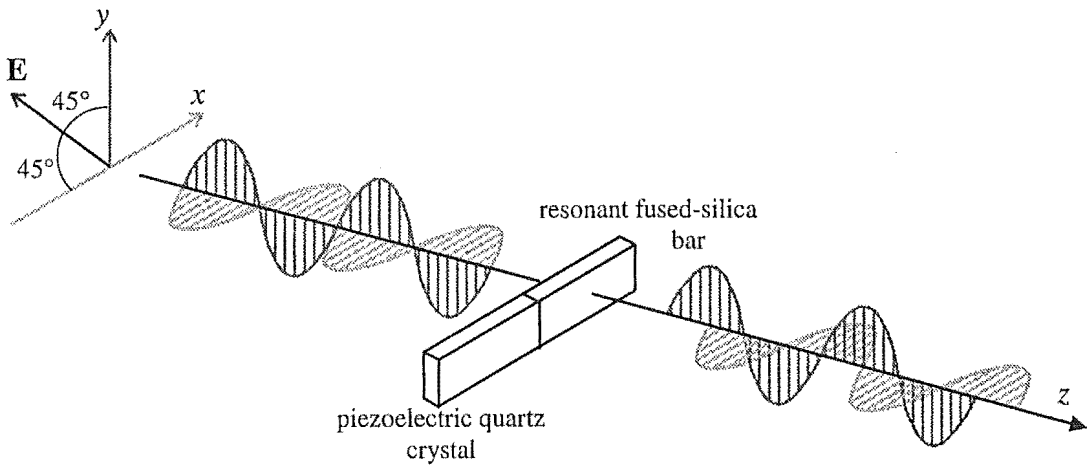

Figure 2.2. The effect of the PEM ($\lambda/4$ retardation) on the electric vector of light.

Over a modulation cycle, the polarisation oscillates between right-circular and left-circular polarisations, with linear and elliptical polarisations in between, as depicted in Figure 2.3. It has been shown by Misener[34] that the amount of lcp and rcp light passing through the sample is actually maximised at a peak retardation slightly greater than $\lambda/4$, but the resulting increase in signal is not large, and this correction has consequently not been made on either MOD3 or MOD4. The ratio of lcp (or rcp) light to total light incident on the sample in a half-cycle is determined by calibrating the spectrometer with *d*-10-camphorsulfonic acid, and comparing the CD and absorbance maximums for a series of concentrations. The ratio between these two values is $\Delta A_{290.5\text{ nm}}/A_{285\text{ nm}} = 6.854 \times 10^{-2}$, as determined by Chen and Yang[38] using optical rotatory dispersion.

It is important to avoid any linear dichroism or birefringences in the optical components between (and including) the PEM and the sample, as these will alter the degree of circular polarisation. In the matrix-isolation experiments reported in this work, a sapphire window is used as the deposition substrate. Since sapphire is linearly birefringent for light propagating in any direction other than exactly along the *c*-axis, the sample must be deposited on the *front* surface of the window, (*i.e.* the surface closest to the light source). Depolarisation of light by the sample

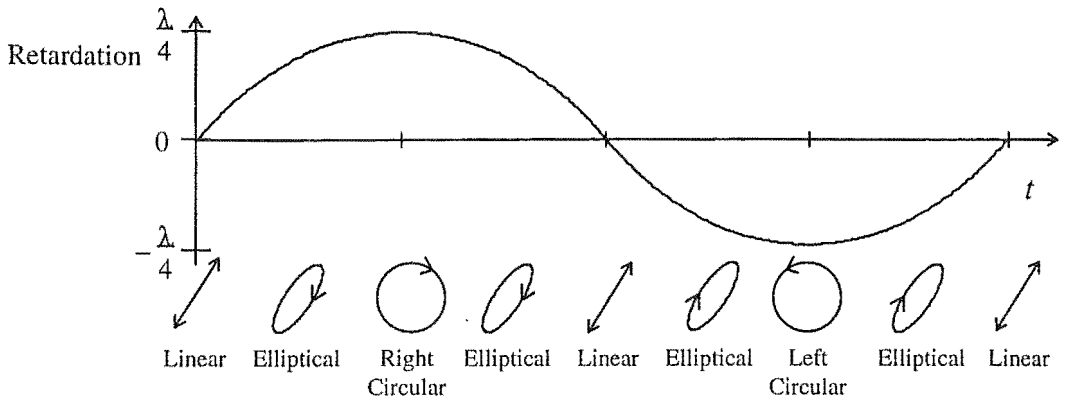

Figure 2.3. The variation in retardation over one PEM cycle, and the corresponding polarisations.

itself (due, for example, to scattering from microcrystals) is checked by comparing the natural CD of a reference solution of Λ-Co(III)tris(ethane-1,2-diamine) placed immediately before the detector, in the presence and absence of the sample. If the sample is causing depolarisation, the amount of lcp or rcp light reaching the reference solution will be diminished, and the CD signal of this solution consequently smaller.

2.2.3 Signal Processing

2.2.3.1 Absorbance

The absorbance of a sample is given by

$$A = -\log \frac{I}{I_0} \tag{2.1}$$

where I_0 is the intensity of the light prior to, and I the intensity of the light after passing through the sample. For the simultaneous measurement of absorption and MCD,

$$I = \frac{I_\mathrm{L} + I_\mathrm{R}}{2} \tag{2.2}$$

the subscripts L and R denoting lcp and rcp light respectively. In practice the signal intensities are determined as voltages, $V \propto I$. Writing A in terms of sample (s), reference (r) and dark (d) signals gives

$$A = -\log \frac{V_\mathrm{s} - V_\mathrm{d}}{V_\mathrm{r} - V_\mathrm{d}} \tag{2.3}$$

where V_s is the average of the 50 kHz alternating voltage due to the absorbance of lcp and rcp light.

The MOD4 spectrometer measures V_s, V_r and V_d explicitly, and calculates A digitally, thus directly determining the absorbance. With MOD3, a feed-back loop holds $V_s - V_d$ at a set level, so that

$$A = K + \log(V_r - V_d) \tag{2.4}$$

where K is a constant. The $V_r - V_d$ signal is passed through a logarithmic amplifier, giving a signal proportional to the absorbance. The proportionality constant depends on the value of $V_s - V_d$ and the amplifier gain, and is determined by calibration with didymium glass.

2.2.3.2 MCD

The circular dichroism of a species is the difference between the absorption of lcp and rcp light;

$$\Delta A = A_L - A_R \tag{2.5}$$

Using (2.1) and noting that the incident intensities of lcp and rcp are equal ($I_{0L} = I_{0R}$),

$$\Delta A = -\log \frac{I_L}{I_{0L}} + \log \frac{I_R}{I_{0R}} \tag{2.6}$$

$$= -\log \frac{I_L}{I_R} \tag{2.7}$$

Modification of the Maclaurin series for $\ln(x-1)$ and $\ln(x+1)$ gives

$$\ln x = 2\left(\frac{x-1}{x+1} + \frac{1}{3}\left(\frac{x-1}{x+1}\right)^3 + \frac{1}{5}\left(\frac{x-1}{x+1}\right)^5 + \frac{1}{7}\left(\frac{x-1}{x+1}\right)^7 \ldots\right) \tag{2.8}$$

Substituting for x and truncating after the first term gives

$$\Delta A = -2\frac{I_L - I_R}{I_L + I_R} \log e \tag{2.9}$$

This approximation is only valid when $I_L - I_R \ll I_L + I_R$, *i.e.* when the MCD is much weaker than the absorbance. It can be shown[34] that for the error introduced by the approximations in (2.9) to reach 1% the MCD required is $\Delta A = 0.15$, an extremely high value considering that MCD is usually a factor of $\sim 10^{-2}$ to 10^{-3}

smaller than A. This approximation also introduces an error into the absorption when it is measured in the presence of MCD, but this error is again negligible unless the MCD is of the same order of magnitude as the absorbance.[34]

2.3 Sample Preparation

2.3.1 The Compounds Studied

A range of metallophthalocyanines and metalloporphyrins have been studied. The majority of these were commercially synthesised, and used without further purification. CoPc, CuPc, ZnPc, and FePc were obtained from Strem, NiPc from Kodak, and nickel octaethylporphyrin (NiOEP) from Aldrich. Lutetium bisphthalocyanine ($LuPc_2$) was synthesised by VanCott.[39]

Copper tetrabenzoporphyrin (CuTBP) was synthesised by means of a template reaction. The zinc analogue was produced by reaction of zinc acetate and 2-acetylbenzoic acid in ammonia,[40] and then converted to the free-base by demetallation in concentrated sulfuric acid. The acid solution was neutralised by filtration into an ammonium hydroxide/ice mixture and the resulting H_2TBP precipitate was washed with boiling water and dried.[41] The H_2TBP was then refluxed with bis(acetylacetonato)copper(II) in chlorobenzene and the precipitate of CuTBP washed with hot methanol.

2.3.2 Matrix Isolation

2.3.2.1 Introduction

Matrix isolation is a technique whereby the molecules to be studied are embedded in, and separated from each other by a rigid host material. This host is usually a frozen gas, which is both chemically inert and transparent in the spectroscopic region of study. The first use of matrix isolation was described by Whittle, Dows and Pimentel[42] in 1954, and today the technique is used widely, especially for the study of unstable species such as radicals, atoms and reaction intermediates.

Matrix isolation also has advantages in the study of stable molecules as exemplified by porphyrins and phthalocyanines, since the separation of the species of

interest by the matrix reduces intermolecular interactions and thus allows molecular rather than bulk properties of the material to be analysed. In general, this leads to sharper spectral bands. Rare-gas elements (in this case Ar) are used as the host material as they are transparent down to vacuum-UV wavelengths, are optically isotropic, and interact only weakly with the embedded molecules.

A large number of reviews of the technique and applications of matrix isolation have been written. References to these, amid a comprehensive review of the literature up to 1986 are found in the excellent volume by Clark and Hester.[43]

2.3.2.2 Deposition of a Matrix

For the experiments described in this thesis, matrix isolation is achieved by sublimation of the material of interest, and co-deposition with Ar gas onto a cooled, *c*-cut sapphire window. An overview of the procedure is given here – the components involved are all described in more detail in the following sections.

The matrix-deposition apparatus is shown in Figure 2.4. It consists of a Knudsen oven attached to the side of either a continuous-flow cryostat (Section 2.4) or the cold head of a closed-cycle helium refrigerator (Section 2.5). The Ar gas is held in a 1-L reservoir and flows through an inlet in the back plate of the Knudsen oven. The sample is placed in the Knudsen oven, and the deposition apparatus evacuated to $< 10^{-5}$ torr with T1 and the needle valve fully open, but T2 closed. T1 is then opened, and the Ar flow rate adjusted to 0.3 - 0.6 torr min^{-1}at a pressure of ~700 torr (where 1 torr min^{-1} = 3.22 mmol hr^{-1}) using a Baratron pressure gauge (Section 2.4.2.7). T1 and T2 are then both closed, leaving the needle valve at its set position. (It has been found that if T2 is not closed, the vacuum affects the position of the needle valve, altering the flow rate.) After the flow rate has been set, the *c*-cut sapphire deposition window is cooled to < 20 K. This window is mounted on the end of either a siphon rod (Section 2.4.2.1) inside the continuous-flow cryostat, or the He refrigerator cold-head (Section 2.5).

The sample is contained in a Knudsen cell, which is positioned inside the furnace of the Knudsen oven. The furnace is then heated to the sublimation temperature of the sample (typically 200 - 400 °C for this work), as monitored by a chromel-alumel thermocouple. While this heating is taking place, the window is

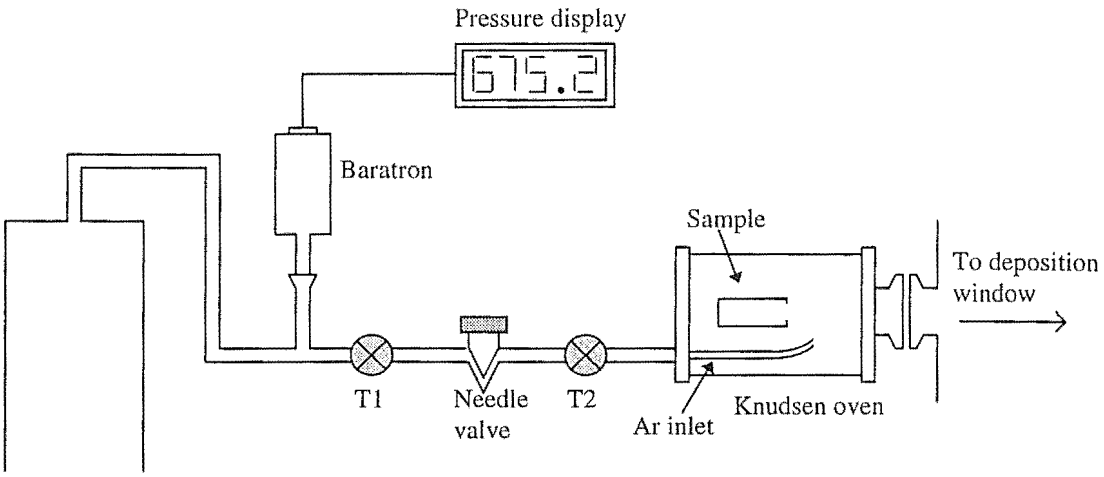

Figure 2.4. An overview of the matrix-deposition apparatus.

kept out of the deposition path and the shutters are closed. When the sublimation temperature is reached, T1 and T2 are opened, the window moved into position, and the shutters opened. Typical deposition times range from 10 min to 1 hr.

2.3.2.3 The Knudsen Oven

The Knudsen oven (Figure 2.5) consists of a brass back plate to which the furnace, thermocouple, argon inlet and shutters are attached. A glass viewing port is inset in the centre of the back plate to allow the cell to be observed. The plate seals by o-ring against a stainless-steel double-walled cylinder. Air or water is passed through the wall cavity to provide cooling. The Knudsen oven is locked to the deposition cryostat by means of a KW-25 Klein flange.

2.3.2.4 The Knudsen Cell

A Knudsen cell is a tube, sealed at one end, from which the material of interest is sublimed. Over the course of this work various designs have been trialed, including quartz open-ended cells, quartz 'pinhole' cells and glass 'pinhole' cells. It was found that the 'pinhole' cells gave the best results, especially in terms in achieving good matrix isolation of the sample. Since glass withstands the temperatures required for sublimation of the Pcs and porphyrins studied, the use of (more expensive) quartz was not necessary. The best, and most easily implemented design for a Knudsen

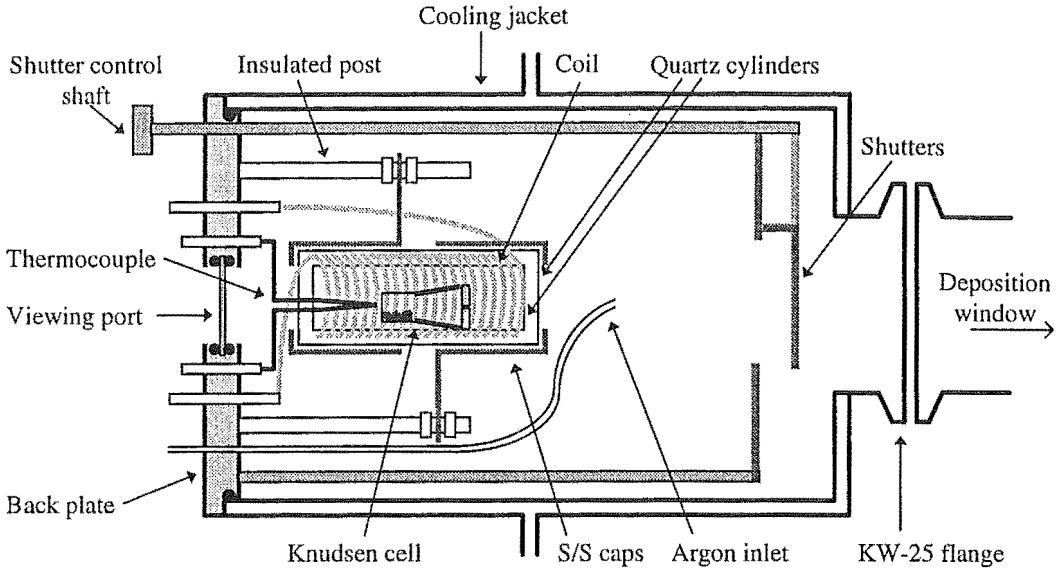

Figure 2.5. The Knudsen oven.

cell was found to be a modified B7 ground-glass joint, with the outer ends of both the cone and socket sealed, a dimple placed in the end of the socket (to position the thermocouple) and a small (ideally < 0.3 mm) hole drilled in the end of the cone. This gave a cell 18 mm in length, and 10 mm in diameter at the widest point.

The Knudsen cell is filled with $\sim$5 mg of the material of interest and then positioned inside the furnace, such that the rear of the cell rests against the thermocouple. An aluminium clip is used to prevent the cell from sliding out the front of the furnace. It is essential that when the system is evacuated, the pressure is reduced slowly, to avoid the material being sucked out of the cell, or the cell out of the furnace.

2.3.2.5 The Furnace

The furnace consists of a tightly wound coil of nichrome wire (21 gauge British Standard) sandwiched between two quartz cylinders. This assembly is held in place by two stainless-steel caps. A $\sim$5 mm clearance between the caps prevents electrical contact of the two ends of the coil. These caps are attached to the back plate of the oven by two insulated posts, and the ends of the coil attached to feedthroughs. It has been found that the tightness of the nichrome wire windings is critical to the success of the deposition. A loosely wound coil may cause temperature gradients along the Knudsen cell which allow redeposition of the sublimed material before it escapes

from the cell - this is likely to cause clogging of the pinhole. Such temperature gradients may also be caused if the front face of the cell is not set back a reasonable distance ($\sim$ 7 mm) from the front of the furnace. It is not necessary to prevent the furnace windings from touching, as the path of least resistance is still along the wire rather than across the windings.

2.3.2.6 The Thermocouple

A chromel-alumel thermocouple intrudes into the back of the furnace and is attached to insulated posts in the back plate of the oven. For consistent thermocouple readings it is important that the thermocouple is firmly attached, and that the position of the wire is not changed between depositions.

2.3.2.7 The Shutters

A set of shutters, placed $\sim$20 mm from the front of the furnace, have proved a very useful addition to the Knudsen oven. These are controlled from a shaft on the back plate, and can be closed while the oven is being heated to the desired temperature. They act both as a radiation shield, preventing warming of the deposition window, and as a visual aid - when closed, the back side of the shutters can be viewed through the glass viewing port, allowing determination of whether the sublimation temperature has been reached.

2.3.2.8 Determination of the Concentration of a Matrix

The concentration of a matrix is commonly described by the molar ratio of guest to host, $c_{\text{guest}} : c_{\text{Ar}}$. The concentration of guest molecules deposited on the window (mol L^{-1}) is,[32]

$$c_{\text{guest}} = \frac{\mathbf{A}_0}{326.6\mathcal{D}_0 l} \tag{2.10}$$

where $\mathbf{A}_0$ is the zeroth moment of the absorption (the area under the absorption band) and $\mathcal{D}_0$ is the dipole strength in (debye)^2. The pathlength, l (cm) is determined by the thickness of the Ar matrix;

$$l = \frac{REtM_{\text{R}}}{\pi r^2 \rho} \tag{2.11}$$

where R is the nominal deposition rate of Ar gas in mol hr^{-1}, E is the fractional efficiency of deposition, t is the deposition time, M_R is the relative molecular mass of Ar (40 g mol^{-1}), r is the radius of the deposition window and ρ is the density of Ar (1.62 g cm^{-3}).[44] The efficiency of deposition for our system was found to be ~10%. This was determined by timing the change in interference colours seen on the window at low Ar concentrations. The wavelength of light reflected is proportional to the thickness of the layer deposited (as quantified by the Bragg condition) hence measurement of the time taken for the reflected colour to cycle from red to red (~ 650 nm) allowed determination of the thickness of the matrix built up during this time.

The concentration of solid argon (mol L^{-1}) is

$$c_{Ar} = \frac{10^3 \rho}{M_R} \tag{2.12}$$

and hence the $c_{guest} : c_{Ar}$ ratio is given by

$$\frac{c_{guest}}{c_{Ar}} = \frac{\pi r^2 \mathbf{A}_0}{3.266 \times 10^5 R E t \mathcal{D}_0} \tag{2.13}$$

In the work reported here, $c_{guest} : c_{Ar}$ ratios are typically 1:2000 - 1:100000.

2.3.3 Polymer Films

While matrix isolation was the main method of sample preparation used in this thesis, a number of the more soluble porphyrins and phthalocyanines were also studied in polymer films. Both polymethylmethacrylate (PMMA, or perspex) and polyvinylchloride (PVC) films were used. These were produced by mixing a solution of the material of interest dissolved in a solvent with a solution of the powdered polymer dissolved in the same solvent. The resulting mixture was poured into a petri dish and left to dry overnight. The film was then mounted on the end of a sample rod which could be inserted into the cryomagnet. The solvents used with PMMA and PVC were chloroform and tetrahydrofuran respectively.

2.4 The Matrix Injection System

2.4.1 Introduction

Quantitative analysis of molecular systems which exhibit temperature-dependent MCD requires that the temperature of the material under examination be accurately known. This is best achieved by immersing the sample in a cryogenic fluid with which it is at thermal equilibrium. However, for matrix-isolation studies, the requirement of near vacuum for matrix preparation makes this very difficult to achieve. The vast majority of previous matrix-isolation spectroscopic studies have been conducted on samples that are mounted in a vacuum and cooled by conduction through the deposition substrate. This can give rise to serious thermometry problems, as thermal gradients, both within the sample and between the sample and the thermal sensor, may be substantial in comparison with the temperature indicated by the sensor. One of the aims of this thesis was to refine an 'injection' technique which overcomes this problem. Our injection instrument is modelled on, and has significant improvements over, one developed at the University of Virginia[45,46] which was unwieldy and difficult to use.

The matrix-injection system is based around three main components; a 6-T Oxford Instruments Spectromag SM4 cryomagnet, a modified CF1204 continuous-flow cryostat and a 1.7-m siphon rod (Figure 2.6). The SM4 sits in the optical bed of either spectrometer, such that the magnetic field is parallel to the light path. The CF1204 is interlocked to the top of the SM4 with the sample spaces of the two cryostats separated by a gate valve so that they can be independently evacuated. The siphon rod is top-loaded into the CF1204. A matrix-deposition window mounted at the end of the rod is cooled by drawing liquid helium through the siphon using a diaphragm pump.

2.4.1.1 Injection Procedure

With the rod retracted and the gate valve closed, the matrix-isolated sample is prepared within the CF1204, as described in Section 2.3.2.2. A turbo pump is used to evacuate the CF1204 and Knudsen oven (*via* V2 and V3 – see Figure 2.7) to $< 10^{-5}$ torr. At the same time, the sample chamber of the cryomagnet is precooled with *l*He (Section 2.4.2.4), and then evacuated by a mercury diffusion pump *via* V5

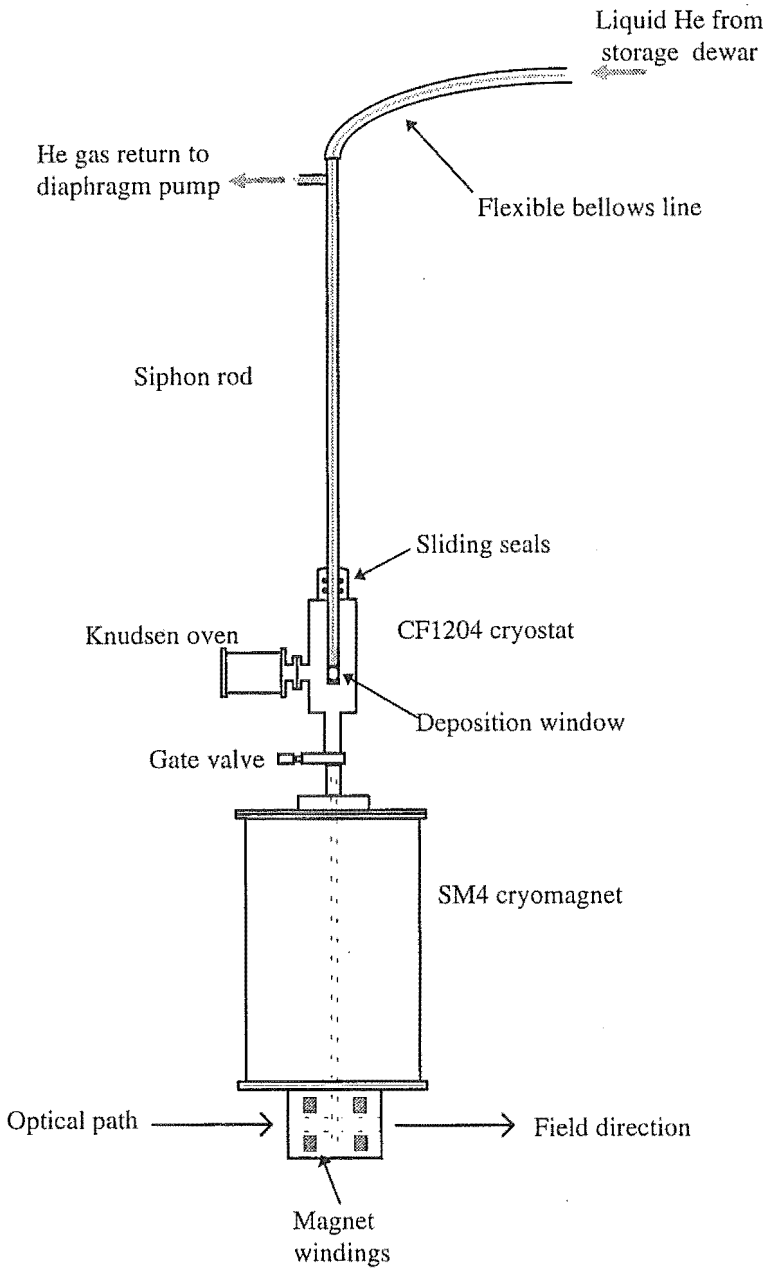

Figure 2.6. An overview of the matrix-injection system.

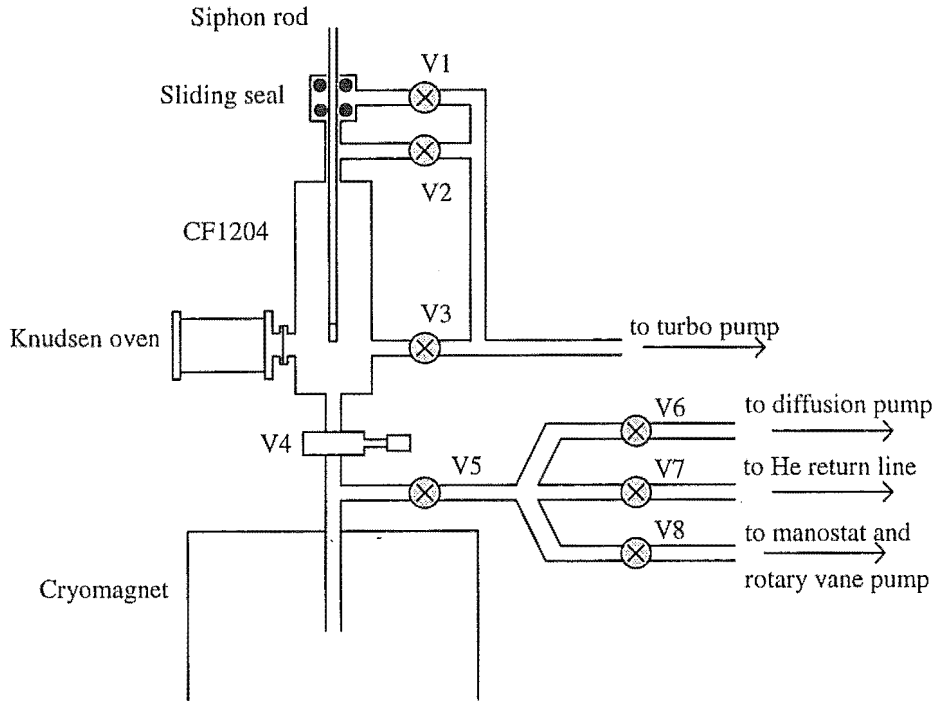

Figure 2.7. The evacuation system for the matrix-injection apparatus.

and V6. If the matrix deposition is complete before the sample chamber has been evacuated, it is important to push the rod down slightly, so that the window is out of the deposition path. If this is not done, the matrix may suddenly go cloudy or crack, for reasons which remain unclear.

After matrix deposition, the gate valve (V4) is opened, and V2 and V3 shut, so that both the deposition system and the sample region of the SM4 are pumped by the mercury diffusion pump. At the same time, a small space between two sliding seals at the top of the CF1204 is evacuated by the turbo pump (*via* V1) to prevent air leaks, which can destroy the matrix and block the internal needle valve of the SM4. The rod is then 'injected' slowly into the precooled sample chamber of the SM4. Care must be taken that the pressure around the sliding seals does not increase above 10^{-4} torr, to avoid air entering the system. Once the deposition window is positioned in the optical path of the spectrometer, V5 is closed, and the sample chamber is flooded with liquid or cold gaseous helium by opening the SM4 needle valve (Section 2.4.2.4). Temperatures between 4.2 and 1.4 K can then be achieved and maintained by pumping on the liquid in the sample chamber using a rotary-vane pump controlled by a manostat (Section 2.4.2.6). Higher temperatures

of 30 - 4.2 K may be obtained by bathing the matrix in cold He vapour and using the SM4 sample chamber as a continuous-flow cryostat.

The SM4 cryomagnet was also used for the study of polymer films. In these cases, the CF1204, siphon rod and Knudsen oven are not necessary, and the sample is mounted on the end of a shorter rod. Admission of air into the sample chamber is prevented by maintaining a positive internal pressure of He gas while the rod is being inserted.

2.4.2 The Components

2.4.2.1 The Siphon Rod

The siphon rod is 1.7 m long and ~12 mm in diameter. It is composed of thin-walled stainless steel, and houses two stainless-steel capillaries surrounded by a vacuum. The rod is connected by ~2 m of bellows to a second leg, which is inserted into the *l*He storage dewar as shown in Figure 2.8. Figure 2.9 shows a close-up view of the end of the rod. The deposition surface, a *c*-cut sapphire window, is mounted on a copper block, with indium used to create good thermal links between these components. A pump is used to draw *l*He from the storage dewar along the flexible bellows and down through one capillary. The cold fluid fills a small reservoir at the end of the rod, cooling the copper block by direct contact, and hence the deposition window, by conduction. The He gas produced as a result of the heat exchange is pumped back up the return capillary to a He recovery line. The temperature is monitored by a carbon resistance thermometer mounted in the He reservoir. A needle-valve controller between the siphon and the diaphragm pump is used to vary the flow of *l*He through the rod. It has been found that a flow rate of 1.5 - 2.0 L hr^{-1} is required to cool the deposition window to $< 20K$.

2.4.2.2 The Continuous-Flow Cryostat

In the system described above, the CF1204 is used primarily as a vacuum vessel to which the Knudsen oven is attached, and in which the sapphire window is positioned during matrix deposition. The CF1204 itself is not used to provide cooling.

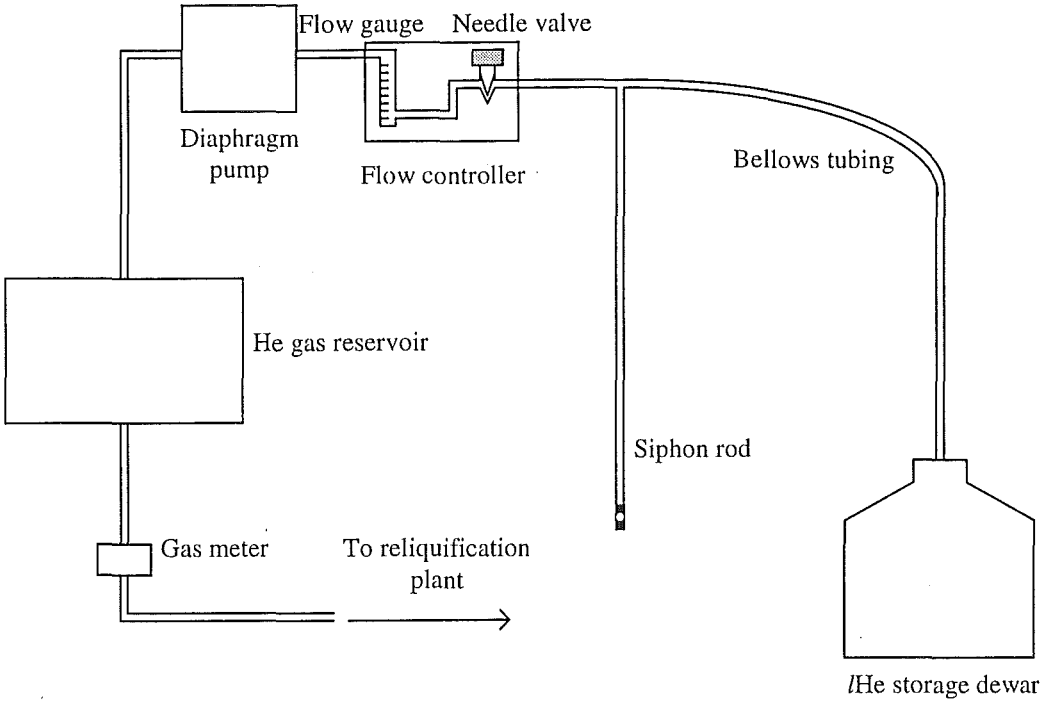

Figure 2.8. Overview of the siphon-rod cooling system.

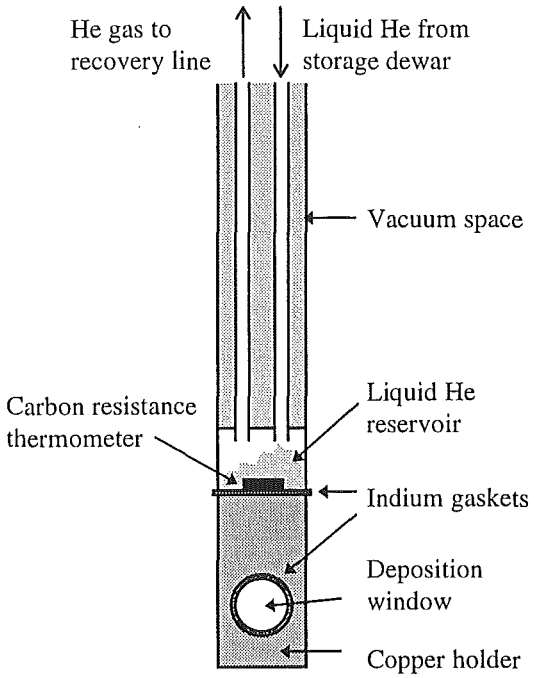

Figure 2.9. The deposition window mounted on the end of the siphon rod.

2.4.2.3 The Cryomagnet

The split-pair superconducting magnet, shown in Figure 2.10, is cooled by a *l*He bath cryostat. In order to minimise the boil off of He due to heat load, an intermediate-temperature radiation shield cooled by a liquid-nitrogen (lN$_2$) jacket, and an insulating vacuum space evacuated to 10^{-5} torr are employed. The emissivity of the lN$_2$-cooled shield is minimised by use of interleaved layers of aluminium and insulation, known as 'super insulation'. Metallic conduction by the struts supporting the cryostat is reduced with the use of stainless-steel tubes of minimum cross-section and maximum possible length. When the matrix is injected, the siphon rod passes down through the centre of the bath cryostat until the matrix is positioned in a sample chamber between the tails of the magnet. This chamber is known as the variable-temperature insert (VTI).

2.4.2.4 The Variable Temperature Insert

The flow of *l*He into the VTI is controlled by a needle valve, which siphons liquid out of the bath cryostat (Figure 2.10). A valuable advantage of our system over other cryomagnets is that in the event of air or Ar gas entering the VTI and blocking the needle valve, a 68-ohm resistive heater coiled around the valve may be used to heat the frozen material and so remove the blockage. In the absence of this very useful device, it would be necessary to let the entire system (including the magnet) warm up to room temperature, thus wasting all the *l*He in the system at the time.

Prior to injection of the matrix, the VTI is cooled to $\sim$10 K. This is achieved by admitting cold He gas through the needle valve. After the chamber has been cooled sufficiently, it must be re-evacuated, to avoid destruction of the matrix by warmer He up around the neck of the cryomagnet.

Once the matrix has been injected, the needle valve is opened and the flow of He through the siphon rod halted, the temperature of the matrix henceforth being controlled by the VTI. To measure temperatures above 4.2 K, the VTI is filled with cold gas by opening the needle valve, but keeping the valve on the He return line (V7 in Figure 2.7) closed. When the pressure in the VTI has risen to 1 atm, flow through the needle valve, and hence the temperature, can be controlled by throttling

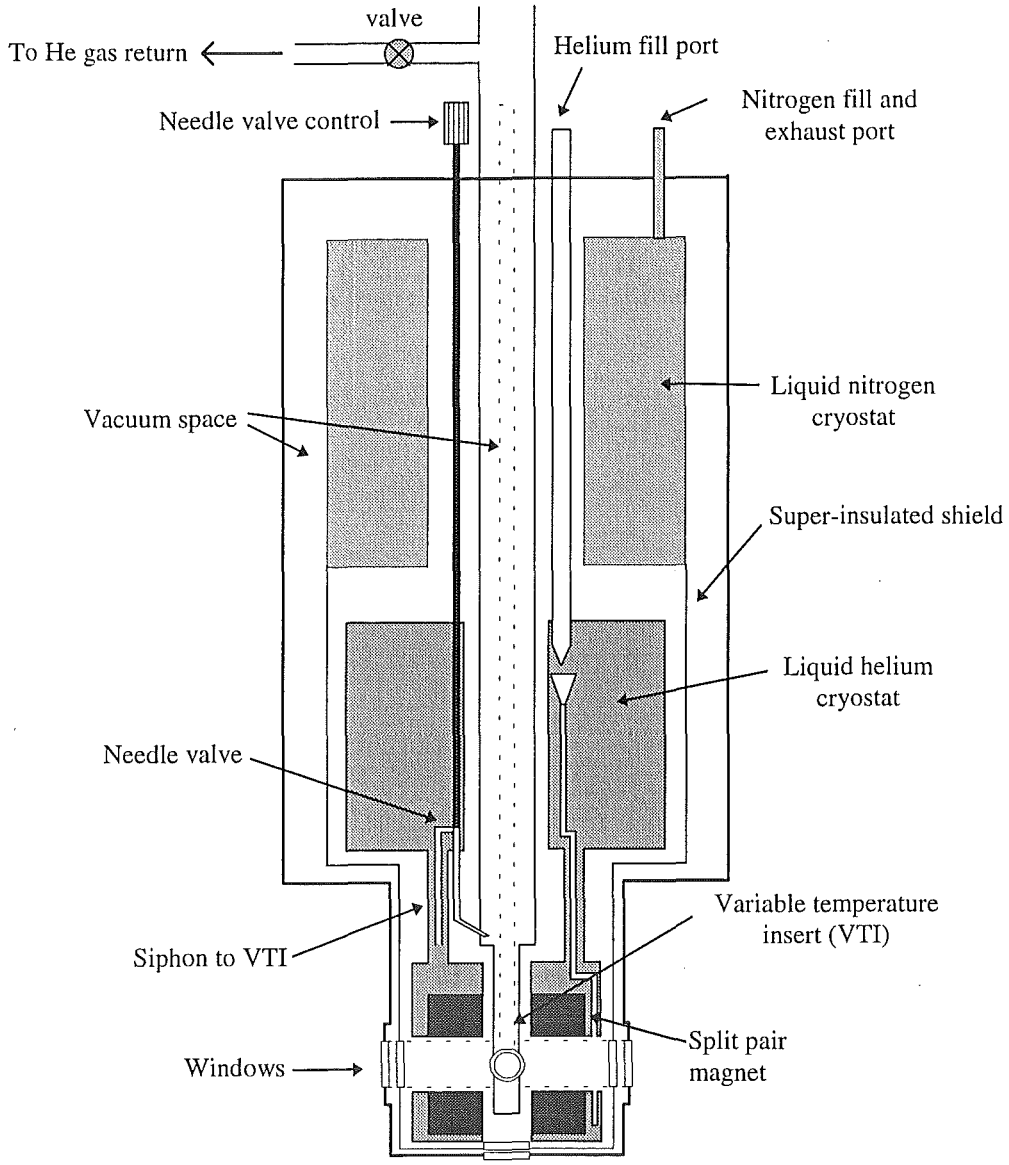

Figure 2.10. The cryomagnet.

the return line. The temperature is measured by means of two carbon resistance thermometers; one in the tip of the rod, the other in the VTI.

Temperatures below 4.2 K are achieved by filling the VTI with *l*He then pumping with a rotary-vane pump (via V8 in Figure 2.7). The *l*He level may be monitored with the VTI He-level indicator. To make maximum use of the helium it is best to fill the VTI to above the maximum level shown on the indicator. It has been found that filling until the metal of the evacuation port at the neck of the cryomagnet feels cold (approx 5 min) gives enough He to allow about three hours of pumping. The temperature is indirectly controlled by controlling the He vapour

pressure with a manostat (Section 2.4.2.6). Temperatures down to 1.4 K may be achieved and maintained, to within 1% precision.[47]

2.4.2.5 The He-Level Indicators

The levels of *l*He in the VTI and the *l*He bath cryostat are monitored by two vertical NbTi wires. The portion of the wire below the surface of the liquid becomes superconducting, while that above the surface is non-superconducting. A current is passed and the resulting voltage (contributed to by the resistive portion of the wire only) is measured. From this voltage, the *l*He level can be determined, and is shown on the display unit. As this procedure dissipates heat, measurements are made using intermittent pulses.

2.4.2.6 The Manostat

An Oxford Instruments MNT manostat (Figure 2.11), in conjunction with a rotary-vane pump, is used to control the vapour pressure of He, allowing temperatures of 1.4 - 4.2 K to be reached. It operates by comparing the vapour pressure over the *l*He with a fixed reference pressure. This reference pressure is set by opening the 'set reference' valve and then slowly opening the bypass valve. When the desired pressure is reached, as determined by the baratron, both valves are closed. The VTI is then open to the pump, *via* the control orifice, until such time as the pressure in

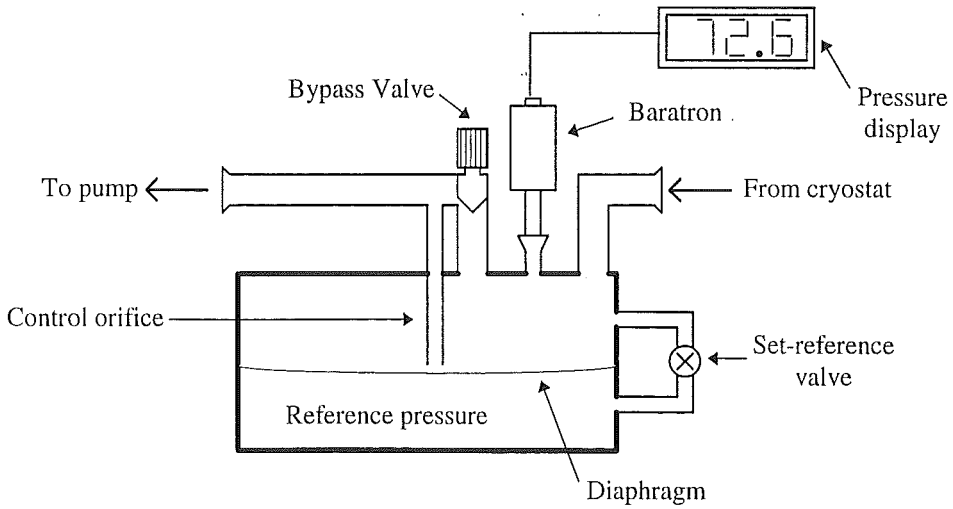

Figure 2.11. The manostat.

this volume falls below the pressure in the reference compartment, when the end of the control orifice is closed by the diaphragm. In this manner the pressure in the VTI is controlled at the set value. The relationship between vapour pressure and temperature of He is well known,[48] and may be used to determine the temperature of the matrix both precisely and accurately.

2.4.2.7 The Baratron

The He vapour pressure and the Ar pressure are measured with a MKS Baratron 662 absolute pressure transducer with a 1000-torr range. The pressure is displayed on a MKS PDR-D-1 power supply/digital readout. The baratron uses a capacitance transducer to determine the absolute pressure of a gas. It consists of two chambers, separated by an elastic metal diaphragm. One chamber is connected through the inlet port to the system to be analysed. The reference chamber is held at 10^{-7} torr by a chemical getter system, and contains a rigidly mounted ceramic block holding two electrodes. Each of these electrodes forms one half of a capacitor, the other half being the diaphragm. The diaphragm deflects with changing absolute pressure (independently of gas composition) causing an imbalance in the two capacitances as the diaphragm moves further away from one electrode than the other. A bridge excited by an AC source is used to determine the DC voltage produced from the changing capacitances. The resulting signal is conditioned, giving a 0-10 V DC signal scaled to the pressure range of the baratron.

2.4.3 Procedures for Preparation of the Cryomagnet

2.4.3.1 Filling the Cryomagnet

- Evacuate the vacuum jacket to $<10^{-5}$ torr for several days.
- Fill the lN$_2$ and lHe jackets with lN$_2$, and leave for 24 hours. It is important to continue evacuating the vacuum space during this time, to avoid condensation of water on the windows in the optical path.
- Top up the lHe jacket with lN$_2$, then use N$_2$ gas to blow the lN$_2$ out into the lN$_2$ jacket. When all the liquid is transferred, evacuate the lHe jacket for at least 10 min using the rotary-vane pump, then back fill with He gas. Repeat this procedure at least twice. Monitor the pressure in the lHe jacket while evacuating.

If the falling pressure seems to halt between 70-100 torr it is likely that lN$_2$ is still present in the lHe jacket. It is very important to remove this completely by means of further pump/purge cycles.

- Open the cryomagnet needle valve, to remove any lN$_2$ remaining in the needle-valve siphon.
- Evacuate the vacuum jacket of the transfer tube and blow He gas through the tube to check for blockages.
- Connect a one-way valve to the cryostat exhaust port.
- Position the lHe dewar on the forklift so that its level can be raised as necessary.
- Close off the return line on the storage dewar to allow this volume to be pressurised. Insert the two ends of the transfer tube into the storage dewar and the entry port on the cryomagnet simultaneously. Push both ends down slowly, allowing the tube to cool, and thus conserving He. Make sure the transfer tube is inserted as far down as possible into the cryomagnet; this places the end of the tube in a cone which forces the liquid through a capillary to the bottom of the magnet (Figure 2.10). In this way, maximum use of the cold gas is made in cooling the large metallic mass of the magnet coils.
- The pressure in the He storage dewar will cause a certain amount of He to be transferred. Once this pressure reduces, transfer may be continued by squeezing the rubber bladder on the dewar. Transfer of liquid begins when the temperature of the cryostat (as measured by a 270-Ω Allen-Bradley resistor) reaches 4.2 K (about $1\frac{1}{2}$ hours after insertion of the transfer tube). The level of the liquid may then be monitored using the cryostat He level indicator. If transfer is very slow, the rate may be increased by pressurising the storage dewar with He from a high-pressure cylinder. When the magnet is full ($\sim \frac{1}{2}$ an hour) transfer may be halted by releasing the pressure in the storage dewar. The magnet is usually filled to $\sim$ 75%, (requiring $\sim$19-23 L of lHe) which provides about 36 hours of static operation. The boil off of the top 25% is too rapid to warrant filling to 100%.

2.4.3.2 Refilling the Cryomagnet

- The boil-off rate under static conditions is 1.5 - 1.8% per hour. This may increase to $\sim$ 3% per hour when the field is being ramped. Rates exceeding these probably

indicate problems with insulation or seals within the SM4.

- Refilling should be carried out before the He level in the bath cryostat falls below 10%.
- It is important not to boil off existing *l*He with the warm gas which will initially pass through the transfer tube. For this reason, slowly insert one leg of the transfer tube into the storage dewar, but leave the other leg out in the open. Again, the return line on the storage dewar should be closed to allow the vessel to pressurise. Eventually a white vapour plume will be seen coming from the open end of the tube. When this changes to a blue tongue, raise the dewar end of the transfer tube out of the liquid, and quickly insert the open end of the tube into the cryostat.
- Do not push the tube right down into the cone on the magnet, as this will disturb the *l*He already present. The newly introduced liquid should be sprayed onto the top of the liquid already in the reservoir.
- Refilling the cryomagnet to 75% requires $\sim$ 8 L of *l*He. Overall, a 60 L storage dewar provides enough *l*He for $\sim$ 4 days operation.

2.4.3.3 Energising the Magnet

Field is put into the magnet by means of a superconducting switch. The magnet consists of coils of superconducting NbTi wire connected to two non-superconducting copper leads. The leads are bridged by the superconducting switch - a length of superconducting wire non-inductively wound with an electrical heater (the switch heater). An equivalent circuit is shown in Figure 2.12(a). The procedure for energising the magnet (once cooled to 4.2 K) is as follows:

- Turn the switch heater on. This raises the temperature of the switch, putting it in a (non-superconducting) resistive state.
- Ramp up the power supply (Oxford Instruments PS 75 Mk III) using the sweep generator (Oxford Instruments SG3). This causes a current to flow in the circuit, setting up magnetic flux through the coils (Figure 2.12(b)).
- When the desired current/field is achieved, turn the switch heater off. This makes the switch superconducting, and so creates a closed resistanceless circuit (Figure 2.12(c)).
- Use the sweep generator to ramp the current out of the leads slowly. As this

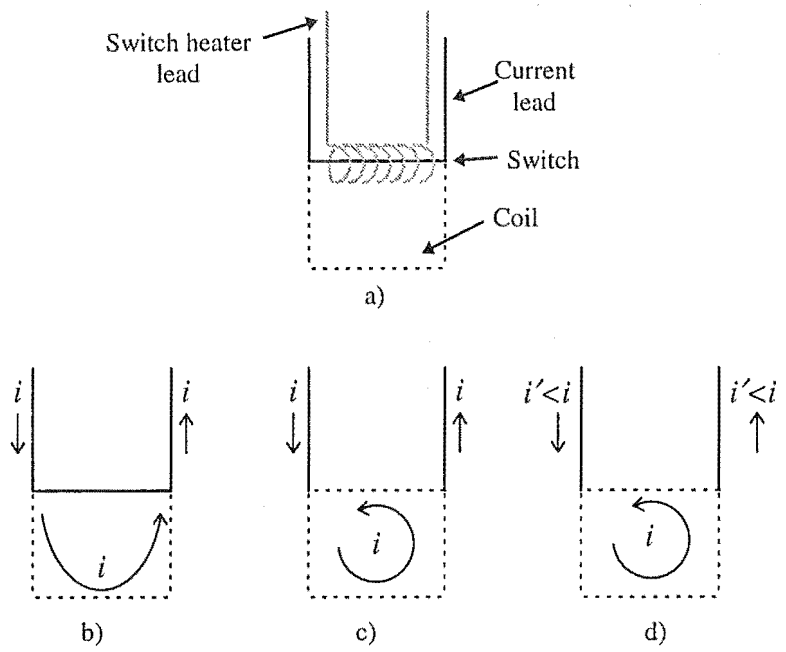

Figure 2.12. Steps involved in energising the super-conducting magnet. Solid lines represent non-superconducting components, and dashed lines represent superconducting components. Part (a) shows the circuit involved. Parts (b) - (d) are explained in the text.

happens, the system will resist any change in the magnetic flux, (Faraday's law of induction) and the magnetic field which was present at the time the switch heater was turned off will remain in the superconducting circuit indefinitely[49,50] (Figure 2.12(d)). This state is known as persistent mode.

- Field is removed from the magnet by heating the switch to make it non-superconducting, and then using the sweep generator to ramp the current back down to zero. Note that it is important that the current in the generator matches the current in the magnet at the time the switch is heated, to avoid quenching the magnet.

2.5 The Helium Refrigerator and Electromagnet

The matrix injection system described above gives excellent results, but is complicated, and, due to the amount of *l*He required, very expensive to use. For these reasons, preliminary absorption and MCD measurements are made using a helium refrigerator and electromagnet. The operation of this system will be described in detail by Langford.[37]

The APD Cryogenics HC-2D He refrigerator consists of a He compressor, an expander unit, and interconnecting gas lines. The expander is a two-stage cryogenic refrigerator operating on the Gifford-McMahon refrigeration cycle. The Knudsen oven is mounted to the side of the expander unit and the matrix deposited, under vacuum, onto a sapphire window cooled to ~12 - 15 K. The inner section of the expander is then rotated by 90° so that the deposition window is in the light path of the spectrometer. The c-frame electromagnet is an Alpha Magnetics Inc. Model 4800 with a 4-inch adjustable gap, and is positioned around the He refrigerator. Current is provided by a Hewlett-Packard 6269B DC power supply. At the pole gap required to accommodate the refrigerator cold-head, the magnet can produce fields of up to 0.7 T, using a current of 50 A.

The range of temperatures and fields which can be explored using this setup is limited, and the temperatures cannot be determined accurately. However, it is far simpler and cheaper to use than the cryomagnet, and so is extremely useful for determining optimum deposition conditions, and for the study of materials which do not exhibit temperature dependence.

2.6 Hole-Burning Measurements

The hole-burning experiments described in this thesis were carried out in the laboratory of Dr Elmars Krausz at the Research School of Chemistry, ANU. The procedure for these experiments was to deposit and inject the matrix, and then measure absorption and MCD spectra before and after irradiation of the sample with high-intensity monochromatic light from a laser.

The matrix deposition and injection techniques were virtually identical to those described thus far, the main exception being that matrices were deposited on to a sapphire window cooled, not via the rod, but by conduction through an Oxford Instruments CF204 continuous-flow cryostat. The injection apparatus was essentially the instrument developed at the University of Virginia,[45,46] with a few modifications.[51] A forcing mechanism at the top of the rod was used to enable contact between the copper block holding the window and the cryostat. Active cooling was suspended during injection, (unlike the UOC injection system) so the process needed to be relatively rapid and well coordinated. If the temperature exceeded ~35 K the

matrix was lost. Because of this method of cooling, heat transfer down the rod to the sample window became a problem. This was overcome by using 0.25-mm titanium tube in the lower sections of the rod rather than stainless steel, to reduce the heat conductivity.

During the deposition, the absorption spectrum of the sample was monitored *in situ* by a single-beam spectrometer based on a $\frac{1}{2}$-m Czerny-Turner monochromator.[52] After injection, the VTI was flooded with *l*He and the temperature lowered to < 2 K. A Spectra-Physics 375 dye laser (line width $\simeq 1$ cm^{-1}) with Exciton DCM dye was then used to irradiate the samples. The wavelength of the laser was monitored with a Burleigh Wavemeter jr WA-2000. The laser beam was defocussed, and the entire area of the sample evenly illuminated with a flux of 1-20 mW cm^{-2}. Absorption and MCD were measured simultaneously using a single-beam spectrometer based on a $\frac{3}{4}$-m SPEX monochromator, with a bandpass of 0.2 nm.[53] A 57 kHz Infrasil PEM is used to create the circularly polarised light, and the resulting beam chopped by a tuning-fork chopper at 800 Hz. The signal processing techniques used were quite different to those described for MOD3 and MOD4. In particular, a double lock-in-amplifier system was used.

Chapter 3

Theoretical Aspects of Data Analysis

3.1 Introduction

In this chapter, the main theoretical aspects of the work discussed in this thesis are presented. It should be noted that the material included is not intended to provide either a full or thorough coverage, but rather is a fairly simple working basis from which to understand the results derived in later chapters. An excellent detailed description of the theory involved with MCD spectroscopy is given by Piepho and Schatz[32], from which this chapter draws heavily.

The chapter begins with a discussion, in Section 3.2, of some of the conventions used in this thesis. The form of the molecular Hamiltonian is then considered (Section 3.3), along with the approximations necessary to reduce this to a solvable form. The treatment of spin-orbit (SO) coupling and the Zeeman effect is also explained.

After a qualitative description of the dispersion forms arising in MCD spectra (Section 3.4), theoretical expressions for these dispersions are derived, beginning with the relationship between the (experimentally observable) absorbance, and the transition-moment integral (Section 3.5). This relationship forms the fundamental basis of the application of group theory to absorption and MCD spectroscopy. Expressions are first derived at zero field, and the effect of an external magnetic field then considered. Simplification of matrix elements is made possible by use of the Wigner-Eckart theorem (Section 3.6). Once theoretical expressions for absorption and MCD have been obtained, some means of relating these to experimentally measured spectra is required. The method used in this work is moment analysis, as discussed in Section 3.7.

Note that theory specific to hole-burning spectroscopy is not covered in this chapter. Discussion of such topics is found at the start of Chapter 7.

3.2 Conventions

In this thesis, a convention common in spectroscopy is followed, where 'energies' are given in units of cm^{-1}, even though these are strictly the units of wavenumbers ($E = hc\overline{\nu}$). Following from this, a number of important coefficients have non-conventional units, with the Bohr magneton, and the Boltzmann and Planck constants given by

$$\mu_B = 0.4669 \text{ cm}^{-1} \text{ T}^{-1} \tag{3.1}$$

$$k = 0.6951 \text{ cm}^{-1} \text{ K}^{-1} \tag{3.2}$$

$$h = 3.336 \times 10^{-11} \text{ cm}^{-1} \text{ s} \tag{3.3}$$

respectively. In the expression of Hamiltonians, atomic units are used, where the unit of mass is the mass of an electron, m_e, the unit of charge is the charge of a proton, e', and the unit of angular momentum is $\hbar = h/2\pi$. Fixed laboratory coordinates are defined as X, Y, Z, with the magnetic field direction as Z. The coordinates x, y, z are used to denote the molecular axes, where z represents the principal symmetry axis.

The components of a vector (or pseudo vector) operator in a real, molecule-fixed cartesian basis are

$$\mathbf{V} = (V_x, V_y, V_z) \tag{3.4}$$

It is often convenient to change to a complex basis,

$$\mathbf{V} = (V_{-1}, V_0, V_{+1}) \tag{3.5}$$

where

$$V_{-1} = \frac{1}{\sqrt{2}}(V_x - iV_y), \quad V_0 = V_z, \quad V_{+1} = -\frac{1}{\sqrt{2}}(V_x + iV_y) \tag{3.6}$$

In addition, one can define raising and lowering operators,

$$V_{\pm} = \mp\sqrt{2}V_{\pm 1} = (V_x \pm iV_y) \tag{3.7}$$

Throughout this work, integrals are represented in Dirac braket notation;

$$\left\langle \Psi_m \left| \widehat{O} \right| \Psi_n \right\rangle = \int \Psi_m^* \, \widehat{O} \, \Psi_n \, d\tau \tag{3.8}$$

where Ψ_m and Ψ_n are functions, $\widehat{O}$ is an operator, $*$ indicates the complex conjugate, and the integral is carried out over all coordinates of the system.

With regard to representation of transitions, the conventions of Piepho and Schatz[32] are followed, with the lower energy state written on the left, and the direction of the arrow indicating the nature of the process. Hence, labelling the ground state as A and the excited state as J, $A \rightarrow J$ represents absorption, and $A \leftarrow J$ represents emission. Similarly, in transition-moment matrix elements, the ground state is written on the left-hand side, *i.e.* $\langle A \left| \mathbf{m} \right| J \rangle$,where $\mathbf{m}$ is the electric-dipole operator.

3.3 The Molecular Hamiltonian

In this section, an expression for the molecular Hamiltonian is given, and a number of approximations useful in its solution are explained. Treatment of effects relevant to the work covered in this thesis, namely SO coupling and the Zeeman effect, are also discussed.

The basic molecular Hamiltonian may be written in atomic units as

$$\mathcal{H}_{\text{mol}} = -\frac{1}{2}\sum_{\alpha} \nabla_{\alpha}^2 - \frac{1}{2}\sum_{i} \nabla_{i}^2 + \sum_{\alpha}\sum_{\beta>\alpha} \frac{Z_\alpha Z_\beta}{r_{\alpha\beta}} - \sum_{\alpha}\sum_{i} \frac{Z_\alpha}{r_{i\alpha}} + \sum_{j}\sum_{i>j} \frac{1}{r_{ij}} \tag{3.9}$$

where α and β refer to nuclei and i and j to electrons. The first and second terms are the operators for the nuclear and electronic kinetic energy respectively. The remaining three terms are potential energy terms. The first of these refers to repulsive interactions between nuclei ($r_{\alpha\beta}$ being the distance between nuclei of atomic number Z_α and Z_β), the next to the attractive interactions between electrons and nuclei, and the last to the repulsive interactions between electrons.

Defining the full set of electronic and nuclear spatial coordinates by q and Q respectively, (3.9) can be rewritten as

$$\begin{aligned} \mathcal{H}_{\text{mol}}(q,Q) &= T_n(Q) + T_e(q) + V_{nn}(Q) + V_{ee}(q) + V_{en}(q,Q) \\ &= T_n(Q) + T_e(q) + V(q,Q) \end{aligned} \tag{3.10}$$

where T and V represent kinetic- and potential-energy operators respectively, and the subscripts indicate nuclear (n) and electronic (e) properties. The full vibronic Schrodinger equation is then given by

$$\mathcal{H}_{\mathrm{mol}}(q,Q)\ \Psi_k(q,Q) = E_k\ \Psi_k(q,Q) \tag{3.11}$$

3.3.1 The Born-Oppenheimer Approximation

Unfortunately, (3.11), requiring simultaneous consideration of all the particles (electrons and nuclei) in the system, is intrinsically unsolvable for a many-body problem such as the case of a polyatomic molecule. The best that can be achieved is an approximate solution using an approximate Hamiltonian. One of the most commonly used steps is to separate out the parts of (3.10) which depend on the electronic coordinates, and are independent of the nuclear kinetic energy, into an electronic Hamiltonian

$$\mathcal{H}_{\mathrm{el}}(q,Q) = T_e(q) + V(q,Q) \tag{3.12}$$

The utility of this separation derives from the fact that nuclear velocities are small compared with electronic velocities (as a consequence of the vastly different masses of the two types of particle) and so the nuclear motions should, at least approximately, be decoupled from those of the electrons. The assumption of such decoupling is known as the Born-Oppenheimer approximation.

For a fixed nuclear configuration, Q, the electronic Schrodinger equation may be written as

$$\mathcal{H}_{\mathrm{el}}(q,Q)\phi_k(q,Q) = W_k(Q)\phi_k(q,Q) \tag{3.13}$$

where the eigenfunction $\phi_k(q,Q)$ depends on Q. The eigenvalue $W_k(Q)$ is also a function of Q, and is generally referred to as the 'electronic potential energy' (though note from (3.12) and (3.10) that it also contains contributions due to nuclear-nuclear repulsion). In many applications, W_k is treated as a model potential, such as that of a harmonic or a Morse oscillator.

In the BO approximation, the solutions of (3.11) now take the form

$$\Psi_k(q,Q) = \phi_k(q,Q)\,\chi_k(Q) \tag{3.14}$$

where the vibrational function $\chi_k(Q)$ is dependent on nuclear coordinates only. The corresponding eigenvalues are

$$E_k = T_{nk}(Q) + W_k(Q) \tag{3.15}$$

i.e. the total energy (which is constant for a given vibronic state) is the sum of a nuclear kinetic term (T_n) and a potential term (W), both of which are Q dependent.

3.3.2 The Franck-Condon Approximation

The Franck-Condon (FC) principle is used to explain the appearance of the vibrational structure of a band. Because the nuclei are much more massive than the electrons, an electronic transition takes place before the nuclei can respond. On an potential-energy diagram, a FC transition is represented by a vertical line, as there is assumed to be no change in nuclear coordinates accompanying the electronic transition.

Consider now the quantum-mechanical formulation of this approximation. Firstly, note that the transition dipole moment operator, $\mathbf{m}$, comprises both electronic and nuclear parts,

$$\begin{aligned} \mathbf{m}(q,Q) &= -\sum_i q_i + \sum_\alpha Z_\alpha Q_\alpha \\ &= \mathbf{m}(q) + \mathbf{m}(Q) \end{aligned} \tag{3.16}$$

Assuming BO separability as given in (3.14), it is obtained that

$$\begin{aligned} \langle \Psi_k(q,Q)|\,\mathbf{m}\,|\Psi_j(q,Q)\rangle &= \langle \phi_k(q,Q)\chi_k(Q)|\,\mathbf{m}(q)+\mathbf{m}(Q)\,|\phi_j(q,Q)\chi_j(Q)\rangle \\ &\simeq \langle \phi_k(q,Q)|\,\mathbf{m}(q)\,|\phi_j(q,Q)\rangle\,\langle \chi_k(Q)|\chi_j(Q)\rangle \\ &\quad + \langle \chi_k(Q)|\,\mathbf{m}(Q)\,|\chi_k(Q)\rangle\,\langle \phi_k(q,Q)|\phi_j(q,Q)\rangle \end{aligned} \tag{3.17}$$

The last term in the expression above requires that the electronic wavefunctions are only weakly dependent on Q. Since the ground- and excited-state electronic wavefunctions are orthogonal, this last term is zero, giving

$$\langle \Psi_k(q,Q)|\,\mathbf{m}\,|\Psi_j(q,Q)\rangle = \langle \phi_k(q,Q_0)|\,\mathbf{m}(q)\,|\phi_j(q,Q_0)\rangle\,\langle \chi_k(Q)|\chi_j(Q)\rangle \tag{3.18}$$

where it has been assumed that the electronic functions are sufficiently slow-varying in Q that the ground-state equilibrium coordinate, Q_0, can be used. The integral $\langle \chi_k(Q) | \chi_j(Q) \rangle$ is known as the FC overlap factor.

3.3.3 Spin-Orbit Coupling

SO coupling may be described as the interaction between the electric field in which an electron moves, and the relativistic electric dipole moment associated with that electron's intrinsic (spin) magnetic moment.[54] Accurate analysis of SO coupling thus involves determination of the component of angular momentum of the electron about each charge centre of the system. For a many-electron molecule, this problem may be simplified by not considering the effect of electrons and nuclei explicitly, but rather assuming that each electron moves in the field of a smaller number of point charges centred on each of the atomic nuclei. This allows the SO operator to be approximated by a sum of one-electron operators;

$$\mathcal{H}_{\mathrm{SO}} = \sum_k \sum_\alpha \mathbf{s}(k) \cdot \mathbf{u}_\alpha(k) \tag{3.19}$$

where k represents the electron, and α the nuclei of the system. $\mathbf{u}_\alpha(k) = \xi_\alpha(k)\mathbf{l}_\alpha(k)$ where $\mathbf{l}_\alpha(k)$ is the operator that represents the orbital angular momentum of electron k about nucleus α, and $\xi_\alpha(k)$ is an effective SO coupling coefficient which is dependent on the charge of nucleus α, its distance from electron k, and the effect of shielding due to other electrons. In practice, calculation of $\xi_\alpha(k)$ is rarely attempted. Rather, its expectation value is regarded as an adjustable parameter, the SO coupling constant, ζ, which is determined empirically for each system.

Following from Section 3.2, $\mathbf{s} \cdot \mathbf{u}$ may be expanded as

$$\begin{aligned} \mathbf{s} \cdot \mathbf{u} &= s_x u_x + s_y u_y + s_z u_z \\ &= -s_1 u_{-1} - s_{-1} u_1 + s_0 u_0 \end{aligned} \tag{3.20}$$

Hence, the introduction of SO coupling adds a term to the zero-field molecular Hamiltonian operator which depends on *both* spin and orbital angular momentum. In this case the Hamiltonian no longer commutes with S^2, S_z, L^2 or L_z, and so the states of the molecule can no longer be described as products of independent spin and orbital parts. They can, however, be described as linear combinations of such

product states using a set of symmetry-determined coefficients in the appropriate double group (Section 3.6).

3.3.4 The Zeeman Effect

The interaction of an external magnetic field, **B**, with the magnetic moment, $\boldsymbol{\mu}$, of the electrons in a molecular system is described by the Hamiltonian term

$$\mathcal{H}_B = -\boldsymbol{\mu} \cdot \mathbf{B} \tag{3.21}$$

In the experiments described in this work, the magnetic field is defined to lie in the laboratory Z direction, and so (3.21) can be simplified to

$$\mathcal{H}_B = \mu_Z B \tag{3.22}$$

In the case of an axial molecule (single unique axis) whose z axis is oriented at an angle θ with respect to the magnetic field, $\mu_Z = \mu_z \cos\theta + \mu_x \sin\theta$. For orbitally degenerate states of such systems, the first-order matrix elements of μ_x are zero and so

$$\mathcal{H}_\mathrm{B} = \mu_\mathrm{B} B \left(L_z + g_e S_z\right) \tag{3.23}$$

where μ_B is the Bohr magneton, and g_e is the electronic g-factor, $g_e = 2.0023$. Given the uncertainties present in the measurements made in this thesis, it is reasonable to make the approximation $g_e \simeq 2$.

3.4 A Qualitative Description of MCD Spectra

Before deriving theoretical equations for MCD parameters, it is instructive to consider, in a qualitative manner, the three types of MCD signals which can arise. Firstly, consider a molecular transition of symmetry $^1\mathrm{A}_1 \rightarrow {}^1\mathrm{E}$, *i.e.* from a spin and orbitally non-degenerate ground state to an excited state which is spin non-degenerate but has 2-fold orbital degeneracy (with partner labels +1 and -1). Figure 3.1 shows the energy-level diagram for this transition in the absence ($B = 0$) and presence ($B > 0$) of a magnetic field.

Recalling from Section 2.2.3 that absorption is given by the average absorbance of lcp and rcp light, and MCD by the difference between these two signals, for $B > 0$ the spectral profiles shown in Figure 3.1 are obtained. At zero field, the lcp and

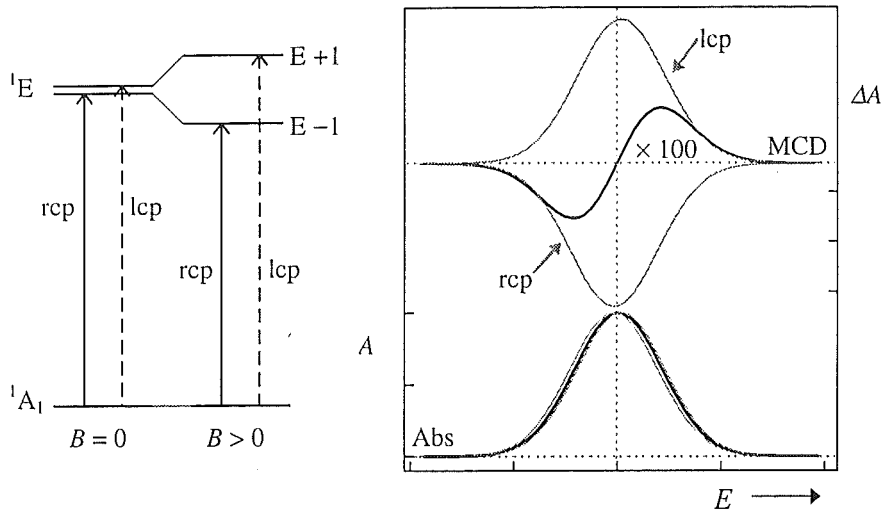

Figure 3.1. The energy-level diagram, and corresponding absorption and MCD spectra of the transition $^1A_1 \rightarrow {}^1E$ in the presence of a magnetic field. The resulting MCD dispersion is known as an $\mathcal{A}$ term.

rcp transitions occur at the same energy, and so there is no MCD signal. When $B > 0$, the Zeeman effect causes splitting of the degenerate excited-state levels, and so the lcp and rcp transitions have different energies (but equal intensities). The Zeeman splittings are, in general, insignificant relative to the width of the inhomogeneously-broadened absorption band, and so the change in the absorption spectrum is imperceptible. However, the MCD spectrum (although weak; note the amplification factor in Figure 3.1) changes dramatically; with the resulting derivative-shaped band known as an $\mathcal{A}$ term. The $\mathcal{A}$ term is said to be positive if the lobe with $\Delta A > 0$ lies at higher energy. Since the population of the ground state is essentially temperature independent, $\mathcal{A}$ terms are temperature independent.

Now consider the transition $^1E \rightarrow {}^1A_1$ shown in Figure 3.2. Again the magnetic field splits the levels of the ^1E state, giving lcp and rcp transitions of higher and lower energies respectively. However, in this case the relative intensities of the two transitions are dependent on the Boltzmann populations of the ground state levels. As the temperature drops, the intensity of the transition from the lower Zeeman level will increase at the expense of that from the higher level. This results in the skewed MCD curve shown. This signal can be considered as the sum of two components; a temperature-independent $\mathcal{A}$ term, and a single-signed absorption-like band known as a $\mathcal{C}$ term, the magnitude of which is dependent on temperature.

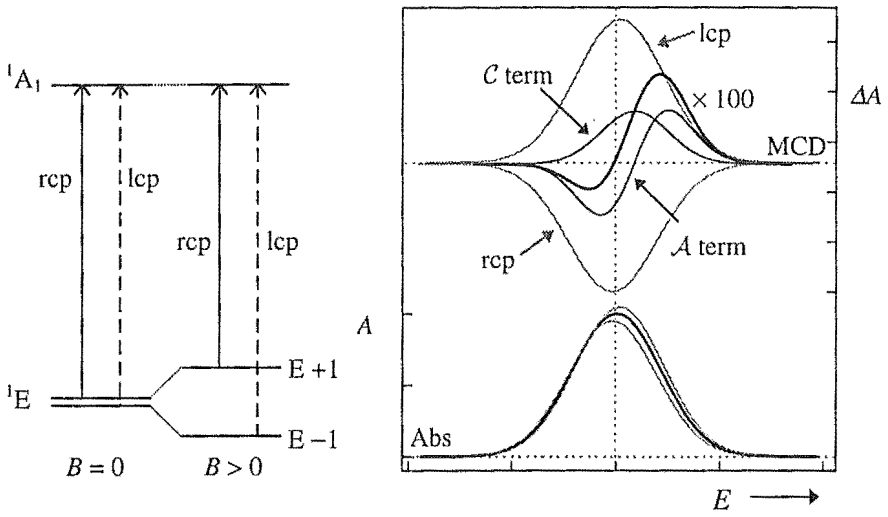

Figure 3.2. The energy-level diagram, and corresponding absorption and MCD spectra of the transition $^1E \rightarrow {}^1A_1$ in the presence of a magnetic field. The intensities of the two transitions are proportional to the Boltzmann populations of the two ground-state levels. The skewed MCD dispersion may be deconvoluted into an $\mathcal{A}$ term and a $\mathcal{C}$ term.

The third type of MCD signal is known as a $\mathcal{B}$ term, and arises from magnetic-field induced mixing of states. In the presence of a magnetic field, the $^1A_1$ and ^1E states will contain small contributions from other zero-field states of the system, the amounts of which depend on the energy separation of the states, and the magnetic matrix elements connecting them. $\mathcal{B}$ terms are single-signed and can be positive or negative. Whereas $\mathcal{A}$ and $\mathcal{C}$ terms are only present if the ground and/or excited states exhibit Zeeman splitting, $\mathcal{B}$ terms are ubiquitous (although often very weak), and hence make MCD a universal phenomenon.

An important case of $\mathcal{B}$ terms occurs when the formally degenerate excited state of Figure 3.1 is split by crystal-field or vibronic effects. By definition, the absence of degeneracy precludes the existence of $\mathcal{A}$ terms. However, the two states (designated E x and E y) are coupled by the presence of a magnetic field to give two $\mathcal{B}$ terms of the same magnitude but opposite sign. (In the absence of the magnetic field, the states are truly $|\mathrm{E}\,x\rangle$ and $|\mathrm{E}\,y\rangle$, and so, from (3.6), contain both $|\mathrm{E}\ +1\rangle$ and $|\mathrm{E}\ -1\rangle$ components. For $B > 0$, field-induced mixing causes one state to become predominantly $|\mathrm{E}\ +1\rangle$ (corresponding to a lcp transition) and the other predominantly $|\mathrm{E}\ -1\rangle$ (corresponding to a rcp transition).) If the zero-field splitting is small compared with the bandwidth, then these $\mathcal{B}$ terms overlap to give MCD with the appearance of an $\mathcal{A}$ term *with the same sign that would occur in*

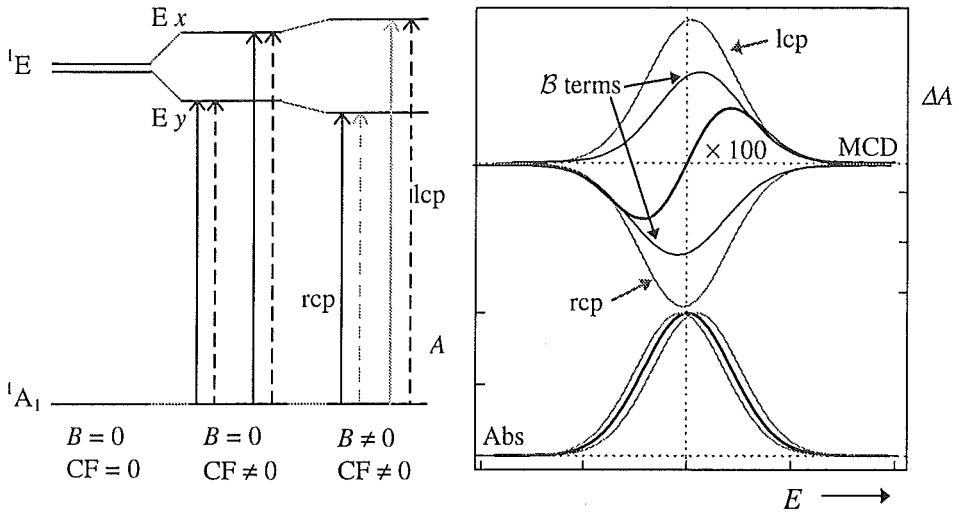

Figure 3.3. The energy-level diagram, and corresponding absorption and MCD spectra of the transition $^1A_1 \rightarrow {}^1E$, split by a crystal-field (CF) effect, in the absence and presence of a magnetic field. The resulting MCD dispersion consists of two oppositely signed $\mathcal{B}$ terms, which combine to produce a pseudo-$\mathcal{A}$ term.

the absence of the splitting (Figure 3.3). Such an MCD feature is referred to as a pseudo-$\mathcal{A}$ term.[19,32] Clearly, a pseudo-$\mathcal{A}$ term must tend to a true $\mathcal{A}$ term as the perturbation vanishes; in fact the method of moments (Section 3.7) allows the former to be treated on exactly the same basis as the latter when the zero-field splitting is small.

3.5 Expressions for Absorption and MCD

3.5.1 Relating Absorbance to Transition Moments

The first step in developing theoretical equations for absorption and MCD is to consider the absorbance at zero field. The absorbance, A, of a sample is defined as

$$A = \log \frac{I_0}{I} \tag{3.24}$$

where I_0 is the intensity of light incident upon, and I the intensity of light emerging from, the sample. The Beer-Lambert law states that for monochromatic light and a homogeneously absorbing sample,

$$A = \varepsilon c l \tag{3.25}$$

where ε is the molar extinction coefficient (dependent on the frequency, ν, of the light) and c and l are the concentration and thickness of the sample respectively. The derivation of this law requires the assumptions that the absorption of light is independent of intermolecular interactions, and that the intensity of light, I, is sufficiently low that the Boltzmann distribution of molecules among energy levels remains essentially unaltered by the absorption process. The former assumption is valid for low sample concentrations, and the latter nearly always holds for conventional spectroscopic measurements of optical transitions, *i.e.* where the light intensity is low, and the lifetime of the excited state is short compared with the probability of absorption of a photon.

The next step is to relate the physical observable A to the transition-moment integral. Consider a beam of light, of intensity $I(\nu)$ (in units of W m^{-2}), incident on a collection of non-interacting molecules which can exist in a ground state, $|a\rangle$, or an excited state, $|j\rangle$. The decrease in intensity of the light per unit length of penetration of the sample is given by

$$-\frac{dI(\nu)}{dl} = h\nu N_a P_{a\rightarrow j} \tag{3.26}$$

where N_a is the number of molecules per unit volume in state $|a\rangle$, and $P_{a\rightarrow j}$ is the probability per molecule of transition between the two states. The differential form of (3.24) is

$$-dI = ln(10) I dA \tag{3.27}$$

Substituting (3.27) into (3.26) and integrating over the pathlength, l, gives

$$A(\nu) = \frac{hl\nu}{ln(10)I(\nu)} N_a P_{a\rightarrow j} \tag{3.28}$$

To evaluate $I(\nu)$, first note that the vector potential, $\mathbf{A}$, of an electromagnetic wave propagating at velocity c in the positive Z direction of a system of fixed laboratory coordinates is

$$\mathbf{A} = \mathbf{A}^0 \exp\left[2\pi i\nu\left(t - \frac{nZ}{c}\right)\right] \tag{3.29}$$

where n is the refractive index of the medium. The vector amplitude of the wave is given by

$$\mathbf{A}^0 = \pi A^0 \tag{3.30}$$

where π is a unit vector which defines the polarisation properties of the wave. The electric field, $\mathbf{E}(\nu)$, and magnetic field, $\mathbf{B}(\nu)$, vectors are defined as

$$\mathbf{E} = -\frac{1}{\mathrm{c}} \cdot \frac{d\mathbf{A}}{dt} \quad \text{and} \quad \mathbf{B} = \nabla \times \mathbf{A} \tag{3.31}$$

From classical electromagnetic theory, $I(\nu)$ is the time average (designated by $\langle\rangle$) of the Poynting vector of the electromagnetic wave:

$$I(\nu) = \left| \frac{\mathrm{c}}{4\pi} \langle \mathcal{R}e\, \mathbf{E}(\nu) \times \mathcal{R}e\, \mathbf{B}(\nu) \rangle \right| \tag{3.32}$$

where $\mathcal{R}e$ designates the real parts. Substitution of (3.29) and (3.30) into (3.31), and the results of this into (3.32) gives

$$I(\nu) = \frac{(A^0)^2 n \pi \nu^2}{2\mathrm{c}} \tag{3.33}$$

$P_{a \to j}$ is treated semiclassically using time-dependent perturbation theory, with the absorbing species considered to interact quantum mechanically with a classical electromagnetic field. Only electric-dipole transitions are considered; the much weaker magnetic-dipole and electric-quadrupole transitions being neglected. It is shown by Piepho and Schatz[32] that

$$P_{a \to j} = \frac{4\pi^4 (A^0)^2 \nu^2 \alpha^2}{h^2 \mathrm{c}^2} \left| \langle a | \mathbf{m} \cdot \pi | j \rangle \right|^2 \rho_{aj}(\nu) \tag{3.34}$$

where $\mathbf{m}$ is the electric dipole operator, $\rho_{aj}(\nu)$ is a density-of-states function and α is a unitless coefficient which takes into account the effect neighbouring solvent or host molecules have on the actual electric field felt by the molecule. It is conventional and convenient to replace $\rho_{aj}(\nu)$ with a phenomenological normalised lineshape function, $f_{aj}(\nu)$. Doing this, and at the same time substituting (3.33) and (3.34) into (3.28), gives

$$A(\nu) = \frac{8\pi^3 \nu \alpha^2 l N_a \log e}{hcn} \left| \langle a | \mathbf{m} \cdot \pi | j \rangle \right|^2 f_{aj}(\nu) \tag{3.35}$$

Note that the concentration of the sample (in mol L^{-1}) can be manipulated such that

Table 3.1. Expressions for the transition moment squared for various light polarisations.

Polarisation	$\pi = \mathbf{e}_X\pi_1 + \mathbf{e}_Y\pi_2$	$\lvert \langle a \rvert \mathbf{m}\cdot\pi \lvert j\rangle\rvert^2$
Linear along X	$\mathbf{e}_X$	$\lvert \langle a \rvert m_x \lvert j\rangle\rvert^2$
Linear along Y	$\mathbf{e}_Y$	$\lvert \langle a \rvert m_y \lvert j\rangle\rvert^2$
rcp	$-\frac{1}{\sqrt{2}}(\mathbf{e}_X + i\mathbf{e}_Y)$	$\lvert \langle a \rvert m_{+1} \lvert j\rangle\rvert^2$
lcp	$\frac{1}{\sqrt{2}}(\mathbf{e}_X - i\mathbf{e}_Y)$	$\lvert \langle a \rvert m_{-1} \lvert j\rangle\rvert^2$
XY unpolarised	$\mathbf{e}_X\cos\phi + \mathbf{e}_Y\sin\phi$ averaged over all ϕ	$\frac{1}{2}\left(\lvert \langle a \rvert m_x \lvert j\rangle\rvert^2 + \lvert \langle a \rvert m_y \lvert j\rangle\rvert^2\right)$

$$c = \frac{N_a}{N_\mathrm{A}\times 10^{-3}} \tag{3.36}$$

where N_A is Avagadro's number. Taking

$$\gamma = \frac{2N_\mathrm{A}\pi^3\alpha^2 cl\log e}{250hcn} \tag{3.37}$$

(3.35) can be simplified to

$$A(\nu) = \gamma\nu \lvert \langle a \rvert \mathbf{m}\cdot\pi \lvert j\rangle\rvert^2 f_{aj}(\nu) \tag{3.38}$$

In general, for light propagating along Z, the polarisation vector π, may be written as $\pi = \mathbf{e}_X\pi_1 + \mathbf{e}_Y\pi_2$ where $\mathbf{e}_X$ and $\mathbf{e}_Y$ are unit vectors in the X and Y directions, and π_1 and π_2 are (potentially time dependent) directional cosines, such that $|\pi_1|^2 + |\pi_2|^2 = 1$. The electric-dipole transition moment integrals in (3.38) for different light polarisations are given in Table 3.1, where $m_{\pm1}$ effectively represent the absorption of rcp and lcp light respectively. Note that $m_{\pm1}$ are not Hermitian. In particular,

$$\langle a \rvert m_{\pm1} \lvert j\rangle = -\langle j \rvert m_{\mp1} \lvert a\rangle^* \tag{3.39}$$

3.5.2 Theoretical Expressions for Absorption and MCD

In Section 3.4 the symbols $\mathcal{A}$, $\mathcal{B}$, and $\mathcal{C}$ were used to describe the MCD dispersion forms arising from various phenomena. In the following discussion it is shown that each of these is associated with a specific mathematical function, $\mathcal{A}_1$, $\mathcal{B}_0$, or $\mathcal{C}_0$, which measures the strength of each effect. $\mathcal{A}_1$, $\mathcal{B}_0$, and $\mathcal{C}_0$ are known

collectively as the Faraday parameters. In addition, the absorption is expressed in terms of the dipole strength, $\mathcal{D}_0$.

In MCD spectroscopy, as introduced in Chapter 2, light of alternately left- and right-circular polarisations is passed through a sample along the direction of a magnetic field. The MCD is the difference between these two signals at a given energy:

$$\Delta A'(\nu) = A'_L(\nu) - A'_R(\nu) \tag{3.40}$$

where the primes are used to represent magnetic field-dependent quantities. The absorbance is the average signal at zero magnetic field;

$$A(\nu) = \frac{A_L(\nu) + A_R(\nu)}{2} \tag{3.41}$$

In deriving the starting equations for theoretical expressions of absorption and MCD, a few changes are made to (3.38). Firstly, an energy scale, $E = h\nu$, in cm^{-1} (see Section 3.2) is used for the incident photons, and so a normalised bandshape function $f_{aj}(E)$ is defined using this scale. Secondly, allowance is made for transitions originating and terminating in several states, the intensities of which must be weighted by fractional population factors, $\frac{N_a}{N}$ where $N = \sum_a N_a$ is the total number of chromophores per unit volume. Hence it is obtained that

$$\frac{\Delta A'(E)}{E} = \gamma \sum_{aj} \frac{N'_a}{N} \left(|\langle a| m_{-1} |j\rangle|^2 - |\langle a| m_{+1} |j\rangle|^2 \right) f'_{aj}(E) \tag{3.42}$$

and

$$\frac{A(E)}{E} = \frac{\gamma}{2} \sum_{aj} \frac{N_a}{N} \left(|\langle a| m_{-1} |j\rangle|^2 + |\langle a| m_{+1} |j\rangle|^2 \right) f_{aj}(E) \tag{3.43}$$

These are the fundamental equations of MCD and absorption spectroscopy.

Consider a generalised allowed electronic transition, $A \rightarrow J$, where A and J each comprise a manifold of degenerate Born-Oppenheimer states (Section 3.3.1). The individual states within these manifolds are designated $|A\alpha g\rangle$ and $|J\lambda j\rangle$; α and λ being the electronic partner labels and g and j representing the vibrational states associated with A and J respectively. The molecules involved are initially assumed to either have cubic symmetry, or to be identically oriented such that their principal symmetry axis (z) is parallel to the laboratory Z axis (defined by the direction of the

radiation and the magnetic field, B). In order to make the desired derivations, it is necessary to assume that work is being carried out within the linear limit: *i.e.* that the Zeeman splittings brought about by the magnetic field are small in comparison to both kT (where k is Boltzmann's constant) and the bandwidth of the transition. The effect of deviations from this limit are discussed in Section 4.4.5.3.

3.5.2.1 Determination of $\mathcal{D}_0$

Using the FC principle (Section 3.3.2),

$$\langle A\alpha g|\, m_{\pm 1}\, |J\lambda j\rangle = \langle A\alpha|\, m_{\pm 1}\, |J\lambda\rangle^0 \langle g\,|\,j\rangle \tag{3.44}$$

where the superscript 0 emphasises the fact that this electronic matrix element pertains to the absence of an external magnetic field. The absorbance, $A(E)$ is defined at zero field, in which case all $|A\alpha\rangle$ states are degenerate and so

$$\frac{N_{A\alpha g}}{N} = \frac{1}{|A|}\frac{N_g}{N_G} \tag{3.45}$$

where $|A|$ is the degeneracy of state A, and $N_G = \sum_g N_g$ is the total population of all vibrational states of the $|A\alpha g\rangle$ manifold. If it is assumed that all transition components have the same lineshape, $f(E)$, (the rigid-shift (RS) approximation - described in Section 3.5.2.2) (3.43) can be rewritten as

$$\frac{A(E)}{E} = \gamma \mathcal{D}_0 f(E) \tag{3.46}$$

where

$$\mathcal{D}_0 = \frac{1}{2\,|A|}\sum_{a\lambda}\left(\left|\langle A\alpha|\, m_{-1}\, |J\lambda\rangle^0\right|^2 + \left|\langle A\alpha|\, m_{+1}\, |J\lambda\rangle^0\right|^2\right) \tag{3.47}$$

In the last step, the completeness theorem ($\sum_j |j\rangle\langle j| = 1$) has been used to remove the contributions from vibrations as follows:

$$\begin{aligned}\sum_g \sum_j \frac{N_g}{N_G}\,|\langle g|j\rangle|^2 &= \sum_g \frac{N_g}{N_G}\sum_j \langle g|j\rangle\langle j|g\rangle \\ &= \sum_g \frac{N_g}{N_G}\langle g|g\rangle \\ &= 1\end{aligned} \tag{3.48}$$

3.5.2.2 Determination of the Faraday Parameters

Development of the MCD equation (3.42) is much more complicated than that of the absorption equation (3.43) because of the field dependence of a number of features, namely the matrix elements, state populations and lineshape functions. This field dependence will be dealt with by considering the field as a weak perturbation on the system. (Zeeman splittings are typically on the order of $10^3 - 10^5$ times smaller than the electronic energies involved.)

First consider the Hamiltonian matrix elements, involving magnetic-field-induced mixing of states. For convenience, the unperturbed wavefunctions A and J are chosen to be to be diagonal (within each degenerate manifold) in the Zeeman perturbation. Applying first-order non-degenerate perturbation theory and the FC principle, it is found that the perturbed wave functions (designated by primes) are

$$\langle A\alpha g|' = \langle A\alpha g|^0 - B \sum_{K\kappa, K\neq A} \frac{\langle A\alpha|\,\mu_z\,|K\kappa\rangle^0}{E_A^0 - E_K^0}\,\langle K\kappa g|^0 \tag{3.49}$$

$$|J\lambda j\rangle' = |J\lambda j\rangle^0 - B \sum_{K\kappa, K\neq J} \frac{\langle K\kappa|\,\mu_z\,|J\lambda\rangle^0}{E_J^0 - E_K^0}\,|K\kappa g\rangle^0 \tag{3.50}$$

where the superscripts 0 indicate unperturbed states, their energies and matrix elements. Combining the above two equations, it is obtained that

$$\begin{aligned}\langle A\alpha g|\,m_{\pm 1}\,|J\lambda j\rangle' = \Bigg[&\langle A\alpha g|\,m_{\pm 1}\,|J\lambda j\rangle^0 - B \sum_{K\kappa, K\neq A} \frac{\langle A\alpha|\,\mu_z\,|K\kappa\rangle^0\,\langle K\kappa|\,m_{\pm 1}\,|J\lambda\rangle^0}{E_A^0 - E_K^0} \\ &- B \sum_{K\kappa, K\neq J} \frac{\langle A\alpha|\,\mu_z\,|K\kappa\rangle^0\,\langle K\kappa|\,m_{\pm 1}\,|J\lambda\rangle^0}{E_J^0 - E_K^0}\Bigg]\,\langle g\,|\,j\rangle\end{aligned} \tag{3.51}$$

where terms of higher than first order have been omitted.

Next, consider the field dependence of the state populations. It is assumed that the ground and excited states are sufficiently well separated that only the ground state is populated. Boltzmann's law states that

$$\frac{N'_{A\alpha g}}{N} = \frac{N'_{A\alpha g}}{\sum\limits_{\alpha g} N'_{A\alpha g}} = \frac{\mathrm{e}^{-E'_{A\alpha g}/kT}}{\sum\limits_{\alpha g} \mathrm{e}^{-E'_{A\alpha g}/kT}} \tag{3.52}$$

From perturbation theory, the energy of the field-dependent states is

$$E'_{A\alpha g} = E_{A\alpha g} - \langle A\alpha|\,\mu_z\,|A\alpha\rangle^0\,B$$

$$E'_{J\lambda j} = E_{J\lambda j} - \langle J\lambda |\, \mu_z \,| J\lambda \rangle^0 B \tag{3.53}$$

and so

$$\frac{N'_{A\alpha g}}{N} = \frac{\mathrm{e}^{-E_{A\alpha g}/kT} \mathrm{e}^{\langle A\alpha|\mu_z|A\alpha\rangle^0 B/kT}}{\sum\limits_{\alpha g} \mathrm{e}^{-E_{A\alpha g}/kT} \mathrm{e}^{\langle A\alpha|\mu_z|A\alpha\rangle^0 B/kT}} \tag{3.54}$$

Making the approximation $\mathrm{e}^a \simeq 1 + a$, which is only valid in the linear limit ($\mu_\mathrm{B} B \ll kT$),

$$\begin{aligned} \frac{N'_{A\alpha g}}{N} &= \frac{N_{A\alpha g}}{\sum\limits_{\alpha g} N_{A\alpha g}} \left(1 + \frac{\langle A\alpha |\, \mu_z \,| A\alpha \rangle^0 B}{kT} \right) \\ &= \frac{1}{|A|} \frac{N_g}{N_G} \left(1 + \frac{\langle A\alpha |\, \mu_z \,| A\alpha \rangle^0 B}{kT} \right) \end{aligned} \tag{3.55}$$

In evaluating the field-dependent line shape, it is first assumed that the magnetic field Zeeman-shifts each vibronic transition contributing to the band, but does not change its shape, *i.e.*,

$$\begin{aligned} f'_{A\alpha g, J\lambda j}(E) &= f_{A\alpha g, J\lambda j} \left(E - \left(\Delta E'_{A\alpha g, J\lambda j} - \Delta E_{A\alpha g, J\lambda j} \right) \right) \\ &= f_{A\alpha g, J\lambda j} \left(E + \left(\langle J\lambda |\, \mu_z \,| J\lambda \rangle^0 - \langle A\alpha |\, \mu_z \,| A\alpha \rangle^0 \right) B \right) \end{aligned} \tag{3.56}$$

where the last step uses (3.53). The right-hand side of the above expression is then expanded as a Taylor series of the form

$$f(x+h) \simeq f(x) + h \frac{\delta f}{\delta x} + \frac{h^2}{2} \frac{df^2}{d^2 x} + \ldots \tag{3.57}$$

which, truncating to first order, gives

$$f'_{A\alpha g, J\lambda j}(E) = f(E) + \left(\langle J\lambda |\, \mu_z \,| J\lambda \rangle^0 - \langle A\alpha |\, \mu_z \,| A\alpha \rangle^0 \right) B \frac{\partial f(E)}{\partial E} \tag{3.58}$$

The approximations made in (3.56) and (3.58) are collectively known as the rigid shift (RS) approximation.

Having expressed all the field-dependent parameters in (3.42) in terms of zero-field values, this equation can now be written in terms of the $\mathcal{A}_1$, $\mathcal{B}_0$ and $\mathcal{C}_0$ parameters which describe the magnitudes of the $\mathcal{A}$, $\mathcal{B}$ and $\mathcal{C}$ dispersions making up MCD spectra. Substituting (3.51), (3.55) and (3.58) into (3.42), and writing $\mu_z = -\mu_\mathrm{B} (L_z + 2S_z)$ gives, in the BO-FC-RS approximation,

$$\frac{\Delta A'}{E} = \gamma \mu_B B \left(\mathcal{A}_1^Z \left(-\frac{\partial f(E)}{\partial E} \right) + \left(\mathcal{B}_0^Z + \frac{\mathcal{C}_0^Z}{kT} \right) f(E) \right) \tag{3.59}$$

where

$$\begin{aligned} \mathcal{A}_1^Z &= -\frac{1}{|A|} \sum_{a\lambda} \left(\langle J\lambda | L_z + 2S_z | J\lambda \rangle^0 - \langle A\alpha | L_z + 2S_z | A\alpha \rangle^0 \right) \\ &\quad \times \left(\left| \langle A\alpha | m_{-1} | J\lambda \rangle^0 \right|^2 - \left| \langle A\alpha | m_{+1} | J\lambda \rangle^0 \right|^2 \right) \end{aligned} \tag{3.60}$$

$$\begin{aligned} \mathcal{B}_0^Z &= \frac{2}{|A|} \mathcal{R}e \sum_{K\kappa, K\neq J} \frac{\langle J\lambda | L_z + 2S_z | K\kappa \rangle^0}{E_K^0 - E_J^0} \times \left(\langle A\alpha | m_{-1} | J\lambda \rangle^0 \langle K\kappa | m_{+1} | A\alpha \rangle^0 \right. \\ &\quad \left. - \langle A\alpha | m_{+1} | J\lambda \rangle^0 \langle K\kappa | m_{-1} | A\alpha \rangle \right) + \sum_{K\kappa, K\neq A} \frac{\langle K\kappa | L_z + 2S_z | A\alpha \rangle^0}{E_K^0 - E_A^0} \\ &\quad \times \left(\langle A\alpha | m_{-1} | J\lambda \rangle^0 \langle J\lambda | m_{+1} | K\kappa \rangle^0 - \langle A\alpha | m_{+1} | J\lambda \rangle^0 \langle J\lambda | m_{-1} | K\kappa \rangle^0 \right) \end{aligned} \tag{3.61}$$

$$\mathcal{C}_0^Z = -\frac{1}{|A|} \sum_{a\lambda} \left(\langle A\alpha | L_z + 2S_z | A\alpha \rangle^0 \right) \times \left(\left| \langle A\alpha | m_{-1} | J\lambda \rangle^0 \right|^2 - \left| \langle A\alpha | m_{+1} | J\lambda \rangle^0 \right|^2 \right) \tag{3.62}$$

The superscripts Z indicate that these results refer to the Z-oriented case. Equation (3.48) has been invoked to remove the population factors in (3.55).

3.5.3 The Effect of Orientational Averaging

The expressions for the dipole strength and Faraday parameters derived above are valid for samples in which molecules are preferentially Z-oriented. It is now shown how simply these can be related to the case of random molecular orientation. (Note that $\mathcal{B}_0$ is not actually required for the work discussed in this thesis, and so, due to the complexity of the expressions involved, will not be considered here.) The intention is not to provide a rigorous analysis; but rather to begin with the expressions derived by Piepho and Schatz,[32] and show how these can be simplified under certain conditions. From the aforementioned reference it is obtained that

$$\overline{\mathcal{D}}_0 = \frac{1}{3|A|} \sum_{\alpha\lambda} \left| \langle A\alpha | \mathbf{m} | J\lambda \rangle^0 \right| \tag{3.63}$$

$$\begin{aligned} \overline{\mathcal{A}}_1 &= \frac{i}{3|A|} \sum_{\alpha\alpha'\lambda\lambda'} \left(\langle J\lambda | \mathbf{L} + 2\mathbf{S} | J\lambda' \rangle^0 \delta_{\alpha\alpha'} - \langle A\alpha' | \mathbf{L} + 2\mathbf{S} | A\alpha \rangle^0 \delta_{\lambda\lambda'} \right) \cdot \\ &\quad \left(\langle A\alpha | \mathbf{m} | J\lambda \rangle^0 \times \langle J\lambda' | \mathbf{m} | A\alpha' \rangle^0 \right) \end{aligned} \tag{3.64}$$

$$\overline{\mathcal{C}}_0 = -\frac{i}{3\,|A|}\sum_{\alpha\alpha'\lambda}\left(\langle A\alpha'|\,\mathbf{L}+2\mathbf{S}\,|A\alpha\rangle^0\right)\cdot\left(\langle A\alpha|\,\mathbf{m}\,|J\lambda\rangle^0\times\langle J\lambda|\,\mathbf{m}\,|A\alpha'\rangle^0\right) \tag{3.65}$$

where $\cdot$ and $\times$ designate scalar and vector products, and all the matrix elements are given in relation to molecule-fixed operators (*i.e.* the x, y, z components of the operators relate to the cartesian axes of the molecule). The bars over the Faraday parameters indicate that they pertain to the case of randomly oriented molecules.

The first simplification to these expressions is to consider only xy-polarised transitions of molecules with a unique principal symmetry axis, in which case all matrix elements of the m_z operator are zero. This scenario is chosen since it is the one relevant to all the systems investigated in this thesis. Secondly, it is assumed that ground- and excited-state wavefunctions have been chosen to be diagonal (within each degenerate manifold) in the Zeeman effect, so $A\alpha = A\alpha'$ and $J\lambda = J\lambda'$. For this reason, a complex basis (as described in Section 3.2) is used.

3.5.3.1 $\overline{\mathcal{D}}_0$

Expanding the electric-dipole operator ($\mathbf{m}$) in (3.63), and noting that all matrix elements involving m_z are zero, it is obtained that

$$\begin{aligned}\overline{\mathcal{D}}_0 &= \frac{1}{3\,|A|}\sum_{\alpha\lambda}\left(\langle A\alpha|\,m_x\,|J\lambda\rangle\,\langle J\lambda|\,m_x\,|A\alpha\rangle+\langle A\alpha|\,m_y\,|J\lambda\rangle\,\langle J\lambda|\,m_y\,|A\alpha\rangle\right)\\ &= \frac{-1}{3\,|A|}\sum_{\alpha\lambda}\left(\langle A\alpha|\,m_{-1}\,|J\lambda\rangle\,\langle J\lambda|\,m_{+1}\,|A\alpha\rangle+\langle A\alpha|\,m_{+1}\,|J\lambda\rangle\,\langle J\lambda|\,m_{-1}\,|A\alpha\rangle\right)\end{aligned} \tag{3.66}$$

and since from (3.39)

$$\begin{aligned}\langle J\lambda|\,m_{+1}\,|A\alpha'\rangle^* &= -\langle A\alpha|\,m_{-1}\,|J\lambda\rangle\\ \langle J\lambda|\,m_{-1}\,|A\alpha'\rangle^* &= -\langle A\alpha|\,m_{+1}\,|J\lambda\rangle\end{aligned} \tag{3.67}$$

it is found that

$$\overline{\mathcal{D}}_0 = \frac{1}{3\,|A|}\sum_{\alpha\lambda}\left(|\langle A\alpha|\,m_{-1}\,|J\lambda\rangle|^2+|\langle A\alpha|\,m_{+1}\,|J\lambda\rangle|^2\right) \tag{3.68}$$

With reference to (3.47), this gives

$$\overline{\mathcal{D}}_0 = \tfrac{2}{3}\mathcal{D}_0^Z \tag{3.69}$$

3.5.3.2 $\overline{C}_0$

The expression for $\overline{C}_0$ in (3.65) involves a triple product, which may be written as the determinant of the appropriate 3×3 matrix,

$$\overline{C}_0 = -\frac{i}{3\,|A|}\sum_{\alpha\alpha'\lambda}\det(\overline{C}_0) \tag{3.70}$$

where

$$\det(\overline{C}_0) = \begin{vmatrix} \langle A\alpha'|\, L_z + 2S_z \,|A\alpha\rangle & \langle A\alpha'|\, L_x + 2S_x \,|A\alpha\rangle & \langle A\alpha'|\, L_y + 2S_y \,|A\alpha\rangle \\ \langle A\alpha|\, m_z \,|J\lambda\rangle & \langle A\alpha|\, m_x \,|J\lambda\rangle & \langle A\alpha|\, m_y \,|J\lambda\rangle \\ \langle J\lambda|\, m_z \,|A\alpha'\rangle & \langle J\lambda|\, m_y \,|A\alpha'\rangle & \langle J\lambda|\, m_y \,|A\alpha'\rangle \end{vmatrix} \tag{3.71}$$

Under the conditions described above, there are no non-zero transition moments involving m_z,and this expression can be simplified to

$$\begin{aligned} \det(\overline{C}_0) &= \langle A\alpha'|\, L_z + 2S_z \,|A\alpha\rangle \\ &\quad (\langle A\alpha|\, m_x \,|J\lambda\rangle \langle J\lambda|\, m_y \,|A\alpha'\rangle - \langle A\alpha|\, m_y \,|J\lambda\rangle \langle J\lambda|\, m_y \,|A\alpha'\rangle) \end{aligned} \tag{3.72}$$

Changing now to a complex basis, and recalling that the ground- and excited-state wavefunctions have been chosen to be diagonal in the Zeeman effect, so that $A\alpha = A\alpha'$,

$$\begin{aligned} \det(\overline{C}_0) &= i\,\langle A\alpha|\, L_z + 2S_z \,|A\alpha\rangle \\ &\quad (\langle A\alpha|\, m_{-1} \,|J\lambda\rangle \langle J\lambda|\, m_{+1} \,|A\alpha\rangle - \langle A\alpha|\, m_{+1} \,|J\lambda\rangle \langle J\lambda|\, m_{-1} \,|A\alpha\rangle) \end{aligned} \tag{3.73}$$

From the complex-conjugate relationships of (3.67), the above can be written as

$$\begin{aligned} \det(\overline{C}_0) &= -i\,\langle A\alpha|\, L_z + 2S_z \,|A\alpha\rangle \\ &\quad (\langle A\alpha|\, m_{-1} \,|J\lambda\rangle \langle A\alpha|\, m_{-1} \,|J\lambda\rangle^* - \langle A\alpha|\, m_{+1} \,|J\lambda\rangle \langle A\alpha|\, m_{+1} \,|J\lambda\rangle^*) \end{aligned} \tag{3.74}$$

and hence

$$\overline{C}_0 = -\frac{1}{3\,|A|}\sum_{\alpha\lambda}\langle A\alpha|\, L_z + 2S_z \,|A\alpha\rangle \left(|\langle A\alpha|\, m_{-1} \,|J\lambda\rangle|^2 - |\langle A\alpha|\, m_{+1} \,|J\lambda\rangle|^2\right) \tag{3.75}$$

So, from (3.62),

$$\overline{C}_0 = \tfrac{1}{3}\mathcal{C}_0^Z \tag{3.76}$$

3.5.3.3 $\overline{\mathcal{A}}_1$

Rewriting the triple product in (3.64) as a determinant,

$$\overline{\mathcal{A}}_1 = \frac{i}{3\,|A|} \sum_{\alpha\alpha'\lambda\lambda'} \det(\overline{\mathcal{A}}_0) \tag{3.77}$$

where $\det(\overline{\mathcal{A}}_0)$ has a similar form to (3.71). Since matrix elements involving m_z are zero and $A\alpha = A\alpha'$, $J\lambda = J\lambda'$, the above can be simplified to

$$\begin{aligned} \det(\overline{\mathcal{A}}_0) &= (\langle J\lambda|\, L_z + 2S_z\,|J\lambda\rangle - \langle A\alpha|\, L_z + 2S_z\,|A\alpha\rangle) \\ &\quad (\langle A\alpha|\, m_x\,|J\lambda\rangle \langle J\lambda|\, m_y\,|A\alpha\rangle - \langle A\alpha|\, m_y\,|J\lambda\rangle \langle J\lambda|\, m_y\,|A\alpha\rangle) \end{aligned} \tag{3.78}$$

Changing to complex coordinates, it is obtained, in an analogous manner to that for $\overline{\mathcal{C}}_0$, that

$$\begin{aligned} \overline{\mathcal{A}}_0 &= \frac{1}{3\,|A|} \sum_{\alpha\lambda} (\langle J\lambda|\, L_z + 2S_z\,|J\lambda\rangle - \langle A\alpha|\, L_z + 2S_z\,|A\alpha\rangle) \\ &\quad \left(|\langle A\alpha|\, m_{-1}\,|J\lambda\rangle|^2 - |\langle A\alpha|\, m_{+1}\,|J\lambda\rangle|^2\right) \end{aligned} \tag{3.79}$$

and hence, with reference to (3.47), this gives

$$\overline{\mathcal{A}}_1 = \tfrac{2}{3}\mathcal{A}_1^Z \tag{3.80}$$

3.5.3.4 Ratios of Parameters

As will be seen in Section 3.7, ratios of the Faraday parameters and dipole strength are very useful, since γ and the dipole-moment matrix elements cancel. Note that the parameters for random orientation and Z orientation are related by

$$\overline{\mathcal{A}}_1/\overline{\mathcal{D}}_0 = \tfrac{1}{2}\mathcal{A}_1^Z/\mathcal{D}_0^Z, \qquad \overline{\mathcal{C}}_0/\overline{\mathcal{D}}_0 = \tfrac{1}{2}\mathcal{C}_0^Z/\mathcal{D}_0^Z \tag{3.81}$$

3.6 The Wigner-Eckart Theorem

As can be seen from the expressions in Section 3.5.2, the simplification and evaluation of matrix elements plays a critical role in the comparison of theoretical and experimental expressions of absorption and MCD spectroscopies. Group-theoretical tools allow simplification of such matrix elements on the basis of the

symmetry of the molecular system. Of particular importance are the expressions of the Wigner-Eckart theorem;

$$\left\langle a\alpha \left| O_\phi^f \right| b\beta \right\rangle = \begin{pmatrix} a \\ \alpha \end{pmatrix} \sum_r \begin{pmatrix} a^* & f & b \\ \alpha^* & \phi & \beta \end{pmatrix}^r \left\langle a \left\| O^f \right\| b \right\rangle_r \tag{3.82}$$

and the expansion equation;

$$|(ab)\, rc\gamma\rangle = \sqrt{|c|} \begin{pmatrix} c \\ \gamma \end{pmatrix} \sum_{\alpha\beta r} \begin{pmatrix} a & b & c^* \\ \alpha & \beta & \gamma^* \end{pmatrix}^{*r} |a\alpha\rangle\, |b\beta\rangle \tag{3.83}$$

In (3.82) and (3.83) $a\alpha$, $b\beta$ and $c\gamma$ represent the irreps and partners of various states and the index r represents the sum over repeated representations. In (3.82), O_ϕ^f is an operator which transforms as irrep and partner $f\phi$, while in (3.83). $|c|$ is the degeneracy of irrep c. The symbols $\begin{pmatrix} a \\ \alpha \end{pmatrix}$ and $\begin{pmatrix} c \\ \gamma \end{pmatrix}$ represent $2jm$ phases, and $\begin{pmatrix} a^* & f & b \\ \alpha^* & \phi & \beta \end{pmatrix}$ and $\begin{pmatrix} a & b & c^* \\ \alpha & \beta & \gamma^* \end{pmatrix}$ are $3jm$ high-symmetry coupling coefficients. $\left\langle a \left\| O^f \right\| b \right\rangle$ is a reduced matrix element which is a function of the irreps a, f and b, but is independent of the partners of these irreps.

The Wigner-Eckart theorem is particularly useful in the determination of ratios, since common reduced matrix elements can be cancelled, and so do not have to be evaluated. Tables of the $2jm$ and $3jm$ coefficients for common point groups are readily available.[32,55,56] Those for the poorly documented D_{4d} group are given in Appendices I and II. The uses of the expansion equation include coupling of one-electron (orbital) functions in the molecular point group to form many-electron terms, and coupling of spin and orbit functions in the appropriate double group to form spin-orbit states. Both of these are made use of in this thesis.

3.7 Moment Analysis

The theoretical expressions for MCD and absorption derived above are only of use if they can be related in some way to the experimentally observed intensities and dispersions of the spectra. There are two methods commonly employed to make this comparison. The first is the method of moments, which is the technique employed throughout this thesis, and which will be described in detail below. The second involves assumption of analytical lineshapes for the bands, and usually invokes the rigid-shift approximation in an attempt to model (or fit) the spectra.

The method of moments may be used whenever some observable, f(E), has been measured as a function of the variable E. The moments of such a function about a reference point, E_0, are defined by

$$\langle \mathrm{f} \rangle_n^{E_0} = \int_0^\infty \mathrm{f}(E)(E - E_0)^n dE \tag{3.84}$$

In the spectroscopic context, f(E) forms a band, *i.e.* there are upper and lower limits (E_1 and E_2) at which f(E) falls essentially to zero. In this case, integration need only be carried out over the range between E_1 and E_2. One of the most useful aspects of moment analysis is that arbitrary, subjective band shapes need not be assumed. It also avoids the necessity of invoking the rigid-shift approximation. Moveover, it turns out that in many important cases the moments obtained from absorption and MCD transitions are invariant to simple unitary transformations of the excited-state basis functions, which substantially simplifies analysis, as will be seen in later chapters.

For absorption spectra, f(E) = $A(E)/E$, and E_0 is most usefully chosen to be the average energy or barycentre of the absorption band, $\overline{E}$, defined such that $\langle A(E)/E \rangle_1^{\overline{E}} = 0$. For MCD spectra, f($E$) = $\Delta A(E)/E$. To apply the method of moments, the experimental data are integrated as specified for the particular moment being considered, and the result from this is compared with that obtained by integrating the corresponding theoretical expression. In the case of either absorption or MCD spectra, consideration of (3.46) and (3.59) indicates that theoretical moment evaluation involves integration over the bandshape function ($f(E)$) or its derivative. It transpires that there are a number of very useful relations between various of these integrals, some of which are defined here.

Firstly, since $f(E)$ is normalised, then

$$\langle f(E) \rangle_0 = \int f(E) dE = 1 \tag{3.85}$$

Also,

$$\langle f(E) \rangle_1^{\overline{E}} = \int_{E_1}^{E_2} f(E)(E - \overline{E}) dE$$

$$= \int_{E_1}^{E_2} f(E)EdE - \overline{E}\int f(E)dE$$

$$= \langle f(E)\rangle_1^0 - \overline{E} \tag{3.86}$$

The first moment about $\overline{E}$ of the bandshape derivative is given by

$$\left\langle \frac{df(E)}{dE} \right\rangle_1^{\overline{E}} = \int_{E_2}^{E_1} \frac{df(E)}{dE}(E-\overline{E})dE$$

$$= \int_{E_2}^{E_1} \frac{df(E)}{dE}EdE - \overline{E}\int_{E_2}^{E_1} \frac{df(E)}{dE}dE$$

$$= \left[f(E)(E-\overline{E})\right]_{E_1}^{E_2} - \int_{E_2}^{E_1} f(E)dE$$

$$= 0 - 1 = -1 \tag{3.87}$$

The third step above employs integration by parts, and the last step uses the fact that $f(E_1) = f(E_2) = 0$.

In the moment analyses carried out in the following chapters, it is the zeroth absorption and zeroth and first MCD moments which are of importance. The theoretical expressions for these, in terms of the dipole strength and Faraday parameters, can be derived be applying the relations given above to (3.46) and (3.59). For convenience, a shorthand notation is adopted for these moments in future chapters, as summarised below for a band consisting of a single transition.

$$\mathbf{A}_0 \equiv \langle A(E)/E\rangle_0 = \gamma cl\mathcal{D}_0 \tag{3.88}$$

$$\mathbf{M}_0 \equiv \langle \Delta A(E)/E\rangle_0 = \gamma cl\mu_B B\left(\mathcal{B}_0 + \mathcal{C}_0/kT\right) \tag{3.89}$$

$$\mathbf{M}_1 \equiv \langle \Delta A(E)/E\rangle_1^{\overline{E}} = \gamma cl\mu_B B\mathcal{A}_1 \tag{3.90}$$

The source of the Faraday parameter subscripts can be seen from the above expressions; for a single transition, the $\mathcal{B}_0$ and $\mathcal{C}_0$ parameters may be obtained experimentally from the *zeroth* MCD moment, and $\mathcal{A}_1$ from the *first* MCD moment.

Part of the utility of taking ratios of moments can now be seen, with

$$\frac{\mathbf{M}_0}{\mathbf{A}_0} = \frac{\mu_B B\,(\mathcal{B}_0 + \mathcal{C}_0/kT)}{\mathcal{D}_0} \tag{3.91}$$

$$\frac{\mathbf{M}_1}{\mathbf{A}_0} = \frac{\mu_B B \mathcal{A}_1}{\mathcal{D}_0} \tag{3.92}$$

being independent of γcl. The Wigner-Eckart theorem also allows $\mathcal{A}_1$, $\mathcal{B}_0$, $\mathcal{C}_0$ and $\mathcal{D}_0$ to be expressed in terms of reduced electric-dipole transition moments which can be cancelled in the above ratios. It can be seen from (3.91) that a plot of $\mathbf{M}_0/\mu_B B\mathbf{A}_0$ against $1/kT$ will have a slope of $\mathcal{C}_0$ and a y-intercept of $\mathcal{B}_0$.

An important exception to (3.91) and (3.92) occurs for the case where a pair of transitions from a degenerate ground state terminate in levels which have the same parentage, but are split by SO interactions. In this case, the transitions give a pair of $\mathcal{C}$ terms of equal magnitude and opposite sign, resulting in something much like a pseudo-$\mathcal{A}$ term, but which exhibits temperature dependence.[57] The associated first MCD moment, obtained by carrying out the integration of (3.90) over the envelope of both bands is also temperature dependent. Such cases are described in Chapters 4, 5 and 6, where the appropriate theory is developed. It turns out that in the linear limit ($\mu_B B \ll kT$), the slope of $\mathbf{M}_0/\mu_B B\mathbf{A}_0$ against $1/kT$ provides information on the magnitude of the SO coupling, whereas the y-intercept yields information about the g (angular momentum) values of the states.

Chapter 4

The MCD Temperature Dependence of CuPc and CoPc

4.1 Introduction

In this chapter, MCD and absorption spectra measured at a range of temperatures are reported for the Q($\pi \rightarrow \pi^*$) transition of CuPc and CoPc. Both were studied in an Ar matrix (MPc/Ar). CoPc was also studied in a PVC polymer film (CoPc/PVC), however this was not possible in the case of CuPc because of its acute insolubility. The MCD temperature dependence of NiPc/Ar and FePc/Ar were also measured for comparison.

There have been few matrix-isolation investigations of CuPc and CoPc. The most comprehensive was carried out by Misener,[34] who measured absorption and MCD spectra at nominal temperatures of 4.2 and 3.0 K. Douglas *et al.*[58] also report the MCD spectrum of CuPc/Ar, and Lucia *et al.*[59] give CuPc/Ar transmittance spectra at a range of matrix concentrations. There are no other reports of CoPc/Ar spectra. A general review of the spectroscopy of CuPc and CoPc is given by Stillman and Nyokong.[29]

In each of the experiments carried out in this work, the absorption spectra were found to be temperature independent, but the magnitude of the MCD bands increased distinctly with decreasing temperature (except in the cases of NiPc and FePc). To quantify the latter, the method of moments was employed, as discussed in Section 3.7. The zeroth moments ($\mathbf{A}_0$ and $\mathbf{M}_0$) were measured, along with the first moment of the MCD, $\mathbf{M}_1$. In each case $\mathbf{M}_0$ was found to be insignificant relative to $\mathbf{M}_1$. Graphs are shown of the dimensionless ratio $\mathbf{M}_1/\mu_B B\mathbf{A}_0$ plotted against $1/kT$ (/cm^{-1}), and the parameters derived from these plots listed in Section 4.3. These parameters are also tabulated and discussed in Section 4.4.5.4. A theoretical explanation for the MCD temperature dependence, in terms of a zero-field splitting of the excited states, is discussed.

Table 4.1. Experimental parameters of the samples discussed in this chapter.

	Spectrometer	Step size (Å)	Slit width (μm)	Field (T)	Matrix conc.
CuPc/Ar (1)	MOD 3	1	100	1	1:2100
CuPc/Ar (2)	ANU	5	500	1	1:2500
CoPc/Ar (1)	MOD 3	1	100	3	1:32000
CoPc/Ar (2)	MOD 3	5	200	1	1:3300
CoPc/Ar (3)	MOD 4	5	400	1	1:37000
CoPc/PVC	MOD 3	5	200	1	
NiPc/Ar	MOD 3	1	100	3	1:12000
FePc/Ar	MOD 3	1	100	3	1:20000

4.2 Experimental Details

A number of spectral and experimental parameters relating to each of the samples discussed in this chapter are listed in Table 4.1. All spectra obtained at Canterbury were measured in the matrix-injection/SM4 system. Matrix deposition times were typically 10 - 30 min, at sublimation temperatures of 275 - 325 °C. Further details of sample preparation and spectral measurement are given in Chapter 2.

4.3 Results

The Q-band spectra presented in the following pages are labelled as shown for CuPc/Ar in Figure 4.2. The main band is the origin transition, Q(0,0); its MCD has the appearance of a positive $\mathcal{A}$ term (Section 3.4), which is indicative of positive orbital angular momentum in the excited state. Q(1,0) contains overlapping contributions from many vibrational overtones, while Q(2,0) comprises contributions both from overtones and a separate electronic transition,[19,60] denoted Q′.

When using moment analysis, integration should be carried out over an entire transition, including all vibrational components, but excluding contributions from other electronic transitions. This is not possible for the Q band of MPcs because of the presence of the Q′ band. In this situation, moment analysis over the whole band will include more than just the Q($\pi \rightarrow \pi^*$) transitions, and hence give incorrect

results. In an attempt to remove the influence of Q′, moments were determined over ranges both including and excluding the Q(2,0) band.

The existence of Q′ is not the only problem with moment analysis of the spectra in this chapter. Because of the $E - \overline{E}$ term in the definition of M_1 (Section 3.7), the first MCD moment (which is of great importance to the analysis of these data) is inherently very sensitive to components which lie a long way from the band barycentre. This is not a significant problem for cases of high signal-to-noise ratio, or where the signal is spread uniformly over the transition envelope. It can, however, cause difficulties when there are weak outlying bands. The latter is exactly the case for the MPcs, which have a strong Q(0,0) band and a long tail of weaker vibrational overtones extending to the blue. Experience in analysing the following data has shown that the magnitude of M_1 is highly sensitive to the choice of MCD spectral baseline and the range of integration. More specifically, if M_1 is plotted against $1/kT$, a change in baseline or integration range has the effect of shifting the plot up or down, *i.e.* changing the y-intercept but not (to such a significant degree) the slope. The last point is of importance since it is the slope of such a plot that provides the new and interesting information of this chapter. Hence, it has proved possible to extract information amenable to quantitative analysis even in the presence of these problems. However, the (g_{orb}) parameters obtained from the intercepts should be regarded sceptically.

4.3.1 CuPc

Absorption and MCD spectra of the Q and B bands of CuPc in an Ar matrix (CuPc/Ar (1)) at 1.5 K and 1 T are shown in Figure 4.1. Figure 4.2 shows the effect of temperature on the Q band, with spectra measured at temperatures between 1.5 and 4.2 K. These data were collected at the University of Canterbury (UOC). Data were also collected at the Australian National University (ANU) over the temperature range 1.5 - 15 K. The latter spectra (CuPc/Ar (2)) are not shown here due to their similarity to Figure 4.2, but the results of moment analysis on these are included in Figure 4.3. The CuPc/Ar spectra are similar to those reported by Misener,[34] and Douglas *et al.*[58] The spectra of Lucia *et al.*[59] are, however, anomalous to all three reports, showing Q(0,0) as a pair of bands at 680 and 703 nm.

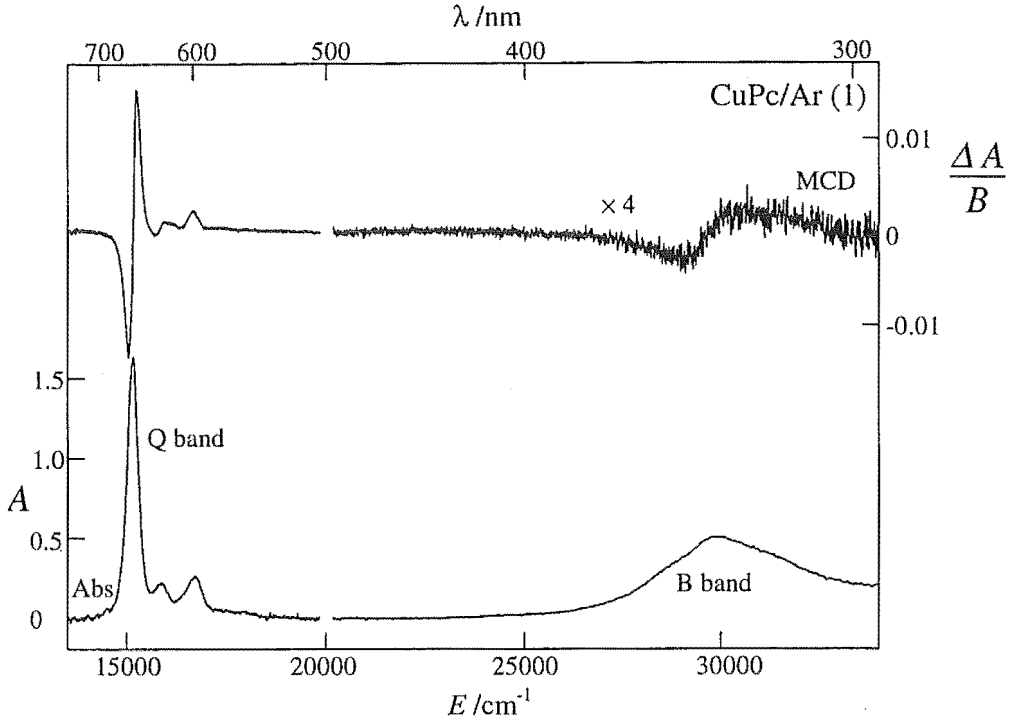

Figure 4.1. Absorption and MCD (per tesla) spectra of CuPc/Ar over the Q- and B-band regions. Spectra were measured at 1.5 K and 1 T.

In an attempt to remove the influence of Q′, moments were determined over ranges both including and excluding the Q(2,0) band. In each case, the zeroth moments ($\mathbf{A}_0$ and $\mathbf{M}_0$) were found to be positive and temperature independent. $\mathbf{M}_0$ is relatively small and arises predominantly from the Q′ transition; integration over the full region of Figure 4.2 yields $\mathbf{M}_0/\mu_B B\mathbf{A}_0 = (1.0\pm0.4) \times 10^{-3}$ T^{-1}, which is reduced by more than an order of magnitude by the exclusion of Q(2,0). For both of the samples $\mathbf{M}_1$ is positive and increases linearly (within experimental uncertainty) with the reciprocal of the temperature, as illustrated in Figure 4.3. Moment analysis over the whole Q band yields, for the UOC data, a slope of 1.6 ± 0.2 cm^{-1} and y-intercept of 4.8 ± 0.2. The plot of the ANU data has a slope of 1.8 ± 0.4 cm^{-1} and y-intercept of 5.6 ± 0.2. When analysis is carried out such that Q(2,0) is excluded, the UOC data has a slope of 1.3 ± 0.1 cm^{-1} and y-intercept of 2.7 ± 0.1 while the ANU data has a slope of 1.3 ± 0.1 cm^{-1} and y-intercept of 3.00 ± 0.06. These results illustrate the comments in the previous section that the y-intercept is very sensitive to the change in integration range, while the slope (within experimental error) is not greatly affected.

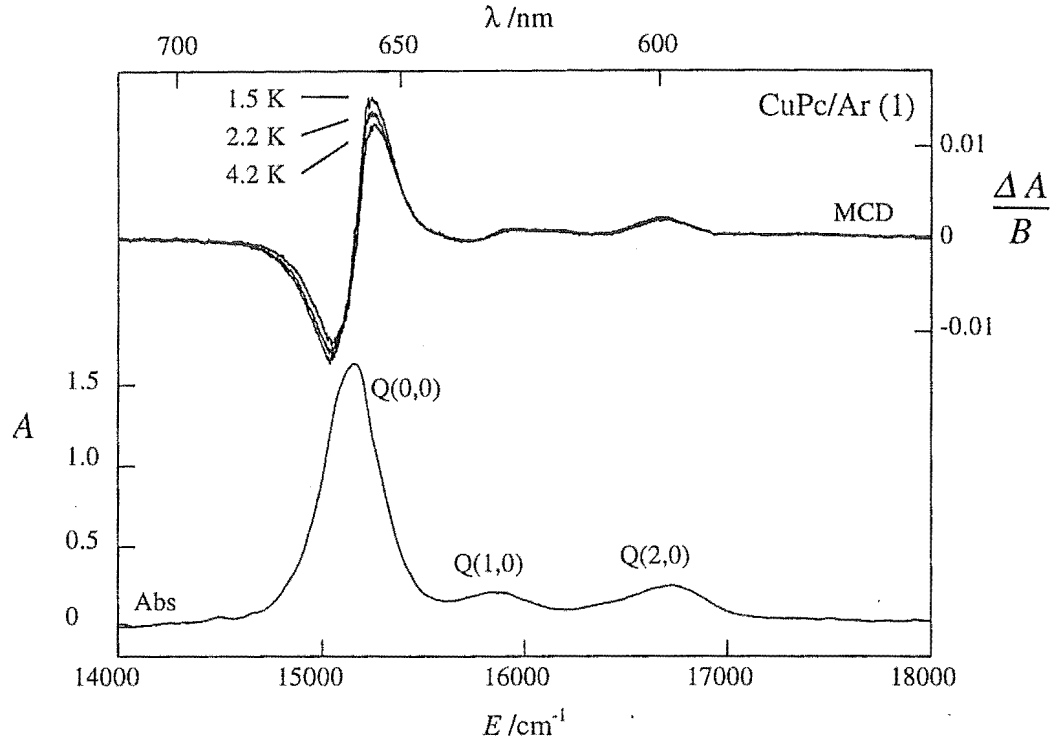

Figure 4.2. CuPc/Ar absorption and MCD (per tesla) spectra obtained at UOC. Spectra were measured at a field of 1 T.

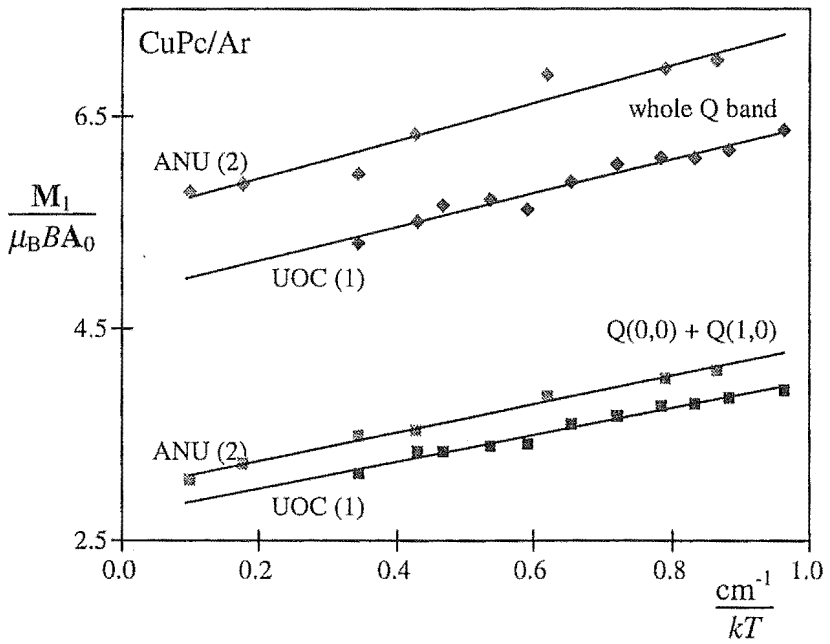

Figure 4.3. The temperature dependence of $M_1/\mu_B BA_0$ for CuPc/Ar spectra. Dark shading represents data obtained at UOC (CuPc/Ar (1)), and light shading represents data obtained at ANU (CuPc/Ar (2)). ♦ indicates moments taken over the whole Q band, and ■ indicates moments taken over Q(0,0) and Q(1,0) only. The line of best fit for each data set is shown - the parameters of these lines are given in the text. Note that the slopes of these lines are very similar, even though their y intercepts are significantly different (see text).

4.3.2 CoPc

The Q- and B-band absorption and MCD spectra of CoPc in a matrix (CoPc/Ar (2)) and a polymer film (CoPc/PVC) are compared in Figures 4.4 and 4.5. The matrix was one of two for which the temperature dependence of the Q band (Figures 4.6 and 4.7) was studied at 1 T (and temperatures of 1.4 - 4.2 K) . The MCD temperature dependence of a third matrix, measured at a field of 3 T, (CoPc/Ar (3), Figure 4.8) appears to be considerably quenched relative to that seen in Figure 4.6. This is due to field-dependent saturation effects, as discussed in Section 4.4.5.3. The Q-band spectra obtained for CoPc/PVC between 1.4 and 20 K are shown in Figure 4.9.

The Q-band MCD spectra of CoPc differ significantly between the two media. The PVC film shows a temperature dependence (Figure 4.9) similar to that of CuPc/Ar (Figure 4.2), the main feature being an increase in intensity of the $\mathcal{A}$-term-shaped Q(0,0) band with decreasing temperature. This effect is also seen in the CoPc/Ar matrix spectra of Figure 4.6, but in addition, oppositely signed bands appear on the outskirts of the $\mathcal{A}$ term as the temperature decreases, having the appearance of a broad negatively-signed temperature-dependent $\mathcal{A}$ term. This negative $\mathcal{A}$-term-shaped band is especially noticeable in the spectra in Figure 4.6 (arrowed lobes), and was present in differing amounts in all three CoPc/Ar temperature-dependence studies carried out. It is probably due to an impurity, perhaps a decomposition product produced at high sublimation temperatures. Unfortunately, its presence prevents accurate quantitative analysis of the spectra. The Q-band CoPc/Ar MCD spectra of Misener[34] also show signs of impurity bands with relatively strong temperature dependence.

Investigation of the CoPc/Ar (2) spectra over a wider energy range, as shown in Figure 4.4, confirms the presence of an impurity, with a number of features apparent (marked with arrows) which are not present in the CoPc/PVC spectra (Figure 4.5), and are not characteristic of MPc spectra in general.[19,34] These include a series of relatively strong MCD features in the region between the Q and B bands with no apparent corresponding absorption bands, a sharp absorption band in the middle of the B-band region, and a positive MCD band on the red edge of the B band. It is interesting to note that Edwards and Gouterman[61] observed an absorption

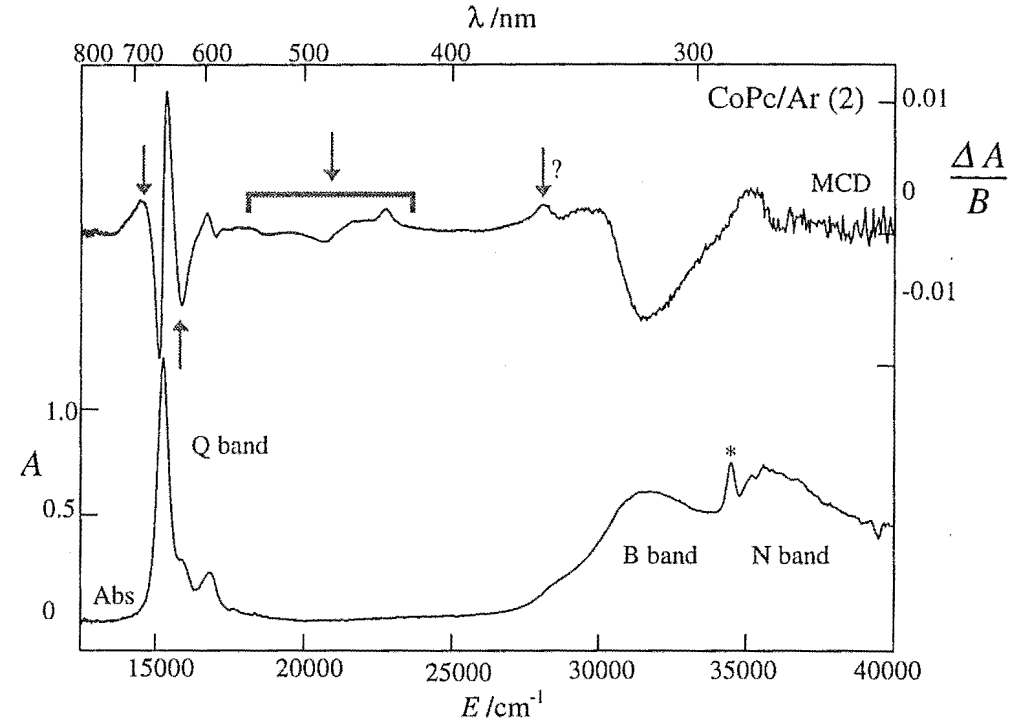

Figure 4.4. Absorption and MCD (per tesla) spectra of CoPc/Ar over the Q-, B- and N-band regions, measured at 1.5 K and 1 T. A phthalonitrile band is marked with a *. Features due to another impurity are indicated with arrows, and discussed in the text.

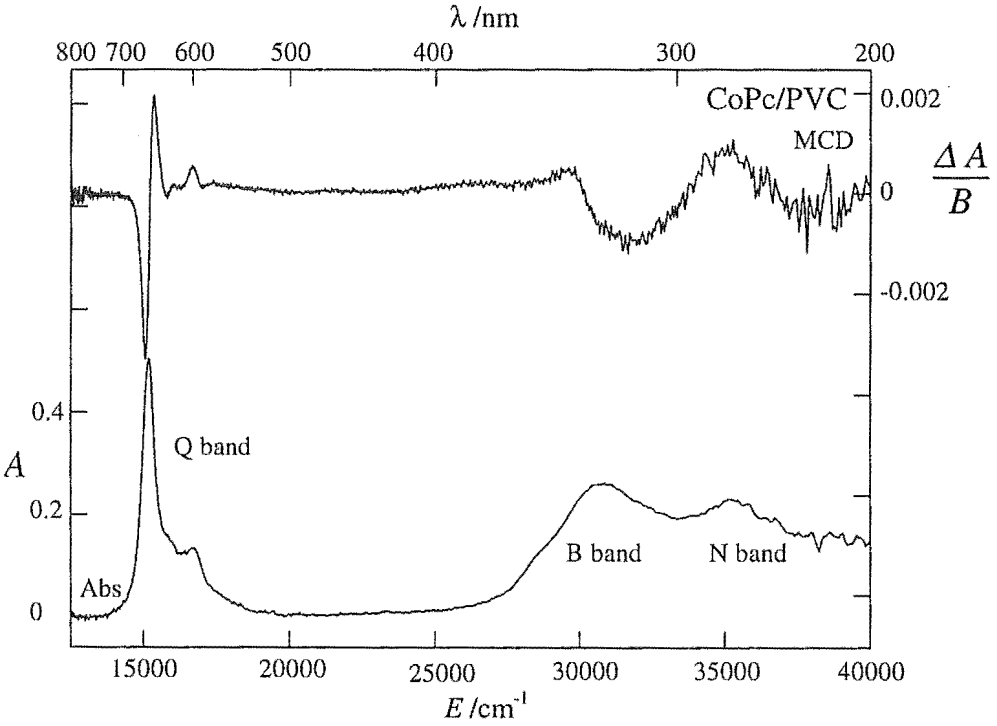

Figure 4.5. Absorption and MCD (per tesla) spectra of CoPc/PVC over the Q-, B- and N-band regions. Spectra were measured at 1.5 K and 1 T.

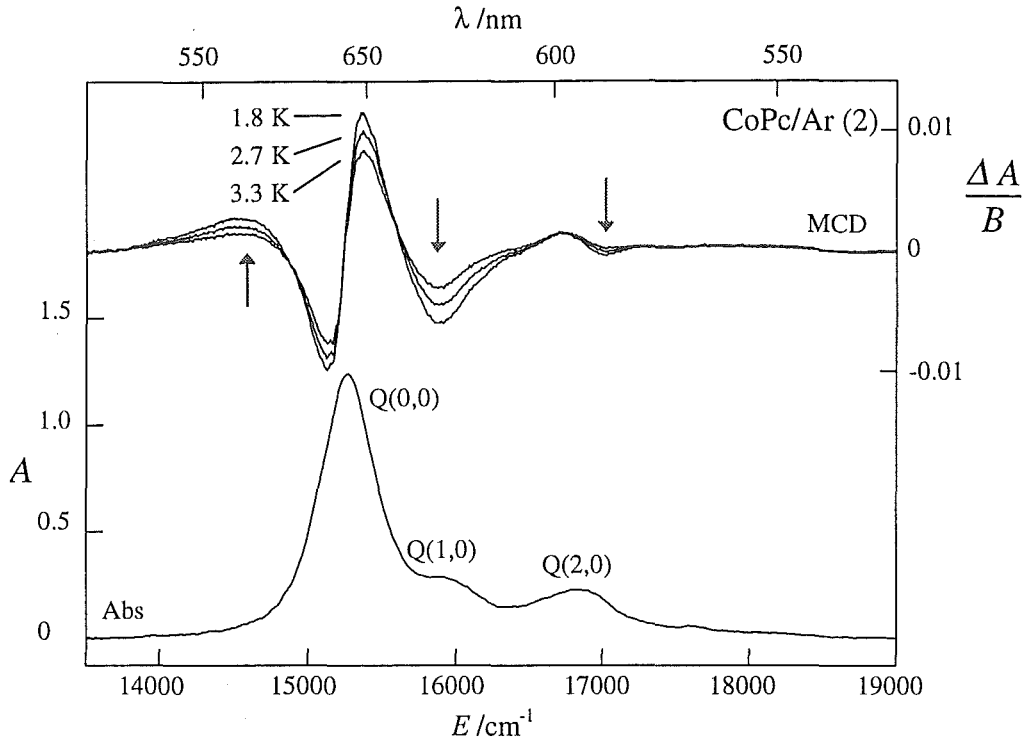

Figure 4.6. A typical set of CoPc/Ar Q-band absorption and MCD (per tesla) spectra measured at a field of 1 T. The arrows indicate impurity bands, and point in the direction of the effect of decreasing temperature.

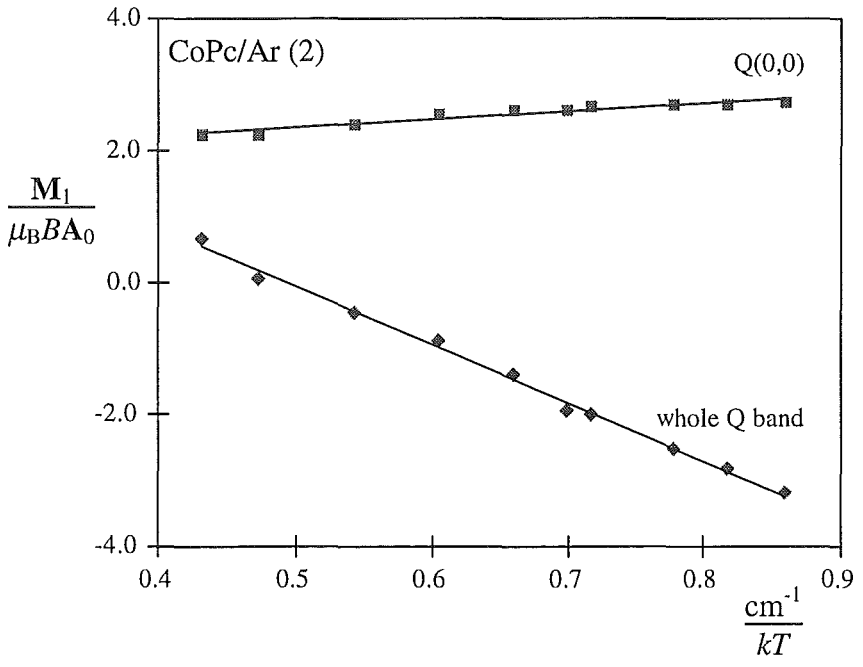

Figure 4.7. The temperature dependence of $M_1/\mu_B BA_0$ for a typical set of CoPc/Ar spectra measured at 1 T. ♦ represents moments taken over the whole Q band, and ■ represents moments taken over Q(0,0) only. The line of best fit for each data set is shown - the parameters of these lines are given in the text.

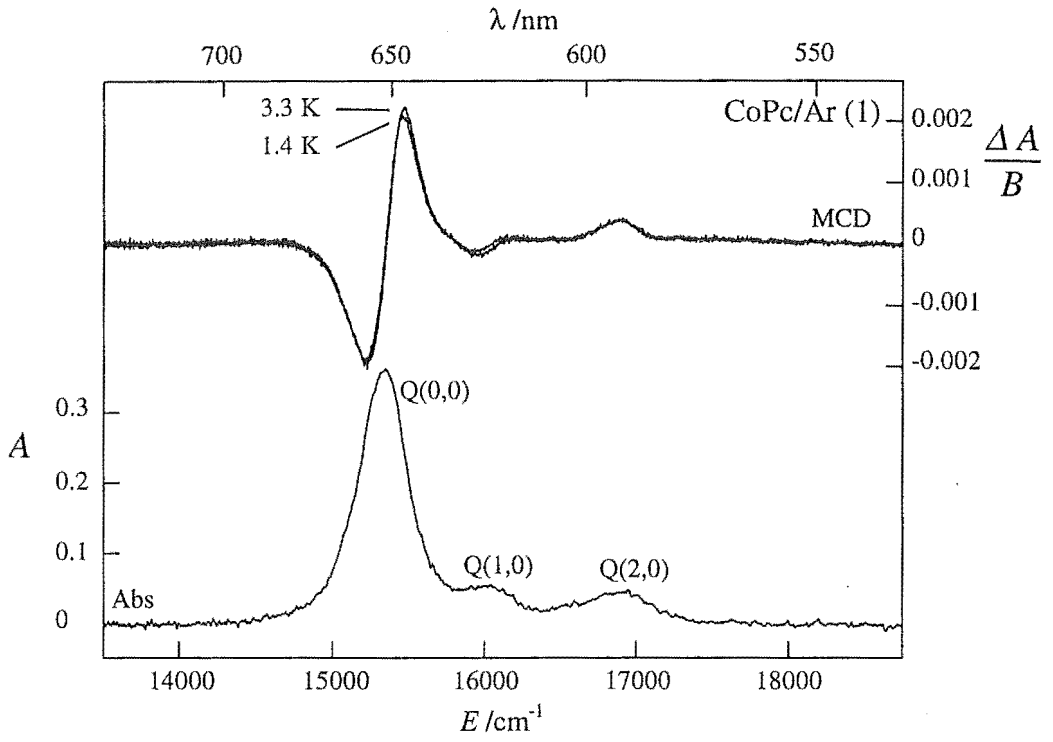

Figure 4.8. CoPc/Ar Q-band absorption and MCD (per tesla) spectra measured at a field of 3 T.

band at 480 nm in a vapour spectrum of (sublimed) CoPc, which was absent in a corresponding solution spectrum measured in dimethylsulfoxide. This is the same wavelength region as the series of MCD features in Figure 4.4 which are attributed to the impurity.

It may be that the CoPc/PVC sample is also not free of this impurity, as indicated by the general decrease in intensity of the Q(1,0) and Q(2,0) MCD bands with decreasing temperature (Figure 4.9). Such temperature dependence of the overtone bands is not seen in the CuPc/Ar spectra of Figure 4.2, and the regions of changing intensity in the CoPc/PVC spectra have the same energy separation from the Q(0,0) band as do the impurity transitions in CoPc/Ar (Figure 4.6). Note, however, that these effects are substantially weaker than those seen in the matrix data, indicating that the impurity is probably related to the sublimation process.

Moment analysis of CoPc/Ar is complicated by the presence of both the Q′ band (as for CuPc), and the impurity, which has a strong MCD temperature dependence. An attempt was made to obtain a reasonable estimate of the true Q-transition moments by carrying out analyses not only over the whole Q band, but

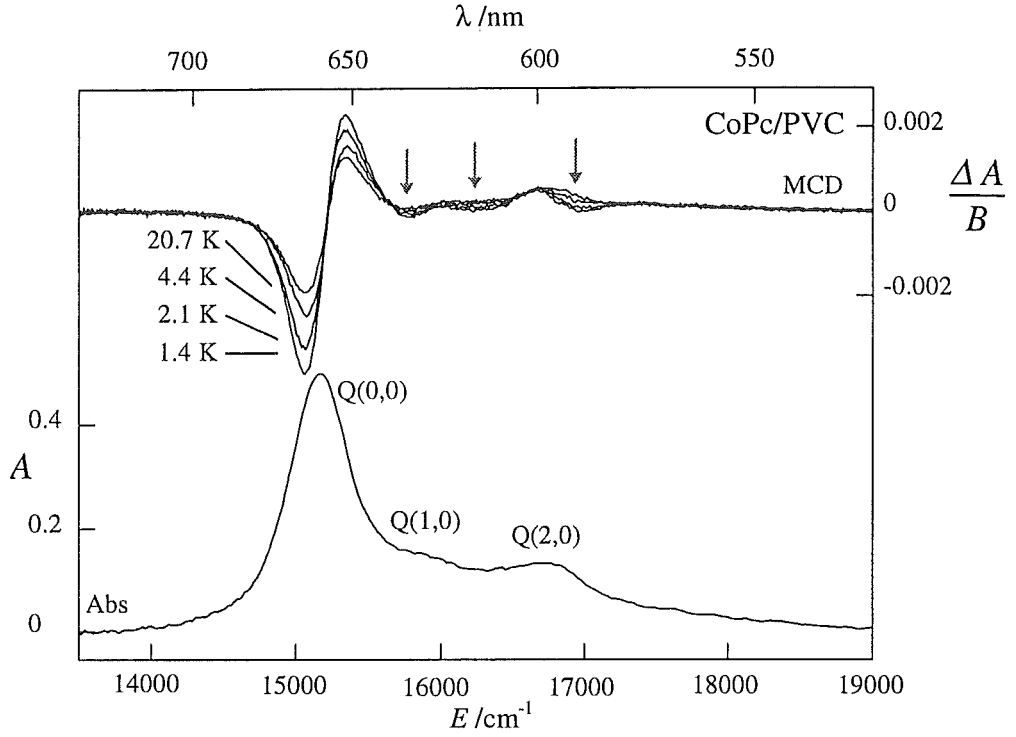

Figure 4.9. CoPc/PVC Q-band absorption and MCD (per tesla) spectra, measured at 1 T. The arrows, pointing in the direction of decreasing temperature, indicate temperature dependence which may be due to an impurity (see text).

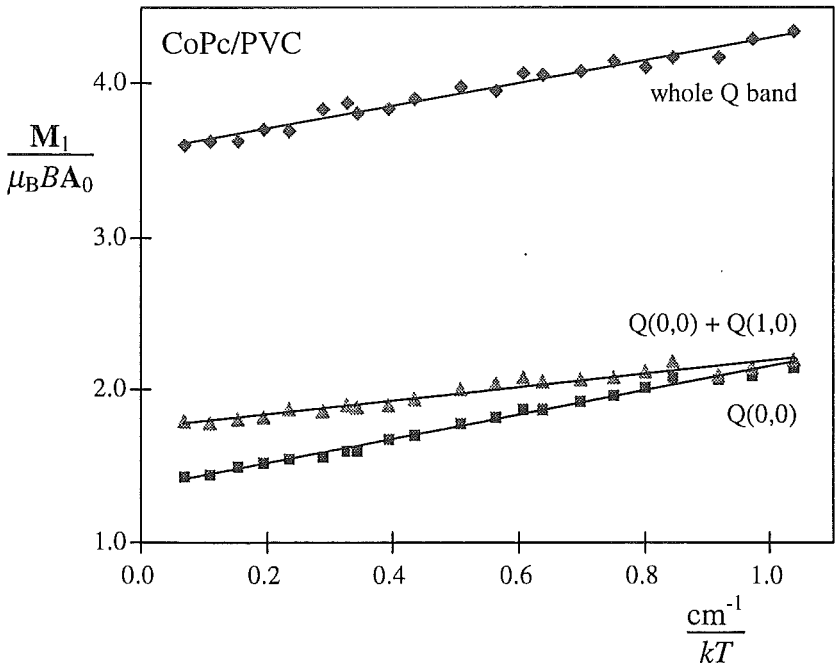

Figure 4.10. The temperature dependence of $M_1/\mu_B BA_0$ for CoPc/PVC spectra. ♦ represents moments taken over the whole Q band, ▲ represents moments taken over Q(0,0) and Q(1,0), and ■ represents moments taken over Q(0,0) only. The line of best fit for each data set is shown - the parameters of these lines are given in the text.

also over Q(0,0) alone. This allows comparison to be made with data obtained from the CoPc/PVC sample, which appears to have relatively little contamination.

All of the $\mathbf{M}_0$ values determined from the CoPc spectra were relatively small - a factor of 10^{-5} less than $\mathbf{M}_1$. A graph of $\mathbf{M}_1/\mu_B B\mathbf{A}_0$ vs $1/kT$ for the CoPc/Ar (2) data (measured at 1 T) is shown in Figure 4.7. The line of best fit over the whole Q band has a slope of -8.9 ± 0.4 cm^{-1} and y-intercept of 4.4 ± 0.3. Over Q(0,0) alone, the line of best fit has a slope of 1.2 ± 0.2 cm^{-1} and y-intercept of 1.7 ± 0.2.

In the case of CoPc/PVC (Figure 4.9), the contribution from the impurity is much smaller, but Q′ must still be taken into consideration. Moment analyses were carried out over three ranges; the whole Q band, Q(0,0) and Q(1,0), and Q(0,0) only, the latter for the sake of comparison with CoPc/Ar data. The temperature dependence of $\mathbf{M}_1/\mu_B B\mathbf{A}_0$ in each case is shown in Figure 4.10. The lines of best fit have slopes of 0.70 ± 0.1, 0.45 ± 0.04 and 0.79 ± 0.02 cm^{-1} and y-intercepts of 3.56 ± 0.03, 1.75 ± 0.03 and 1.36 ± 0.02 respectively.

Variable-temperature studies have also been carried out on the B band of CoPc/Ar (2) and CoPc/PVC, as shown in Figures 4.11 and 4.12. Because of the overlap between the B-band and N-band regions, moment analysis was carried out using a deconvolution process. The individual (Gaussian) and overall calculated bands giving the best fit to the data are shown in the relevant figures. In the case of the matrix spectra, the B region was fitted with two bands,[19] and the sum of these used in the moment analysis. The B-band spectra presented here are similar to the CoPc/Ar spectra of Misener,[34] which also show an MCD band to the red of the main band.

Moments were taken over two ranges, including and excluding the MCD band to the red, which may be due to an impurity. The results of moment analysis are shown as a plot of $\mathbf{M}_1/\mu_B B\mathbf{A}_0$ vs $1/kT$ in Figure 4.13. When moments are taken over the reduced range (28600 - 34300 cm^{-1} for the matrix and 27700 - 30650 cm^{-1} for the film) the lines of best fit have slopes of -21 ± 2 cm^{-1} and -10.4 ± 0.5 cm^{-1} and y-intercepts of -0.4 ± 1.2 and 0.1 ± 0.2 for CoPc/Ar and CoPc/PVC respectively. For moments taken over the whole B band, (25000 - 34300 cm^{-1} for the matrix and 23500 - 30650 cm^{-1} for the film) the lines of best fit have slopes of -35 ± 2 cm^{-1} and -18.2 ± 0.5 cm^{-1} and y-intercepts of 1.3 ± 1.0 and 0.2 ± 0.3 for CoPc/Ar and CoPc/PVC respectively.

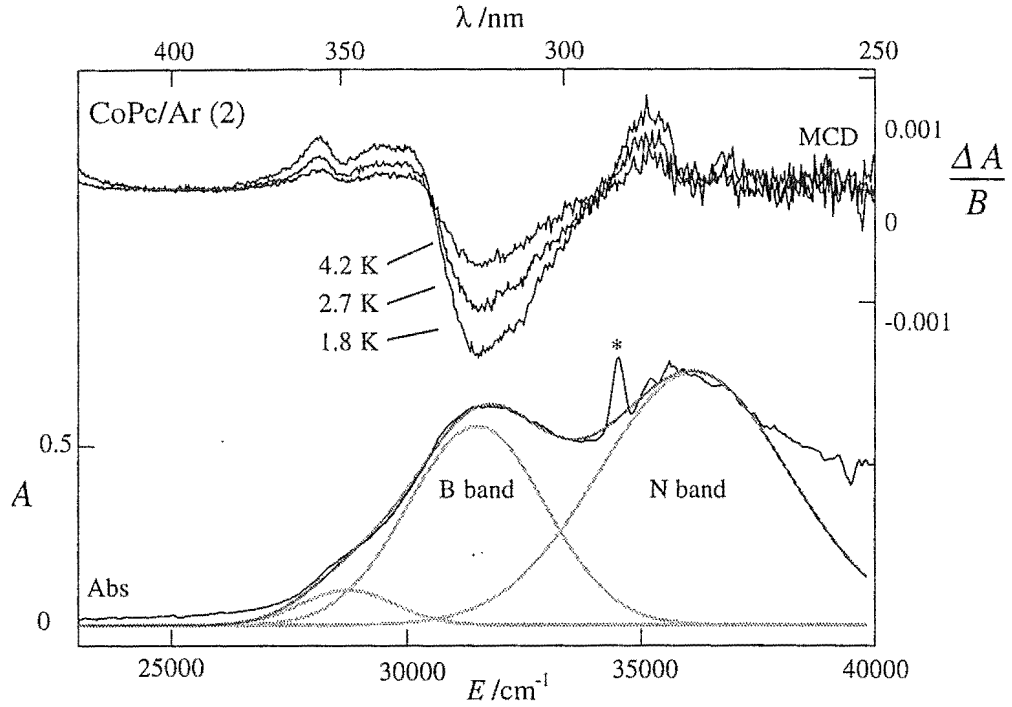

Figure 4.11. CoPc/Ar B- and N-band absorption and MCD (per tesla) spectra, measured at 1 T. A phthalonitrile impurity band is indicated by an asterisk. The dark grey line is a best fit to the absorption data using three Gaussian bands (light grey) The two lower-energy bands were used to obtain an estimate of $\mathbf{A}_0$ for the B region.

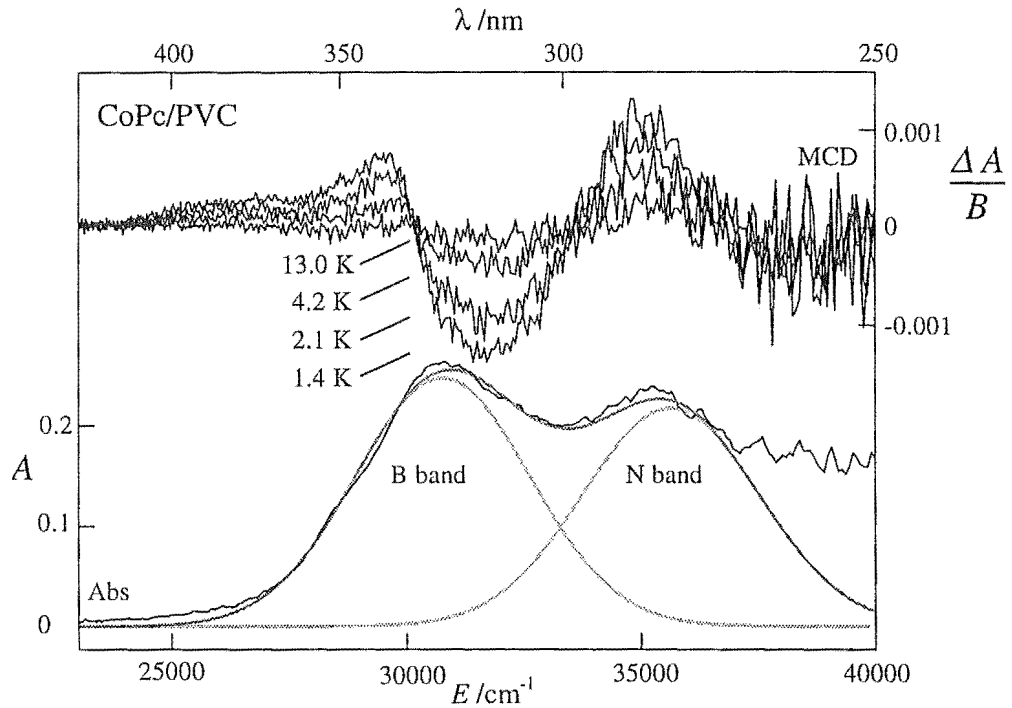

Figure 4.12. CoPc/PVC B- and N-band absorption and MCD (per tesla) spectra measured at 1 T. The dark grey line is a best fit to the absorption data using two Gaussian bands (light grey) The lower-energy band was used to obtain an estimate of $\mathbf{A}_0$ for the B region.

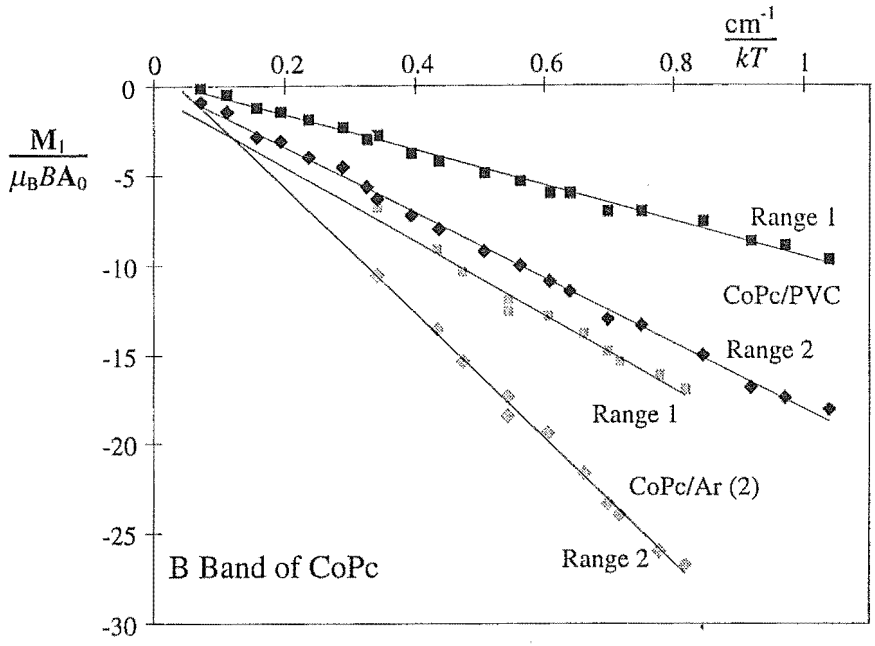

Figure 4.13. The temperature dependence of $\mathbf{M}_1/\mu_B B\mathbf{A}_0$ for CoPc/Ar and CoPc/PVC B-band spectra. Moments taken over two ranges are shown: for CoPc/Ar, range 1 = 28600 - 34300 cm^{-1}, range 2 = 25000 - 34300 cm^{-1}. For CoPc/PVC, range 1 = 27700 - 30650 cm^{-1} and range 2 = 23500 - 30650 cm^{-1} The parameters of the lines of best fit are given in the text.

4.3.3 NiPc and FePc

It might be reasonable to question whether the observed temperature dependences are in fact experimental artifacts. This has been shown not to be the case by the measurement of Q-band spectra of NiPc/Ar and FePc/Ar (Figures 4.14 and 4.16 respectively) between 1.4 and 4.2 K. As will be seen later (Section 4.4.1), the essential difference between CuPc and CoPc on one hand, and NiPc and FePc on the other, lies in the degeneracy of their ground states. The former are paramagnetic (doublet ground states), while the latter are diamagnetic (singlet ground states). Since MCD temperature dependence arises from changing ground-state populations (Section 3.4), NiPc and FePc would not be expected to show any temperature effects.

This is borne out experimentally, as can be seen from the $\mathbf{M}_1/\mu_B B\mathbf{A}_0$ vs $1/kT$ plots for NiPc/Ar in Figure 4.15, and for FePc/Ar in Figure 4.17. For NiPc/Ar, analysis over the whole Q band gives a line of best fit with a slope of 0.4 ± 0.3 cm^{-1} and y-intercept of 4.7 ± 0.2. When the Q(2,0) band is excluded, these parameters drop to 0.2 ± 0.1 cm^{-1} and 2.94 ± 0.06 respectively. For FePc/Ar, the line of best fit for analysis over the whole Q band has a slope of 0.4 ± 0.7 cm^{-1} and y-intercept of 4.3 ± 0.5. When the Q(2,0) band is excluded, the slope is 0.1 ± 0.3 cm^{-1} and the y-intercept is 4.0 ± 0.2. Given the errors involved, the values of these slopes are essentially zero.

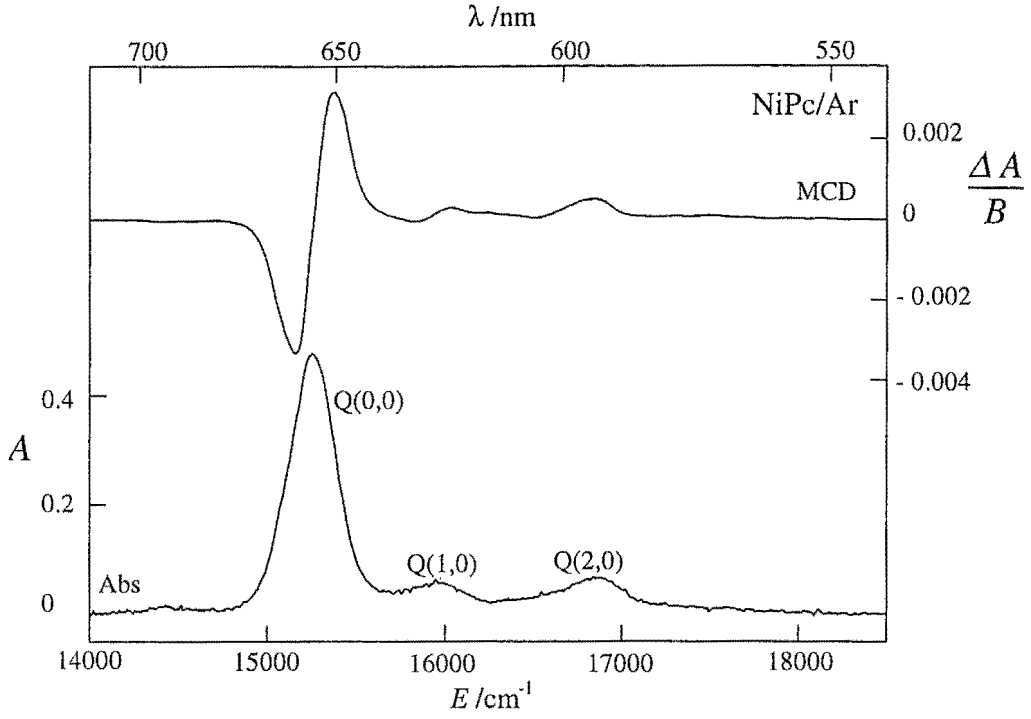

Figure 4.14. Absorption and MCD (per tesla) spectra of NiPc/Ar, measured at 3 T.

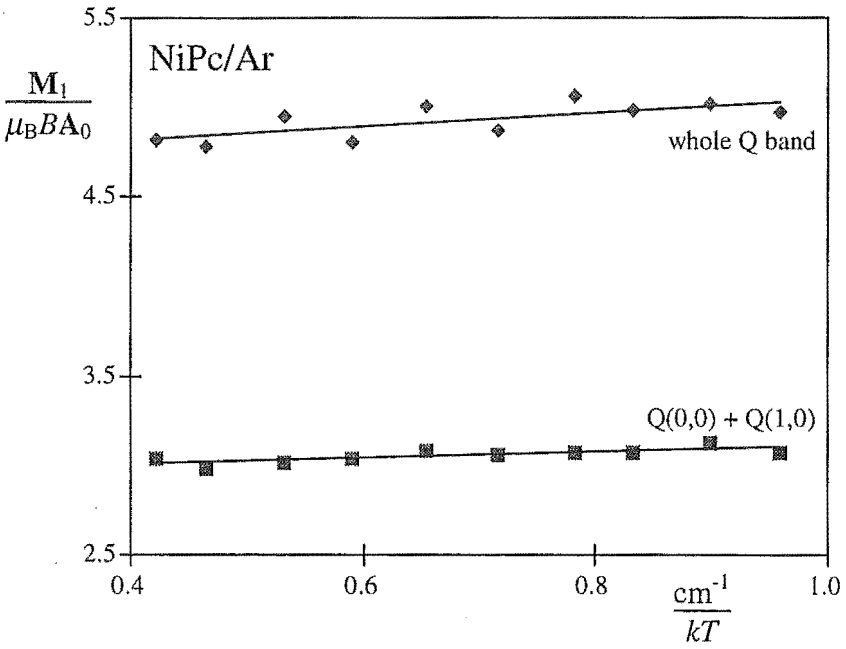

'igure 4.15. Variation of $M_1/\mu_B BA_0$ with $1/kT$ for NiPc/Ar spectra. ♦ represents moments ıken over the whole Q band, and ■ represents moments taken over Q(0,0) and Q(1,0) only. The ne of best fit for each data set is shown - the parameters of these lines are given in the text.

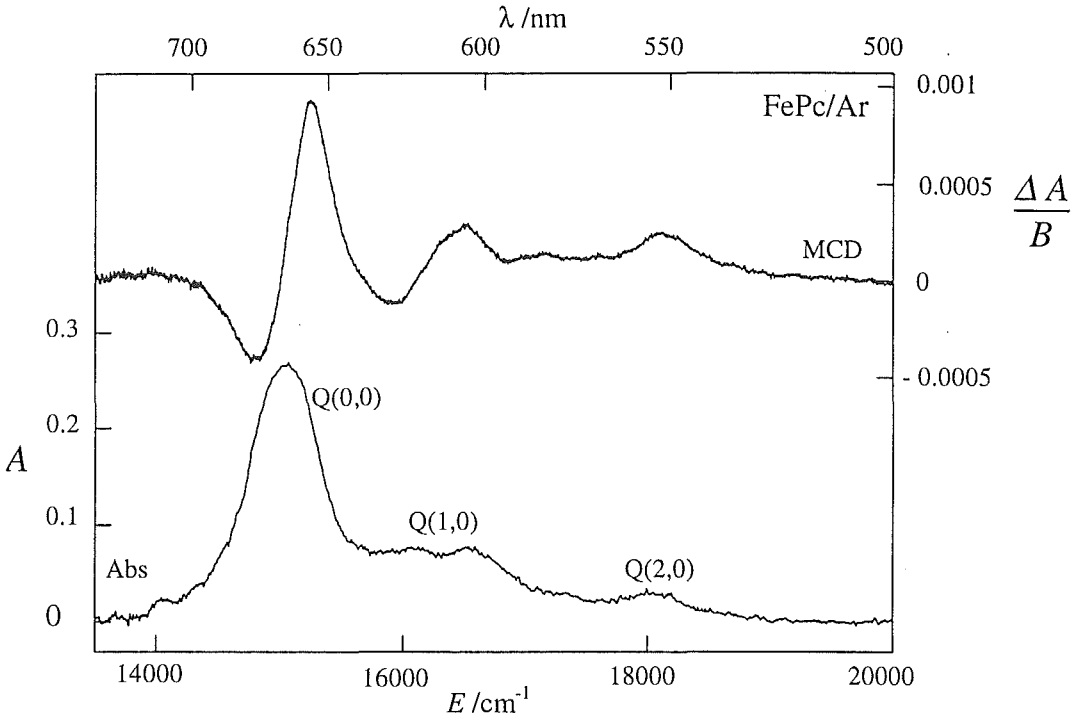

Figure 4.16. Absorption and MCD (per tesla) spectra of FePc/Ar, measured at 3 T.

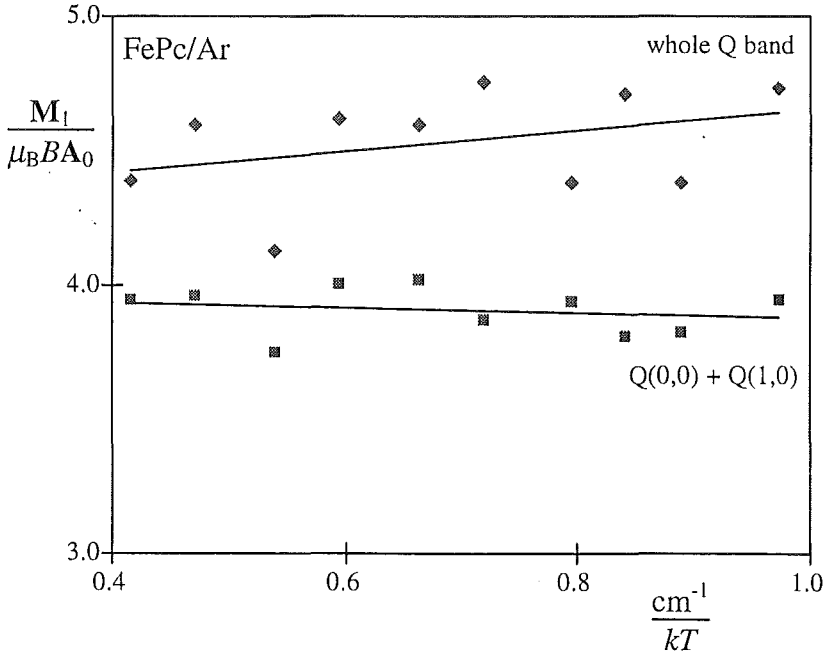

Figure 4.17. Variation in $M_1/\mu_B BA_0$ with $1/kT$ for FePc/Ar spectra. ♦ represents moments taken over the whole Q band, and ■ represents moments taken over Q(0,0) and Q(1,0) only. The line of best fit for each data set is shown - the parameters of these lines are given in the text.

4.4 Discussion

4.4.1 The Q($\pi \rightarrow \pi^*$) Transition

Cu^{2+} and Co^{2+} are odd-electron ions, of d^9 and d^7 configuration respectively. Complexation of the metal by a phthalocyanine ring lowers the degeneracy of the d-orbital manifold. In the ground state, the unpaired electron resides in a non-degenerate molecular orbital, m, which is primarily of metal d-orbital character. The crystal structures of CuPc[62] and CoPc[63,64] have been determined, and the molecules are found to have symmetry close to D_{4h}, with minor deviations from planarity. It seems likely that such deviations arise from crystal packing forces, and D_{4h} symmetry is consequently assumed in the matrix-isolated and polymer samples of these molecules. (In fact, the moments $\mathbf{M}_1$, $\mathbf{M}_0$ and $\mathbf{A}_0$ are invariant to unitary transformations of the excited-state basis,[32] and so are independent of first-order crystal-field and vibronic effects. Thus the assumption of D_{4h} symmetry does not negate the following analysis.) In this symmetry group both molecules have doublet ground states, with the configuration a_{1u}^2 m, where a_{1u} is the HOMO of the ligand.

The excitation predominantly responsible for the Q band is the xy-polarised ligand-based $a_{1u}(\pi) \rightarrow e_g(\pi^*)$ excitation. There are three excited-state terms arising from this excitation, referred to (in order of ascending energy) as the quartet (^4E_u), tripdoublet ($^2E_u^T$) and singdoublet ($^2E_u^S$).[65] The orbital diagrams for these terms are shown in Figure 4.18. The two doublets arise from coupling of the metal electron to the triplet and singlet states of the ligand respectively. Only the excitation terminating in the singdoublet is spin allowed.

There have been a number of theoretical calculations carried out on CuPc.[66–69] Of these, an early study by Henriksson *et al.*[66] appears to be the most accurate and comprehensive. This study used a semi-empirical self-consistent field (SCF) MO 'peel' method which takes explicit account of electron-electron valence interactions. D_{4h} symmetry was assumed, with a coordinate system in which x and y axes pass through the centre of the benzo rings. In this case CuPc has a $^2B_{1g}$ ground-state term - the orbital m having b_{1g} symmetry. (Rotation of the axis system by 45° in the xy plane would change the ground-state orbital symmetry label to b_{2g}.) The half-filled b_{1g} orbital was calculated to be predominantly ($\sim 71\%$) of metal $d_{x^2-y^2}$ character.

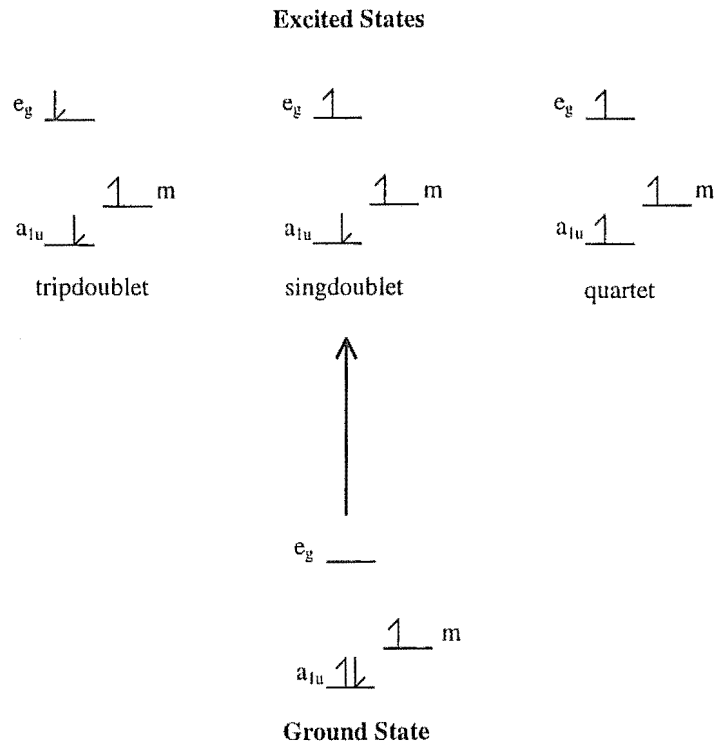

Figure 4.18. Possible electron configurations for the Q(a_{1u} (π) → e_g (π^*)) excitation of CuPc and CoPc.

^4E_u and $^2E_u^T$ were found to be principally (∼ 94%) single-configuration terms, while $^2E_u^S$ contained a small but significant (∼16%) admixture from $a_{2u}(\pi)$→$e_g(\pi^*)$.

There has been some discussion over the ground-state symmetry of CoPc, with disagreement between the results of theoretical calculations[67,70–72] and experiment. ESR measurements[73–76] have conclusively shown the ground state (for crystalline samples) to be $^2A_{1g}$ with the unpaired electron in an a_{1g} orbital of metal d_{z^2} character. Further analysis of these experiments,[77] along with magnetic measurements[78–80] and a recent charge-density study[81] show, however, that significant configuration interaction in the ground state is necessary to fully explain the observed ESR magnetic behaviour.

Spin-orbit (SO) wavefunctions for the relevant CuPc and CoPc ground and excited states were calculated under a complex basis using the chain $D_{4h} \supset D_4 \supset C_{4h}$, and are listed in Tables 4.2 and 4.3 respectively. Coefficients of the wavefunctions were determined using the expansion equation, (3.83). The three spins were first coupled under SO_3 symmetry, and appropriate phase choices then made to relate these to a D_{4h} basis. The three spatial orbitals were coupled together in D_{4h}, and the

Table 4.2. CuPc Q transition-ground- and excited-state wavefunctions and Zeeman shifts. The orbital m is given in bold in the wavefunctions and the parity labels u and g have been omitted. The spin associated with each orbital is denoted by a superscript ± for $m_s = \pm\frac{1}{2}$

State	Level	Wavefunction	Zeeman Shift
$^2B_{1g}$	$\left\vert\left(^2B_{1g}\ -\frac{1}{2}\ 0\right) E_{3/2g}\ \frac{3}{2}\right\rangle$	$\left\vert a_1^+ a_1^- b_1^-\right\rangle$	$-\mu_B B$
	$\left\vert\left(^2B_{1g}\ \frac{1}{2}\ 0\right) E_{3/2g}\ -\frac{3}{2}\right\rangle$	$-\left\vert a_1^+ a_1^- b_1^+\right\rangle$	$\mu_B B$
$^2E_u^S$	$\left\vert\left(^2E_u^S\ -\frac{1}{2}\ 1\right) E_{1/2u}\ \frac{1}{2}\right\rangle$	$-\frac{1}{\sqrt{2}}\left(\left\vert a_1^+ e_{-1}^- b_1^-\right\rangle - \left\vert a_1^- e_{-1}^+ b_1^-\right\rangle\right)$	$\left(-\frac{1}{2}g_{orb} - 1\right)\mu_B B$
	$\left\vert\left(^2E_u^S\ \frac{1}{2}\ -1\right) E_{1/2u}\ -\frac{1}{2}\right\rangle$	$\frac{1}{\sqrt{2}}\left(\left\vert a_1^+ e_{+1}^- b_1^+\right\rangle - \left\vert a_1^- e_{+1}^+ b_1^+\right\rangle\right)$	$\left(\frac{1}{2}g_{orb} + 1\right)\mu_B B$
	$\left\vert\left(^2E_u^S\ \frac{1}{2}\ 1\right) E_{3/2u}\ \frac{3}{2}\right\rangle$	$-\frac{1}{\sqrt{2}}\left(\left\vert a_1^+ e_{-1}^- b_1^+\right\rangle - \left\vert a_1^- e_{-1}^+ b_1^+\right\rangle\right)$	$\left(-\frac{1}{2}g_{orb} + 1\right)\mu_B B$
	$\left\vert\left(^2E_u^S\ -\frac{1}{2}\ -1\right) E_{3/2u}\ -\frac{3}{2}\right\rangle$	$-\frac{1}{\sqrt{2}}\left(\left\vert a_1^+ e_{+1}^- b_1^-\right\rangle - \left\vert a_1^- e_{+1}^+ b_1^-\right\rangle\right)$	$\left(\frac{1}{2}g_{orb} - 1\right)\mu_B B$
$^2E_u^T$	$\left\vert\left(^2E_u^T\ -\frac{1}{2}\ 1\right) E_{1/2u}\ \frac{1}{2}\right\rangle$	$-\frac{1}{\sqrt{6}}\left(\left\vert a_1^+ e_{-1}^- b_1^-\right\rangle + \left\vert a_1^- e_{-1}^+ b_1^-\right\rangle - 2\left\vert a_1^- e_{-1}^- b_1^+\right\rangle\right)$	$\left(-\frac{1}{2}g_{orb} - 1\right)\mu_B B$
	$\left\vert\left(^2E_u^T\ \frac{1}{2}\ -1\right) E_{1/2u}\ -\frac{1}{2}\right\rangle$	$-\frac{1}{\sqrt{6}}\left(\left\vert a_1^+ e_{+1}^- b_1^+\right\rangle + \left\vert a_1^- e_{+1}^+ b_1^+\right\rangle - 2\left\vert a_1^+ e_{+1}^+ b_1^-\right\rangle\right)$	$\left(\frac{1}{2}g_{orb} + 1\right)\mu_B B$
	$\left\vert\left(^2E_u^T\ \frac{1}{2}\ 1\right) E_{3/2u}\ \frac{3}{2}\right\rangle$	$\frac{1}{\sqrt{6}}\left(\left\vert a_1^+ e_{-1}^- b_1^+\right\rangle + \left\vert a_1^- e_{-1}^+ b_1^+\right\rangle - 2\left\vert a_1^+ e_{-1}^+ b_1^-\right\rangle\right)$	$\left(-\frac{1}{2}g_{orb} + 1\right)\mu_B B$
	$\left\vert\left(^2E_u^T\ -\frac{1}{2}\ -1\right) E_{3/2u}\ -\frac{3}{2}\right\rangle$	$-\frac{1}{\sqrt{6}}\left(\left\vert a_1^+ e_{+1}^- b_1^-\right\rangle + \left\vert a_1^- e_{+1}^+ b_1^-\right\rangle - 2\left\vert a_1^- e_{+1}^- b_1^+\right\rangle\right)$	$\left(\frac{1}{2}g_{orb} - 1\right)\mu_B B$
^4E_u	$\left\vert\left(^4E_u\ -\frac{1}{2}\ 1\right) E_{1/2u}\ \frac{1}{2}\right\rangle$	$\frac{1}{\sqrt{3}}\left(\left\vert a_1^+ e_{-1}^- b_1^-\right\rangle + \left\vert a_1^- e_{-1}^+ b_1^-\right\rangle + \left\vert a_1^- e_{-1}^- b_1^+\right\rangle\right)$	$\left(-\frac{1}{2}g_{orb} - 1\right)\mu_B B$
	$\left\vert\left(^4E_u\ \frac{1}{2}\ -1\right) E_{1/2u}\ -\frac{1}{2}\right\rangle$	$\frac{1}{\sqrt{3}}\left(\left\vert a_1^+ e_{+1}^- b_1^+\right\rangle + \left\vert a_1^- e_{+1}^+ b_1^+\right\rangle + \left\vert a_1^+ e_{+1}^+ b_1^-\right\rangle\right)$	$\left(\frac{1}{2}g_{orb} + 1\right)\mu_B B$
	$\left\vert\left(^4E_u\ \frac{1}{2}\ 1\right) E_{3/2u}\ \frac{3}{2}\right\rangle$	$-\frac{1}{\sqrt{3}}\left(\left\vert a_1^+ e_{-1}^- b_1^+\right\rangle + \left\vert a_1^- e_{-1}^+ b_1^+\right\rangle + \left\vert a_1^+ e_{-1}^+ b_1^-\right\rangle\right)$	$\left(-\frac{1}{2}g_{orb} + 1\right)\mu_B B$
	$\left\vert\left(^4E_u\ -\frac{1}{2}\ -1\right) E_{3/2u}\ -\frac{3}{2}\right\rangle$	$\frac{1}{\sqrt{3}}\left(\left\vert a_1^+ e_{+1}^- b_1^-\right\rangle + \left\vert a_1^- e_{+1}^+ b_1^-\right\rangle + \left\vert a_1^- e_{+1}^- b_1^+\right\rangle\right)$	$\left(\frac{1}{2}g_{orb} - 1\right)\mu_B B$
	$\left\vert\left(^4E_u\ \frac{3}{2}\ -1\right) E_{1/2u}\ \frac{1}{2}\right\rangle$	$-\left\vert a_1^+ e_{+1}^+ b_1^+\right\rangle$	$\left(\frac{1}{2}g_{orb} + 3\right)\mu_B B$
	$\left\vert\left(^4E_u\ -\frac{3}{2}\ 1\right) E_{1/2u}\ -\frac{1}{2}\right\rangle$	$-\left\vert a_1^- e_{-1}^- b_1^-\right\rangle$	$\left(-\frac{1}{2}g_{orb} - 3\right)\mu_B B$
	$\left\vert\left(^4E_u\ -\frac{3}{2}\ -1\right) E_{3/2u}\ \frac{3}{2}\right\rangle$	$-\left\vert a_1^- e_{+1}^- b_1^-\right\rangle$	$\left(\frac{1}{2}g_{orb} - 3\right)\mu_B B$
	$\left\vert\left(^4E_u\ \frac{3}{2}\ 1\right) E_{3/2u}\ -\frac{3}{2}\right\rangle$	$\left\vert a_1^+ e_{-1}^+ b_1^+\right\rangle$	$\left(-\frac{1}{2}g_{orb} + 3\right)\mu_B B$

Table 4.3. CoPc Q-transition ground- and excited-state wavefunctions and Zeeman shifts. The orbital m is given in bold in the wavefunctions and the parity labels u and g have been omitted. The spin associated with each orbital is denoted by a superscript ± for $m_s = \pm\frac{1}{2}$

State	Level	Wavefunction	Zeeman Shift
$^2B_{1g}$	$\left\vert\left(^2B_{1g}\ -\frac{1}{2}\ 0\right) E_{3/2g}\ \frac{1}{2}\right\rangle$	$-\left\vert a_1^+ a_1^- \mathbf{a_1^+}\right\rangle$	$\mu_B B$
	$\left\vert\left(^2B_{1g}\ \frac{1}{2}\ 0\right) E_{3/2g}\ -\frac{1}{2}\right\rangle$	$-\left\vert a_1^+ a_1^- \mathbf{a_1^-}\right\rangle$	$-\mu_B B$
$^2E_u^S$	$\left\vert\left(^2E_u^S\ -\frac{1}{2}\ 1\right) E_{1/2u}\ \frac{1}{2}\right\rangle$	$\frac{1}{\sqrt{2}}\left(\left\vert a_1^+ e_{+1}^- \mathbf{a_1^-}\right\rangle - \left\vert a_1^- e_{+1}^+ \mathbf{a_1^-}\right\rangle\right)$	$\left(\frac{1}{2}g_{orb} - 1\right)\mu_B B$
	$\left\vert\left(^2E_u^S\ \frac{1}{2}\ -1\right) E_{1/2u}\ -\frac{1}{2}\right\rangle$	$-\frac{1}{\sqrt{2}}\left(\left\vert a_1^+ e_{-1}^- \mathbf{a_1^+}\right\rangle - \left\vert a_1^- e_{-1}^+ \mathbf{a_1^+}\right\rangle\right)$	$\left(-\frac{1}{2}g_{orb} + 1\right)\mu_B B$
	$\left\vert\left(^2E_u^S\ \frac{1}{2}\ 1\right) E_{3/2u}\ \frac{3}{2}\right\rangle$	$\frac{1}{\sqrt{2}}\left(\left\vert a_1^+ e_{+1}^- \mathbf{a_1^+}\right\rangle - \left\vert a_1^- e_{+1}^+ \mathbf{a_1^+}\right\rangle\right)$	$\left(\frac{1}{2}g_{orb} + 1\right)\mu_B B$
	$\left\vert\left(^2E_u^S\ -\frac{1}{2}\ -1\right) E_{3/2u}\ -\frac{3}{2}\right\rangle$	$\frac{1}{\sqrt{2}}\left(\left\vert a_1^+ e_{-1}^- \mathbf{a_1^-}\right\rangle - \left\vert a_1^- e_{-1}^+ \mathbf{a_1^-}\right\rangle\right)$	$\left(-\frac{1}{2}g_{orb} - 1\right)\mu_B B$
$^2E_u^T$	$\left\vert\left(^2E_u^T\ -\frac{1}{2}\ 1\right) E_{1/2u}\ \frac{1}{2}\right\rangle$	$\frac{1}{\sqrt{6}}\left(\left\vert a_1^+ e_{+1}^- \mathbf{a_1^-}\right\rangle + \left\vert a_1^- e_{+1}^+ \mathbf{a_1^-}\right\rangle - 2\left\vert a_1^- e_{+1}^- \mathbf{a_1^+}\right\rangle\right)$	$\left(\frac{1}{2}g_{orb} - 1\right)\mu_B B$
	$\left\vert\left(^2E_u^T\ \frac{1}{2}\ -1\right) E_{1/2u}\ -\frac{1}{2}\right\rangle$	$\frac{1}{\sqrt{6}}\left(\left\vert a_1^+ e_{-1}^- \mathbf{a_1^+}\right\rangle + \left\vert a_1^- e_{-1}^+ \mathbf{a_1^+}\right\rangle - 2\left\vert a_1^+ e_{-1}^+ \mathbf{a_1^-}\right\rangle\right)$	$\left(-\frac{1}{2}g_{orb} + 1\right)\mu_B B$
	$\left\vert\left(^2E_u^T\ \frac{1}{2}\ 1\right) E_{3/2u}\ \frac{3}{2}\right\rangle$	$-\frac{1}{\sqrt{6}}\left(\left\vert a_1^+ e_{+1}^- \mathbf{a_1^+}\right\rangle + \left\vert a_1^- e_{+1}^+ \mathbf{a_1^+}\right\rangle - 2\left\vert a_1^+ e_{+1}^+ \mathbf{a_1^-}\right\rangle\right)$	$\left(\frac{1}{2}g_{orb} + 1\right)\mu_B B$
	$\left\vert\left(^2E_u^T\ -\frac{1}{2}\ -1\right) E_{3/2u}\ -\frac{3}{2}\right\rangle$	$\frac{1}{\sqrt{6}}\left(\left\vert a_1^+ e_{-1}^- \mathbf{a_1^-}\right\rangle + \left\vert a_1^- e_{-1}^+ \mathbf{a_1^-}\right\rangle - 2\left\vert a_1^- e_{-1}^- \mathbf{a_1^+}\right\rangle\right)$	$\left(-\frac{1}{2}g_{orb} - 1\right)\mu_B B$
^4E_u	$\left\vert\left(^4E_u\ -\frac{1}{2}\ 1\right) E_{1/2u}\ \frac{1}{2}\right\rangle$	$-\frac{1}{\sqrt{3}}\left(\left\vert a_1^+ e_{+1}^- \mathbf{a_1^-}\right\rangle + \left\vert a_1^- e_{+1}^+ \mathbf{a_1^-}\right\rangle + \left\vert a_1^- e_{+1}^- \mathbf{a_1^+}\right\rangle\right)$	$\left(\frac{1}{2}g_{orb} - 1\right)\mu_B B$
	$\left\vert\left(^4E_u\ \frac{1}{2}\ -1\right) E_{1/2u}\ -\frac{1}{2}\right\rangle$	$-\frac{1}{\sqrt{3}}\left(\left\vert a_1^+ e_{-1}^- \mathbf{a_1^+}\right\rangle + \left\vert a_1^- e_{-1}^+ \mathbf{a_1^+}\right\rangle + \left\vert a_1^+ e_{-1}^+ \mathbf{a_1^-}\right\rangle\right)$	$\left(-\frac{1}{2}g_{orb} + 1\right)\mu_B B$
	$\left\vert\left(^4E_u\ \frac{1}{2}\ 1\right) E_{3/2u}\ \frac{3}{2}\right\rangle$	$\frac{1}{\sqrt{3}}\left(\left\vert a_1^+ e_{+1}^- \mathbf{a_1^+}\right\rangle + \left\vert a_1^- e_{+1}^+ \mathbf{a_1^+}\right\rangle + \left\vert a_1^+ e_{+1}^+ \mathbf{a_1^-}\right\rangle\right)$	$\left(\frac{1}{2}g_{orb} + 1\right)\mu_B B$
	$\left\vert\left(^4E_u\ -\frac{1}{2}\ -1\right) E_{3/2u}\ -\frac{3}{2}\right\rangle$	$-\frac{1}{\sqrt{3}}\left(\left\vert a_1^+ e_{-1}^- \mathbf{a_1^-}\right\rangle + \left\vert a_1^- e_{-1}^+ \mathbf{a_1^-}\right\rangle + \left\vert a_1^- e_{-1}^- \mathbf{a_1^+}\right\rangle\right)$	$\left(-\frac{1}{2}g_{orb} - 1\right)\mu_B B$
	$\left\vert\left(^4E_u\ \frac{3}{2}\ -1\right) E_{1/2u}\ \frac{1}{2}\right\rangle$	$\left\vert a_1^+ e_{-1}^+ \mathbf{a_1^+}\right\rangle$	$\left(-\frac{1}{2}g_{orb} + 3\right)\mu_B B$
	$\left\vert\left(^4E_u\ -\frac{3}{2}\ 1\right) E_{1/2u}\ -\frac{1}{2}\right\rangle$	$\left\vert a_1^- e_{+1}^- \mathbf{a_1^-}\right\rangle$	$\left(\frac{1}{2}g_{orb} - 3\right)\mu_B B$
	$\left\vert\left(^4E_u\ -\frac{3}{2}\ -1\right) E_{3/2u}\ \frac{3}{2}\right\rangle$	$\left\vert a_1^- e_{-1}^- \mathbf{a_1^-}\right\rangle$	$\left(-\frac{1}{2}g_{orb} - 3\right)\mu_B B$
	$\left\vert\left(^4E_u\ \frac{3}{2}\ 1\right) E_{3/2u}\ -\frac{3}{2}\right\rangle$	$-\left\vert a_1^+ e_{+1}^+ \mathbf{b_1^+}\right\rangle$	$\left(\frac{1}{2}g_{orb} + 3\right)\mu_B B$

spins and orbitals then coupled to each other. The wavefunctions are represented by double-group irrep and partner labels E_J and M, where $J = \frac{1}{2}$ or $\frac{3}{2}$ and $M = \pm J$. (In a commonly used alternative notation, $E' = E_{1/2}$ and $E'' = E_{3/2}$.) The ground states are orbitally non-degenerate and transform as Kramers pairs; $^2B_{1g} \sim E_{3/2g}$ for CuPc and $^2A_{1g} \sim E_{1/2g}$ for CoPc. The Q excited states, on the other hand, have orbital degeneracy which leads to splittings ($^2E_u \sim E_{1/2u} \oplus E_{3/2u}$, $^4E_u \sim 2E_{1/2u} \oplus 2E_{3/2u}$). In Tables 4.2 and 4.3, the one-electron orbital parity labels u and g have been omitted for simplicity, and the orbital m is given in bold. The spin associated with each orbital is denoted by a superscript $\pm$ for $m_s = \pm\frac{1}{2}$. The singdoublets listed here for CuPc agree with those of Misener,[34] but the tripdoublets and quartets do not. Although Misener's wavefunctions span the same subspace, they do not describe the tripdoublets and quartets accurately. In particular, he incorrectly labels four of the quartet states as tripdoublets.

4.4.2 Energy Levels

The zero-field splitting of the excited states is denoted Δ, and defined as

$$\Delta = \overline{E}_{3/2} - \overline{E}_{1/2} \tag{4.1}$$

where $\overline{E}_{3/2}$ and $\overline{E}_{1/2}$ are the band barycentres for the transitions terminating in levels $E_{3/2u}$ and $E_{1/2u}$ respectively. The energy-level diagrams relevant to the following discussion, both in the absence ($B = 0$) and presence ($B > 0$) of an external magnetic field, are shown in Figures 4.19 and 4.20 for CuPc and CoPc respectively. The inset to each of these figures shows the energy levels when $\Delta = 0$ and $B > 0$. Note that the sign of Δ in these figures is positive for CuPc and negative for CoPc. As will be seen later, this is a consequence of the symmetry of the metal orbital, m.

When a magnetic field is applied to a system, the Zeeman effect will remove any remaining degeneracies. The first-order ground- and excited-state Zeeman shifts for CuPc and CoPc are listed in Tables 4.2 and 4.3 respectively and illustrated in Figures 4.19 and 4.20, for the case where the field is applied along the molecular symmetry axis ($B \parallel z$). g_{orb} is a measure of the excited-state orbital angular momentum;

$$g_{\mathrm{orb}} = \pm 2 \langle e_{\pm 1} \mid l_z \mid e_{\pm 1} \rangle \tag{4.2}$$

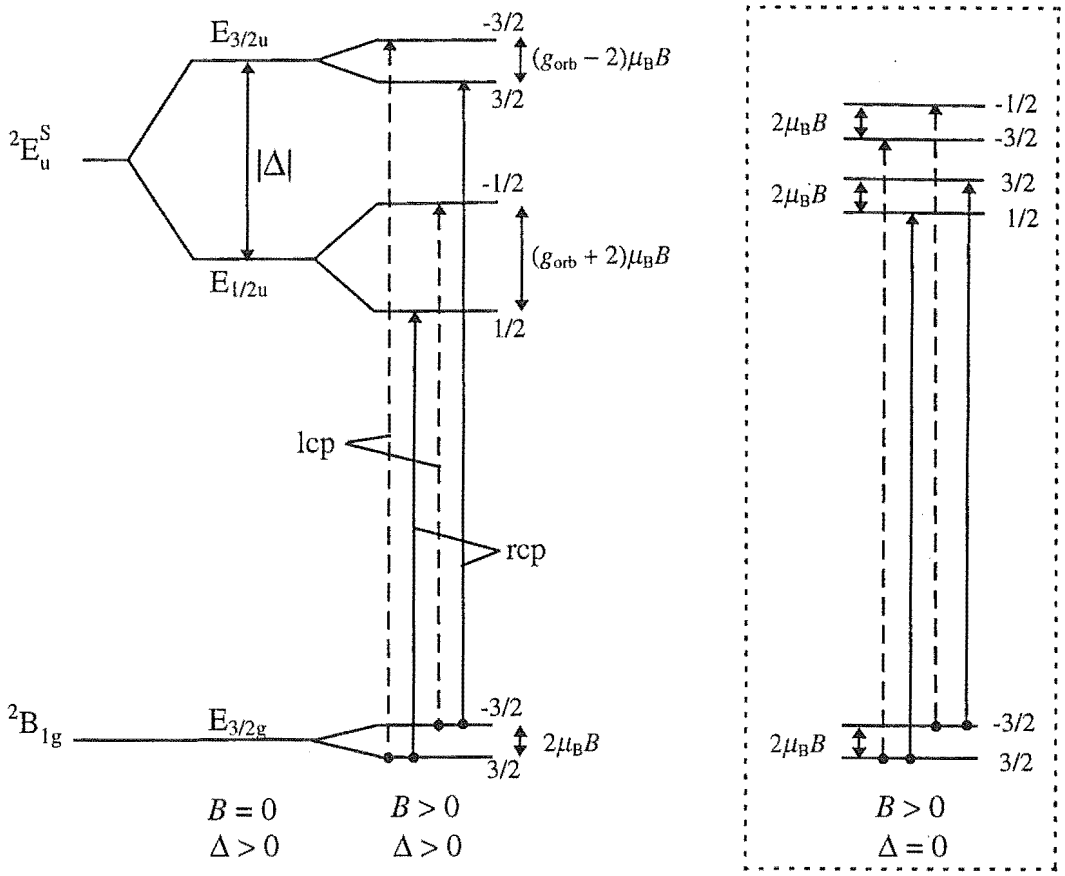

Figure 4.19. The energy-level diagram for CuPc, with $B = 0$ and $B > 0$. The inset shows the case where $B > 0$, $\Delta = 0$.

where l_z is the component of the one-electron orbital angular momentum operator along the z axis. In terms of excited states,

$$g_{\mathrm{orb}} = \pm 2 s_{\mathrm{m}} \left\langle \mathrm{E}_{1/2u} \pm \tfrac{1}{2} \left| L_z \right| \mathrm{E}_{1/2u} \pm \tfrac{1}{2} \right\rangle = \pm 2 s_{\mathrm{m}} \left\langle \mathrm{E}_{3/2u} \pm \tfrac{3}{2} \left| L_z \right| \mathrm{E}_{3/2u} \pm \tfrac{3}{2} \right\rangle \qquad (4.3)$$

where L_z is the component of the many-electron orbital angular momentum operator ($L_z = \sum_i l_z(i)$) along z and s_{m} is a phase factor whose sign depends on the irrep m;[19] $s_{\mathrm{a_1}} = 1$, $s_{\mathrm{b_1}} = -1$. The sign of s_{m} has direct bearing on the sign of the Zeeman splitting, so for CuPc ($s_{\mathrm{m}} = s_{\mathrm{b_1}}$) the Zeeman states with *negative* M partners lie at higher energy, while for CoPc ($s_{\mathrm{m}} = s_{\mathrm{a_1}}$) the states with *positive* M lie higher.

4.4.3 Transition Intensities

Figures 4.19 and 4.20 also show the four allowed Zeeman transitions and their polarisations (again assuming $B \parallel z$). In addition, the polarisations are summarised as one-electron transition moments in Table 4.4, where $\mathcal{M}_{\pm} = \sqrt{2} \left\langle \mathrm{a_1} \left| m_{\pm 1} \right| \mathrm{e}_{\mp 1} \right\rangle$. In

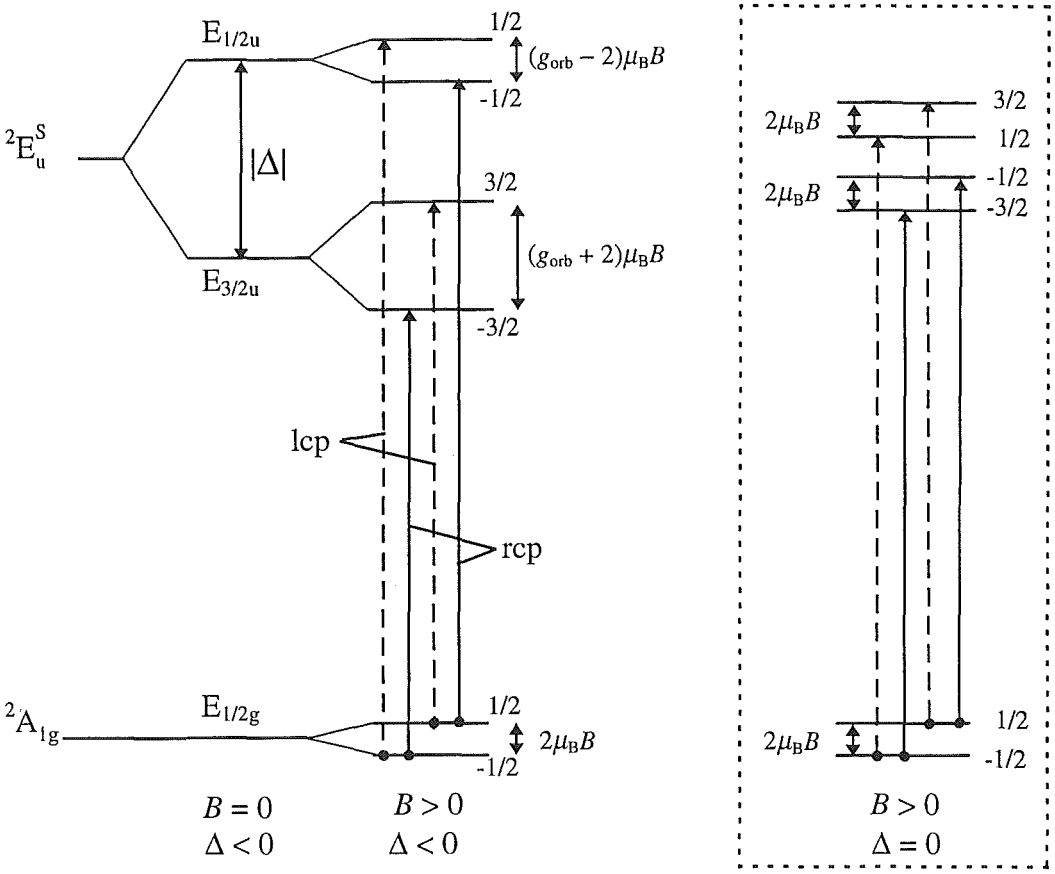

Figure 4.20. The energy-level diagram for CoPc, with $B = 0$ and $B > 0$. The inset shows the case where $B >$, $\Delta = 0$.

the convention used here (Section 3.2), m_{-1} and m_{+1} represent the electric dipole moment operators for lcp and rcp transitions respectively.

The dipole strengths and Faraday parameters were determined using the equations of Section 3.5.2, and are summarised in Table 4.5 where the subscripts 1/2 and 3/2 indicate the SO level ($E_{1/2u}$ or $E_{3/2u}$) in which the transition terminates and $|\mathcal{M}_+|^2 = |\mathcal{M}_-|^2 \equiv |\mathcal{M}|^2$. Note that the parameters are given for the case of Z-oriented molecules (superscript Z); for orientational averaging, $\overline{\mathcal{A}}_1 = \frac{1}{3}\mathcal{A}_1^Z$, $\overline{\mathcal{C}}_0 = \frac{1}{3}\mathcal{C}_1^Z$ and $\overline{\mathcal{D}}_0 = \frac{2}{3}\mathcal{D}_1^Z$, as shown in Section 3.5.3.

4.4.4 Qualitative Analysis of the Spectra

The temperature dependence of the Q-band MCD can be qualitatively rationalised in terms of Figures 4.19 and 4.20. The four Zeeman transitions have the same dipole strengths (Table 4.5), so their relative intensities are determined by the

Table 4.4. Transition moments for CuPc and CoPc. $\mathcal{M}_{\pm} = \frac{1}{\sqrt{2}} \langle a_1 | m_{\pm 1} | e_{\pm 1} \rangle$, where m_{-1} and m_{+1} effectively represent the operators for lcp and rcp transitions respectively.

CuPc	$\lvert E_{3/2u}\ -\frac{3}{2}\rangle$	$\lvert E_{1/2u}\ -\frac{1}{2}\rangle$	$\lvert E_{1/2u}\ \frac{1}{2}\rangle$	$\lvert E_{3/2u}\ \frac{3}{2}\rangle$
$\langle E_{3/2g}\ -\frac{3}{2}\rvert$		$-\mathcal{M}_-$		$\mathcal{M}_+$
$\langle E_{3/2g}\ \frac{3}{2}\rvert$	$-\mathcal{M}_-$		$-\mathcal{M}_+$	

CoPc	$\lvert E_{1/2u}\ \frac{1}{2}\rangle$	$\lvert E_{3/2u}\ \frac{3}{2}\rangle$	$\lvert E_{3/2u}\ -\frac{3}{2}\rangle$	$\lvert E_{1/2u}\ -\frac{1}{2}\rangle$
$\langle E_{1/2g}\ \frac{1}{2}\rvert$		$-\mathcal{M}_-$		$\mathcal{M}_+$
$\langle E_{1/2g}\ -\frac{1}{2}\rvert$	$-\mathcal{M}_-$		$-\mathcal{M}_+$	

Table 4.5. One-electron expressions for dipole strengths and Faraday parameters of the two excited states of CuPc and CoPc

Parameter	CuPc	CoPc
$\mathcal{D}^Z_{3/2}$	$\frac{1}{2}\lvert\mathcal{M}\rvert^2$	$\frac{1}{2}\lvert\mathcal{M}\rvert^2$
$\mathcal{D}^Z_{1/2}$	$\frac{1}{2}\lvert\mathcal{M}\rvert^2$	$\frac{1}{2}\lvert\mathcal{M}\rvert^2$
$\mathcal{A}^Z_{3/2}$	$\frac{1}{2}g_{\mathrm{orb}}\lvert\mathcal{M}\rvert^2$	$\frac{1}{2}g_{\mathrm{orb}}\lvert\mathcal{M}\rvert^2$
$\mathcal{A}^Z_{1/2}$	$\frac{1}{2}g_{\mathrm{orb}}\lvert\mathcal{M}\rvert^2$	$\frac{1}{2}g_{\mathrm{orb}}\lvert\mathcal{M}\rvert^2$
$\mathcal{C}^Z_{3/2}$	$\lvert\mathcal{M}\rvert^2$	$-\lvert\mathcal{M}\rvert^2$
$\mathcal{C}^Z_{1/2}$	$-\lvert\mathcal{M}\rvert^2$	$\lvert\mathcal{M}\rvert^2$

Boltzmann populations of the ground-state Zeeman levels. First consider the insets to the figures, which show the case where $g_{\mathrm{orb}} > 0$ and $\Delta = 0$. The higher-energy transitions are lcp, so the MCD has the overall appearance of a positive $\mathcal{A}$-term, with $\mathrm{M_1} > 0$. However, since the pairs of transitions with the same circular polarisation occur at the same energy, their sum (and hence $\mathrm{M_1}$) is temperature independent. In other words, Zeeman splitting alone cannot account for the observed temperature dependence.

Next consider the situation shown on the left of the figures, where for CuPc, $\Delta > 0$, and for CoPc, $\Delta < 0$. As the temperature is decreased, the intensities of the transitions furthest from the band barycentre are enhanced, and $\mathrm{M_1}$ increases. If the energy order of $E_{1/2u}$ and $E_{3/2u}$ were reversed, $\mathrm{M_1}$ would decrease with cooling. Hence it can be concluded that the experimental data require $\Delta > 0$ for CuPc and $\Delta < 0$ for CoPc. Note that this result is a direct consequence of the nature of the

partially occupied metal orbital, m, which is made explicit through the theoretical parameters s_{a_1} and s_{b_1}.

4.4.5 Extracting Δ and g_{orb} Values From the Spectra

In order to quantitatively analyse the absorption and MCD spectra, they must be related to the theoretical parameters of Table 4.5. The method employed for this purpose is moment analysis (Section 3.7). Assuming a zero-field splitting ($\Delta \neq 0$) in the Q-band excited states, two separate allowed transitions terminating in the singdoublet $E_{3/2u}$ and $E_{1/2u}$ SO levels must be considered.

4.4.5.1 Absorption Moments

It is necessary to derive theoretical expressions for both $\mathbf{A}_0$ (the zeroth absorption moment) and the band barycentres. The overall Q-band absorbance is

$$A(E) = A_{3/2}(E) + A_{1/2}(E) \tag{4.4}$$

where the subscripts indicate the SO level in which the transition terminates. From (3.88),

$$A(E)/E = \gamma(\mathcal{D}_{3/2} f_{3/2}(E) + \mathcal{D}_{1/2} f_{1/2}(E)) \tag{4.5}$$

where $f_{3/2}(E)$ and $f_{1/2}(E)$ are normalised bandshape functions for the transitions terminating in $E_{3/2u}$ and $E_{1/2u}$ respectively. Integrating, and noting from Table 4.5 that $\mathcal{D}_{3/2} = \mathcal{D}_{1/2}$ it is obtained that

$$\langle A(E)/E \rangle_1^0 = \gamma \mathcal{D}_{3/2} \left(\langle f_{3/2}(E) \rangle_1^0 + \langle f_{1/2}(E) \rangle_1^0 \right) \tag{4.6}$$

and

$$\mathbf{A}_0 \equiv \langle A(E)/E \rangle_0 = 2\gamma \mathcal{D}_{3/2} \tag{4.7}$$

where the last step uses the fact that $f_{3/2}(E)$ and $f_{1/2}(E)$ are normalised. From Section 3.7 it can be derived that the band barycentre, $\overline{E}$, is defined as

$$\overline{E} = \frac{\langle A(E)/E \rangle_1^0}{\langle A(E)/E \rangle_0} = \langle f(E) \rangle_1^0 \tag{4.8}$$

(4.6) and (4.7) can be combined to give

$$\begin{aligned}\overline{E} &= \tfrac{1}{2}\left(\langle f_{3/2}(E)\rangle_1^0 + \langle f_{1/2}(E)\rangle_1^0\right) \\ &= \tfrac{1}{2}\left(\overline{E}_{3/2} + \overline{E}_{1/2}\right) \end{aligned} \tag{4.9}$$

Thus the barycentre of the Q band is just the average of the barycentres of the individual transitions.

4.4.5.2 MCD Moments

The theoretical expression for MCD in the linear limit, derived in Section 3.5.2.2, is

$$\Delta A(E)/E = \gamma\mu_B B\left[\mathcal{A}_1\left(\frac{-\partial f(E)}{\partial E}\right) + \left(\mathcal{B}_0 + \frac{\mathcal{C}_0}{kT}\right) f(E)\right] \tag{4.10}$$

As discussed in Section 3.4, $\mathcal{B}$ terms arise from field-induced mixing of states; their magnitude being inversely proportional to the energy separation of these states. Since the nearest state that could couple with the Q transition is the B transition, which is over 9000 cm^{-1} away, $\mathcal{B}$ terms are small in the systems studied here. In addition, $\mathcal{B}_0$ will not contribute to the value of M_1,[32] so $\mathcal{B}$ terms will be ignored hereafter.

Initially considering only $\mathcal{C}$ terms,

$$\Delta A_C(E)/E = \gamma\mu_B B\mathcal{C}_0 f(E)/kT \tag{4.11}$$

Since the total MCD is the sum over the two transitions,

$$\begin{aligned}\Delta A_C(E)/E &= \gamma\mu_B B\left(\mathcal{C}_{3/2} f_{3/2}(E) + \mathcal{C}_{1/2} f_{1/2}(E)\right)/kT \\ &= \gamma\mu_B B\mathcal{C}_{3/2}\left(f_{3/2}(E) - f_{1/2}(E)\right)/kT \end{aligned} \tag{4.12}$$

The last equality holds since $\mathcal{C}_{1/2} = -\mathcal{C}_{3/2}$ (Table 4.5). Using the results of Section 3.7 the first moment of the MCD about $\overline{E}$ is

$$\langle \Delta A_C(E)/E\rangle_1^{\overline{E}} = \gamma\mu_B B\mathcal{C}_{3/2}\left(\langle f_{3/2}(E)\rangle_1^0 - \langle f_{1/2}(E)\rangle_1^0\right)/kT \tag{4.13}$$

Hence

$$\begin{aligned}\langle \Delta A_C(E)/E\rangle_1^{\overline{E}} &= \gamma\mu_B B\mathcal{C}_{3/2}\left(\overline{E}_{3/2} - \overline{E}_{1/2}\right)/kT \\ &= \gamma\mu_B B\mathcal{C}_{3/2}\Delta/kT \end{aligned} \tag{4.14}$$

where Δ is defined by (4.1).

Now, considering $\mathcal{A}$ terms,

$$\Delta A_{\mathcal{A}}(E)/E = \gamma\mu_{\mathrm{B}}B\mathcal{A}_1\frac{-\partial f(E)}{\partial E} \tag{4.15}$$

Noting again that the MCD is the sum over the two transitions, and that $\mathcal{A}_{3/2} = \mathcal{A}_{1/2}$ (Table 4.5),

$$\Delta A_{\mathcal{A}}(E)/E = -\gamma\mu_{\mathrm{B}}B\mathcal{A}_{3/2}\left(\frac{\partial f_{3/2}(E)}{\partial E} + \frac{\partial f_{1/2}(E)}{\partial E}\right) \tag{4.16}$$

Hence for the first MCD moment

$$\langle\Delta A_{\mathcal{A}}(E)/E\rangle_1^{\overline{E}} = \gamma\mu_{\mathrm{B}}B\mathcal{A}_{3/2}\left(\int\frac{\partial f_{3/2}(E)}{\partial E}(E-\overline{E})dE + \int\frac{\partial f_{1/2}(E)}{\partial E}(E-\overline{E})dE\right) \tag{4.17}$$

Integrating by parts, and using the results of Section 3.7,

$$\langle\Delta A_{\mathcal{A}}(E)/E\rangle_1^{\overline{E}} = 2\gamma\mu_{\mathrm{B}}B\mathcal{A}_{3/2} \tag{4.18}$$

Combining (4.18) with (4.14) gives

$$\mathrm{M}_1 \equiv \langle\Delta A(E)/E\rangle_1^{\overline{E}} = \gamma\mu_{\mathrm{B}}B(2\mathcal{A}_{3/2} + \mathcal{C}_{3/2}\Delta/kT) \tag{4.19}$$

With reference to (4.7) this yields

$$\frac{\mathrm{M}_1}{\mathrm{A}_0} = \mu_{\mathrm{B}}B\left(\frac{\mathcal{A}_{3/2}}{\mathcal{D}_{3/2}} + \frac{\Delta\mathcal{C}_{3/2}}{2kT\mathcal{D}_{3/2}}\right) \tag{4.20}$$

Substituting for $\mathcal{D}_{3/2}$, $\mathcal{A}_{3/2}$ and $\mathcal{C}_{3/2}$ from the expressions in Table 4.5, and allowing for the possibility of random or Z orientation, this reduces to

$$\frac{\mathrm{M}_1}{\mu_{\mathrm{B}}B\mathrm{A}_0} = c_{\mathrm{o}}\left(g_{\mathrm{orb}} - \frac{s_{\mathrm{m}}\Delta}{kT}\right) \tag{4.21}$$

where c_{o} is an orientational factor such that $c_{\mathrm{o}} = 1$ for preferential Z orientation, and $c_{\mathrm{o}} = 0.5$ for random orientation of molecules, (see discussion at the end of Section 4.4.3) and $s_{\mathrm{m}} = -1$ for CuPc, $s_{\mathrm{m}} = 1$ for CoPc (Section 4.4.2).

4.4.5.3 Saturation Effects

From the theoretical expression for MCD given in (4.10) it is seen that, in the linear limit, the MCD associated with a $\mathcal{C}$ term will increase linearly with B/T. This increase is due to redistribution of the Boltzmann population in the ground state

to favour the lowest Zeeman level. It is clear, however, that if this ratio becomes sufficiently large, all the molecules will have dropped into the lowest level, and any further increase in B/T will have no effect on population. At this stage the system is said to be saturated, and the MCD will no longer increase.

Saturation effects have been ignored in deriving (4.10), and from it, the $\mathbf{M}_1/\mathbf{A}_0$ ratio in (4.21). This is justifiable if work is carried out inside the linear limit; in other words, if the Zeeman splittings are small relative to kT and the band width. The latter is not an issue in the experiments described here, but the former is. In the linear limit it is valid to make the approximation $e^a = 1 + a$, when evaluating the population factor in the ground states (Section 3.5.2). Outside this limit a significant error may be introduced by this approximation. It is, however, possible to correct for this error. Schatz *et al.*[82] show that if the linear-limit approximation is not made, the $\mathcal{C}$-term MCD for a ground state consisting of a single Kramers pair (states $|A\alpha\rangle$ and $|A\beta\rangle$) for oriented molecules is given by

$$\Delta A_C(E)/E = \gamma \Delta\alpha f(E) \tanh\left(\frac{|\langle \mathrm{A}\alpha\,|L_z + 2S_z|\,\mathrm{A}\alpha\rangle|\,\mu_\mathrm{B}B}{kT}\right) \tag{4.22}$$

where

$$\Delta\alpha = \sum_\lambda |\langle \mathrm{A}\alpha\,|m_{-1}|\,\mathrm{J}\lambda\rangle|^2 - |\langle \mathrm{A}\alpha\,|m_{+1}|\,\mathrm{J}\lambda\rangle|^2 \tag{4.23}$$

In the linear limit however,

$$\Delta A_C(E)/E = \gamma \Delta\alpha f(E) \left(\frac{|\langle \mathrm{A}\alpha\,|L_z + 2S_z|\,\mathrm{A}\alpha\rangle|\,\mu_\mathrm{B}B}{kT}\right) \tag{4.24}$$

Hence the effective approximation made in assuming the linear limit for $\mathcal{C}$ terms is that

$$\tanh\left(\frac{|\langle \mathrm{A}\alpha\,|L_z + 2S_z|\,\mathrm{A}\alpha\rangle|\,\mu_\mathrm{B}B}{kT}\right) \approx \left(\frac{|\langle \mathrm{A}\alpha\,|L_z + 2S_z|\,\mathrm{A}\alpha\rangle|\,\mu_\mathrm{B}B}{kT}\right) \tag{4.25}$$

which requires $\mu_\mathrm{B}B \gg kT$. For the ground states of CuPc and CoPc, which are Kramers pairs with spin degeneracy only, the Zeeman splitting is $2\mu_\mathrm{B}B$. A graph of the MCD saturation behaviour of $\mathcal{C}$ terms for this case is shown in Figure 4.21. It can be seen that the linear limit breaks down significantly for $\mu_\mathrm{B}B/kT \geq 0.2$.

In order to be able to use the moment equation (4.21), the data (obtained under conditions of partial saturation) must be adjusted to what they would have been if obtained in the linear limit. The first MCD moment, $\mathbf{M}_1$, is made up of

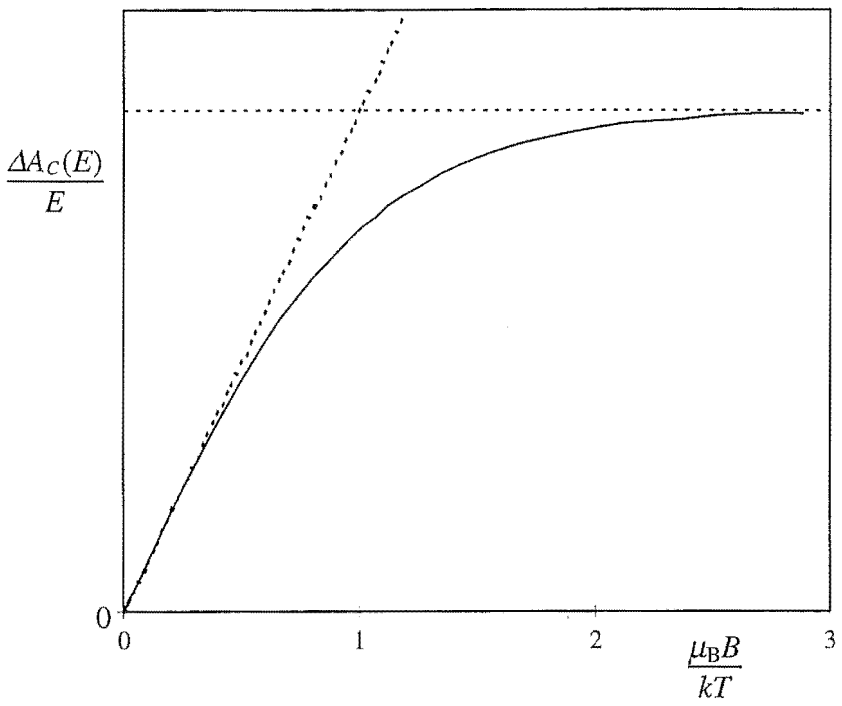

Figure 4.21. MCD saturation behaviour for Z oriented molecules with a single Kramers-pair ground state with spin degeneracy only.

contributions from $\mathcal{A}$ and $\mathcal{C}$ terms. A correction should be made to the latter of these only, as $\mathcal{A}$ terms are not greatly affected by saturation,[32] arising, by definition, from ground states which are equally populated.

$\mathcal{A}$ terms constitute the temperature-independent part of $\mathbf{M}_1$, *i.e.* the area below the y-intercept in a plot of $\mathbf{M}_1/\mu_B B\mathbf{A}_0$ (at constant B) vs $1/kT$. Thus correction for saturation is made by subtracting this intercept from each $\mathbf{M}_1/\mu_B B\mathbf{A}_0$ value, and then adjusting each resulting value by a factor of c_{sat};

$$c_{\text{sat}} = 1 + \frac{x - \tanh(x)}{x}, \text{ where } x = \frac{\mu_B B}{kT} \tag{4.26}$$

The correction factor is the same in the case of samples with averaged molecular orientation, since the molecules have Kramers-pair ground states with near-isotropic g values.

4.4.5.4 Δ and g_{orb} Values

The values of Δ and g_{orb} obtained for CuPc and CoPc are given in Table 4.6. For samples in Ar matrices, the values given assume complete Z orientation of molecules, while for PVC polymer samples, random orientation is assumed. (The

Table 4.6. Δ and g_{orb} values for the samples studied. Unless noted otherwise, values have been calculated assuming complete Z orientation of the molecules. Δ_{sat} include a correction for saturation, as explained in the text. The moment analysis range is also given. The error values listed are those obtained from the least-squares fit of the moment data.

Sample	Range	Range (cm^{-1})	g_{orb}	Δ (cm^{-1})	Δ_{sat} (cm^{-1})
CuPc/Ar (1)	whole Q band	13500-18300	4.8 ± 0.2	1.6 ± 0.2	1.7 ± 0.2
	Q(0,0) + Q(1,0)	13500-16425	2.7 ± 0.1	1.3 ± 0.1	1.4 ± 0.1
CuPc/Ar (2)	whole Q band	13500-18300	5.6 ± 0.2	1.8 ± 0.4	1.9 ± 0.4
	Q(0,0) + Q(1,0)	13500-16450	3.00 ± 0.06	1.3 ± 0.1	1.4 ± 0.1
CoPc/Ar (1)	whole Q band	13600-18700	5.1 ± 0.2	0.9 ± 0.2	1.8 ± 0.2
	Q(0,0)	14680-15820	2.22 ± 0.02	0.08 ± 0.03	0.16 ± 0.04
CoPc/Ar (2)	whole Q band	13000-19300	4.4 ± 0.3	8.9 ± 0.4	9.7 ± 0.4
	Q(0,0)	14806-15660	1.7 ± 0.2	-1.2 ± 0.2	-1.3 ± 0.2
CoPc/Ar (3)	whole Q band	13600-18100	4.0 ± 0.6	7.4 ± 1.0	8.0 ± 1.0
	Q(0,0)	14920-15720	1.68 ± 0.06	-1.1 ± 0.1	-1.28 ± 0.07
CoPc/PVC	whole Q band	13400-19800	7.12 ± 0.06^a	-1.4 ± 0.2^a	-1.6 ± 0.1^a
	Q(0,0) + Q(1,0)	13400-16300	3.51 ± 0.06^a	-0.9 ± 0.1^a	-1.0 ± 0.1^a
	Q(0,0)	14300-15700	2.72 ± 0.04^a	-1.58 ± 0.04^a	-1.70 ± 0.06^a

[a] Values for film data are calculated assuming random molecular orientation

relationship between these two situations is given by (4.21).) Δ_{sat} represents values corrected for saturation effects. Note, as discussed in Section 4.3, that the g_{orb} values (obtained from the y-intercepts) should be treated with caution, and indeed, their magnitude is observed to be significantly dependent on integration range. However, the Δ values show much smaller variation.

For CuPc/Ar, the true values of Δ_{sat} and g_{orb} for the Q transition will be somewhere between those obtained over the two integration ranges given above. Hence it is estimated that $\Delta = 1.6 \pm 0.5$ cm^{-1} and $g_{\mathrm{orb}} = 4.1 \pm 1.5$, assuming preferential Z orientation of the molecules in matrices. This assumption can be justified for two reasons. Firstly, $g_{\mathrm{orb}} \simeq 4.1$ accords closely with the previous result for ZnPc/Ar ($g_{\mathrm{orb}} = 4.2$) and falls within the range from ~ 3 to 4.6[19,83] found for other MPcs. Secondly it has consistently been found that metalloporphyrins and MPcs isolated in Ar take such a preferential orientation.[15,16,19,33,35] In the case of ZnPc/Ar, the existence of orientational effects was confirmed by monitoring of the z-polarised B_3 absorption band ($\sim$ 310 nm) as the deposition window was rotated by $\sim 30°$ with

respect to the optical path.[19] As the window was rotated away from its perpendicular position, the relative intensity of the B_3 band increased. This test was repeated for one of the CuPc/Ar matrices, but an equivalent of the B_3 band was not observed. However, rather than being evidence that the CuPc molecules were randomly oriented, it is likely that this result indicates that energy of the B_3 transition is strongly dependent on the metal ion.

For each of the CoPc/Ar matrices investigated at 1 T (samples (2) and (3)), Δ is, as expected, negative for moments taken over Q(0,0). However, when moments are taken over the whole Q transition, Δ is positive, as a consequence of the strong temperature-dependent MCD of the impurity. The value of Δ obtained over Q(0,0) alone presumably contains a relatively small contribution from the impurity, but does not include the legitimate Q(1,0) and Q(2,0) contributions, and so should yield a low value for M_1. Note that value of Δ obtained for the CoPc/Ar(1) matrix is considerably different from those of the other two. Spectra of this first matrix were measured at 3 T, with consequent saturation errors of between 12% and 60%, depending on the temperature. It appears that the method used to compensate for saturation is not adequate for such large errors, and thus data from this run will be disregarded. From the latter two matrices it is found that $\Delta \lesssim -1.3$ cm^{-1}. Hence it seems reasonable to assume that $\Delta_{\mathrm{CoPc}} \simeq -\Delta_{\mathrm{CuPc}}$ for the matrix-isolated samples, within the error limits of the latter.

The change in the absorption spectrum of CoPc/Ar due to the impurity is very small, as is the change in the MCD spectra above ~15 K. At lower temperatures, however, the MCD alters dramatically. From this it can be concluded that the impurity must have strong MCD $\mathcal{C}$ terms and relatively weak $\mathcal{A}$ terms. From (4.20) and (4.21) it can be seen that Δ arises from $\mathcal{C}$ terms and g_{orb} from $\mathcal{A}$ terms, consequently it might be expected that while Δ will be greatly affected by the impurity, g_{orb} will not. In this case, g_{orb} would have a value between 1.7 and 4.4 , *i.e.* $g_{\mathrm{orb}} \simeq 3 \pm 2$.

The values of Δ and g_{orb} listed in the table for CoPc/PVC assume random orientation of the chromophores within the film. The sharp decrease in Δ between the Q(0,0) and Q(0,0) + Q(1,0) integration ranges is probably due to the presence of the same impurity as seen in the CoPc/Ar spectra (Section 4.3.2), and hence, as

for the latter data, the primary conclusion which can be drawn from these values is a lower limit for Δ, *i.e.* $|\Delta| > 1.7$ cm^{-1}. This finding supports the assumption of Z orientation of the CoPc molecules in the Ar matrix, with $\Delta_{Ar} \simeq \Delta_{PVC}$. Combining the film and matrix data, with a greater emphasis on the film (because of the reduced contribution from the impurity) a tentative assignment of $\Delta_{CoPc} \simeq 1.8 \pm 0.5$ cm^{-1} is made. The g_{orb} values vary from 2.7 to 7.1, giving $g_{orb} = 5 \pm 3$, consistent, within experimental error, with the matrix data. The large errors quoted arise from the strong dependence of g_{orb} on the chosen integration range and spectral baseline (Section 4.3).

4.4.6 The Source of Δ

The new information deduced in this work pertains to Δ, the zero-field splitting of the excited state. For a term with both orbital and spin degeneracy (such as ^{2}E), Δ might be expected to arise predominantly from first-order SO coupling. However, such interactions are non-existent for a pure singdoublet, as the unpaired spin resides on the metal ion and the orbital angular momentum is confined to the ligand. Explication of the splitting of ^{2}E therefore requires consideration of coupling with other electronic states, the most important of which are likely to share the same electronic configuration. It will now be shown that Δ can be semi-quantitatively accounted for by ignoring configuration interaction and considering coupling between the $a_{1u}b_{1g}e_g$-configuration basis states defined in Table 4.2.

The excited-state energy matrix was determined by employing the effective electronic Hamiltonian

$$\begin{aligned} \mathcal{H}_{el} &= \mathcal{H}_0 + \mathcal{H}_{rep} + \mathcal{H}_{SO} \\ &= -\frac{1}{2}\sum_i \nabla_i^2 - \sum_\alpha \sum_i \frac{Z_\alpha}{r_{i\alpha}} + \sum_j \sum_{i>j} \frac{1}{r_{ij}} + \sum_i \mathbf{s}_i \cdot \mathbf{u}_i \end{aligned} \qquad (4.27)$$

as defined in Section 3.3. The last two terms ($\mathcal{H}_{rep} + \mathcal{H}_{SO}$) represent inter-electron repulsion and SO coupling respectively. The energy matrix, which may be factored into $E_{3/2u}$ and $E_{1/2u}$ sub-matrices, is given in Table 4.7.

The matrix elements involving $\mathcal{H}_0 + \mathcal{H}_{rep}$ were expanded using the Condon-Slater rules.[84] Such expansion breaks the expressions down into a mixture of one-electron, Coulomb and exchange integrals, but, as can be seen from Table 4.7, these

Table 4.7. The Hamiltonian matrix for CuPc and CoPc. In each case, the upper sign represents the $E_{3/2u}$ case, and the lower sign the $E_{1/2u}$ case. E_c is a common energy, Z represents a one-electron excited-state SO matrix element, and K is an exchange integral, as defined in the text. s_m is a phase factor such that $s_{a_1} = +1$ and $s_{b_1} = -1$.

	Singdoublet	Tripdoublet	Quartet, $S = \frac{1}{2}$	Quartet, $S = \frac{3}{2}$
Singdoublet	$E_c + 2K_{ae}$	$\frac{\sqrt{3}}{2}(K_{am} - K_{em})$ $\pm\frac{s_m}{2\sqrt{3}}Z$	$\mp\frac{s_m}{\sqrt{6}}Z$	
Tripdoublet	$\frac{\sqrt{3}}{2}(K_{am} - K_{em})$ $\pm\frac{s_m}{2\sqrt{3}}Z$	$E_c + K_{am} + K_{em}$ $\pm\frac{s_m}{3}Z$	$\pm\frac{s_m}{3\sqrt{2}}Z$	
Quartet, $S = \frac{1}{2}$	$\mp\frac{s_m}{\sqrt{6}}Z$	$\pm\frac{s_m}{3\sqrt{2}}Z$	$E_c - \frac{1}{2}(K_{am} + K_{em})$ $\pm\frac{s_m}{6}Z$	
Quartet, $S = \frac{3}{2}$				$E_c - \frac{1}{2}(K_{am} + K_{am})$ $\pm\frac{s_m}{2}Z$

can be simplified to the sum of an average configurational energy (E_c), and various combinations of exchange integrals, K_{ae}, K_{am}, and K_{em} where, for example,

$$K_{ae} = \langle a_{1u}e_g \,|\mathcal{H}_{rep}|\, e_g a_{1u}\rangle \equiv \int\int a_{1u}^*(1)\, e_g^*(2)\, \mathcal{H}_{rep}\, e_g(1)\, a_{1u}(2)\, d\tau_1\, d\tau_2 \qquad (4.28)$$

The diagonal elements shown in Table 4.7 agree with those given by Ake and Gouterman,[65] and later by Cory and Zerner.[85] However the singdoublet-tripdoublet off-diagonal term is found to have the opposite sign to that given in the earlier work. The phase of this overlap term was immaterial to Ake and Gouterman, but is highly significant in the following analysis of the excited-state splitting.

The final term in (4.27) is the SO operator. The SO matrix elements are given in Table 4.7 as fractions of Z, which is a measure of the SO coupling for an e_g electron;

$$Z = \sum_k \langle e_{+1} \,|\xi_e(k)\, l_z(k)|\, e_{+1}\rangle \qquad (4.29)$$

where $l_z(k)$ is the z-component operator for the orbital angular momentum of the electron about nucleus k, $\xi_e(k)$ is the corresponding SO coupling coefficient, and the sum is carried over all nuclei.

Within the model outlined earlier in this section, Δ arises directly from the elements of Table 4.7 that couple the singdoublet and tripdoublet states. In the

context of the current problem, the critical property of these elements is that they involve interference between SO and exchange terms, and that this interference is different for $E_{3/2u}$ and $E_{1/2u}$. (Note that in the absence of the exchange terms, there will still be an energy separation between $E_{1/2u}$ and $E_{3/2u}$ due to mixing with the tripdoublet and quartet, which have non-zero diagonal SO elements. However, using an appropriate value for Z as discussed below, the splitting obtained is extremely small – a factor of over 10^6 less than observed.)

4.4.6.1 The Sign of Δ

Prediction of the sign of Δ is simply a matter of deciding the sense (constructive or destructive) of the interference between these two terms for each of $E_{3/2u}$ and $E_{1/2u}$. Note firstly that exchange integrals are intrinsically real and positive, hence the sign of the exchange term is determined by the relative magnitudes of K_{ab} and K_{eb}. For CuPc, the electron density associated with the b_{1g} orbital is confined to the metal ion and the directly coordinated pyrrole N atoms,[66] as is the electron density of the a_{1g} orbital of CoPc.[69] In each case, the e_g orbital has density on the same atoms, whereas the a_{1u} orbital does not;[66] hence $K_{ab} < K_{eb}$ and the off-diagonal exchange interaction is negative.

Secondly, McClure has shown that SO coupling in planar $\pi(p_z)$ molecules (such as free-base porphyrins) must be weak.[86] For metalloporphyrins and MPcs, however, a relatively large one-centre contribution can arise from π-d mixing. In the case of the e_g MO, this involves the metal d_{xz} and d_{yz} orbitals, for which the contribution to Z is

$$Z_d = |c_d|^2 \zeta_d \langle d_{+1} | l_z(M) | d_{+1} \rangle \qquad (4.30)$$

where M = Cu or Co, c_d is the amplitude of the d-orbital contribution to the molecular orbital, and ζ_d is the SO-coupling constant for the M^{2+} 3d electron. For Cu^{2+}, $\zeta_d \simeq 830$ cm^{-1}, and for Co^{2+}, $\zeta_d \simeq 540$ cm^{-1}.[87] Since all factors on the right of (4.30) are positive, then $Z_d > 0$.

Applying these results to Table 4.7 it is found that in the case of CuPc, interference is constructive for $E_{3/2u}$ and destructive for $E_{1/2u}$. Consequently, $E_{3/2u}$ lies at higher energy and $\Delta > 0$ in agreement with experiment. The opposite is

found for CoPc, with $E_{3/2u}$ lying at lower energy, and $\Delta < 0$, again concurring with experimental evidence.

4.4.6.2 The Magnitude of Δ

Theoretical estimation of the magnitude of Δ is a much more difficult proposition since appropriate parameters of demonstrable reliability are not available. Nevertheless, it will be shown that the experimental values can reasonably be considered in accord with theoretical expectations for CuPc and CoPc. The analysis and discussion in this section primarily centres on CuPc, as this molecule has the greatest amount of theoretical information available in the literature, and also has a fairly precisely defined Δ value. The relevance to CoPc will then be considered.

Ake and Gouterman[65] have estimated exchange parameters for a generic Cu porphyrin on the basis of an extended Hückel calculation, *viz* $K_{ae} = 2605$ cm^{-1}, $K_{eb} = 95.5$ cm^{-1} and $K_{ab} = 396$ cm^{-1}. They also suggest $Z_d = 3.5$ cm^{-1} (based on $|c_d|^2 = 4.3 \times 10^{-3}$), which gives $\Delta \simeq 0.2$ cm^{-1}, an order of magnitude smaller than the experimental value. On the other hand, the semi-empirical SCF-MO calculation of Henriksson *et al.*[66] (specific to CuPc) yields $|c_d|^2 = 1.7 \times 10^{-2}$, which in turn gives $Z_d \simeq 15$ cm^{-1} and $\Delta \simeq 0.9$ cm^{-1}, within a factor of 2 of the observed value. A density-functional calculation by Rosa and Barends[69] gives a similar value, with $|c_d|^2 = 1.5 \times 10^{-2}$.

There are other effects (including configuration interaction) that could potentially have a bearing on Δ, and bring the theoretical value into closer agreement with experiment. To speculate on their importance is of dubious worth in the absence of reliable theoretical parameters. However, it can be shown that three-centre SO-coupling terms of the type described by McClure[86] are unlikely to contribute significantly, even though the molecule contains the relatively heavy Cu nucleus. The most important of these terms arises from the fact that electron dynamics responsible for g_{orb} occur in the field of the central metal ion. An estimate for the corresponding contribution to Z can be obtained by considering the e_g molecular orbital as a quasi atomic orbital of Cu. This gives

$$Z_\pi \simeq S_\pi \zeta_d \frac{g_{orb}}{2} \frac{\langle r_\pi^{-3} \rangle}{\langle r_d^{-3} \rangle} \tag{4.31}$$

The distances of the 3d and $e_g(\pi)$ electrons from the Cu nucleus are denoted r_d and r_π respectively. $\langle r_d^{-3} \rangle = 55.8$ Å^{-3},[88] and $\langle r_\pi^{-3} \rangle \simeq 0.0441$ Å^{-3} is estimated from molecular-orbital coefficients for e_g.[66] S_π is a screening factor, which takes into account the presence of other Cu and Pc electrons. Setting $S_\pi = 1$ yields an upper limit for Z_π of 1.6 cm^{-1}. In fact S_π is certainly very much less than unity, so it can safely be assumed that $Z_\pi \ll 1.6$ cm^{-1}, and hence that three-centre SO contributions are of no consequence in determining Δ.

The only calculation which has been carried out on CoPc is a density-functional calculation by Rosa and Barends,[69] which gave $|c_d|^2 = 5.3 \times 10^{-2}$, leading to values of $Z_d \simeq 29$ cm^{-1} and $\Delta \simeq -1.8$ cm^{-1}. This Δ value is very close to that observed experimentally, but since the density functional calculation appears to give flawed results in assigning transition energies, it is of dubious reliability, and hence it can be concluded only that the theoretical value is consistent with experiment. Note also that the difference between Δ_{CuPc} and Δ_{CoPc} values obtained from this calculation is not borne by the experimental results.

4.4.7 The B Band of CoPc

The near-UV spectra of CoPc/Ar and CoPc/PVC, in Figures 4.11 and 4.12 respectively, show two overlapping bands labelled B and N. The B band of MPcs is thought to consist of at least three transitions, including two strongly allowed $\pi \rightarrow \pi^*$ transitions, which are comprised of admixtures of excitations terminating in the e_g LUMO.[19,66] The N band seen for MPcs is usually significantly weaker than the B band,[19,61] and thought to arise from at least one partially forbidden $\pi \rightarrow \pi^*$ transition.[66] The relative intensity of the band at $\sim$ 275 nm in CoPc led Edwards and Gouterman[61] to label this as an 'extra band', possibly due to MLCT transitions.

The evident complexity of this spectral region precludes quantitative analysis of the zero-field splittings. However, in a phenomenological approach, application of (4.21) to the moment analysis data of Section 4.3.2 (assuming orientation of the matrix) gives $\Delta_{Ar} = 35 \pm 2$ cm^{-1}and $\Delta_{PVC} = 36 \pm 1$ cm^{-1} over the whole B band, and $\Delta_{Ar} = 21 \pm 2$ cm^{-1}and $\Delta_{PVC} = 21 \pm 1$ cm^{-1} over a range excluding the MCD band to the red. The excellent agreement of Δ between the matrix and film over *both* ranges seems to indicate that the red band is *not* due to the impurity, since

Q-band data showed that the intensity of this impurity was significantly greater in the matrix than in the film.

4.5 Conclusion

Q-band absorption and MCD spectra of CuPc/Ar and CoPc/Ar have been measured between 4.2 and 1.4 K, and of CoPc/PVC, between 50 and 1.4 K. All samples showed weak MCD temperature dependence, with band magnitude increasing with decreasing temperature. Variable-temperature studies of (even-electron) NiPc and FePc were also carried out - the temperature independence of the MCD spectra of these species confirming that the weak effects seen for CuPc and CoPc are real. Temperature dependence of the B and N bands of CoPc was also observed.

The Q-band temperature dependence of CuPc and CoPc arises because of a splitting of the ^2E_u excited state. This splitting has been quantified by use of moment analysis, with $\Delta_{CuPc} = 1.6 \pm 0.5$ cm^{-1} and $\Delta_{CoPc} \simeq -1.8 \pm 0.5$ cm^{-1}. (The value obtained for CoPc is an estimate only, as the presence of an impurity in the Ar matrices (and probably, to a much lesser extent, in the PVC film) complicated the analysis.) Althought the precision of these Δ values is not at first sight particularly good, it must be noted that these splittings were obtained in the presence of absorption bandwidths of $300 - 400$ cm^{-1}, illustrating the ability of MCD to extract information on weak effects not accessible by absorption spectroscopy.

Theoretical analysis has shown that for both CuPc and CoPc, Δ arises from interference between exchange coupling and spin-orbit coupling of the singdoublet and tripdoublet excited states. This interference is different for the two components of the ^2E_u excited state, $E_{1/2u}$ and $E_{3/2u}$, leading to a splitting of their energies. Given this explanation, it has been shown that the observed splittings are in reasonable accord with theoretical expectations, with $|\Delta_{theor}| \simeq 1 - 2$ cm^{-1}.

Chapter 5

Absorption and MCD Spectra of CuTBP

5.1 Introduction

The metallotetrabenzoporphyrins (MTBPs) in general, and CuTBP in particular, have not received the same degree of attention in the literature as their MPc relatives. Spectroscopic work on CuTBP has been limited to solution absorption spectra measured in a variety of solvents, mainly by Russian groups,[89–92] and an MCD spectrum measured in chloroform.[93] There have been no reports of CuTBP/Ar spectra.

The UV-visible absorption spectra of MTBPs are reasonable typical of metalloporphyrins, and quite similar to those of MPcs, as shown for the Zn analogues in Figure 5.2. The main differences seen in these spectra are the relative intensities, and energy separation of the Q and B bands. These features are explained quite well by the four-orbital model[18,94,95] (Section 1.2.4) in terms of configuration interaction between the Q and B excited-state configurations, with the MTBPs showing a greater degree of mixing than the MPcs. The fact that the MTBPs tend to have sharper Q and B bands than the MPcs, combined with the absence of the Q′ band (which causes complications in spectral analysis of the latter compounds), makes MTBPs very amenable to spectral study.

In this chapter, absorption and MCD spectra of the Q and B bands of CuTBP/Ar and CuTBP/PVC are presented. The relatively sharp bands seen in the Q-band region of CuTBP/Ar makes identification of a number of vibrational frequencies possible. The temperature dependence of the MCD spectra is reported, and interpreted in terms of SO and exchange coupling interactions between the excited states, in a similar manner to that presented in Chapter 4 for odd-electron MPcs.

5.2 Experimental Details

The CuTBP/Ar and CuTBP/PVC spectra shown in this chapter were obtained using the apparatus and conditions described in Table 5.1. All temperature-dependence measurements were carried out using the matrix-injection/SM4 system. Spectra of the matrix prepared in the refrigerator/electromagnet system were measured at ~15 K. The matrices were deposited for ~45 min with the CuTBP heated to ~300 - 350 °C. Further experimental and instrumental details are given in Chapter 2.

Table 5.1. Experimental parameters of the samples discussed in this chapter.

	System	Spectrometer	Step size (Å)	Slit width (μm)	Field (T)	Matrix conc.
CuTBP/Ar	He frig./emag	MOD 4	2	200	.7	1:105000
CuTBP/Ar	MI/SM4	MOD 3	2	50	1	1:113000
CuTBP/PVC	MI/SM4	MOD 3	3	200	1	

5.3 Results

5.3.1 Vibrational Structure

One of the advantages of matrix isolation is the removal of intermolecular interactions, and subsequent narrowing of spectral bandwidths compared to those observed in many other condensed phases. In the case of the CuTBP/Ar Q-band spectra shown in Figure 5.1, this increase in resolution allows identification of a number of vibrational frequencies, which are listed, and compared with frequencies for ZnTBP and CuPc, in Table 5.2.

5.3.2 Temperature Dependence

Absorption and MCD spectra of the Q band of CuTBP/Ar and CuTBP/PVC at range of temperatures are shown in Figures 5.2 and 5.3 respectively. In each case, the MCD spectra exhibit weak temperature dependence, with band intensity increasing with decreasing temperature.

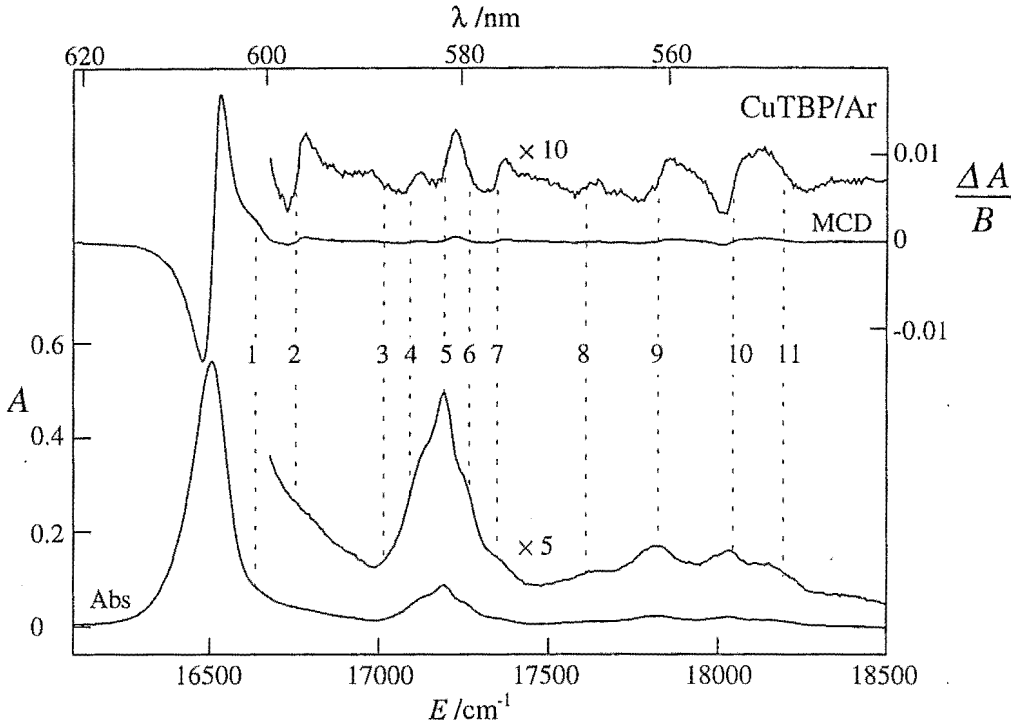

Figure 5.1. Q-band absorption and MCD (per tesla) spectra of CuTBP/Ar measured at 0.7 T. A number of vibrational frequencies are identified, and labelled for comparison with Table 5.2.

Table 5.2. Q-band vibrational frequencies (cm^{-1}) and symmetries of CuTBP and related compounds. The numbering allows for comparison with the spectra in Figure 5.1. Symmetry labels (a_{1g} or b_{ig}, where $i = 1$ or 2) have been determined from the sign of the MCD pseudo-$\mathcal{A}$ terms (see text).

Label	CuTBP (this work)	ZnTBP (Ref[15])	ZnTBP (Ref[96])	CuPc (Chapter 7)	Symmetry
1	153	129	123	174	b_{ig}
2	248	243	248	251	a_{1g}
3	500	491	468	500	b_{ig}
4	580	583	577	590	a_{1g}
5	691	691	691	685	a_{1g}
6	760	734*	763*	752	b_{ig}
7	839	824	833	848	a_{1g}
8	1103	1107	1114	1159	a_{1g}
9	1318	1316	1315	1341	a_{1g}
10	1538	1515	1516	1583	a_{1g}
11	1683	1660			b_{ig}

* Frequencies obtained from B-band spectra

As was carried out for CuPc and CoPc (Chapter 4), the temperature dependence of CuTBP has been quantified using moment analysis (Section 3.7), with $\mathbf{A}_0$, $\mathbf{M}_0$, and $\mathbf{M}_1$ being measured. The absence of the Q′ band (present in MPc spectra) considerably simplifies the spectral analysis, since integration can be carried out over the whole band. The other difficulty with Q-band moment analysis discussed in Section 4.3 is still present in CuTBP, however; namely that the value of $\mathbf{M}_1$ is highly sensitive to choice of both integration range and MCD baseline. This sensitivity arises from the $(E - \overline{E})$ term in the $\mathbf{M}_1$ expression, which magnifies the importance of components lying a long way from the band barycentre, such as the long tail of weak vibrational overtones seen in Figures 5.2 and 5.3. It has been found that this sensitivity can have a significant effect on the y intercept of a plot of $\mathbf{M}_1/\mu_B B\mathbf{A}_0$ vs $1/kT$, but not (to the same degree) on the slope, as is borne out by the values given below.

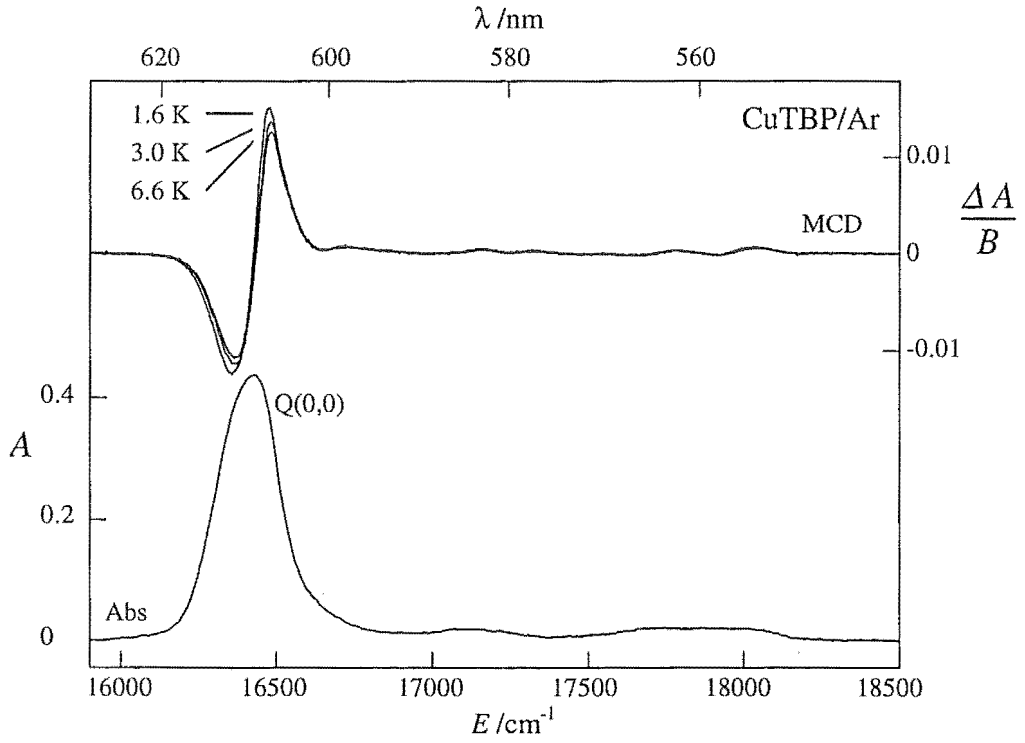

Figure 5.2. Q-band absorption and MCD (per tesla) spectra of CuTBP/Ar measured at a field of 1 T.

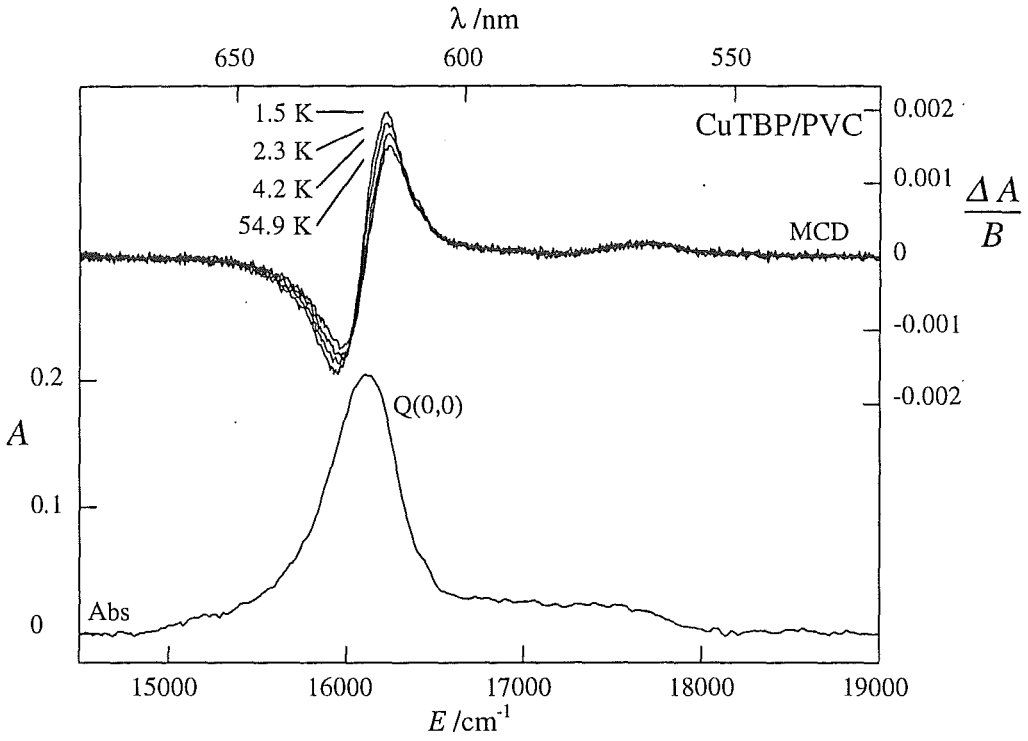

Figure 5.3. Q-band absorption and MCD (per tesla) spectra of CuTBP/PVC, measured at 1 T.

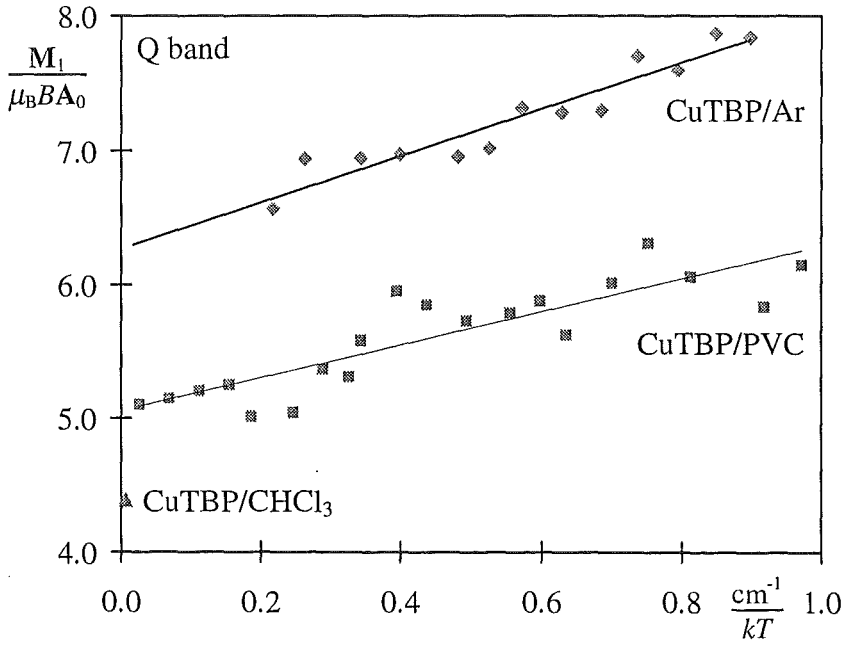

Figure 5.4. The temperature dependence of $\mathbf{M}_1/\mu_B B\mathbf{A}_0$ for CuTBP/Ar and CuTBP/PVC over the whole Q band. The lines of best fit are shown - parameters of these lines are given in the text.

For each sample M_0 was found to be insignificant (a factor of $\sim 10^{-4}$ smaller than M_1). Figure 5.4 shows plots of $M_1/\mu_B B A_0$ vs $1/kT$ for both CuTBP/Ar and CuTBP/PVC. A linear least-squares fit gives a slope of 1.8 ± 0.4 cm^{-1} and y-intercept of 6.3 ± 0.2 for the matrix, and a slope of 1.1 ± 0.4 cm^{-1} and y-intercept of 5.1 ± 0.2 for the film.

Room-temperature absorption and MCD spectra of CuTBP in chloroform have also been measured, and are similar to the film data of Figure 5.3. The $M_1/\mu_B B A_0$ ratio obtained from the solution spectra is shown in Figure 5.4; the data point lies sufficiently close to the y axis to indicate a y-intercept value of $\sim$4.4.

Temperature-dependence studies have also been carried out on the B band of CuTBP/PVC, as shown in Figure 5.5. The results of moment analysis over the full range of these spectra is shown in Figure 5.6 as a plot of $M_1/\mu_B B A_0$ vs $1/kT$. The line of best fit of the data has a slope of 2.2 ± 0.3 cm^{-1} and a y-intercept of 1.5 ± 0.2. Room-temperature B-band spectra of CuTBP in chloroform have also been measured; again having an appearance very similar to the film data. The $M_0/\mu_B B A_0$ ratio obtained from the solution spectra is shown in Figure 5.6, representing an approximate y-intercept value of ~ 1.6.

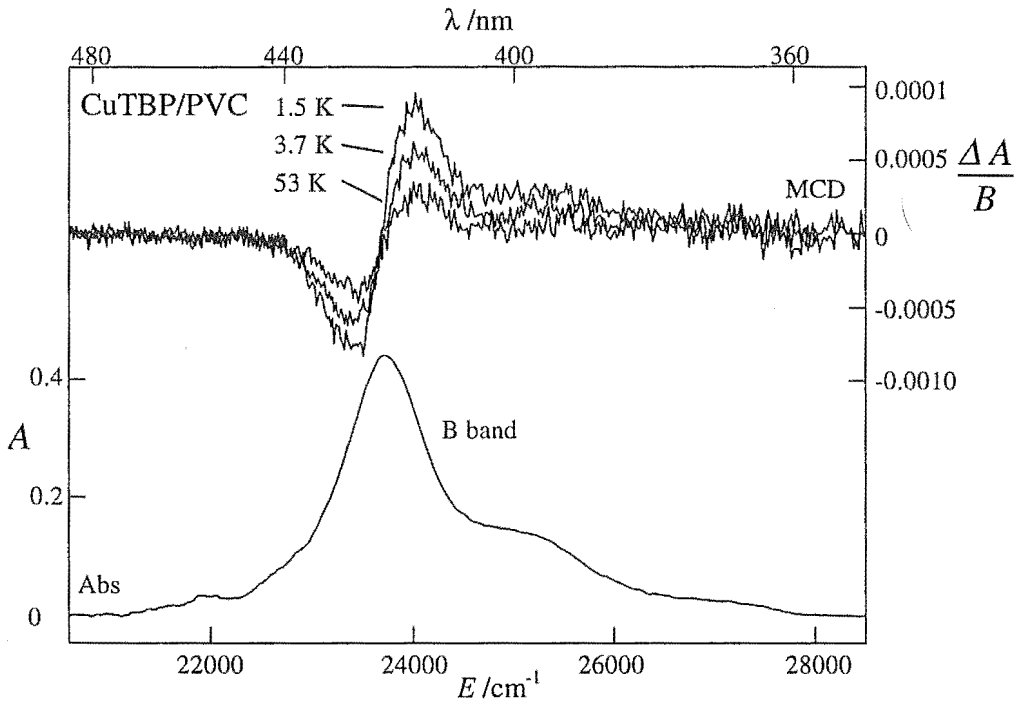

Figure 5.5. B-band absorption and MCD (per tesla) spectra of CuTBP/PVC, obtained at 1 T.

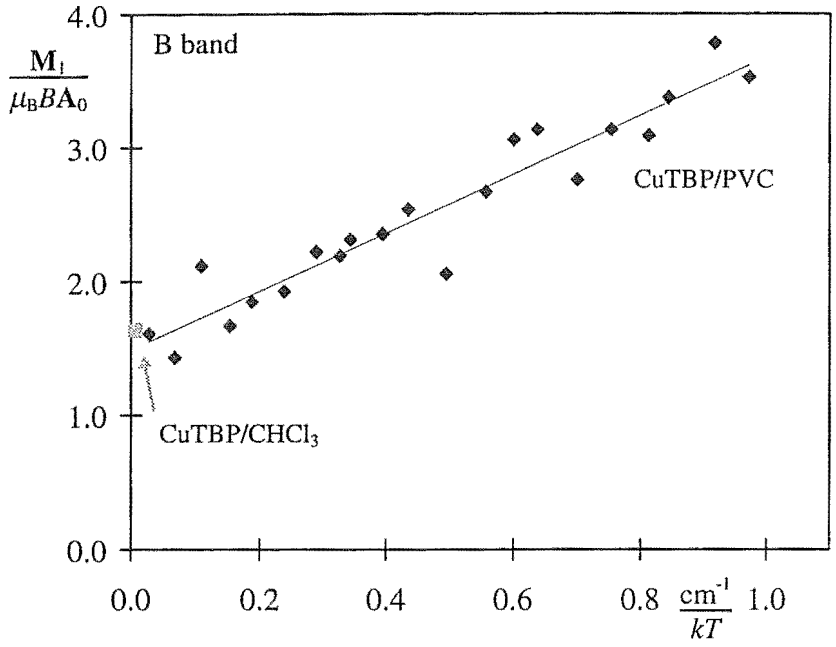

Figure 5.6. The temperature dependence of $M_1/\mu_B B A_0$ over the B band of CuTBP/PVC. The line of best fit is shown - parameters of this line are given in the text.

5.4 Discussion

While there is a dearth of detailed information on CuTBP, either experimental or theoretical, it is known that the situation is basically the same as for CuPc (Section 4.4.1). The molecule has D_{4h} symmetry, with the unpaired electron of the Cu^{2+} residing in a non-degenerate b_{1g} molecular orbital.[97,98] The ground-state configuration is thus $a_{1u}^2 b_{1g}$, where a_{1u} is the HOMO of the ligand.

The Q band arises from a ligand $\pi \rightarrow \pi^*$ excitation, which is primarily of $a_{1u} \rightarrow e_g$ character. The main theoretical difference between Pcs and TBPs is the extent to which configuration interaction is important (Section 1.2.4) - the filled a_{1u} and a_{2u} orbitals are closer to each other in TBPs than in Pcs,[18,95,99,100] and so the Q-band transition for CuTBP is a stronger admixture of $a_{1u} \rightarrow e_g$ and $a_{2u} \rightarrow e_g$ than that of CuPc. For simplicity, and in the absence of any theoretical calculations specific to CuTBP, the contribution from the latter transition will be ignored in development of the theory. Making this assumption, the analysis is exactly the same as that given for CuPc in Chapter 4, and will not be repeated here, other than to say that the Q and B transitions are both of symmetry $^2B_{1g} \rightarrow {}^2E_u$, and terminate in singdoublet

states. The excited states are susceptible to second-order SO splittings involving coupling between the singdoublets and tripdoublets.

5.4.1 Vibrational Analysis

It has been shown[15,16,19] that metalloporphyrins in Ar matrices are susceptible to crystal-field stabilised Jahn-Teller (JT) effects, which lower the orbital degeneracy of the Q and B excited states. That this is also the case for the Q state of CuTBP is seen by inspection of the vibrational overtones shown in Figure 5.1. Band 1, the first overtone to the blue of Q(0,0), exhibits the single-signed positive MCD indicative of a mode involved in relatively strong JT coupling.[16] Other bands, (*e.g.* 3, 6 and 11) exhibit (pseudo-) $\mathcal{A}$ terms which are opposite in sign to the origin band. The latter are evidenced by the negative-going MCD at the energy of the absorption maximum, and are indicative of excited-state (JT and/or Herzberg-Teller) vibronic effects involving modes of b_{1g} or b_{2g} parentage.[15,16] Overtones with (pseudo-) $\mathcal{A}$ terms of the same sign as the origin arise from a_{1g} modes. The frequencies of these vibrational overtones have been determined as the midpoint of each identifiable $\mathcal{A}$-term-shaped MCD signal. Note that the frequencies obtained for CuTBP agree well with the literature values given in Table 5.2, in general lying between the vibrational frequencies of ZnTBP and CuPc. The assignment of JT b_{ig} ($i = 1$ or 2) modes also matches that for ZnTBP[15] and ZnPc;[19] in particular, the 153 cm^{-1} vibration appears to be the dominant JT mode, as has been found for the latter molecules.

5.4.2 Δ and g_{orb} Values

The values of Δ and g_{orb} obtained for CuTBP are given in Table 5.3. These were determined by moment analysis, using the expression (Section 4.4.5)

$$\frac{\mathbf{M}_1}{\mu_B B \mathbf{A}_0} = c_o \left(g_{\mathrm{orb}} + \frac{\Delta}{kT} \right) \tag{5.1}$$

where c_o is an orientational factor such that $c_o = 1$ for preferential Z orientation, and $c_o = 0.5$ for random orientation of molecules, g_{orb} is a measure of the excited-state orbital angular momentum and Δ is the excited-state zero-field splitting;

$$g_{\mathrm{orb}} = \pm 2 \langle e_{\pm 1} \mid l_z \mid e_{\pm 1} \rangle \tag{5.2}$$

$$\Delta = \overline{E}_{3/2} - \overline{E}_{1/2} \tag{5.3}$$

Table 5.3. Δ and g_{orb} values for the CuTBP samples studied. Unless noted otherwise, values have been calculated assuming random molecular orientation of the molecules. Δ_{sat} include a correction for saturation, as explained in Chapter 4. The moment analysis range is also given. The errors listed pertain to the least-squares fit of the data.

Sample	Range	Range (cm^{-1})	g_{orb}	Δ (cm^{-1})	Δ_{sat} (cm^{-1})
CuTBP/Ar	whole Q band	16000-18400	6.3 ± 0.2^a	1.8 ± 0.3^a	1.9 ± 0.3^a
CuTBP/PVC	whole Q band	14500-19000	10.2 ± 0.4	2.4 ± 0.6	2.6 ± 0.6
CuTBP/$CHCl_3$	whole Q band	14300-18300	8.8		

[a] Matrix parameters calculated assuming preferential Z orientation

Preferential Z orientation was assumed for the matrix, and random orientation for the polymer film and solution, for reasons discussed in Section 4.4.5.4.

As can be seen from Table 5.3, the Q-band Δ values for the matrix and film agree within experimental error, with an overall value of $\Delta_{CuTBP} = 2.2 \pm .6$ cm^{-1}. This is slightly larger than, but within experimental error of the value obtained for CuPc ($\Delta_{CuPc} = 1.6 \pm 0.5$, Section 4.4.5.4). However, as was anticipated in Section 5.3.2, there is considerable variation between the g_{orb} values, leading to a large uncertainty in the overall value of $g_{orb} = 8 \pm 2.5$. In comparison, Platenkamp and Canters[101] have obtained a value of $g_{orb} = 7.4$ for CdTBP from analysis of the Zeeman shifts of a single oriented site in an n-octane crystal, and Vancott *et al.*[15] determined a value of $g_{orb} = 7.7$ for ZnTBP/Ar from magnetooptical measurements. Given the comparatively low value of $g_{orb} = 6.3 \pm 0.2$ obtained for CuTBP/Ar, it is possible that this matrix has only partial Z orientation. If this was so, it would also bring the Δ values of the matrix and film into closer agreement.

5.4.3 The Source of Δ

As shown for CuPc in Section 4.4.6, Δ_{CuTBP} can be accounted for by considering coupling between the $^2E_u^S$, $^2E_u^T$ and ^4E_u excited-state terms, but requires a degree of mixing of metal orbitals into the π system of the ligand. Unfortunately, no theoretical calculations have been carried out on CuTBP, and so the amount of metal mixing into the $e_g(\pi)$ orbital is not known. However, the relative Δ values suggest that the extent of mixing is similar to (or perhaps marginally greater than) that for CuPc, *i.e.* $|c_d|^2 = 2$ - 4%.

5.4.4 B-Band Analysis

Analysis of the B band is complicated by the fact that, according to a calculation by Lee *et al.*,[100] the four-orbital excitations ($a_{1u} \rightarrow e_g$ and $a_{2u} \rightarrow e_g$) comprise only $\sim$ 60% of the B band of TBP^{2-}. This precludes a quantitative analysis of the zero-field splittings of this band. However, in a phenomenological approach, application of (5.1) to the CuTBP/PVC and CuTBP/$CHCl_3$ data of Figure 5.6 gives $\Delta = 4.5 \pm 0.6$ and $g_{orb} = 3.1 \pm 0.5$. Unlike the Q band, good agreement is seen between the g_{orb} values from the film and the solution. As was the case for the Q band, the zero-field splitting of the four-orbital transitions of the B band arises from SO coupling of the e_g orbital in which the excitation terminates. Thus the Q and B bands should have the same Δ value, and the larger value observed for the latter must arise from the 'extra' transitions noted by Lee *et al.*[100] This is quantitatively confirmed by the calculation of Henriksson *et al.*[66] who find that for CuPc, there is an 8% contribution to the B band transitions from an excitation involving a lower e_g MO, which has 6 times the degree of metal mixing than the four-orbital model e_g MO.

5.5 Conclusion

The relatively sharp bands afforded by the matrix-isolation technique have made possible identification of vibrational frequencies of the Q band of CuTBP, with the sign of the MCD of each overtone giving the symmetry of the vibrational mode. JT activity is evident with the 153 cm^{-1} mode predominating, which is consistent with observations for other metalloporphyrins and MPcs.

Weak MCD temperature dependence of both the Q and B bands has been observed, with a magnitude that increases with decreasing temperature. The temperature dependence arises from a zero-field splitting of the ^2E_u excited state. Moment analysis has been used to quantify this splitting as $\Delta(Q) = 2.2 \pm 0.6$ cm^{-1}, $\Delta(B) = 4.5 \pm 0.6$ cm^{-1}. The former value is close to those found for CuPc and CoPc (Chapter 4) suggesting that the mechanism by which the splitting arises is very similar, despite the fact that the Q transitions of MTBPs are purported to involve a greater degree of configuration interaction than those of the MPcs.

Chapter 6

The MCD Temperature Dependence of $LuPc_2$

6.1 Introduction

$LuPc_2$ is a member of the lanthanide bisphthalocyanine ($LnPc_2$) series. The molecules in this class have generated a great deal of interest, because of the potentially useful electrochromic, nonlinear optical, and semiconducting properties[102] they display. $LnPc_2$s have been shown by X-ray diffraction[102] to exist in a sandwich-like configuration with the metal ion held between the two Pc rings and coordinated to all eight pyrrole nitrogen atoms. The rings are in essentially parallel planes, and staggered by 45°, as depicted in Figure 6.1.

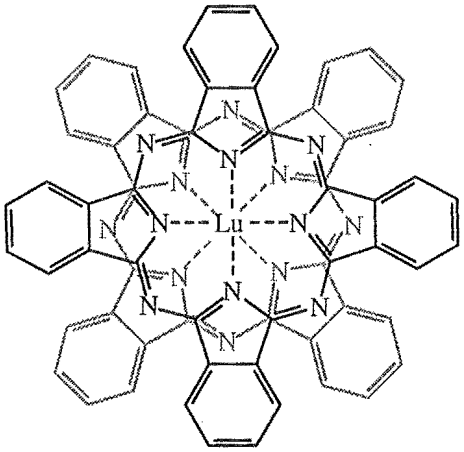

Figure 6.1. The molecular structure of $LuPc_2$, viewed from above. One Pc ring (grey) sits below, and the other (black) above the plane of the Lu^{3+} ion.

A number of spectral studies of $LuPc_2$ have been carried out,[103–106] including reports of the MCD spectrum.[39,107] The most detailed and complete analysis is given by VanCott *et al.*[39] who measured absorption and MCD spectra of $LuPc_2$/Ar at ~ 7 K. The molecule has also been the subject of several theoretical calculations.[108–111]

In this chapter, absorption and MCD spectra are presented for the Q and the RV (red vibronic) transitions of $LuPc_2$. The MCD temperature dependence of each

of these bands is reported, for samples of $LuPc_2$ both an Ar matrix ($LuPc_2$/Ar), and a polymethylmethacrylate polymer film ($LuPc_2$/PMMA).

The absorption spectra were found to be temperature independent, but the magnitude of the MCD altered distinctly with changing temperature. To quantify the latter, the method of moments was employed, as discussed in Section 3.7. The zeroth absorption moment, $\mathbf{A}_0$, and first MCD moment, $\mathbf{M}_1$, were measured. Graphs are shown of the dimensionless ratio $\mathbf{M}_1/\mu_B B\mathbf{A}_0$ plotted against $1/kT$ (cm^{-1}), and the parameters derived from these plots are listed in Section 6.3.2. These parameters are also tabulated and discussed in Section 6.4.6.3. A theoretical explanation for the Q-band MCD temperature dependence, in terms of a zero-field splitting of the excited states, is discussed. The effects of temperature on the MCD of the Q and RV bands are compared, and information about the nature of the latter state is deduced. It is also shown that the Q(3,0) band is not part of the Q transition.

6.2 Experimental

The $LuPc_2$/Ar and $LuPc_2$/PMMA spectra shown in this chapter were obtained using the apparatus and conditions described in Table 6.1. All temperature-dependence measurements were made using the matrix-injection/SM4 apparatus. For the matrix-isolated samples, the sublimation temperature used was ~330 °C, and the deposition time was typically 20 min. Further experimental and instrumental details are given in Chapter 2.

Table 6.1. Experimental parameters of the $LuPc_2$ samples discussed in this chapter.

	Region	System	Spectrometer	Step size (Å)	Slit width (μm)	Field (T)	Matrix conc.
$LuPc_2$/Ar	Q	MI/SM4	MOD 3	5	100	2	1:58000
$LuPc_2$/Ar	RV	MI/SM4	ANU	5	200	1	1:1800
$LuPc_2$/Ar	Q	He frig./emag	MOD 4	5	200	0.7	1:23000
$LuPc_2$/PMMA	Q	MI/SM4	MOD 3	8	100	1	
$LuPc_2$/PMMA	RV	MI/SM4	MOD 4	40	400	1	

6.3 Results

Figure 6.2 gives an overview of the absorption and MCD spectra of $LuPc_2$/PMMA between 9500 and 35000 cm^{-1}, measured at 1.5 K. The Q and B spectral features are so labelled for their similarity to those of transition-metal monophthalocyanines. The RV and BV (blue vibronic) bands are labelled as per VanCott *et al.*[39]

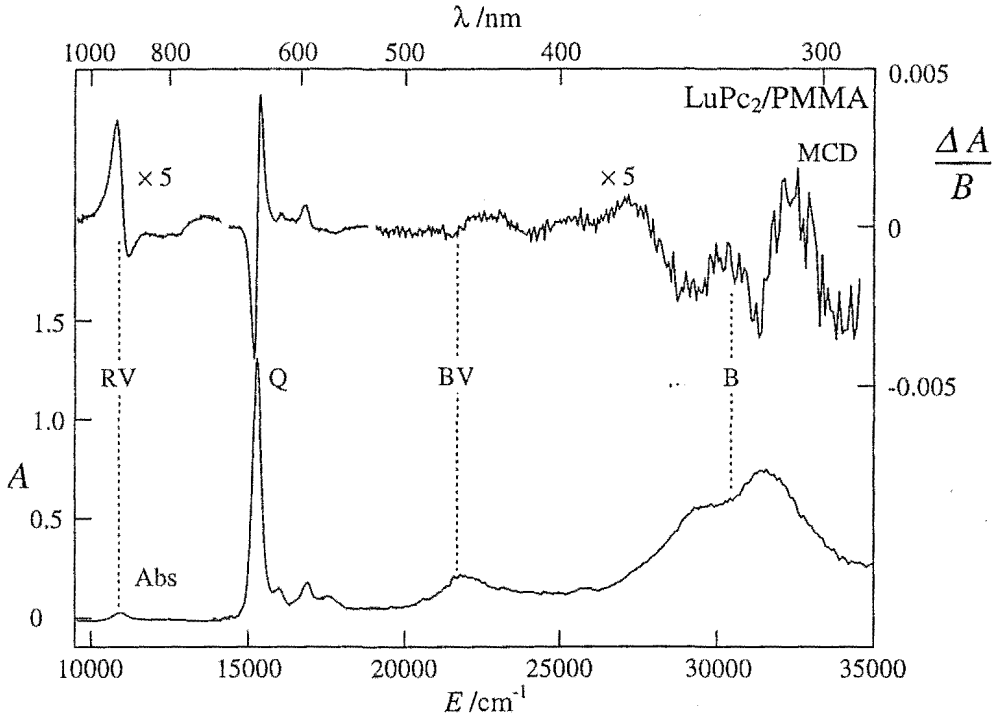

Figure 6.2. An overview of the absorption and MCD (per tesla) spectra (at 1.5 K and 1 T) of $LuPc_2$/PMMA between 9500 and 35000 cm^{-1}.

Spectra of $LuPc_2$/Ar measured using the matrix-injection apparatus are similar to the PMMA film data of Figure 6.2. However, $LuPc_2$/Ar Q-band spectra measured using the helium refrigerator and electromagnet show bands that are substantially narrower and blue shifted, being very similar in appearance to those reported by VanCott *et al.*[39] A comparison between the refrigerator and matrix-injection Q-band spectra (measured at $\sim$ 15 K and 5.8 K respectively) is shown in Figure 6.3. The differences between these two sets of spectra have been found to be due to the degree of annealing of the matrix, as discussed in Section 6.3.1. It did not prove possible to achieve sharp Ar-matrix spectra using the matrix-injection system (necessary for measurement of temperature dependence). This was probably due to problems relating to the heat load on the siphon rod used to cool the matrix during deposition.

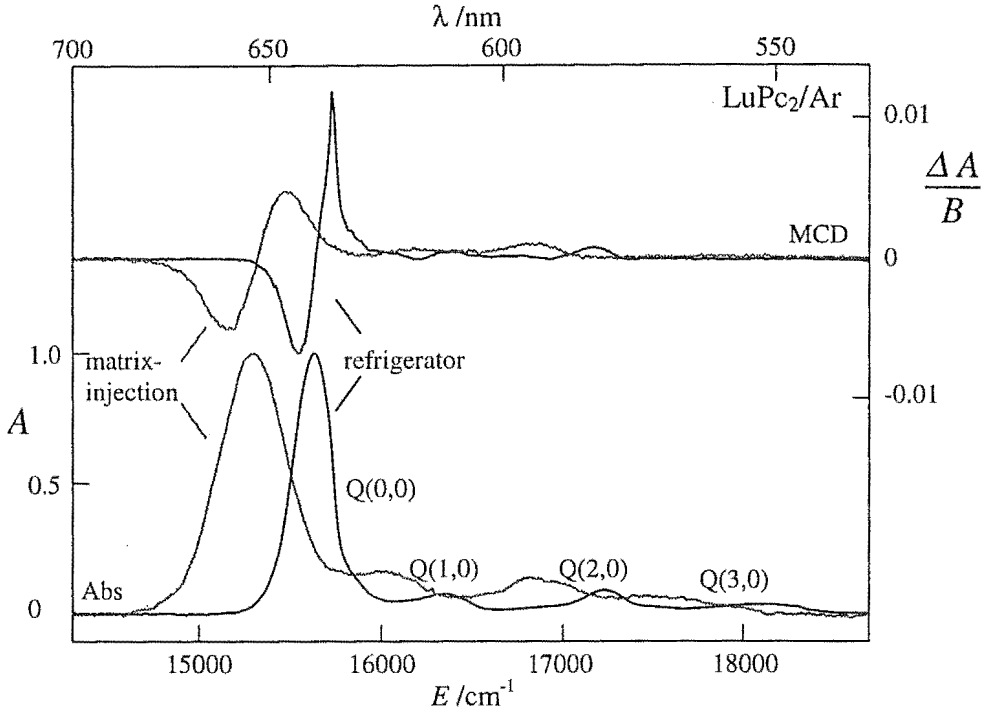

Figure 6.3. Comparison of Q-band spectra of $LuPc_2$/Ar matrices produced using the helium refrigerator (black) and the matrix-injection apparatus (grey), at fields of 0.7 and 2 T respectively. Absorption and MCD spectra have been scaled so that the absorption maxima of the Q(0,0) bands have equal intensity.

The features of the Q-band spectra (Figure 6.3) are similar to those seen in transition-metal phthalocyanine spectra. The most intense band is the origin transition, Q(0,0), with a positive-$\mathcal{A}$-term shaped band in the MCD. Q(1,0) and Q(2,0) are composed of overlapping contributions from many vibrational overtones, with Q(2,0) thought to have a contribution from a separate electronic transition,[19,60] denoted Q′. The Q(3,0) band does not appear in the spectra of mono-phthalocyanines, and is proposed[39] to be due to another electronic transition. This assignment is confirmed by the MCD temperature dependence seen here (Section 6.3.2) and discussed in Section 6.4.6.3.

6.3.1 The Effect of Annealing

The absorption and MCD spectra of $LuPc_2$/Ar have been found to be highly dependent on the degree of annealing of the matrix. This is shown in Figure 6.4, for a sample prepared in the helium refrigerator. All spectra were measured at $\sim$ 15 K and 0.7 T (using the electromagnet). The initial spectrum is shown in black, with

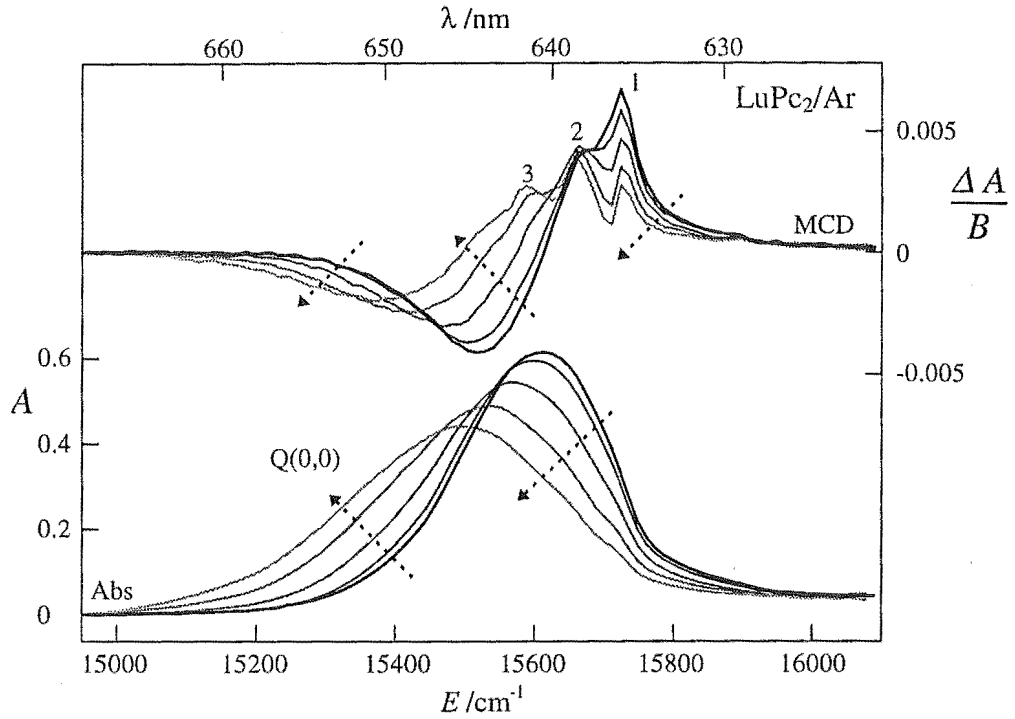

Figure 6.4. The effect of annealing on $LuPc_2$/Ar. The spectrum of the original matrix is plotted in black, with the results of progressive anneals shown in lighter shades of grey. Arrows indicate the direction of change with increasing annealing. Spectra were measured at 0.7 T.

the spectra in increasingly light shades of grey showing the results of progressively annealing for 10-15 min at $\sim$ 20, 28, 34, and 38 K respectively. It can be seen that both the absorption and MCD become increasingly broad and red-shifted, with some structure appearing in the positive lobe of the MCD signal. Within this lobe, intensity appears to shift from the highest energy site (labelled **1** in Figure 6.4) to at least two other sites (labelled **2** and **3**).

Use of moment analysis (Section 3.7) allows quantification of these changes. The band barycentre, $\overline{E}$, of the Q(0,0) band shifts from 15615 to 15500 cm^{-1}, but interestingly both the $\mathbf{M}_1$ and $\mathbf{A}_0$ moments are invariant to the degree of annealing, with $\mathbf{M}_1/\mu_B B\mathbf{A}_0 = 2.3 \pm 0.2$. This invariance is significant for two reasons. Firstly, it shows that the annealing-induced changes are not due to altering alignment of the molecules (see (6.7)). Secondly, it means that the parameters obtained from the MCD temperature-dependence studies described below are not dependent on the state of annealing of the matrix. The latter point is further borne out by the fact that moment analysis over Q(0,0) of the (considerably annealed) matrix used

for Q-band temperature-dependence studies gives a very similar moment ratio of $M_1/\mu_B B A_0 = 2.6 \pm 0.1$ at 16 K (Section 6.3.2.1). Considering that these moments depend on a somewhat subjective choice of moment range (Q(0,0) is not completely isolated, and overlaps with Q(1,0)), this agreement between $M_1/\mu_B B A_0$ values is very good. VanCott *et al.*[39] report $\overline{E}$ = 15573 $cm^{-1}$and $M_1/\mu_B B A_0 = 2.6$ (equivalent to $\mathcal{A}_1/\mathcal{D}_0$ in their analysis) for Q(0,0), in excellent agreement with the results given here.

From a study of the absorption temperature dependence of the intervalence band of $LuPc_2$ in $CDCl_3$, between 268 and 328 K, Gasyna *et al.*[103] have concluded that $LuPc_2$ exists in two conformeric forms. However the annealing-induced changes seen in Figure 6.4 cannot be explained by a change in proportion of only two conformers, as there is no isosbestic point in the spectra. (This is a point at which all spectra have the same intensity, and must be present in a system involving 'competition' between two interconvertible chromophores with overlapping absorption bands.) It is possible that a combination of conformer and site structure is being observed, creating a system with more than two components.

6.3.2 Temperature-Dependence Measurements

Temperature-dependence studies have been carried out on both the Q and RV bands of $LuPc_2$. A suitable method of quantifying the observed spectral changes is moment analysis. As discussed in Section 4.3, moment analysis should be carried out over an entire transition including all vibrational components, but excluding contributions from other electronic transitions. This is made difficult in the case of the Q band, since Q(3,0) and part of Q(2,0) are considered to arise from a different electronic transition. In an attempt to determine the influence of this other transition, moments have been determined over a variety of ranges both including and excluding the Q(2,0) band.

An additional problem arises from the sensitivity of the first MCD moment, M_1, to weak outlying bands such as the vibrational overtones of the Q band. This sensitivity means that the magnitude of M_1 can alter significantly with choice of MCD baseline and integration range. Such changes have been found to affect the y-intercept of a plot of M_1 vs $1/kT$, but not (to the same extent) the slope. Hence, it is

possible to extract quantitative information even in the presence of such problems. However any parameters obtained from the intercepts of plots of $\mathbf{M}_1/\mu_B B\mathbf{A}_0$ vs $1/kT$ (*i.e.* g_{orb}) should be regarded with a degree of scepticism.

6.3.2.1 The Q Band

MCD and absorption spectra of the Q band of $LuPc_2$/Ar have been measured at 15 temperatures between 1.7 and 5.8 K; a selection of these is shown in Figure 6.5. Measurements were also made on two other matrices, both at UOC and ANU (not shown). Results from these are not as good, as fewer temperatures were used, and in the case of the ANU data, the temperatures were not as precisely known (being determined using a roughly calibrated carbon resistor rather than by measurement of the He vapour pressure). However, in each case the same trends were seen, with a definite decrease in MCD intensity of the Q(0,0) band with decreasing temperature. Figure 6.6 shows the results of moment analysis over various portions of the Q band (the numerical ranges are given later in Table 6.5). The slopes of the $\mathbf{M}_1/\mu_B B\mathbf{A}_0$ vs $1/kT$ plots as labelled from top to bottom in Figure 6.6 are -0.3 $\pm$ 0.1, -0.5 $\pm$ 0.1, and -0.6 $\pm$ 0.1 cm^{-1} respectively. The corresponding y intercepts are 4.18 $\pm$ 0.08, 3.04 $\pm$ 0.03, and 2.59 $\pm$ 0.03.

The Q-band absorption and MCD spectra of $LuPc_2$/PMMA are shown in Figure 6.7. These were measured at 17 temperatures between 1.5 and 126 K. The spectra are very similar to, and slightly narrower than the $LuPc_2$/Ar spectra in Figure 6.5. Again, the Q(0,0) band MCD decreases in intensity with decreasing temperature. $\mathbf{M}_1/\mu_B B\mathbf{A}_0$ values have been determined for each of the spectra over a number of ranges, (numerical values given later in Table 6.5) and are plotted vs $1/kT$ in Figure 6.8. The slopes of these plots as labelled from top to bottom in Figure 6.8 are -0.74 $\pm$ 0.04, -0.80 $\pm$ 0.04, and -0.84 $\pm$ 0.04 cm^{-1} respectively. The corresponding y intercepts are 3.10 $\pm$ 0.02, 2.29 $\pm$ 0.02, and 1.97 $\pm$ 0.02.

In both the $LuPc_2$/Ar (Figure 6.5) and $LuPc_2$/PMMA spectra (Figure 6.7), the Q(3,0) band appears as a positive single-signed band at high temperature which changes to a negative band as the temperature drops. The sharper spectra obtained by VanCott *et al.*[39] clearly show a number of $\mathcal{A}$-term shaped bands in this region, with a broader positive band to higher energy extending past the corresponding absorption band. It is probably the latter feature which dominates the spectra shown here.

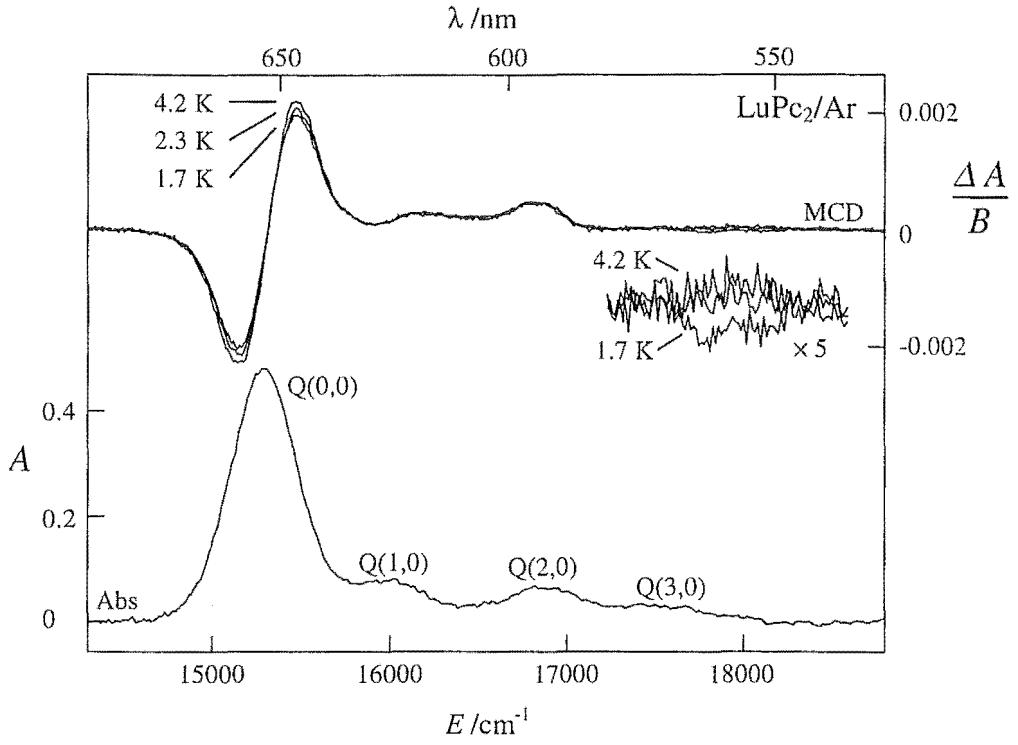

Figure 6.5. Q-band absorption and MCD (per tesla) spectra of $LuPc_2$/Ar, at a field of 2 T.

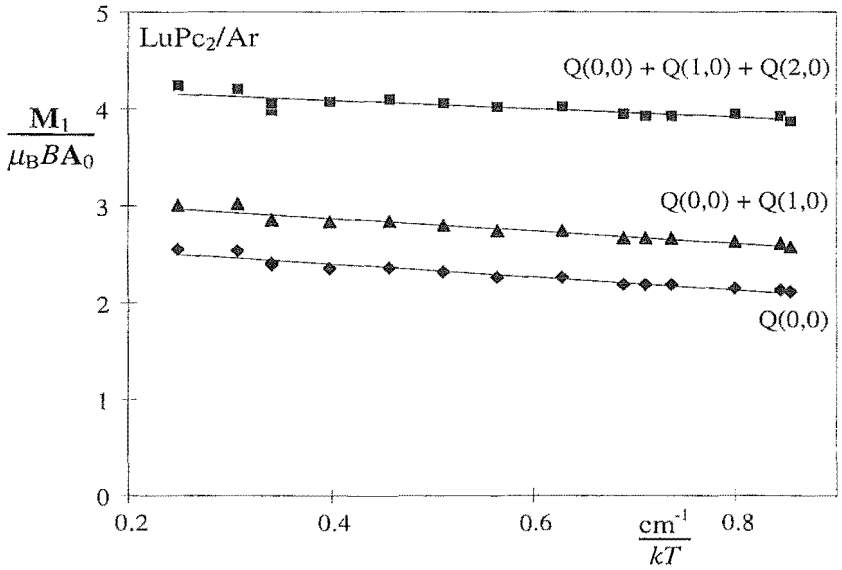

Figure 6.6. The results of moment analysis of the Q band of $LuPc_2$/Ar over three integration ranges. The parameters of the lines of best fit are given in the text.

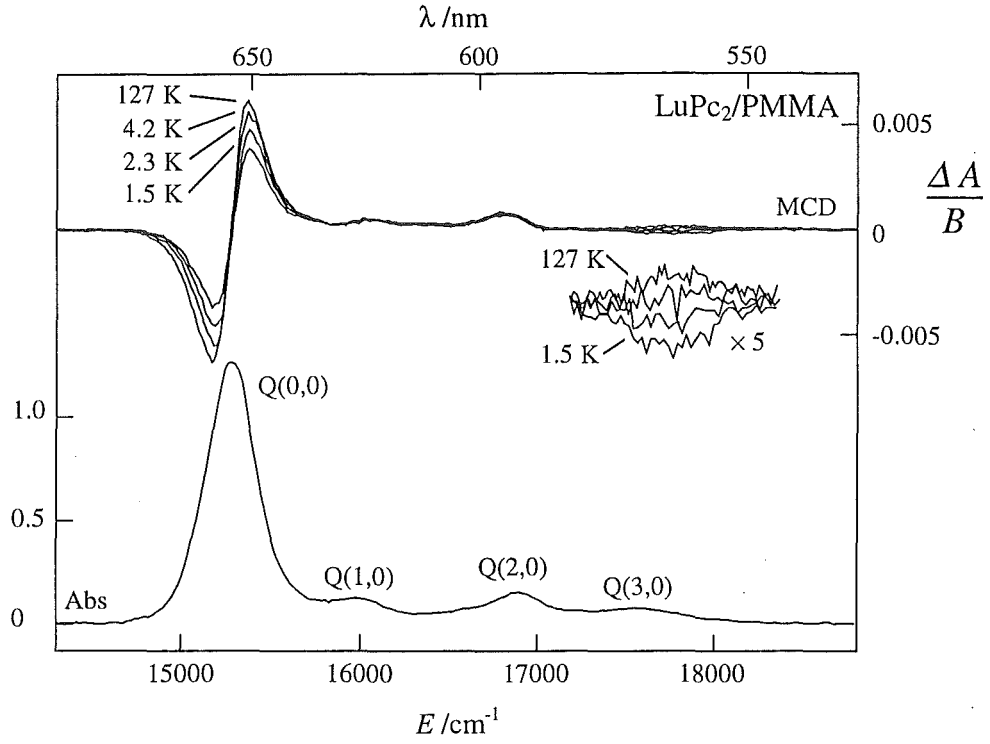

Figure 6.7. Q-band absorption and MCD (per tesla) spectra of $LuPc_2$/PMMA, at a field of 1 T.

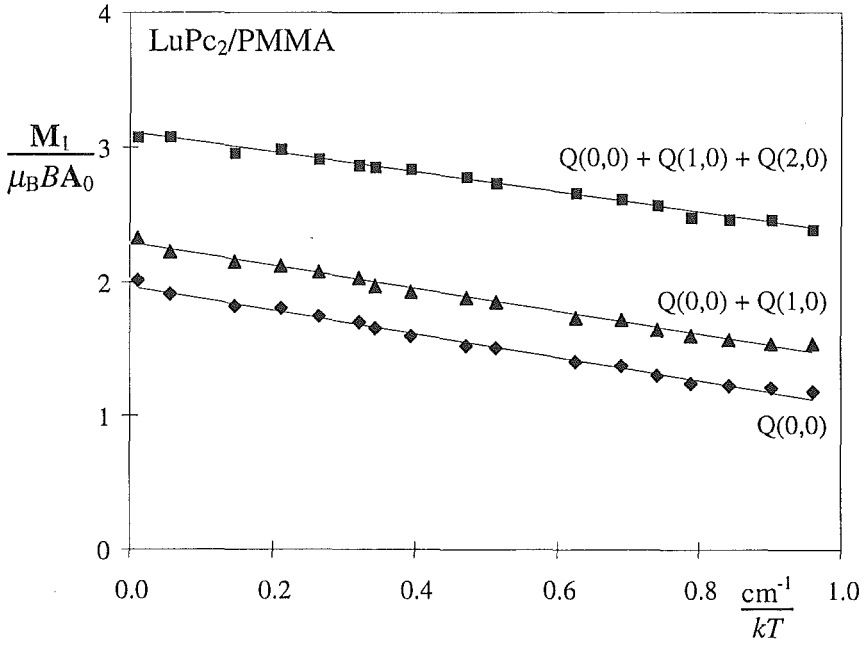

Figure 6.8. The results of moment analysis of the Q band of $LuPc_2$/PMMA over three integration ranges. The parameters of the lines of best fit are given in the text.

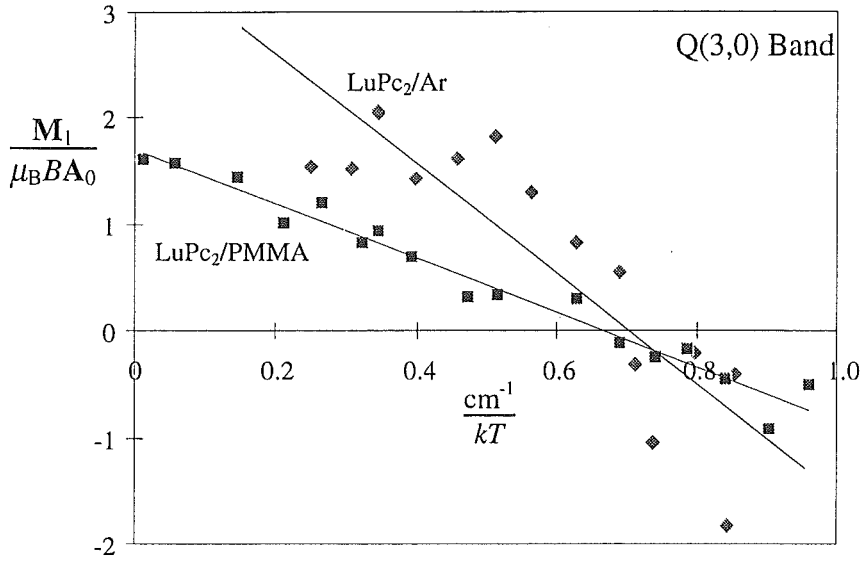

Figure 6.9. The results of moment analysis over the Q(3,0) band of $LuPc_2$/Ar (♦) and $LuPc_2$/PMMA (■). Parameters of the lines of best fit are given in the text.

Relative to the intensity of the absorption bands, the temperature dependence of the Q(3,0) band is significantly stronger than that of the Q(0,0) band. This is again quantified by moment analysis, with the line of best fit of a plot of $\mathbf{M}_1/\mu_B B\mathbf{A}_0$ vs $1/kT$ (Figure 6.9) having slope and y-intercept of -6.2 $\pm$ 1.7 cm^{-1} and 4.4 $\pm$ 1.1 respectively for the Ar matrix, and -2.4 $\pm$ 0.2 cm^{-1} and 1.7 $\pm$ 0.1 respectively for the PMMA film.

6.3.2.2 The RV Band

The absorption and MCD spectra of the RV band of $LuPc_2$/Ar and $LuPc_2$/PMMA at a range of temperatures are shown in Figures 6.10 and 6.11 respectively. In each case a weaker band is seen to the blue of the main band. This band can also be seen in the data of VanCott *et al.*[39], although they exclude it in their specific analysis of this region. The MCD spectra are highly temperature dependent, and at low temperatures have the appearance of a lopsided negative-$\mathcal{A}$-term, the intensity of which decreases with *increasing* temperature (opposite to the case for the Q band). As can be seen in the PMMA-film spectra of Figure 6.11, the sign of the $\mathcal{A}$-shaped band reverses between 6 and 65 K. The MCD of the overtone band is negative at low temperatures, and decreases in intensity with increasing

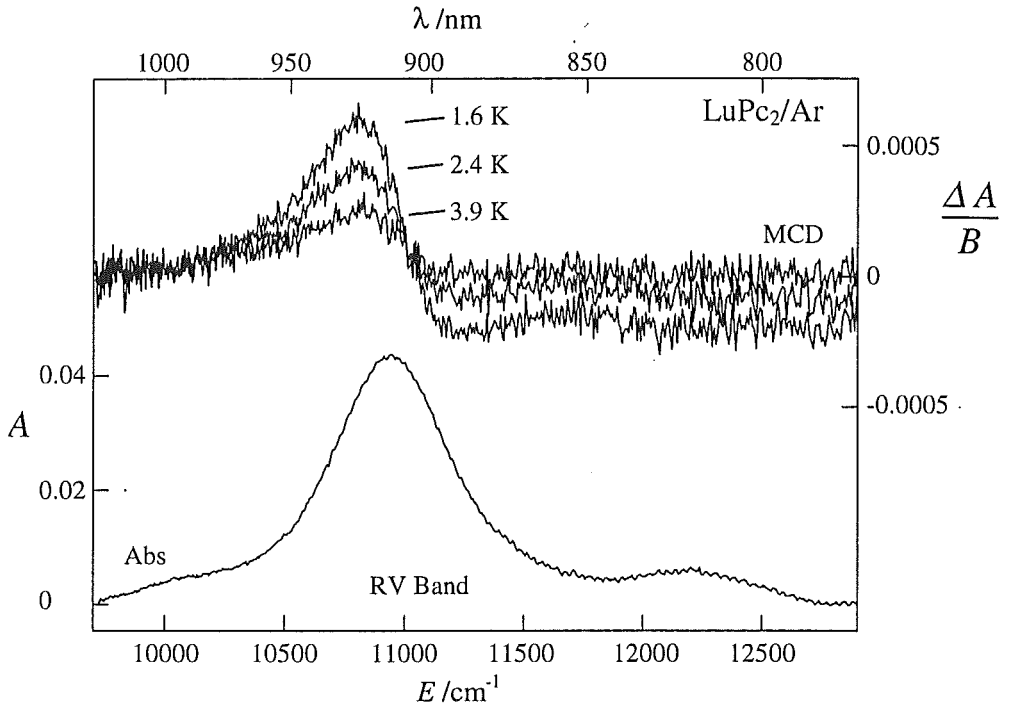

Figure 6.10. Absorption and MCD (per tesla) spectra of the RV band of $LuPc_2$/Ar, at a field of 1 T.

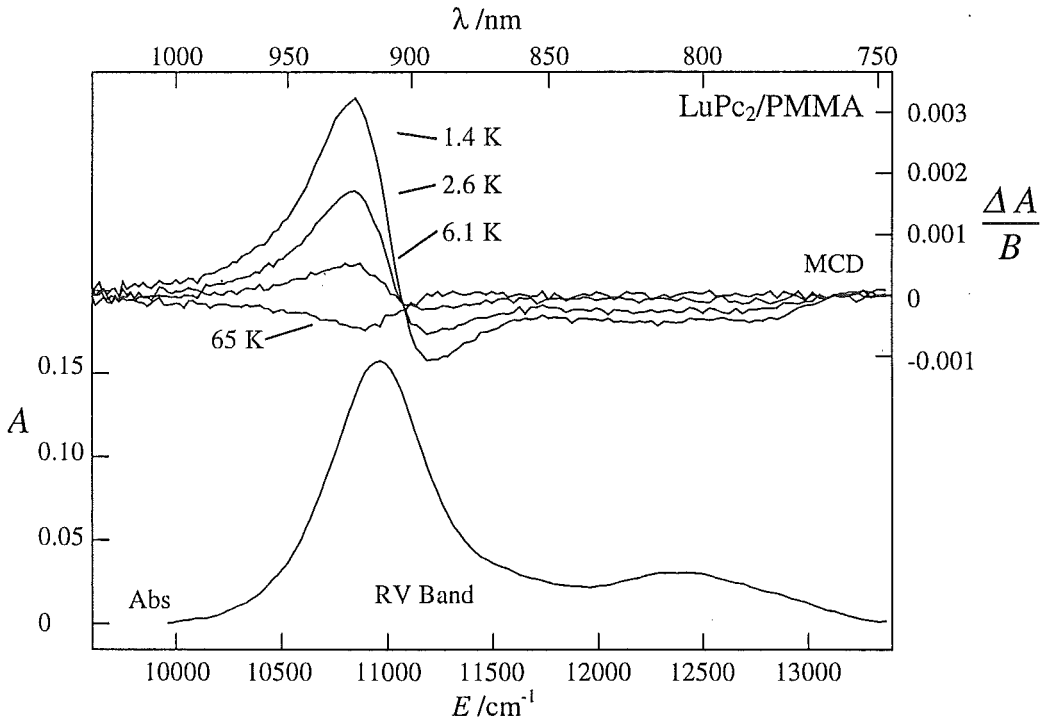

Figure 6.11. Absorption and MCD (per tesla) spectra of the RV band of $LuPc_2$/PMMA, at a field of 1 T.

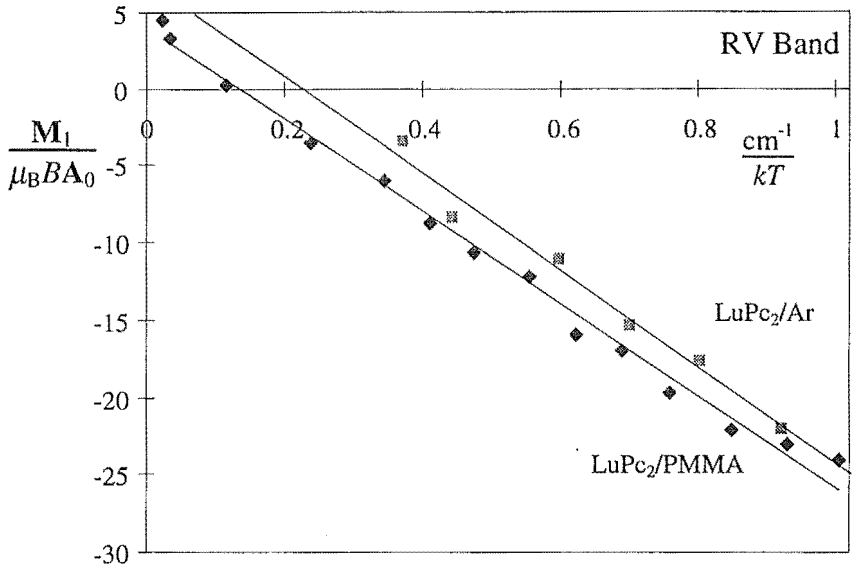

Figure 6.12. The results of moment analysis over the RV band of $LuPc_2$/Ar (■) and $LuPc_2$/PMMA (♦). Parameters of the lines of best fit are given in the text.

temperature (without changing sign). Plots of $M_1/\mu_B B A_0$ vs $1/kT$ (Figure 6.12) produce lines of best fit with slopes of -31 ± 4 and -29 ± 2 cm^{-1} and y-intercepts of 7 ± 3 and 4 ± 1 for the matrix and film respectively. The ratio of absorption intensities of the RV and Q bands is $A_0(RV) : A_0(Q) = 1 : 22$, where the moment over Q excludes the Q(3,0) band.

6.4 Discussion

6.4.1 Electronic Configurations

Following VanCott *et al.*,[39] the π molecular orbitals(MOs) of $LuPc_2$ (D_{4d} symmetry[112]) are approximated by linear combinations of the MOs of two isolated Pc rings (D_{4h} symmetry), staggered by 45°. The resulting orbital diagram is shown in Figure 6.13; the ground-state orbital configuration is $b_1^2a_2$. The Q transition arises from ligand-based excitations of $a_{1u} \rightarrow e_g$ parentage; resulting in (allowed) transitions to the $b_1a_2e_3$ and b_1^2e excited-state configurations. Calculations[111] have shown that there is little mixing of Lu^{3+} metal orbitals into the Pc ring orbitals, and any such interactions will initially be neglected. However, as will be shown

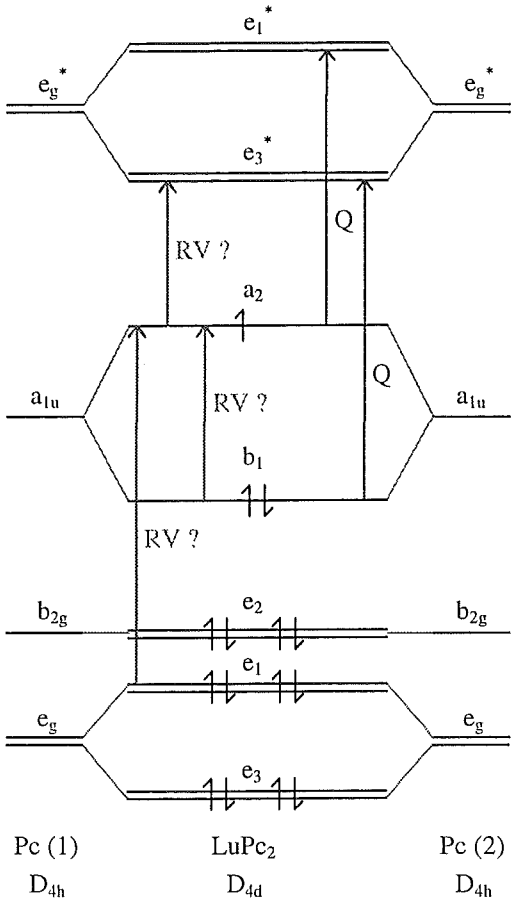

Figure 6.13. Molecular orbitals for $LuPc_2$, indicating the Pc orbitals of which they are linear combinations. The ordering of the lower orbitals is taken from Rousseau *et al.*[111] The ground-state electron configuration, and Q transitions are shown. Various proposed assignments for the transitions responsible for the RV band are shown in grey.

later, metal contributions (however small) must be considered in order to explain the observed temperature dependence of the bands.

The nature of the transitions corresponding to the RV band has not been unambiguously determined. Orti *et al.*[108] carried out valence effective Hamiltonian calculations, and correlated the band with an $a_2 \rightarrow e_3$ transition, which is forbidden in D_{4d}. This agrees with the assignment of VanCott *et al.*,[39] who tentatively propose, on the basis of an observed change in the sign of an MCD $\mathcal{A}$ term between a solution at 300 K and a matrix at 7 K, that the band observed arises from an allowed vibronic overtone of the $a_2 \rightarrow e_3$ excitation, involving a mode of e_2 symmetry in the matrix, and modes of b_1 or b_2 symmetry in the solution.

A number of papers give results in contradiction to the $a_2 \rightarrow e_3$ assignment. Markovitsi *et al.*[104] assign the band to a fully allowed transition resulting from excitation from a low-lying e_1 or e_3 level to the HOMO a_2. Rousseau *et al.*[111], who carry out an extended Hückel MO calculation, consider the RV band to arise from the same excitation as the intervalence (IV) band, and correspondingly assign it to $b_1 \rightarrow a_2$. Using a localised-orbital calculation, Ishikawa *et al.*[107,109] correlate the RV band with spin-forbidden versions of the Q band transitions, which gain intensity through configuration interaction with other doublet excited states.

Given the uncertainty surrounding the assignment of the RV band, the development of theory in the following sections concentrates on the Q-band transitions. The relevance of this analysis to the RV band, and consequences for its assignment are discussed in Section 6.4.8.

6.4.2 Q-Band Wavefunctions

SO wavefunctions for the $LuPc_2$ ground and excited states were calculated under a complex basis using the chain $D_{4d} \supset D_4 \supset C_4$. Coefficients of the wavefunctions were determined using the expansion equation (3.83). The necessary $2jms$ and $3jms$ were obtained using the program RACAH,[56] and are listed in Appendices I and II respectively. The three spins were first coupled under SO_3 symmetry, and transformation coefficients (Appendix III, determined using the method of Butler[113]) applied to relate these to the D_{4d} basis. The three orbitals were coupled in D_{4d}, and the overall spin and orbital functions then coupled together.

The $b_1^2a_2$ ground-state configuration is orbitally non-degenerate and gives a single $^2A_2$ term, which transforms as a Kramers pair. The two excited-state configurations both give $^2E_1$ terms. The wavefunctions for the ground and excited states are listed in Table 6.2. For simplicity, these are displayed in Butler notation; the correlation of this with Mulliken notation is given in the table of $2jms$ in Appendix I. There are four times as many microstates arising from the $b_1a_2e_3$ as from the $b_1^2e_1$ configuration, because of the extra spin arrangements possible for the former. As well as a spin quartet (^4E), the $b_1a_2e_3$ configuration gives rise to two independent $^2E_1$ terms, here denoted as $^2E_1^0$ and $^2E_1^1$, in which the spins of the b_1 and a_2 orbitals are coupled to give a singlet and triplet respectively.

Table 6.2. The ground- and excited-state wavefunctions and Zeeman splittings for the $Q(\pi \rightarrow \pi^*)$ transitions of $LuPc_2$. The spin associated with each orbital is denoted by a superscript $\pm$ for $m_s = \pm\frac{1}{2}$, and the orbital partner for the degenerate orbitals as a subscript. $g_{\rm orb}$ is defined in the text. The level is denoted as $\left|(^{2S+1}h\ M\ \theta)\ t\ \tau\right\rangle$ where the spin, orbital and overall irrep labels are given by S, h and t, with M, θ and τ representing the corresponding partner labels.

Config.	State	Level	Wavefunction	Zeeman Shift
$b_1^2a_2$	$^2A_2$	$\left\|(^2A_2\ -\frac{1}{2}\ 0)\ \frac{1}{2}\ \frac{1}{2}\right\rangle$	$\left\|4^+4^-\tilde{0}^+\right\rangle$	$\mu_B B$
		$\left\|(^2A_2\ \frac{1}{2}\ 0)\ \frac{1}{2}\ -\frac{1}{2}\right\rangle$	$-\left\|4^+4^-\tilde{0}^-\right\rangle$	$-\mu_B B$
$b_1^2e_1$	$^2E_1$	$\left\|(^2E_1\ -\frac{1}{2}\ 1)\ \frac{7}{2}\ \frac{1}{2}\right\rangle$	$-\left\|4^+\tilde{0}^-3^-_{+1}\right\rangle$	$(\frac{1}{2}g_{\rm orb}-1)\,\mu_B B$
		$\left\|(^2E_1\ \frac{1}{2}\ -1)\ \frac{7}{2}\ -\frac{1}{2}\right\rangle$	$\left\|4^+\tilde{0}^-3^+_{-1}\right\rangle$	$(-\frac{1}{2}g_{\rm orb}+1)\,\mu_B B$
		$\left\|(^2E_1\ \frac{1}{2}\ 1)\ \frac{5}{2}\ \frac{3}{2}\right\rangle$	$\left\|4^+\tilde{0}^-3^+_{+1}\right\rangle$	$(\frac{1}{2}g_{\rm orb}+1)\,\mu_B B$
		$\left\|(^2E_1\ -\frac{1}{2}\ -1)\ \frac{5}{2}\ -\frac{3}{2}\right\rangle$	$\left\|4^+\tilde{0}^-3^-_{-1}\right\rangle$	$(-\frac{1}{2}g_{\rm orb}-1)\,\mu_B B$
$b_1a_2e_3$	$^2E_1^0$	$\left\|(^2E_1^0\ -\frac{1}{2}\ 1)\ \frac{7}{2}\ \frac{1}{2}\right\rangle$	$-\frac{1}{\sqrt{2}}\left(\left\|4^+\tilde{0}^-1^-_{+1}\right\rangle-\left\|4^-\tilde{0}^+1^-_{+1}\right\rangle\right)$	$(\frac{1}{2}g_{\rm orb}-1)\,\mu_B B$
		$\left\|(^2E_1^0\ \frac{1}{2}\ -1)\ \frac{7}{2}\ -\frac{1}{2}\right\rangle$	$-\frac{1}{\sqrt{2}}\left(\left\|4^+\tilde{0}^-1^+_{-1}\right\rangle-\left\|4^-\tilde{0}^+1^+_{-1}\right\rangle\right)$	$(-\frac{1}{2}g_{\rm orb}+1)\,\mu_B B$
		$\left\|(^2E_1^0\ \frac{1}{2}\ 1)\ \frac{5}{2}\ \frac{3}{2}\right\rangle$	$\frac{1}{\sqrt{2}}\left(\left\|4^+\tilde{0}^-1^+_{+1}\right\rangle-\left\|4^-\tilde{0}^+1^+_{+1}\right\rangle\right)$	$(\frac{1}{2}g_{\rm orb}+1)\,\mu_B B$
		$\left\|(^2E_1^0\ -\frac{1}{2}\ -1)\ \frac{5}{2}\ -\frac{3}{2}\right\rangle$	$-\frac{1}{\sqrt{2}}\left(\left\|4^+\tilde{0}^-1^-_{-1}\right\rangle-\left\|4^-\tilde{0}^+1^-_{-1}\right\rangle\right)$	$(-\frac{1}{2}g_{\rm orb}-1)\,\mu_B B$
	$^2E_1^1$	$\left\|(^2E_1^1\ -\frac{1}{2}\ 1)\ \frac{7}{2}\ \frac{1}{2}\right\rangle$	$-\frac{1}{\sqrt{6}}\left(\left\|4^+\tilde{0}^-1^-_{+1}\right\rangle-\left\|4^-\tilde{0}^+1^-_{+1}\right\rangle-2\left\|4^-\tilde{0}^-1^+_{+1}\right\rangle\right)$	$(\frac{1}{2}g_{\rm orb}-1)\,\mu_B B$
		$\left\|(^2E_1^1\ \frac{1}{2}\ -1)\ \frac{7}{2}\ -\frac{1}{2}\right\rangle$	$\frac{1}{\sqrt{6}}\left(\left\|4^+\tilde{0}^-1^+_{-1}\right\rangle-\left\|4^-\tilde{0}^+1^+_{-1}\right\rangle-2\left\|4^+\tilde{0}^+1^-_{-1}\right\rangle\right)$	$(-\frac{1}{2}g_{\rm orb}+1)\,\mu_B B$
		$\left\|(^2E_1^1\ \frac{1}{2}\ 1)\ \frac{5}{2}\ \frac{3}{2}\right\rangle$	$-\frac{1}{\sqrt{6}}\left(\left\|4^+\tilde{0}^-1^+_{+1}\right\rangle-\left\|4^-\tilde{0}^+1^+_{+1}\right\rangle-2\left\|4^+\tilde{0}^+1^-_{+1}\right\rangle\right)$	$(\frac{1}{2}g_{\rm orb}+1)\,\mu_B B$
		$\left\|(^2E_1^1\ -\frac{1}{2}\ -1)\ \frac{5}{2}\ -\frac{3}{2}\right\rangle$	$-\frac{1}{\sqrt{6}}\left(\left\|4^+\tilde{0}^-1^-_{-1}\right\rangle-\left\|4^-\tilde{0}^+1^-_{-1}\right\rangle-2\left\|4^-\tilde{0}^-1^+_{-1}\right\rangle\right)$	$(-\frac{1}{2}g_{\rm orb}-1)\,\mu_B B$
	$^4E_1$	$\left\|(^4E_1\ -\frac{1}{2}\ 1)\ \frac{7}{2}\ \frac{1}{2}\right\rangle$	$-\frac{1}{\sqrt{3}}\left(\left\|4^+\tilde{0}^-1^-_{+1}\right\rangle+\left\|4^-\tilde{0}^+1^-_{+1}\right\rangle+\left\|4^-\tilde{0}^-1^+_{+1}\right\rangle\right)$	$(\frac{1}{2}g_{\rm orb}-1)\,\mu_B B$
		$\left\|(^4E_1\ \frac{1}{2}\ -1)\ \frac{7}{2}\ -\frac{1}{2}\right\rangle$	$\frac{1}{\sqrt{3}}\left(\left\|4^+\tilde{0}^-1^+_{-1}\right\rangle+\left\|4^-\tilde{0}^+1^+_{-1}\right\rangle+\left\|4^+\tilde{0}^+1^-_{-1}\right\rangle\right)$	$(-\frac{1}{2}g_{\rm orb}+1)\,\mu_B B$
		$\left\|(^4E_1\ \frac{1}{2}\ 1)\ \frac{5}{2}\ \frac{3}{2}\right\rangle$	$-\frac{1}{\sqrt{3}}\left(\left\|4^+\tilde{0}^-1^+_{+1}\right\rangle+\left\|4^-\tilde{0}^+1^+_{+1}\right\rangle+\left\|4^+\tilde{0}^+1^-_{+1}\right\rangle\right)$	$(\frac{1}{2}g_{\rm orb}+1)\,\mu_B B$
		$\left\|(^4E_1\ -\frac{1}{2}\ -1)\ \frac{5}{2}\ -\frac{3}{2}\right\rangle$	$-\frac{1}{\sqrt{3}}\left(\left\|4^+\tilde{0}^-1^-_{-1}\right\rangle+\left\|4^-\tilde{0}^+1^-_{-1}\right\rangle+\left\|4^-\tilde{0}^-1^+_{-1}\right\rangle\right)$	$(-\frac{1}{2}g_{\rm orb}-1)\,\mu_B B$
		$\left\|(^4E_1\ \frac{3}{2}\ -1)\ \frac{7}{2}\ \frac{1}{2}\right\rangle$	$-\left\|4^+\tilde{0}^+1^+_{-1}\right\rangle$	$(-\frac{1}{2}g_{\rm orb}+3)\,\mu_B B$
		$\left\|(^4E_1\ -\frac{3}{2}\ 1)\ \frac{7}{2}\ -\frac{1}{2}\right\rangle$	$\left\|4^-\tilde{0}^-1^-_{+1}\right\rangle$	$(\frac{1}{2}g_{\rm orb}-3)\,\mu_B B$
		$\left\|(^4E_1\ -\frac{3}{2}\ -1)\ \frac{3}{2}\ \frac{3}{2}\right\rangle$	$-\left\|4^-\tilde{0}^-1^-_{-1}\right\rangle$	$(-\frac{1}{2}g_{\rm orb}-3)\,\mu_B B$
		$\left\|(^4E_1\ \frac{3}{2}\ 1)\ \frac{3}{2}\ -\frac{3}{2}\right\rangle$	$-\left\|4^+\tilde{0}^+1^+_{+1}\right\rangle$	$(\frac{1}{2}g_{\rm orb}+3)\,\mu_B B$

Note that $^2E_1^0$ and $^2E_1^1$ are similar to the singdoublet and tripdoublet terms derived in Chapter 4 for CuPc and CoPc, where the spins of the ligand-based orbitals were coupled to give a singlet and a triplet respectively. However, in the case of $LuPc_2$, all three orbitals involved in the excited-state configurations are ligand based, and so the singdoublet/tripdoublet labelling does not apply. In fact, the order of the orbitals in this configuration has been chosen differently for $LuPc_2$ ($b_1a_2e_3$) than it was for CuPc and CoPc (which would correspond to $b_1e_3a_2$), in order to minimise off-diagonal elements in the final Hamiltonian matrix. Note that both orbital orders give the same eigenvalues when all off-diagonals are taken into account.

6.4.3 Energy Levels

The energy-level diagram for all three Q-band transitions is given in Figure 6.14. This shows the effect of both zero-field splitting (Δ) of the excited states and Zeeman splittings, each of which will be explained in detail below.

For each of the allowed excited states, $^2E_1$, $^2E_1^0$, and $^2E_1^1$, the zero-field splitting is defined

$$\Delta = \overline{E}_{5/2} - \overline{E}_{7/2} \tag{6.1}$$

where $\overline{E}_{5/2}$ and $\overline{E}_{7/2}$ are the band barycentres for transitions terminating in the $\frac{5}{2}$ and $\frac{7}{2}$ levels respectively. The energy levels in Figure 6.14 are shown assuming $\Delta > 0$, both in the absence ($B = 0$) and in the presence ($B > 0$) of an external magnetic field. The inset represents the case where $\Delta = 0$ and $B > 0$.

When a magnetic field is applied to a system, the Zeeman effect will remove any remaining degeneracies. The ground- and excited-state Zeeman splittings for $LuPc_2$ are listed in Table 6.2 and illustrated in Figure 6.14 for the case where the field is applied along the molecular symmetry axis ($B \parallel z$). g_{orb} is a measure of the excited-state orbital angular momentum;

$$g_{\mathrm{orb}} = \pm 2\langle 1_{\pm 1} \mid l_z \mid 1_{\pm 1}\rangle = \pm 2\langle 3_{\pm 1} \mid l_z \mid 3_{\pm 1}\rangle \tag{6.2}$$

where l_z is the component of the one-electron orbital angular momentum operator along the z axis. The one-electron matrix elements $\langle 1_{\pm 1} \mid l_z \mid 1_{\pm 1}\rangle$ and $\langle 3_{\pm 1} \mid l_z \mid 3_{\pm 1}\rangle$ pertain to the $b_1a_2e_3$ and $b_1^2e_1$ configurations respectively. Their equality can be

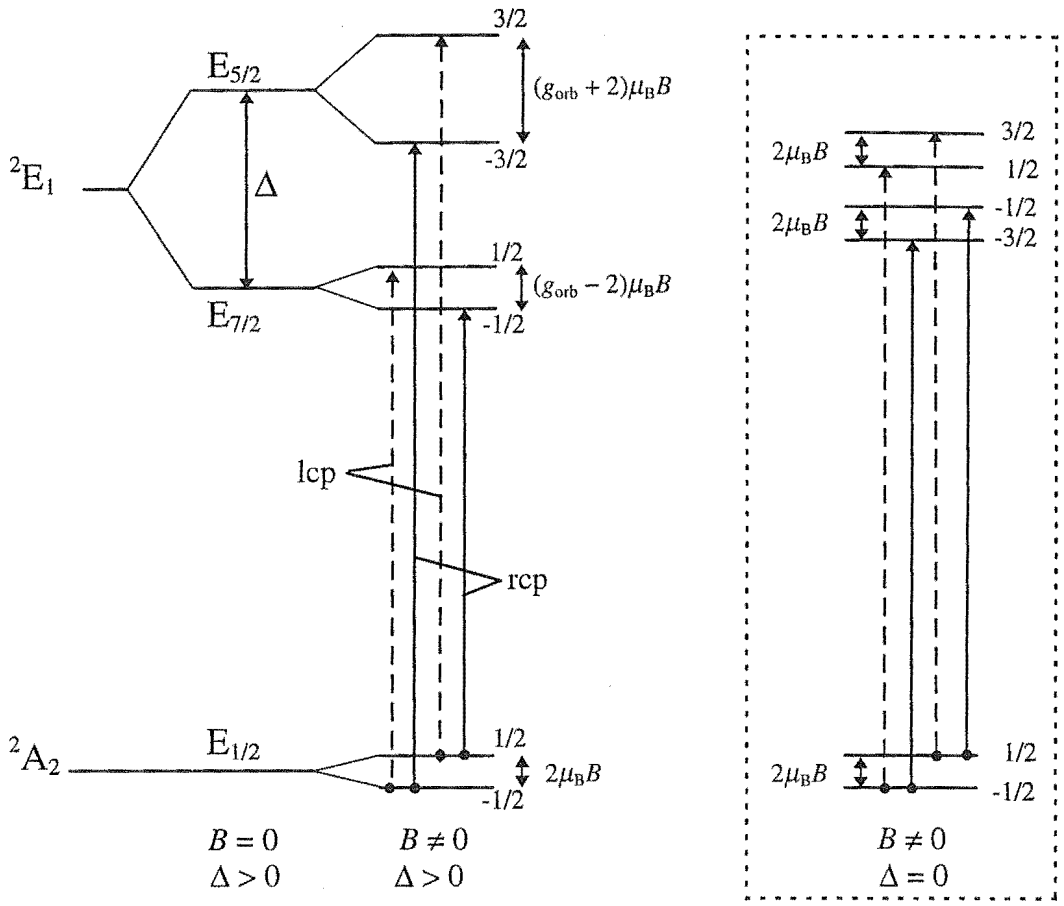

Figure 6.14. The energy-level diagram for $LuPc_2$, showing the effect of zero-field splitting (Δ) in the absence ($B = 0$) and presence ($B > 0$) of magnetic field. The inset shows the situation when $B > 0$ and $\Delta = 0$.

shown by decomposing the excited-state wavefunctions into their component Pc MOs, neglecting cross terms between MOs on different rings. In terms of excited states

$$g_{\text{orb}} = \pm 2 \left\langle \tfrac{7}{2} \pm \tfrac{1}{2} \left| L_z \right| \tfrac{7}{2} \pm \tfrac{1}{2} \right\rangle = \pm 2 \left\langle \tfrac{5}{2} \pm \tfrac{3}{2} \left| L_z \right| \tfrac{5}{2} \pm \tfrac{3}{2} \right\rangle \tag{6.3}$$

where L_z is the component of the many-electron orbital angular momentum operator $\left(L_z = \sum_i l_z(i) \right)$ along z.

6.4.4 Transition Intensities

The four allowed Zeeman transitions and their polarisations (assuming $B \parallel z$) are shown in Figure 6.14, and given as one-electron elements in Table 6.3, where $\mathcal{M}_{\pm} = \langle 4 \left| m_{\pm 1} \right| 1_{\mp 1} \rangle = \left\langle \widetilde{0} \left| m_{\pm 1} \right| 3_{\mp 1} \right\rangle$. (In the convention used here (Section

3.2), m_{-1} and m_{+1} effectively represent the operators for lcp and rcp transitions respectively.)

The dipole strength and Faraday parameters for each transition were determined using the results of Section 3.5.2, and are summarised in Table 6.4 where the subscripts $\frac{5}{2}$ and $\frac{7}{2}$ indicate the SO level in which the transition terminates, and $|\mathcal{M}|^2 \equiv |\mathcal{M}_+|^2 = |\mathcal{M}_-|^2$. The parameters are given for the case of oriented molecules (superscript Z); for orientational averaging, $\overline{\mathcal{A}}_1 = \frac{1}{3}\mathcal{A}_1^Z$, $\overline{C}_0 = \frac{1}{3}C_1^Z$ and $\overline{\mathcal{D}}_0 = \frac{2}{3}\mathcal{D}_1^Z$, as shown in Section 3.5.3.

Table 6.3. Transition moments for the three LuPc$_2$ transitions. $\mathcal{M}_\pm = \langle 4|m_{\pm1}|1_{\mp1}\rangle = \langle \widetilde{0}|m_{\pm1}|3_{\mp1}\rangle$ where m_{-1} and m_{+1} effectively represent the operators for lcp and rcp transitions respectively.

$^2E_1$	$\left\|\frac{5}{2}\ -\frac{3}{2}\right\rangle$	$\left\|\frac{7}{2}\ -\frac{1}{2}\right\rangle$	$\left\|\frac{7}{2}\ \frac{1}{2}\right\rangle$	$\left\|\frac{5}{2}\ \frac{3}{2}\right\rangle$
$\left\langle\frac{1}{2}\ -\frac{1}{2}\right\|$	$-\mathcal{M}_+$		$\mathcal{M}_-$	
$\left\langle\frac{1}{2}\ \frac{1}{2}\right\|$		$\mathcal{M}_+$		$\mathcal{M}_-$

$^2E_1^0$	$\left\|\frac{5}{2}\ -\frac{3}{2}\right\rangle$	$\left\|\frac{7}{2}\ -\frac{1}{2}\right\rangle$	$\left\|\frac{7}{2}\ \frac{1}{2}\right\rangle$	$\left\|\frac{5}{2}\ \frac{3}{2}\right\rangle$
$\left\langle\frac{1}{2}\ -\frac{1}{2}\right\|$	$-\frac{1}{\sqrt{2}}\mathcal{M}_+$		$-\frac{1}{\sqrt{2}}\mathcal{M}_-$	
$\left\langle\frac{1}{2}\ \frac{1}{2}\right\|$		$-\frac{1}{\sqrt{2}}\mathcal{M}_+$		$\frac{1}{\sqrt{2}}\mathcal{M}_-$

$^2E_1^1$	$\left\|\frac{5}{2}\ -\frac{3}{2}\right\rangle$	$\left\|\frac{7}{2}\ -\frac{1}{2}\right\rangle$	$\left\|\frac{7}{2}\ \frac{1}{2}\right\rangle$	$\left\|\frac{5}{2}\ \frac{3}{2}\right\rangle$
$\left\langle\frac{1}{2}\ -\frac{1}{2}\right\|$	$-\frac{\sqrt{3}}{\sqrt{2}}\mathcal{M}_+$		$-\frac{\sqrt{3}}{\sqrt{2}}\mathcal{M}_-$	
$\left\langle\frac{1}{2}\ \frac{1}{2}\right\|$		$-\frac{\sqrt{3}}{\sqrt{2}}\mathcal{M}_+$		$\frac{\sqrt{3}}{\sqrt{2}}\mathcal{M}_-$

6.4.5 Qualitative Analysis of the Spectra

As in the case of the transition-metal complexes discussed in Chapters 4 and 5, the temperature dependence of the Q-band MCD of LuPc$_2$ can be qualitatively rationalised in terms of Figure 6.14. Since the four Zeeman transitions within each electronic transition have the same dipole strengths (Table 6.4), their relative intensities are determined by the Boltzmann populations of the ground-state Zeeman levels. First consider the inset to Figure 6.14, which show the case where $B > 0$ and $\Delta = 0$. The higher-energy transitions are lcp, so the MCD has the overall appearance

Table 6.4. The dipole strength and Faraday parameters of each of the three Q-band transitions of $LuPc_2$.

Parameter	$^2E_1^0$	$^2E_1^1$	$^2E_1$
$\mathcal{D}^Z_{5/2}$	$\frac{1}{4}\|\mathcal{M}\|^2$	$\frac{3}{4}\|\mathcal{M}\|^2$	$\frac{1}{2}\|\mathcal{M}\|^2$
$\mathcal{D}^Z_{7/2}$	$\frac{1}{4}\|\mathcal{M}\|^2$	$\frac{3}{4}\|\mathcal{M}\|^2$	$\frac{1}{2}\|\mathcal{M}\|^2$
$\mathcal{A}^Z_{5/2}$	$\frac{1}{4}g_{\rm orb}\|\mathcal{M}\|^2$	$\frac{3}{4}g_{\rm orb}\|\mathcal{M}\|^2$	$\frac{1}{2}g_{\rm orb}\|\mathcal{M}\|^2$
$\mathcal{A}^Z_{7/2}$	$\frac{1}{4}g_{\rm orb}\|\mathcal{M}\|^2$	$\frac{3}{4}g_{\rm orb}\|\mathcal{M}\|^2$	$\frac{1}{2}g_{\rm orb}\|\mathcal{M}\|^2$
$\mathcal{C}^Z_{5/2}$	$-\frac{1}{2}\|\mathcal{M}\|^2$	$-\frac{3}{2}\|\mathcal{M}\|^2$	$-\|\mathcal{M}\|^2$
$\mathcal{C}^Z_{7/2}$	$\frac{1}{2}\|\mathcal{M}\|^2$	$\frac{3}{2}\|\mathcal{M}\|^2$	$\|\mathcal{M}\|^2$

of a positive A-term, with $\mathbf{M}_1 > 0$. However, since the pairs of transitions with the same circular polarisation occur at the same energy, their sum (and hence $\mathbf{M}_1$) is temperature independent. In other words, Zeeman splitting alone cannot account for the observed temperature dependence.

Next consider the situation shown on the left of the figures, where $\Delta > 0$. As the temperature is decreased, the intensities of the transitions furthest from the band barycenter are reduced, and $\mathbf{M}_1$ decreases. If the energy order of the $\frac{5}{2}$ and $\frac{7}{2}$ levels were reversed, $\mathbf{M}_1$ would increase with cooling. Hence it can be concluded that the experimental observations require $\Delta > 0$. Note, however, that the experimental data give information only on the *overall* temperature dependence of the Q band, as contributed to by all three transitions. Hence it cannot be concluded that all three of the individual excited states have $\Delta > 0$, but rather only that this is the dominating contribution.

6.4.6 Extracting Δ and $g_{\rm orb}$ Values from the Spectra

6.4.6.1 Moment Expressions

In order to quantitatively analyse the absorption and MCD spectra, they must be related to the theoretical parameters of Table 6.4. The method employed for this purpose is moment analysis. For each of the $^2E_1$, $^2E_1^0$, and $^2E_1^1$ excited states two separate transitions terminating in the $\frac{5}{2}$ and $\frac{7}{2}$ SO levels must be considered. This is thus identical to the case for CuPc and CoPc presented in Section 4.4.5. Following the analysis given in that section, it is found that

$$\overline{E} = \tfrac{1}{2}\left(\overline{E}_{5/2} + \overline{E}_{7/2}\right) \tag{6.4}$$

$$\mathrm{A}_0 = 2\gamma\mathcal{D}_{7/2} \tag{6.5}$$

$$\mathrm{M}_1 = \gamma\mu_\mathrm{B}B(2\mathcal{A}_{7/2} - \mathcal{C}_{7/2}\frac{\Delta}{kT}) \tag{6.6}$$

Substituting for $\mathcal{D}_{7/2}$, $\mathcal{A}_{7/2}$ and $\mathcal{C}_{7/2}$ from the expressions in Table 6.4, it is obtained for each transition that

$$\frac{\mathrm{M}_1(i)}{\mu_\mathrm{B}B\mathrm{A}_0(i)} = c_\mathrm{o}\left(g_{\mathrm{orb}(i)} - \frac{\Delta_i}{kT}\right) \tag{6.7}$$

where c_o is an orientational factor such that $c_\mathrm{o} = 1$ for preferential Z orientation, and $c_\mathrm{o} = 0.5$ for random orientation of molecules (Section 3.5.3) and the expression is for the ith of the three individual transitions.

Since the three transitions overlap and are unresolved within the Q band, only the overall $\mathrm{M}_1/\mu_\mathrm{B}B\mathrm{A}_0$ ratio can be measured experimentally, and so an expression must be developed for this. A_0 is simply the area under the absorption band, and so

$$\mathrm{A}_0 = \sum_i \mathrm{A}_0(i) \tag{6.8}$$

Denoting $\overline{E}$ as the overall band barycentre, $\overline{E}_i$ as the barycentre of the ith band and δ_i as the separation between the two, the expression for the first MCD moment may be expanded as

$$\begin{aligned}
\mathrm{M}_1^{\overline{E}} &= \int (\Delta A/E)\left(E - \overline{E}\right) dE \\
&= \sum_i \int (\Delta A(i)/E)\left(E - \overline{E}_i - \delta_i\right) dE \\
&= \sum_i \left(-\delta_i \int (\Delta A(i)/E)\ dE + \int (\Delta A(i)/E)\left(E - \overline{E}_i\right)\ dE\right) \\
&= \sum_i \left(-\delta_i \mathrm{M}_0 + \mathrm{M}_1^{\overline{E}_i}(i)\right)
\end{aligned} \tag{6.9}$$

Assuming M_0 (due to $\mathcal{B}$ terms) is negligible (as is indeed found experimentally), it is obtained that

$$\mathrm{M}_1^{\overline{E}} = \sum_i \mathrm{M}_1^{\overline{E}_i}(i) \tag{6.10}$$

in other words, the overall M_1 is the sum of the M_1s of the individual components.

Now consider the $g_{\rm orb}$ and Δ parameters of the three transitions. It can be seen from (6.2) that the $g_{\rm orb}$ values of the three Q-band transitions are equal. However, the relationships of the Δ values have not yet been determined (these will be discussed in Section 6.4.7). The assumption will be made that these Δ values are all related to each other, *i.e.*

$$\Delta_1 = ax, \quad \Delta_2 = bx, \quad \Delta_3 = cx \tag{6.11}$$

and so

$$\Delta_2 = \tfrac{b}{a}\Delta_1, \quad \Delta_3 = \tfrac{c}{a}\Delta_1 \tag{6.12}$$

where a, b and c are constants. Using the results of (6.7), (6.8) and (6.10), $M_1^{\overline{E}}$ for the overall Q band can be written as

$$\begin{aligned} M_1^{\overline{E}} &= c_o\mu_B B \sum_{i=1}^{3}\left(g_{\rm orb} - \frac{\Delta_i}{kT}\right)A_0(i) \\ &= c_o\mu_B B\left[\sum_{i=1}^{3} g_{\rm orb}A_0(i) - \frac{\Delta_1}{kT}\left(A_0(1) + \tfrac{b}{a}A_0(2) + \tfrac{c}{a}A_0(3)\right)\right] \\ &= c_o\mu_B B\left[g_{\rm orb}A_0 - \frac{\Delta_1}{kT}\left(A_0 + \left(\tfrac{b}{a}-1\right)A_0(2) + \left(\tfrac{c}{a}-1\right)A_0(3)\right)\right] \end{aligned} \tag{6.13}$$

and so

$$\begin{aligned} \frac{M_1^{\overline{E}}}{\mu_B B A_0} &= c_o\left[g_{\rm orb} - \frac{\Delta_1}{kT}\left(1 + \frac{\left(\frac{b}{a}-1\right)A_0(2) + \left(\frac{c}{a}-1\right)A_0(3)}{A_0}\right)\right] \\ &= c_o\left(g_{\rm orb} - \frac{\Delta_{\rm av}}{kT}\right) \end{aligned} \tag{6.14}$$

where

$$\Delta_{\rm av} = \frac{A_0 + \left(\frac{b}{a}-1\right)A_0(2) + \left(\frac{c}{a}-1\right)A_0(3)}{A_0}\Delta_1 \tag{6.15}$$

Neglecting the effects of configuration interaction, the relative intensities of the component absorption bands are given by the relative dipole strengths ($\mathcal{D}_0$) of the three transitions, as listed in Table 6.4. Taking the labels 1, 2 and 3 in the derivation above to refer to the $^2E_1^0$, $^2E_1^1$ and $^2E_1$ excited states respectively gives

$$A_0(1) : A_0(2) : A_0(3) = 1 : 3 : 2 \tag{6.16}$$

and so (6.15) can be simplified to

$$\begin{aligned}\Delta_{\text{av}} &= \frac{6+\left(\frac{b}{a}-1\right)3+\left(\frac{c}{a}-1\right)2}{6}\,\Delta_1 \\ &= \frac{1+3\frac{b}{a}+2\frac{c}{a}}{6}\,\Delta_1 \end{aligned} \tag{6.17}$$

In other words, Δ_{av} is the average of the Δs for the individual bands, weighted by their relative absorption intensities.

6.4.6.2 Saturation Effects

Saturation effects have been ignored in deriving the $\mathbf{M}_1/\mathbf{A}_0$ ratios given by (6.7) and (6.14). This is only justifiable if work is carried out within the linear limit; *i.e.* if $\mu_{\text{B}}B \gg kT$. As shown in Section 4.4.5.3, the effective approximation made in assuming the linear limit for $\mathcal{C}$ terms is that

$$\tanh\left(\frac{|\langle \text{A}\alpha\,|L_z+2S_z|\,\text{A}\alpha\rangle|\,\mu_{\text{B}}B}{kT}\right) \simeq \left(\frac{|\langle \text{A}\alpha\,|L_z+2S_z|\,\text{A}\alpha\rangle|\,\mu_{\text{B}}B}{kT}\right) \tag{6.18}$$

where A and α are the ground-state irrep and partner labels. The $\mathbf{M}_1/\mu_{\text{B}}B\mathbf{A}_0$ vs $1/kT$ plots may be corrected for saturation by subtracting the intercept of the line of best fit (due to $\mathcal{A}$ terms) from each point, and adjusting each resulting value by a factor of c_{sat};

$$c_{\text{sat}} = 1+\frac{x-\tanh(x)}{x},\ \text{where } x=\frac{\mu_{\text{B}}B}{kT} \tag{6.19}$$

Since the molecules have Kramers-pair ground states with near-isotropic g values, this correction factor holds for both Z-oriented and randomly oriented samples.

6.4.6.3 Δ_{av} and g_{orb} Values

The values of Δ_{av} and g_{orb} obtained for $LuPc_2$ are given in Table 6.5. Random orientation is assumed for samples in both Ar matrices and films. (Unlike the case of MPc/Ar matrices (Section 4.4.5.4), there is no reason to suggest that $LuPc_2$ molecules will assume a preferential orientation in an Ar matrix, since they are much bulkier than the mono-phthalocyanines, and don't have such a plate-like structure.) $\Delta_{\text{av(sat)}}$ represents values corrected for saturation effects. Note, as discussed in Section 6.3.2, that the g_{orb} values (obtained from the y-intercepts) should be

Table 6.5. Δ and $g_{\rm orb}$ values obtained for $LuPc_2$/Ar and $LuPc_2$/PMMA. Values have been calculated assuming random orientation of the $LuPc_2$ molecules in the host. $\Delta_{\rm sat}$ includes a correction for field saturation, as explained in the text. The moment-analysis range is also given.

Sample	Range	Range (cm^{-1})	$g_{\rm orb}$	$\Delta_{\rm av}$ (cm^{-1})	$\Delta_{\rm av(sat)}$ (cm^{-1})
$LuPc_2$/Ar	Q(0,0) + Q(1,0) + Q(2,0)	14250-17250	8.4 ± 0.2	0.6 ± 0.3	0.8 ± 0.3
	Q(0,0) + Q(1,0)	14350-16400	6.08 ± 0.06	1.0 ± 0.1	1.3 ± 0.1
	Q(0,0)	14350-15900	5.19 ± 0.07	1.1 ± 0.1	1.5 ± 0.1
	Q(3,0)	17250-19100	9 ± 2	12 ± 3	16 ± 4
$LuPc_2$/PMMA	Q(0,0) + Q(1,0) + Q(2,0)	14250-17100	6.21 ± 0.04	1.47 ± 0.08	1.56 ± 0.09
	Q(0,0) + Q(1,0)	14250-16300	4.57 ± 0.05	1.60 ± 0.08	1.79 ± 0.07
	Q(0,0)	14250-15830	3.94 ± 0.05	1.67 ± 0.09	1.87 ± 0.08
	Q(3,0)	17100-19100	3.4 ± 0.3	4.8 ± 0.5	5.4 ± 0.5

treated with caution; their magnitude is observed to be significantly dependent on integration range. However, the Δ_{av} values show much smaller variation.

The $g_{\rm orb}$ value obtained from moment analysis over the Q(0,0) band of $LuPc_2$/Ar is in excellent accord with the value obtained (over the same integration range) by VanCott *et al.*[39] of 5.2 (equal to $2\mathcal{A}_1/\mathcal{D}_0$ by their analysis). It is stated in that paper that $\mathbf{M}_1/\mathbf{A}_0$ for the whole band can be reasonably well approximated by moments taken only over Q(0,0), since the vibrational overtones contain only a few percent of the overall intensity. However, the results shown here in Table 6.5 disprove this assumption, with the $g_{\rm orb}$ values increasing significantly with increasing integration range. Consideration of the expression for $\mathbf{M}_1$ given in (6.9) shows that this is to be expected, since the $(E - \overline{E})$ term will emphasise bands further from the barycentre, even if they are weak.

Since the Q(2,0) band is thought to contain some contribution from a separate transition,[19,39] it would be expected that the Δ and $g_{\rm orb}$ parameters obtained for moments including Q(2,0) and excluding Q(2,0) would be overestimated and underestimated respectively. Thus, after correction for saturation, parameters for $LuPc_2$/Ar of $\Delta_{\rm av}^{\rm Ar} = 1.1 \pm 0.4$ cm^{-1},and $g_{\rm orb}^{\rm Ar} = 7.2 \pm 1.5$ are obtained. For the film, $\Delta_{\rm av}$ values seem to be slightly higher (except for the Q(3,0) band), and $g_{\rm orb}$ values

to be slightly lower ($\Delta_{\rm av}^{\rm PMMA} = 1.7 \pm 0.2$ cm^{-1},and $g_{\rm orb}^{\rm PMMA} = 5.3 \pm 1.0$) but these overlap, within experimental error, with the Ar matrix results.

It can be seen from Table 6.5 that the Q(3,0) band has a significantly different temperature dependence to the rest of the Q band. This provides further evidence for it being due to a separate transition. Note also that it appears that the transition responsible for Q(3,0) is different to the Q′ transition which contributes to Q(2,0), as the latter band shows virtually no temperature dependence.

6.4.7 The Source of $\Delta_{\rm av}$

The (zero-field) Q-band excited-state energy matrix for $LuPc_2$ was determined by employing the effective electronic Hamiltonian

$$\begin{aligned} \mathcal{H}_{\rm el} &= \mathcal{H}_0 + \mathcal{H}_{\rm rep} + \mathcal{H}_{\rm SO} \\ &= -\frac{1}{2}\sum_i \nabla_i^2 - \sum_\alpha \sum_i \frac{Z_\alpha}{r_{i\alpha}} + \sum_j \sum_{i>j} \frac{1}{r_{ij}} + \sum_i \mathbf{s}_i \cdot \mathbf{u}_i \end{aligned} \tag{6.20}$$

as defined in Section 3.3.1. The last two terms represent inter-electron repulsion and SO coupling respectively. This matrix, which may be factored into $E_{7/2}$ and $E_{5/2}$ sub-matrices, is given in Table 6.6. The upper and lower signs represent termination in the $\frac{5}{2}$ and $\frac{7}{2}$ levels respectively.

The matrix elements involving $\mathcal{H}_0 + \mathcal{H}_{\rm rep}$ were expanded using the Condon-Slater rules.[84] Such expansion breaks the expressions down into a mixture of one-electron, Coulomb and exchange integrals, but as can be seen from Table 6.6, these can be simplified to the sum of an average configurational energy (E_{c_1} or E_{c_2}), and various combinations of exchange integrals, $K_{\rm ba}$, $K_{\rm ae}$, and $K_{\rm be}$ where, for example,

$$K_{\rm ae} = \langle {\rm a_2 e_3} \,|\mathcal{H}_{\rm rep}|\, {\rm e_3 a_2} \rangle \equiv \int\int {\rm a_2^*}(1)\, {\rm e_3^*}(2)\, \mathcal{H}_{\rm rep}\, {\rm e_3}(1)\, {\rm a_2}(2)\, d\tau_1\, d\tau_2 \tag{6.21}$$

The SO matrix elements for each of the three transitions are given in Table 6.6 as fractions of Z, which is a measure of the SO coupling for an e electron;

$$Z_{\rm b_1 a_2 e_3} = \sum_k \pm \left\langle 1_{\pm 1} \left| \xi_{\rm e_3}(k) l_z(k) \right| 1_{\pm 1} \right\rangle \tag{6.22}$$

$$Z_{\rm b_1^2 e_1} = \sum_k \pm \left\langle 3_{\pm 1} \left| \xi_{\rm e_1}(k) l_z(k) \right| 3_{\pm 1} \right\rangle \tag{6.23}$$

Table 6.6. The zero-field Hamiltonian matrix for the three Q-band transitions of $LuPc_2$. In each case, the upper sign represents the $E_{5/2}$ level, and the lower sign the $E_{7/2}$ level. As discussed in the text, E_{c_1} and E_{c_2} are common configurational energies, Z represents a one-electron excited-state SO matrix element, and K is an exchange integral.

	$^2E_1$	$^2E_1^0$	$^2E_1^1$	$^4E_1^{S=\frac{1}{2}}$	$^4E_1^{S=\frac{3}{2}}$
$^2E_1$	$E_{c_1} \pm \frac{1}{2}Z$				
$^2E_1^0$		$E_{c_2} + 2K_{ba}$ $\pm\frac{1}{2}Z$	$\frac{\sqrt{3}}{2}(K_{ae} - K_{be})$		
$^2E_1^1$		$\frac{\sqrt{3}}{2}(K_{ae} - K_{be})$	$E_{c_2} + K_{ae} + K_{be}$ $\mp\frac{1}{6}Z$	$\pm\frac{\sqrt{2}}{3}Z$	
$^4E_1^{S=\frac{1}{2}}$			$\pm\frac{\sqrt{2}}{3}Z$	$E_{c_2} - \frac{1}{2}(K_{ae} + K_{be})$ $\pm\frac{1}{6}Z$	
$^4E_1^{S=\frac{3}{2}}$					$E_{c_2} - \frac{1}{2}(K_{ae} + K_{be})$ $\pm\frac{1}{2}Z$

where $l_z(k)$ is the z-component operator for the orbital angular momentum of the electron about nucleus k, $\xi(k)$ is the corresponding SO coupling coefficient, and the sum is carried over all nuclei. Provided $\xi_{e_3}(k)$ and $\xi_{e_1}(k)$ are equal, $Z_{b_1a_2e_3} = Z_{b_1^2e_1}$, as can be shown by decomposing the excited-state wavefunctions into their component Pc MOs, neglecting cross terms between MOs on different rings. However, due to the importance of metal-ligand SO coupling, as discussed below, this is unlikely to be the case.

The diagonal elements of the energy matrix in Table 6.6 contain terms representing first-order SO splittings between the $\frac{5}{2}$ and $\frac{7}{2}$ levels of each of the three Q transitions. In addition, there are off-diagonal SO elements linking the $^2E_1^1$ and $^4E_1^{S=\frac{1}{2}}$ states. Estimation of the energy separation of these states is difficult, since theoretical values for the exchange parameters are not available. However, use of $K_{\pi\pi^*}$ values of 2500 - 3300 cm^{-1} as calculated by Ake and Gouterman[65] for a range of Cu, Co and VO porphyrin derivatives, gives a doublet-quartet energy difference of 7500 - 10000 cm^{-1}. The magnitude of this separation indicates that SO coupling between these doublet and quartet states will be negligible. Thus, the magnitude of

the SO splitting for transitions terminating in the $^2E_1^0$, $^2E_1^1$ and $^2E_1$ excited states should be well approximated by $\Delta = Z_{b_1a_2e_3}$, $-\frac{1}{3}Z_{b_1a_2e_3}$ and $Z_{b_1^2e_1}$ respectively.

6.4.7.1 Moment Expressions Revisited

Now that expressions for the Δ values of the three excited states have been obtained, let us revisit the results of Section 6.4.6.1. Since only the Δ values of the states corresponding to the $b_1a_2e_3$ configuration are related to each other, the overall moment ratio for these two transitions alone will first be considered. From (6.14) it is obtained that

$$\frac{M_1^{\overline{E}}(b_1a_2e_3)}{\mu_B B \mathbf{A}_0(b_1a_2e_3)} = c_o\left(g_{orb} - \frac{\Delta_1}{kT}\left(1 + \frac{-\frac{4}{3}\mathbf{A}_0(2)}{\mathbf{A}_0(b_1a_2e_3)}\right)\right) \tag{6.24}$$

and so taking into account the relative transition intensities given by (6.16),

$$\begin{aligned}\frac{M_1^{\overline{E}}(b_1a_2e_3)}{\mu_B B \mathbf{A}_0(b_1a_2e_3)} &= c_o\left(g_{orb} - \frac{\Delta_1}{kT}\left(1 + \frac{-\frac{4}{3}\times 3}{4}\right)\right) \\ &= c_o g_{orb}\end{aligned} \tag{6.25}$$

In other words, the combination of transition intensities and zero-field splittings of the $^2E_1^0$ and $^2E_1^1$ excited states are such that when integrating over the whole spectral region, there is no net temperature dependence arising from transitions to these states. Because of this cancellation, moment analysis over the Q band can give no information on the zero-field splittings of these two excited states.

The $M_1/\mu_B B\mathbf{A}_0$ ratio over the whole Q band is now obtained by including the transitions to $^2E_1$, *i.e.*

$$\begin{aligned}\frac{M_1^{\overline{E}}}{\mu_B B \mathbf{A}_0} &= \frac{M_1^{\overline{E}}(b_1a_2e_3) + M_1^{\overline{E}}(b_1^2e_1)}{\mu_B B\left(\mathbf{A}_0(b_1a_2e_3) + \mathbf{A}_0(b_1^2e_1)\right)} \\ &= c_o\left(g_{orb} - \frac{1}{3}\frac{\Delta_3}{kT}\right)\end{aligned} \tag{6.26}$$

and so

$$\Delta_{av} = \tfrac{1}{3}\Delta_{b_1^2e_1} = \tfrac{1}{3}Z_{b_1^2e_1} \tag{6.27}$$

6.4.7.2 The Magnitude of Δ_{av}

McClure has shown that SO coupling in planar $\pi(p_z)$ molecules (such as free-base porphyrins) must be weak,[86] and the spatial separation of the two Pc rings in a bisphthalocyanine will preclude any significant inter-ring SO interactions. The presence of a metal in the molecule, however, can introduce a relatively large one-centre contribution arising from π-metal mixing. Symmetry tables[114] show that the e_3 orbital can mix with d_{xz}, d_{yz} and $f_{x(x^2-y^2)}$, $f_{z(x^2-y^2)}$ metal orbitals, and the e_1 orbital with p_x, p_y and f_{xz^2}, f_{yz^2} metal orbitals. The Z values are thus approximated by

$$Z_{b_1a_2e_3} \simeq |c_d|^2 \zeta_d \langle d_{+1} | l_z(Lu^{3+}) | d_{+1} \rangle + |c_{f(e_3)}|^2 \zeta_f \langle f_{+3} | l_z(Lu^{3+}) | f_{+3} \rangle \quad (6.28)$$

$$Z_{b_1^2e_1} \simeq |c_p|^2 \zeta_p \langle p_{+1} | l_z(Lu^{3+}) | p_{+1} \rangle + |c_{f(e_1)}|^2 \zeta_f \langle f_{+3} | l_z(Lu^{3+}) | f_{+3} \rangle \quad (6.29)$$

where c_i is the amplitude of the i-orbital contribution of the metal to the molecular orbital, and ζ_i is the SO coupling constant for a Lu^{3+} i electron.

Determination of the theoretical magnitudes of $Z_{b_1a_2e_3}$ and $Z_{b_1^2e_1}$ requires knowledge of both ζ_i and c_i. The former cannot be easily determined experimentally, since Lu^{3+} has closed electron shells, and so, in isolation, shows *no* SO coupling. However, effective $\zeta(Lu^{3+})$ parameters may be estimated from the trend across the rest of the Ln^{3+} ions, as shown in Figure 6.15. The ζ_{4f} values shown in this figure were obtained from Dieke,[115] and the ζ_{5d} and ζ_{6p} values from Wybourne.[116] By extrapolation of these series, Lu^{3+} parameters of $\zeta_{4f} \simeq 3100$ cm^{-1}, $\zeta_{5d} \simeq 1300$ cm^{-1}, and $\zeta_{6p} \simeq 4400$ cm^{-1} are obtained. However, the estimate of ζ_{5d} may be low, since, as pointed out by Wybourne,[116] the $f^{13}d$ configuration of Yb^{3+} may constitute a special case.

Note that values of ζ_p and ζ_d given above are actually for the lowest *unoccupied* metal orbitals, whereas it is the filled 4d and 5p orbitals which are likely to interact with the ligand. It can be shown[117] that

$$\zeta \propto \frac{Z_{eff}^4}{n^3} \quad (6.30)$$

where n is the principal quantum number, and Z_{eff} is the effective nuclear charge of the metal. Assuming that the difference between Z_{eff} for the 4d and 5d, and the 5p and 6p orbitals (dependent on the degree of shielding) is relatively small, approximate lower estimates for the required parameters are

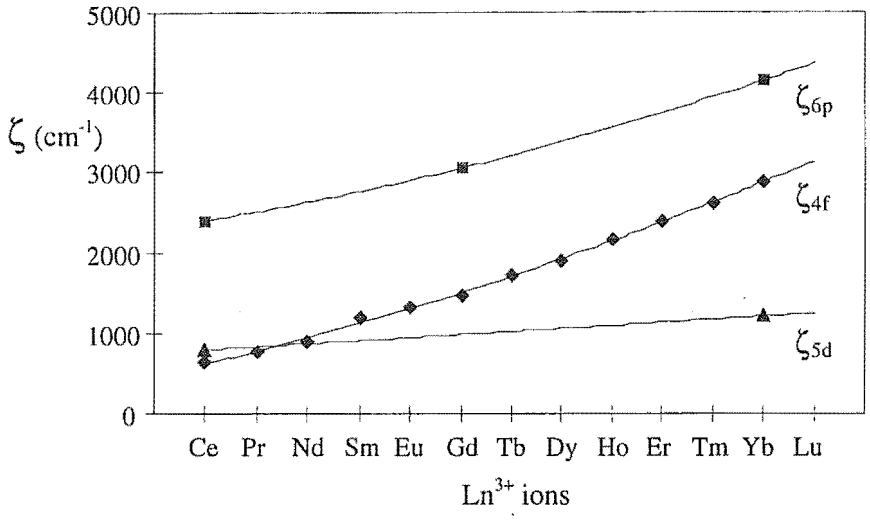

Figure 6.15. The variation in ζ values across the lanthanide 3+ ions. Curves have been fitted to the experimentally determined values,[115,116] and extrapolated to Lu^{3+}.

$$\zeta_{4d} \gtrsim 2\zeta_{5d} \simeq 2600 \text{ cm}^{-1} \tag{6.31}$$

$$\zeta_{5p} \gtrsim 2\zeta_{6p} \simeq 9000 \text{ cm}^{-1} \tag{6.32}$$

The only $LuPc_2$ calculation mentioning π-metal overlap is that of Rousseau *et al.*[111] Unfortunately, they do not list the mixing coefficients for each molecular orbital, only stating that the b_1 and a_2 HOMO orbitals have no metal character, and that the e_3 LUMO has 'insignificant' overlap with metal d orbitals. No mention is made of the e_1 second LUMO. They also state that lower occupied e_3 and e_1 orbitals (shown in Figure 6.13) have weak overlap with metal d and p orbitals respectively. The metal f electrons are not considered, due to the high degree of contraction.

Even with complete neglect of any f-orbital overlap, explanation of the observed $\Delta_{av} = \frac{1}{3}Z_{b_1^2e_1} = 1.5 \text{ cm}^{-1}$ by (6.29) requires only that $|c_p|^2 \lesssim 5 \times 10^{-4}$, *i.e.*, that the required Lu^{3+} 5p orbital contribution to the e_1 molecular orbital has a maximum value of only 0.05%. This seems entirely possible.

6.4.8 Assignment of the RV Band

As stated in Section 6.4.1, literature reports give conflicting assignments of transitions to the RV band. The results of the temperature-dependence studies reported here provide a useful basis for comparison of these assignments.

Consider first the proposal of Rousseau *et al.*,[111] that the RV band arises from the same excitation as the intervalence band, namely $b_1 \rightarrow a_2$. In this case, the excited state would be orbitally non-degenerate ($^2B_1$), and so could have no spin-orbit splitting. This is clearly not in accordance with our MCD temperature-dependence results.

The assignment of the RV band to the excitation of an electron from a lower-lying e_1 orbital to the half-filled a_2 HOMO (Markovitsi *et al.*[104]) gives a transition of type $^2A_2 \rightarrow {}^2E_1$, which is fully allowed and of the same symmetry as the Q-band transition. But since the e_1 orbital is not the same as that involved in the Q-band excited-state configuration, the Z values of these transitions need not be the same. In fact, Rousseau *et al.*[111] predict that this lower e_1 molecular orbital will have appreciable overlap with Lu^{3+} p orbitals, which would explain the increased temperature dependence of the RV band relative to the Q band. Moreover, monophthalocyanine cation radicals also show a weak band to the red of the Q band, which has been assigned by Minor *et al.*[118] to an excitation analogous to that proposed here, namely $e_g \rightarrow a_{1u}$ (in D_{4h}, see Figure 6.13). It must be noted, however, that the $LuPc_2$ calculations of both Orti *et al.*[108] and Rousseau *et al.*[111] find the energy of the $e_1 \rightarrow a_2$ excitation to be greater than that of the Q band excitations, (ascribing it to the BV band, ~460 nm).

Orti *et al.*[108] and VanCott *et al.*[39] assign the RV band to the excitation $a_2 \rightarrow e_3$. This transition has symmetry $^2A_2 \rightarrow {}^2E_3$, which is formally forbidden in D_{4h}. However, as pointed out by VanCott *et al.*,[39] vibronic overtones of symmetry B_1, B_2 or E_2 will be allowed, since the direct product of each of these symmetries with E_3 contains E_1, and $^2A_2 \rightarrow {}^2E_1$ is allowed. The results given in Section 6.3.2.2 indicate that the temperature *independent* part of the band is a positive $\mathcal{A}$ term (as seen at high temperatures), which is swamped at lower temperatures by opposing temperature-dependent $\mathcal{C}$ terms. This is consistent with the activating vibration having b_1 or b_2 symmetry. Note that VanCott *et al.*[39] were not aware of this temperature dependence, and so explained the negative-$\mathcal{A}$-term appearance of $LuPc_2$/Ar at $\sim$ 7 K as arising from an Jahn-Teller-active vibration of e_2 symmetry. (JT activity reverses the sign of the MCD.)

The weak absorption intensity observed for the RV band (1/22 of the Q band) is consistent with its assignment as a vibronically activated forbidden transition. In this case the absorption intensity would be expected to show temperature dependence,[119] with

$$\mathbf{A}_0 = \mathbf{A}_{0(T=0)} \left(1 + e^{-h\nu/kT}\right) \tag{6.33}$$

where $\mathbf{A}_{0(T=0)}$ is the zeroth absorption moment at 0 K and $h\nu$ is the energy (in cm^{-1}) of the activating vibration. Such temperature dependence has not been observed here (between 1.4 and 65 K), however since for $h\nu > 200$ cm^{-1}, the change in absorption intensity between 0 and 65 K is expected to be $< 1\%$, this is perhaps not surprising. (The intensity change increases to $\sim$10% for $h\nu = 100$ cm^{-1}).

It is interesting to note that the skewed-$\mathcal{A}$-term shape in the MCD of the main RV band (Figure 6.11) and the negative single-signed feature corresponding to the absorption band to the blue of this (at low temperatures) have a similar appearance to an 'upside down' version of the Q(0,0) and first-overtone bands of ZnOEP.[16] In the latter case, these features are ascribed to a lowering of the excited state degeneracy by a combination of JT and crystal field effects. The similarity between the general shapes of these two spectra (with the negative sign of the RV band at low temperatures arising from $\mathcal{C}$-term contributions not present in the even-electron Zn molecule) seems to suggest that the RV band of $LuPc_2$ could reasonably be considered as consisting of an origin band, RV(0,0) and two overtone bands, RV(1,0) and RV(2,0), analogous to the Q labels (where origin and the first overtone are not well resolved in Figure 6.11). Such an description is consistent with the assignment of Markovitsi *et al.*[104], but not with that of Orti *et al.*[108] and VanCott *et al.*[39]

From the results presented here, it is not possible to make a definitive assignment of the RV band. However, for either of the two proposals discussed above, the overall symmetry of the transition is the same as that of the Q transitions (*i.e.* $^2A_2 \rightarrow {}^2E_1$), and so the same moment equation, (6.7), may be applied. This yields values of $\Delta_{RV}^{Ar} = 68 \pm 9$ cm^{-1}, $\Delta_{RV}^{PMMA} = 63 \pm 3$ cm^{-1}, $g_{orb(RV)}^{Ar} = 14 \pm 6$, and $g_{orb(RV)}^{PMMA} = 8 \pm 2$, assuming random molecular orientation. Such zero-field splitting would require, in the case of the proposed fully-allowed transition (Markovitsi *et al.*[104]), a contribution to the lower, filled e_1 MO of $|c_p|^2 \lesssim 0.7\%$ 5p metal orbital.

In the case of the vibrationally activated forbidden transition (VanCott *et al.*[39]), the e_3 orbital would require a $|c_d|^2 \lesssim 3\%$ contribution from the Lu^{3+} 4d orbitals. (Note that although the e_3 orbital in which the proposed RV excitation terminates is the same as that for one of the Q-band excitations, this is not negated by the very different Δ values observed for these two bands, since it was shown in Section 6.4.7.1 that moment analysis of the Q band gives no information on the zero-field splitting of the states corresponding to this excitation.)

6.5 Conclusion

Absorption and MCD spectra of the Q and RV bands of $LuPc_2$/Ar and $LuPc_2$/PMMA, have been measured over a range of temperatures. It has been found that the appearances of $LuPc_2$/Ar Q-band absorption and MCD spectra are highly dependent on the degree of annealing of the matrix, with bands broadening and red-shifting, and intensity redistributed between sites with increased annealing. Importantly, however, the $\mathbf{M}_1/\mathbf{A}_0$ moment ratio is invariant to such annealing effects, and so the parameters derived from the variable-temperature data are not dependent on the state of the matrix.

Q-band spectra of both the matrix and the film show weak MCD temperature dependence, with band intensity decreasing with decreasing temperature. The temperature dependence arises because of first-order spin-orbit splitting of the $^2E_1$ excited states in which each of the three allowed transitions terminate. This splitting has been quantified by use of moment analysis, with $\Delta_{av} = 1.5 \pm 0.5$ cm^{-1}. To first order, the temperature-dependence contributions to $\mathbf{M}_1/\mu_B B\mathbf{A}_0$ from the $^2E_1^0$ and $^2E_1^1$ excited states cancel, and so no information can be obtained on the magnitude of the zero-field splitting of these states. This gives, for the $^2E_1$ excited state, $\Delta_{b_1^2e_1} = 4.5 \pm 1.5$ cm^{-1}, the magnitude of which can be explained by $\lesssim 0.05\%$ Lu^{3+} 5p orbital character in the e_1 molecular orbital. The Q(3,0) band gave significantly higher Δ values, confirming its assignment to a separate (unassigned) transition.

The temperature dependence of the RV band was found to be much stronger than that of the Q band. The MCD appears as a negative (skewed) $\mathcal{A}$ term at low ($\lesssim 10$ K) temperatures, changing sign as the temperature increases. The presence of such temperature dependence indicates that the transition responsible for the RV

band must terminate in an orbitally degenerate excited state. Two such assignments have been proposed in the literature, both of which have overall symmetry $^2A_2 \rightarrow {}^2E_1$. The data presented here does not allow for definitive assignment of this band, however, in either case moment analysis gives $\Delta = 65 \pm 10$ cm^{-1} and $g_{orb} = 10 \pm 6$. The very much larger spin-orbit splitting of this band (relative to the Q band) is ascribed to a larger metal contribution to either the e_3 (LUMO) orbital or the lower, filled e_1 orbital, depending on the transition responsible. Assignment of the RV band would be aided by further theoretical calculations (explicitly considering metal contributions), measurement of absorption temperature dependence over a wider temperature range, and, possibly, investigation of the (MCD and absorption) temperature dependence of the BV band.

Chapter 7

Spectral Hole Burning of Metallophthalocyanines

7.1 Introduction

Spectral hole-burning is a technique that employs photochemistry and/or photophysics for spectroscopic investigation of species doped into glasses, polymers, matrices and crystals. These materials are collectively known as host-guest systems; the guest being the molecule of spectroscopic interest, and the host the material in which it is embedded. Hole burning allows probing of spectral features otherwise hidden within the inhomogeneously broadened bands characteristic of such systems. As well as providing information of scientific interest, it also has technological applications, primarily in the field of optical information-storage systems. The term 'hole burning' was first used in 1948 by Bloembergen *et al.*[120] in reference to a nuclear magnetic resonance experiment. With the invention of the laser in 1958, hole burning at optical wavelengths became possible, although it was not until the mid 1970s that such measurements were made.[121–123] For a more detailed description of the applications and literature of hole burning the reader is referred to a number of reviews,[124–128] in particular the monograph edited by Moerner.[129]

In a 'perfect' host medium, all absorbing guest centres would have exactly the same local environment, and the resulting absorption bandwidth would thus be due solely to excited-state lifetimes. The linewidth of such a spectral feature is known as the homogeneous linewidth, and varies (from 10 - 10^{-4}cm^{-1}) with temperature and the strength of electron-phonon coupling (discussed later). In reality, no medium is perfect, and inhomogeneous broadening will occur due to strain, impurities and/or imperfections in the host material, which cause each guest absorber to experience a slightly different environment. Inhomogeneous bandwidths vary from a few cm^{-1} in a crystal, to hundreds or thousands of cm^{-1} for less-ordered hosts such as polymers or glasses. For the MPc/Ar matrices discussed in this chapter, inhomogeneous bandwidths are on the order of 300-400 cm^{-1}.

In hole-burning spectroscopy, the host-guest system of interest is first acted upon by a laser beam of narrow spectral linewidth. The species that absorb at the laser wavelength are excited, and some of these then decay to a new ground state with a different energy. The absorption or excitation spectrum of the system is then measured using a lower-intensity light source. The spectrum produced will be similar to the normal, inhomogeneously broadened absorption spectrum, except that the absorbance near the burn wavelength will be decreased, due to the reduced number of molecules with the appropriate energy levels. The region of decreased absorption is referred to as the 'hole'. Conventionally, the hole spectrum is displayed as the difference between the post-burn and pre-burn absorbance; $\delta A = A_{\text{post}} - A_{\text{pre}}$.

The type of hole burning described above is known as persistent spectral hole burning, as holes will last almost indefinitely, provided a sufficiently low temperature is maintained. (In transient spectral hole burning, the 'burnt' molecules do not decay to a different ground state, and hole spectra must be measured within the lifetime of the excited state.) Persistent spectral hole burning may be categorised into two types, depending on the mechanism by which the alternate ground state is reached. In photochemical hole burning (PHB) the molecules excited by the laser undergo some photochemical change. The resulting product is usually sufficiently different from the starting material for its absorption spectrum to be well separated from that of the original absorption. A well-studied example of reversible PHB is proton transfer in H_2Pc and H_2P.[123,130] Other mechanisms are photoionisation and subsequent electron trapping,[131] and hydrogen-bond rearrangement[132] within the guest, or between the guest and the host. PHB may also be irreversible, for example the photodecomposition of dimethyl-s-tetrazine.[133,134]

Non-photochemical hole burning (NPHB) usually requires a photophysical change in the local environment, or reorientation of the guest relative to the host. In such cases, the product absorption is only slightly shifted from the original absorption, and may appear as areas of increased absorption immediately adjacent to the hole - these are known as photoproduct antiholes. Examples of NPHB mechanisms are hydrogen-bond rearrangement within the host, as seen for pentacene in benzoic acid crystals,[135] and transitions between host two-level-systems (TLS, see Section 7.1.2.1)[122,136] in disordered solids such asglasses and polymers.

7.1.1 Hole Burning of Matrix-Isolated Porphyrins and Pcs

Although a range of metallo- and free-base porphyrins and phthalocyanines have been used for hole-burning spectroscopy,[129] especially as systems suitable for optical information storage,[137] very few studies have been carried out on these molecules in rare-gas matrices. The literature reports of Pcs in Ar consist of investigations of H_2Pc by Geissinger and Haarer,[138–141] and studies of H_2P[142] and SiPc derivatives.[143] One reason for the limited number of studies is the apparent incompatibility between matrix-isolation and hole-burning experimental techniques, primarily due to the fact that matrices must be deposited in a vacuum, while hole-burning studies are best carried out below 2 K, with the sample immersed in *l*He. This difficulty was overcome by use of the matrix-injection system described in Chapter 2.

MCD is the main spectroscopic technique used in work detailed in this thesis. It allows indirect investigation of relatively weak perturbations even in the presence of very broad bands, *e.g.* determination of effective excited-state Zeeman shifts, vibronic effects and second-order SO coupling. However, the parameters thus obtained represent weighted averages over an inhomogeneous distribution of chromophores. Since hole burning provides a means of directly probing discrete (or a narrow distribution of) sites within an inhomogeneously broadened band, it was thought this technique could be used to obtain information about individual splittings and shifts. In order to investigate magnetic (Zeeman and SO) effects, experiments were designed and carried out in which a magnetic field was applied after holes had been burned; facilitating the measurement of the MCD of spectral holes (hereafter called hole-MCD). Such spectra have not been previously reported. Unfortunately, the hole-absorption and hole-MCD spectra obtained turned out to be far more complicated than expected, and quantitative analysis was not possible. However a qualitative investigation of these and other unforeseen hole-burning phenomena has been carried out.

The data presented here provide the first report of hole burning of transition-metal phthalocyanines in Ar matrices, and also of the first hole-MCD spectra in any medium. The experiments were carried out at the Research School of Chemistry, ANU, over a hectic two-week period in June, 1995. After analysis of the obtained

spectra it was found that repetition of some aspects of these experiments would have been desirable, in order that more definite conclusions could be reached. However, due to financial and temporal constraints, this has not been possible. Nonetheless, the preliminary data presented here both show that hole burning is possible for MPcs in rare-gas matrices, and present an overview of the interesting phenomena observed when hole-burning is combined with MCD.

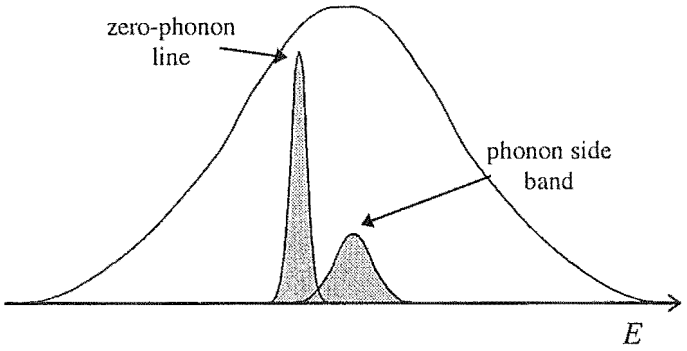

Figure 7.1. A homogeneous line shape (shaded), shown within an inhomogeneously broadened band.

7.1.2 Hole Shape

Figure 7.1 shows one of the homogeneous lineshapes making up an inhomogeneously broadened band. The homogeneous feature consists of two parts - a sharp, intense zero-phonon line, and a less intense, broader phonon side band to higher energy. The latter is due to coupling between the electronic transition of the guest and the lattice modes (phonons) of the host. Phonon states typically have energies 10 - 100 cm^{-1} above the electronic energy level. For a truly homogeneous system, the greater breadth of the phonon side band is strictly due to the reduced lifetime of the phonon states, which can rapidly decay to the zero-phonon state. However, in real systems, several (or many) sites may have the same zero-phonon line, but the phonon states of each will not be so well correlated, leading to a broader overall phonon side band.

One might at first expect that a hole would have a lineshape similar to the homogeneous feature, but in fact it is somewhat more complicated, as can be seen by considering Figure 7.2. Excitation at E_{burn}, the frequency of the zero-phonon line

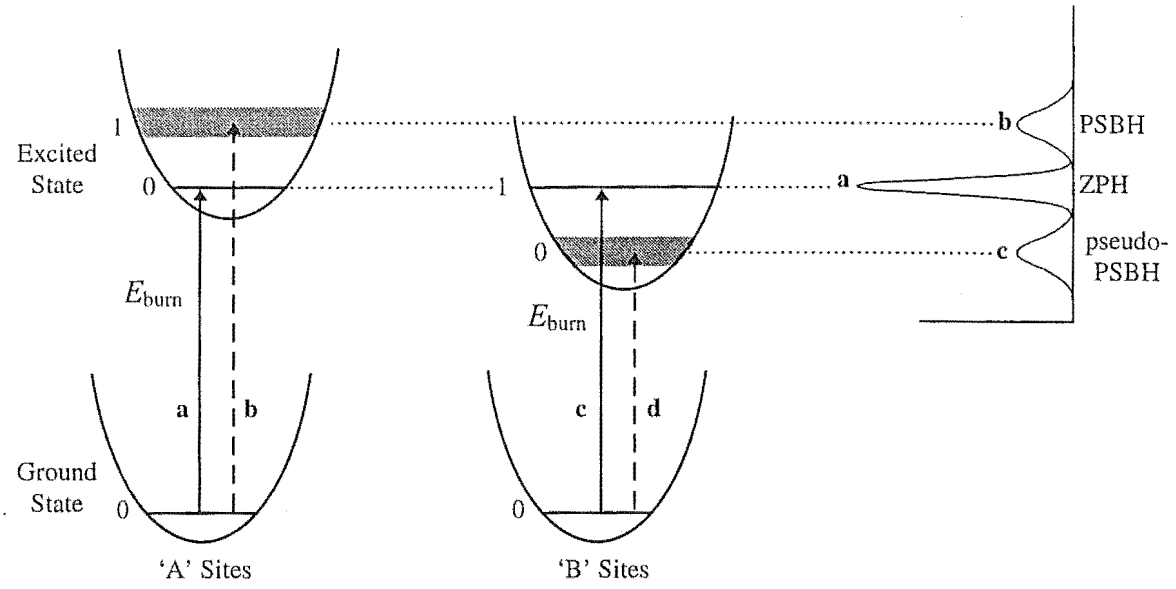

Figure 7.2. The features contributing to the line shape of a hole, from two types of sites; A and B. For A sites, transition **a** contributes to the ZPH while **b** gives the PSBH. For B sites, the phonon side-band transition (**c**) contributes to the 'ZPH', and the zero phonon line (d) produces the pseudo-PSBH. The relative widths of the zero- and one-phonon levels indicates the effect of correlation between the different discrete sites comprising the A or B ensembles.

of 'A' sites, will cause not only the formation of a zero-phonon hole (ZPH) and a phonon side-band hole (PSBH), but also a hole on the lower-energy side of the ZPH, known as a pseudo-phonon side-band hole (pseudo-PSBH). This feature is due to sites (such as the 'B' sites in Figure 7.2), which have a zero-phonon line at energies lower than E_{burn}, but which absorb the incident radiation through their phonon side band. Thus the band referred to as the ZPH also contains a small contribution arising from burning into phonon side bands. The relative widths of the zero- and one-phonon levels shown in Figure 7.2 indicate the effects of lack of correlation of phonon energies, arising from the fact that A and B sites actually comprise a set of sites, overlapping at the burn energy.

7.1.2.1 ZPH Linewidth

The linewidth of a homogeneous feature is

$$\begin{aligned} \Gamma_{\mathrm{hom}} &= \frac{1}{\pi c T_2} \\ &= \frac{1}{2\pi c T_1} + \frac{1}{\pi c T_2^*} \end{aligned} \tag{7.1}$$

where τ_2 is the overall coherence time, τ_1 is the lifetime, and τ_2^* is the phase relaxation (or pure dephasing) time, of the excited state. τ_2^* is due to thermally induced fluctuations of the excited-state energy, caused principally by phonon scattering. τ_1 is made up of both radiative and non-radiative components. The former has negligible temperature dependence, while, at *l*He temperatures, the latter is usually either absent or has a constant value. In contrast, the temperature dependence of the dephasing time, τ_2^* is significant, and increases with temperature. For molecules doped into crystalline hosts, it has been found that at 2 K, Γ_{hom} is due solely to the energy relaxation time, τ_1.[126] However, in disordered hosts such as glasses and Ar matrices, the temperature dependence of Γ_{hom} is quite different; in particular, τ_2^* still makes a considerable contribution to Γ_{hom} at 2 K. This difference has been explained by the concept of two-level systems (TLSs).[144]

TLSs are the near-isoenergetic configurations adopted by groups of host molecules in disordered solids, which may couple to guest molecules by means of electron-phonon coupling. Interconversion of TLSs is facilitated by hole burning, as the barriers to interconversion of the guest-coupled TLSs are reduced when the guest molecule is in its excited state. This is shown in Figure 7.3 where photoexcitation

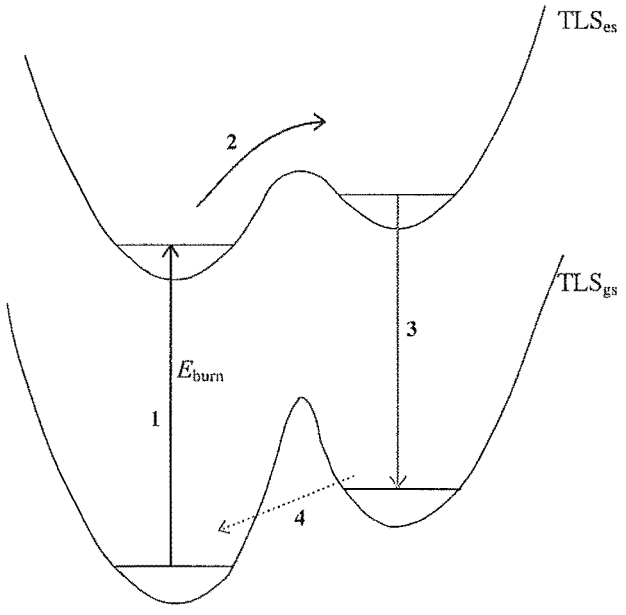

Figure 7.3. Potential-energy curves for a two-level system (TLS) coupled to a guest. The ground (gs) and excited states (es) are shown. The numbered steps are explained in the text.

at the burn energy (**1**) is followed by interconversion (**2**) and subsequent decay (**3**) to the new metastable ground state, with shifted absorption. Because TLSs provide a high density of low-energy states, 'freezing out' of the τ_2^* contribution of Γ_{hom} will occur at lower temperatures than in crystals.

At a minimum, the width of a ZPH is $2\Gamma_{\text{hom}}$. (The factor of two is due to the fact that excitation at a certain wavelength will burn into not just one, but rather a distribution of zero-phonon lines, each of which has some intensity at the burn wavelength.) There are two main factors that will cause this width to increase. Firstly, in disordered hosts, spectral diffusion will cause the hole to broaden as a function of the time elapsed since burning.[145] This is due to very low energy rearrangements of the host, which can be understood in terms of tunnelling between TLS ground states, of the type shown as (4) in Figure 7.3. Note, however, that this process does not involve the burnt molecules themselves (which may have their absorption energy shifted considerably), but rather molecules which absorb close to the burn energy. (The diffusion process is analogous to that which occurs when a hole is dug in sand, with numerous small movements of the sand particles causing the hole to become shallower and broader.) Secondly, there is a contribution to the ZPH from molecules absorbing through their phonon side band (transition **c** in Figure 7.2). The relative intensity of this contribution to the ZPH will increase with increasing burn fluence (total burn energy per sample area, J cm^{-2}), in concert with the relative intensity of the pseudo-PSBH, and so cause a broadening of the hole beyond $2\Gamma_{\text{hom}}$.

7.1.2.2 Vibrational Side-Band Holes

Figure 7.4 shows an example of PHB in the origin, or (0,0), band of a guest chromophore with two vibrations (labelled α and β), which give rise to overtone bands in the electronic absorption spectrum. The photoproduct absorption is well removed from the region of the original absorption band and consequently the photoproduct antiholes are not observed. Since the sites that contribute to the origin-band hole also contribute to the (1_α,0) and (1_β,0) vibrational bands, holes will also appear in these overtones - these are known as vibrational side-band holes (VSBHs). If, on the other hand, the hole is burnt in one of the vibrational bands, as shown in Figure 7.5, pseudo-vibrational side-band holes (pseudo-VSBHs) are generated in the origin band. This is shown in the insert, where the transitions coincident with the burn energy are (1_α,0) for site A and (1_β,0) for site B.

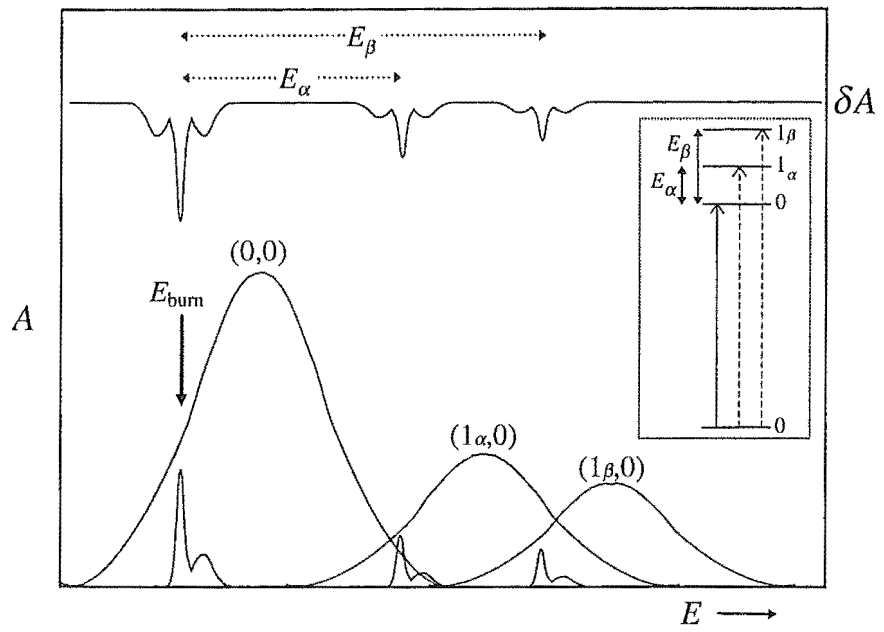

Figure 7.4. The result of (photochemical) hole burning at E_{burn} into the (0,0) origin band of a species with two vibrational overtone bands, $(1_\alpha,0)$ and $(1_\beta,0)$. Absorption (A) and hole (δA) spectra are shown. The insert shows the corresponding energy-level diagram. Figure adapted from Raja *et al.*[146]

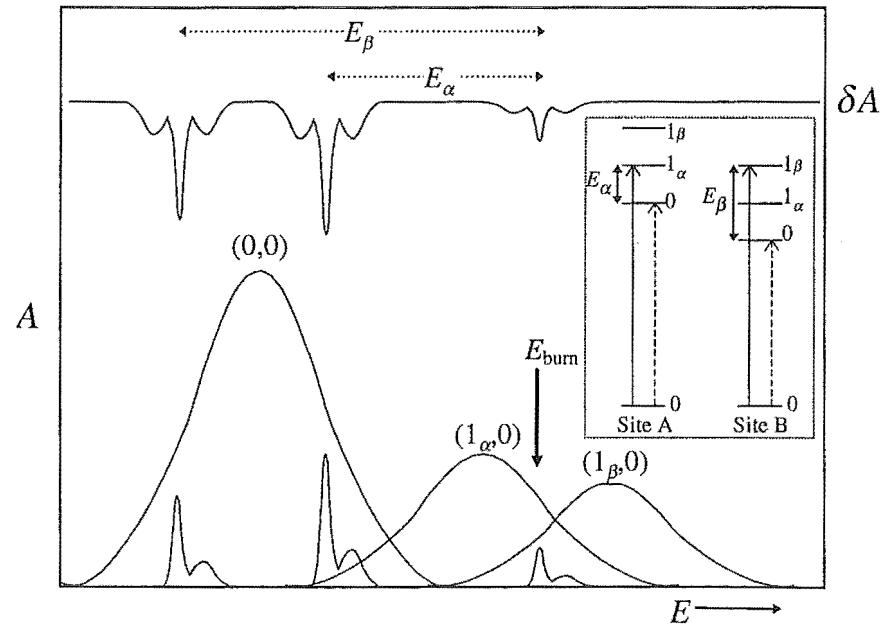

Figure 7.5. The result of hole burning at E_{burn} into the vibrational bands of a species with two overtones, $(1_\alpha,0)$ and $(1_\beta,0)$. Absorption (A) and hole (δA) spectra are shown. The insert shows the corresponding energy-level diagram. Figure adapted from Raja *et al.*[146]

7.1.2.3 Photoproduct Antiholes

In the case of NPHB, the situation is further complicated by the presence of photoproduct antiholes in the same spectral region as the holes, making analysis of the hole shape more difficult. The antihole bands are broad, and, in the case of $\pi \rightarrow \pi^*$ transitions in polyatomic molecules, have invariably been found to lie predominantly to the high-energy side of the ZPH,[147] overlaying the PSBH. Overall, the positive and negative areas of the hole spectrum should cancel. (The latter is not necessarily so for PHB, as the photoproduct may be a different chemical species with different transition intensities.)

7.1.2.4 Simulated Hole Shapes

The hole shapes shown in Figures 7.4 and 7.5 are idealised. In reality the ratios of the ZPH, PSBH and pseudo–PSBH are dependent on a number of factors, including the burn time, the position of the burn within the inhomogeneously broadened band, and the strength of the electron-phonon coupling. A QuickBASIC program, HOLES.BAS, was written to investigate the effect of these variables – the relevant code is given in Appendix IV.

In this program, calculation of the pre- and post-burn band shapes is carried out according to the equations of Lee *et al.*[148] The inhomogeneous band is built up from a large number of evenly spaced single-site profiles adjusted in intensity so as to give a roughly Gaussian bandshape overall. Each single-site profile consists of a zero-phonon line and a series of phonon side bands, all assumed to have a Lorentzian lineshape given by

$$l\left(E - E_{\max}\right) = \frac{\Delta}{2\pi\left(\left(E - E_{\max}\right)^2 + \frac{1}{4}\Delta^2\right)} \tag{7.2}$$

where Δ is the full-width at half-maximum (FWHM), and $E_{\max}$ is the band maximum. The single-site profile is given by

$$L\left(E - E_{\mathrm{ZPL}}\right) = \sum_{r=0}^{\infty} \frac{S^r e^{-S}}{r!}\, l_r\left(E - E_{\mathrm{ZPL}} - rE_{\mathrm{phonon}}\right) \tag{7.3}$$

where E_{ZPL} is the energy of the zero-phonon line, E_{phonon} is the average energy separation of the phonon states and $r = 0, 1, 2, \ldots$ represents the number of quanta of phonons in the excited state. (The sum is truncated at $r = 6$ in the following

simulations.) The relative intensities of the component Lorentzians are determined by the coefficient of l_r; the phonon Franck-Condon factor. S is the Huang-Rhys factor, which measures the displacement of the excited-state potential-energy curve with respect to the ground state, and is related to the Debye-Waller factor (the intensity of the zero-phonon line relative to the total intensity of the single-site band).[124] Values of $S \leq 1$ represent weak electron-phonon coupling.[148] The higher the value of S, the more significant the contribution from the phonon side bands.

The post-burn spectrum is calculated by determining the contribution of each single-site Lorentzian to the absorption intensity at the burn wavelength (E_{burn}), and then reducing the intensity of these Lorentzians by a factor f,

$$f = \exp\left[-\sigma I \Phi t \, L\left(E_{\text{burn}} - E_{\text{ZPL}}\right)\right] \tag{7.4}$$

where σ is the absorption cross-section per molecule, I is the intensity of the laser beam, Φ is the hole-burning quantum yield and t is the burn time. In this manner, pseudo-PSBH contributions are taken into account. No attempt has been made to simulate photoproduct antiholes.

Figure 7.6 shows three simulated hole spectra, the burn energy respectively occurring at the centre, to the red, and to the blue of an inhomogeneously broadened band with FWHM of $\Delta_{\text{inhom}} = 400$ cm^{-1}. (Note that this band does not have a true Gaussian band shape, as phonon side-band contributions cause skewing toward higher energy.) The parameters of the spectra have been chosen to imitate the ZnPc absorption-hole spectra shown later (Figure 7.10). The zero-phonon line is relatively narrow ($\Delta_{\text{ZPL}} = 5$ cm^{-1}) and both the phonon line-width and the phonon energy are large ($\Delta_{\text{1-phonon}} = 150$ cm^{-1}, $E_{\text{phonon}} = 200$ cm^{-1}). Weak electron-phonon coupling is assumed, with $S = 1$. The variables σ, I, Φ and t are not considered individually; instead $\sigma I \Phi$ is treated as a constant, and t given in arbitrary units.

Note that the relative intensity of the pseudo-PSBH depends on the position of the hole in the inhomogeneously broadened band, and grows as the burn wavelength moves to higher energy. As stated above, the pseudo-PSBH is due to molecules with zero-phonon lines to the red of the burn wavelength, which absorb through their phonon side band. Fewer of these sites will exist on the red side of the

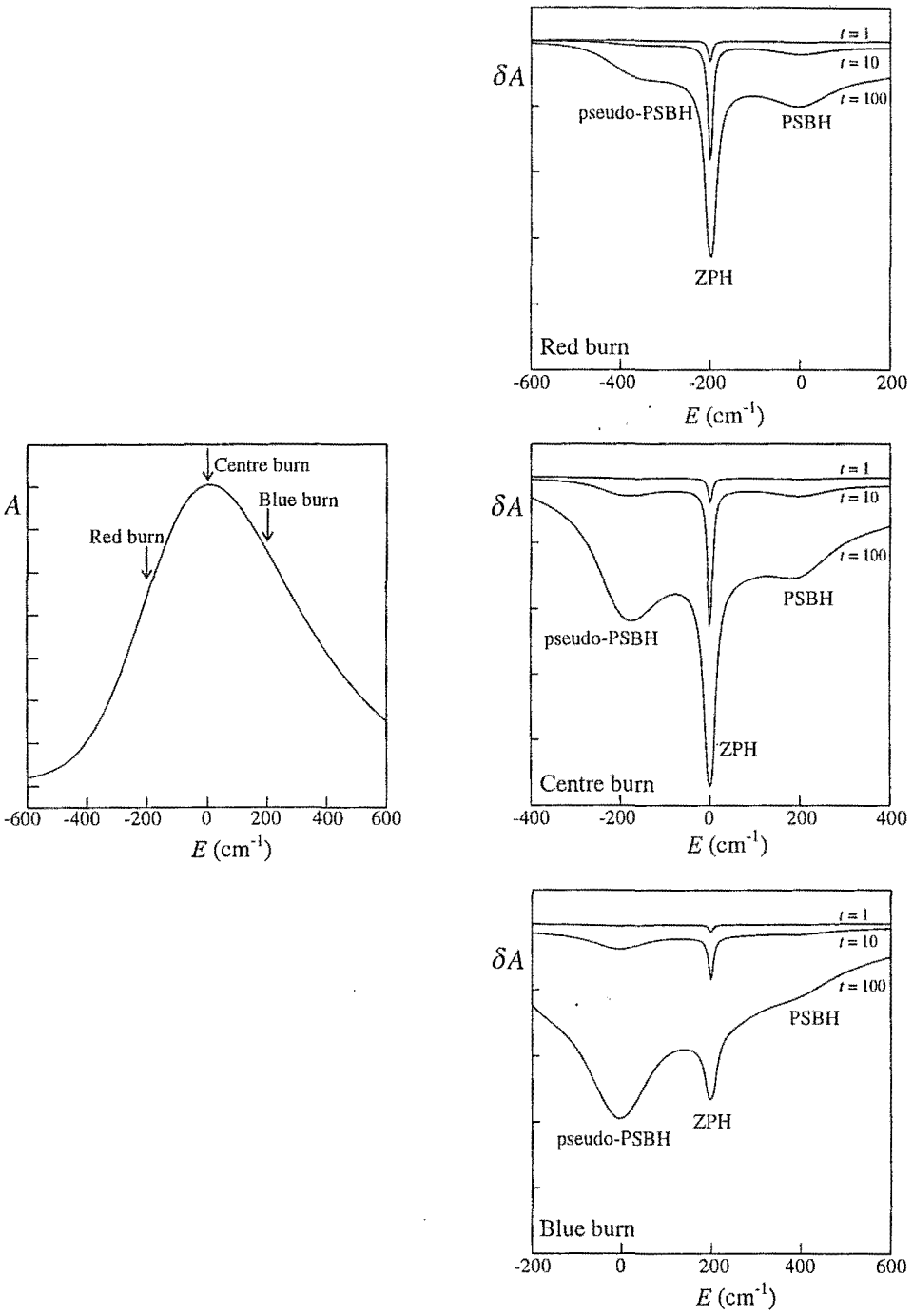

Figure 7.6. Simulated hole shapes for burns at -200 cm^{-1}, 0 cm^{-1}, and 200 cm^{-1} into an inhomogeneously broadened band ($\Delta_{\text{inhom}} = 400\ cm^{-1}$) centred at 0 cm^{-1}. Burn times are relative only. The single-site parameters are $\Delta_{\text{ZPL}} = 3\ cm^{-1}$, $\Delta_{\text{1-phonon}} = 150\ cm^{-1}$, $E_{\text{phonon}} = 200\ cm^{-1}$, $S = 1$. The ordinate scale interval is the same in all plots.

absorption band than on the blue, and hence the intensity of the pseudo-PSBH will vary accordingly.

The relative intensity of the pseudo-PSBH also grows with increasing burn time. After a certain period all molecules with zero-phonon lines at the burn wavelength will have been burnt, and subsequently, the ZPH and PSBH will cease to grow. This is known as saturation. However, the pseudo-PSBH will continue to increase, as it corresponds to burning into the broader phonon side band for which many sites overlap with the burn energy. This leads to asymmetric hole shapes at long burn times. The growth of the pseudo-PSBH occurs in concert with an apparent increase of the bandwidth of the ZPH, as can be seen in Figure 7.6. This is due to the increasing importance of the phonon side-band contribution to the ZPH.

Figure 7.7 shows the case where the zero-phonon line is relatively broad, and the phonon energy is small. The parameters of the spectra are $\Delta_{\mathrm{ZPL}} = 15$ cm^{-1}, $\Delta_{\text{1-phonon}} = 100$ cm^{-1}, $E_{\text{phonon}} = 20$ cm^{-1} and $S = 1$ (similar to those obtained by fitting the CuPc/Ar absorption-hole spectra of Figure 7.8). In this case, the ZPH, PSBH and pseudo-PSBH coalesce to give a single apparent hole which broadens rapidly. At longer burn times the asymmetry of the hole due to the pseudo-PSBH becomes more evident. Note, however, that for such small values of E_{phonon} the true phonon side bands will be highly asymmetric, and hence the model used here, which approximates these phonon side bands as Lorentzians, will not provide a particularly accurate representation of hole spectra.

7.2 Experimental Details

Hole-absorption and hole-MCD spectra have been measured for CuPc/Ar, ZnPc/Ar and $LuPc_2$/Ar. Matrix deposition times were typically 10 - 20 min, with sublimation temperatures of ~275 °C for ZnPc and CuPc and ~330 °C for $LuPc_2$. A number of spectral and experimental parameters relating to each of the samples discussed in this chapter are listed in Table 7.1. In general, holes were burnt at ~1.6 K and 0 T, in samples immersed in *l*He. However some (absorption) spectra were also recorded for holes burnt in samples held in a vacuum and cooled by conduction through the metallic sample holder. The latter method resulted in both higher

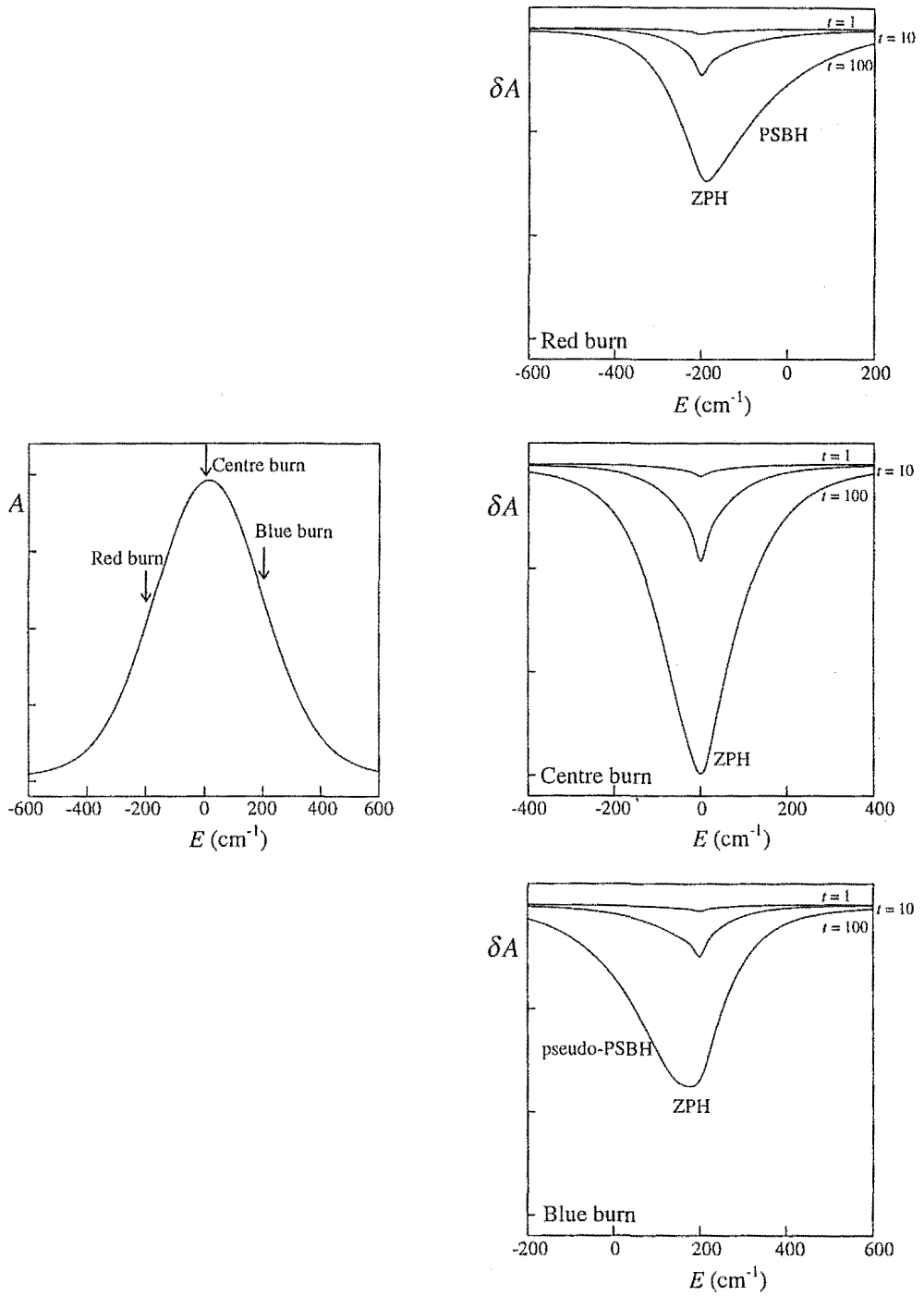

Figure 7.7. Simulated hole shapes for burns into the centre of an inhomogeneously broadened band ($\Delta_{\text{inhom}} = 400\ \text{cm}^{-1}$) centred at 0 cm^{-1}. Burn times are relative only. The single-site parameters are $\Delta_{\text{ZPL}} = 15\ \text{cm}^{-1}$, $\Delta_{\text{1-phonon}} = 100\ \text{cm}^{-1}$, $E_{\text{phonon}} = 20\ \text{cm}^{-1}$, $S = 1$. The ordinate scale interval is the same in all plots.

temperatures (11 - 15 K) and less efficient heat dissipation. For each burn, the laser beam was defocussed to ensure that the whole sample was evenly illuminated. The spectral bandpass of the spectrometer between 600 - 700 nm was ~ 6 cm^{-1}. Further experimental details are given in Chapter 2.

Table 7.1. Experimental parameters of the hole-burning samples discussed in this chapter.

	Temperature (K)	Step size (Å)	Slit width (μm)	Field (T)	Matrix concentration	(mol L^{-1})
CuPc/Ar	~1.6	1 - 2	200	5	1:2500	1.6×10^{-2}
ZnPc/Ar	11 - 15	1 - 2	200	5	1:9300	4.4×10^{-3}
ZnPc/Ar	~1.6	1	100	0	1:2000	2.0×10^{-2}
$LuPc_2$/Ar	~1.6	0.5 - 1	100	5	1:1800	2.3×10^{-2}

7.3 Results and Discussion

The Q-band absorption and MCD spectra of CuPc/Ar, ZnPc/Ar and $LuPc_2$/Ar have similar appearances, and consist of three main bands. Q(0,0) arises principally from origin transitions, with some contribution from low-frequency vibrational sidelines, while Q(1,0) and Q(2,0) are composed of unresolved overlapping vibrational sidelines.[19,149,150] $LuPc_2$ also has a third vibrational overtone, Q(3,0). The Q(2,0) bands of all three species, along with the Q(3,0) band of $LuPc_2$ (Chapter 6), are thought to also contain contributions from a separate electronic transition.[19,39,60]

Hole spectra for each species are detailed below — in general, holes are similar to those found for dye molecules in amorphous hosts[128,147,151] where a NPHB mechanism is evident. In particular, holes are relatively broad, and the photoproduct predominately appears to the blue of the burn energy.

7.3.1 Electronic Structure

The symmetry and electronic configurations of the odd-electron CuPc molecule are described in Chapter 4. The Q band is a $\pi \rightarrow \pi^*$ transition of $^2B_{1g} \rightarrow {}^2E_u$ symmetry in D_{4h}. The excited-state term formally has 2-fold orbital and 2-fold spin degeneracy. The electronic structure of ZnPc is very similar except that, due to the closed valence shell of Zn^{2+}, there is no spin degeneracy in the ground or

excited states, the Q-band transition being $^1A_{1g} \rightarrow {}^1E_u$. The nature of the electronic configuration of $LuPc_2$ has been described in Chapter 6. It too is an odd-electron system, but with the unpaired electron in a ring orbital rather than on the metal. In D_{4d} symmetry, there are three Q transitions of the type $^2A_2 \rightarrow {}^2E_1$.[39] Each of these is susceptible to crystal-field (CF) and SO splittings, which could yield as many six bands in the Q(0,0) region. Moreover, recent measurements on the temperature dependence of the intervalence-band absorbance[103] suggest that the complex can adopt two conformations, further complicating the spectra. Note that the absorption and MCD spectra of the matrix under investigation here are substantially different in band position and shape from those reported by VanCott *et al.*[39] Helium-refrigerator experiments (Section 6.3.1) have shown that this is probably due to the relatively 'annealed' state of the matrix.

All three of the phthalocyanines studied are vulnerable to splitting of the excited state by CF, and, in the cases of CuPc and $LuPc_2$, SO effects. CF splittings have been identified for ZnPc in the range from 0-50 cm^{-1},[19] and the SO splittings of CuPc and $LuPc_2$ are given in Chapter 4 and Chapter 6 respectively. In any case, each excited-state term is split by an amount denoted here as ΔQ to form two levels (Kramers doublets in the case of CuPc and $LuPc_2$), denoted Q_- and Q_+. These are mixed by a second-order Zeeman interaction which varies as $1/\Delta Q$. Transitions to the lower CF- and SO-split state, Q_-, will be predominantly right circularly polarized (rcp, $\Delta A < 0$), while those to Q_+ will be predominantly left circularly polarized (lcp, $\Delta A > 0$). Since the individual MCD bands are too broad to be resolved, in a conventional MCD spectrum they overlap to give a feature with the appearance of a positive $\mathcal{A}$ term (positive lobe at higher energy). However, 'hole-MCD' spectra allow partial resolution of these components, as will be seen in Section 7.3.3.

7.3.2 Hole-Absorption Spectra

7.3.2.1 CuPc/Ar

Hole spectra obtained by burning at 628.9, 667.9, 659.9 and 651.0 nm (in that order) into the CuPc/Ar matrix are compared with the pre-burn absorption spectrum in Figure 7.8. The matrix was annealed for 10 - 20 min at ~28 K between

shifts in burn wavelength, to fill holes from the previous burn. All but the first hole spectra listed above represent burning into the Q(0,0) band. General features of the burn include a hole at the burn wavelength, and broad antihole photoproduct bands to higher energy (shaded).

The hole profiles for CuPc/Ar in the region of E_{burn} are similar to those simulated in Figure 7.7, *i.e.*, to the case where $\Delta_{\text{ZPL}} \simeq E_{\text{phonon}}$. In principle, the HOLES.BAS program could be used to model the experimental hole shapes. Although it proved possible to do so quite accurately in one attempt, the amount of effort and time required made the practice unreasonable in view of the large number of parameters and inherent uncertainty in their values. Instead, a more approximate but much faster method was used, whereby the hole spectra were fitted in the region of E_{burn} with a Lorentzian band corresponding to the ZPH, and a Gaussian band to the pseudo-PSBH. In order to minimise antihole complications, energies to the blue of the burn energy were not considered. Note that in the case of these CuPc holes, the Gaussian also accounts for the PSBH, due to the small value of E_{phonon}. Although there are obvious problems with this technique, it does allow approximate determination of Δ_{ZPH}. An example (for the case of the 667.9 nm spectrum) is shown in Figure 7.9.

This approach gave $\Delta_{\text{ZPH}} \simeq 15$ cm^{-1} for burns in Q(0,0), independent of burn energy. The broadness of the holes (significantly greater than the spectral bandpass of ~ 6 cm^{-1}) suggests short excited-state lifetimes, perhaps due to rapid radiationless deactivation of the excited state. The holes are also shallow, with depths of 1-8% of the pre-burn absorbance. The deepest burn occurs on the red side of the Q(0,0) band. The relative intensity of the pseudo-PSBH increases as the burn wavelength moves to the higher energy side of the band, as predicted in Section 7.1.2.4.

Consider now the individual spectra in Figure 7.8:

- The 667.9 nm burn spectrum shows a relatively weak pseudo-PSBH, appearing as a slight broadening of the red side of the ZPH (as seen in the simulation in Figure 7.7). To the blue, photoproduct antiholes (shaded) overlap with vibrational side holes and the PSBH.
- The pseudo-PSBH is (as expected) more evident in the 659.9 nm burn, and can

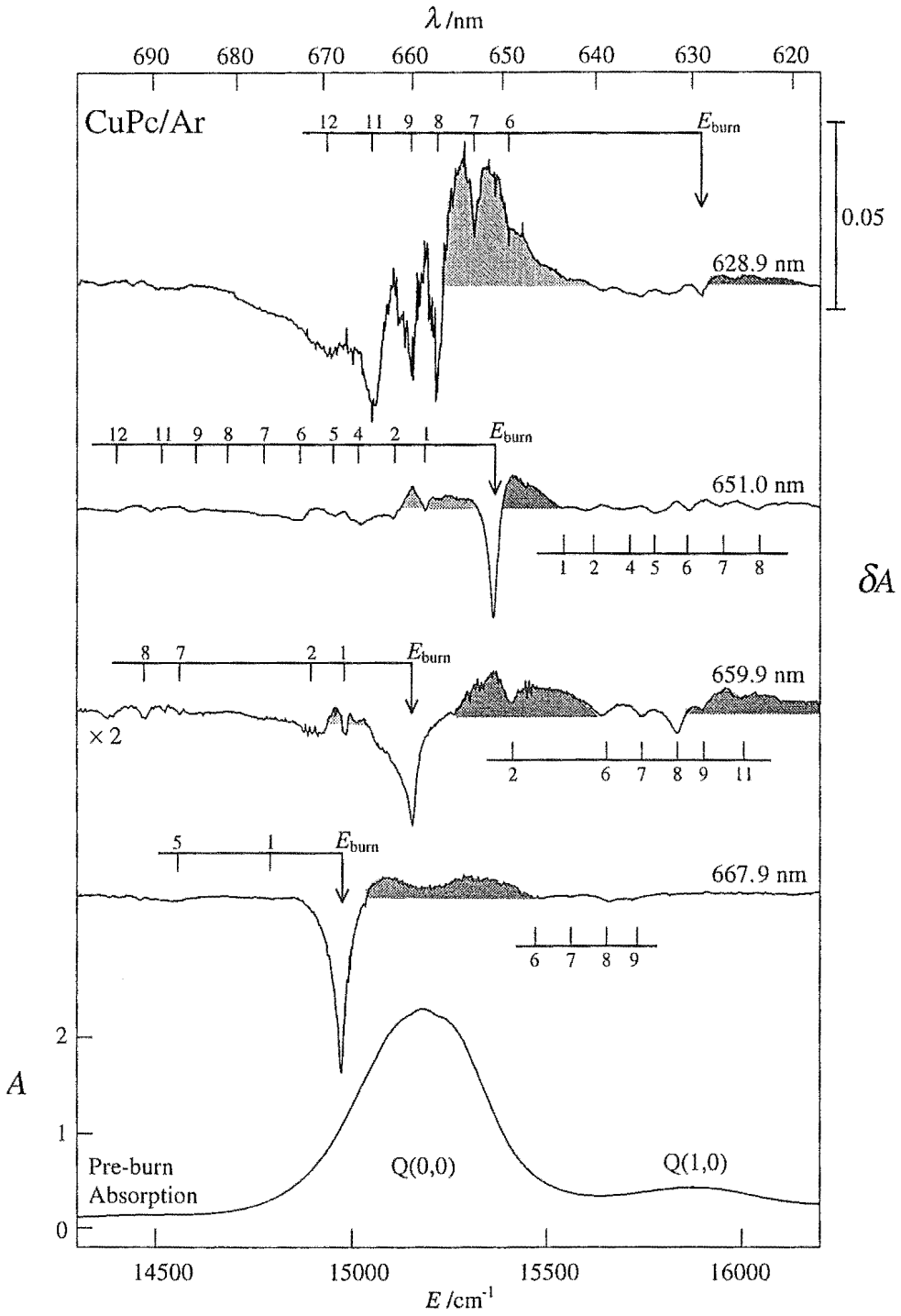

Figure 7.8. Hole-absorption spectra for CuPc/Ar. Burn wavelengths are given on the right-hand side. The pre-burn absorption spectrum is shown for comparison. Arrows indicate the burn positions, with grids extending to the left and right showing the positions of pseudo-VSBHs and VSBHs respectively. The numbering of these holes allows cross-referencing with Table 6.2. Photoproduct antiholes are shaded.

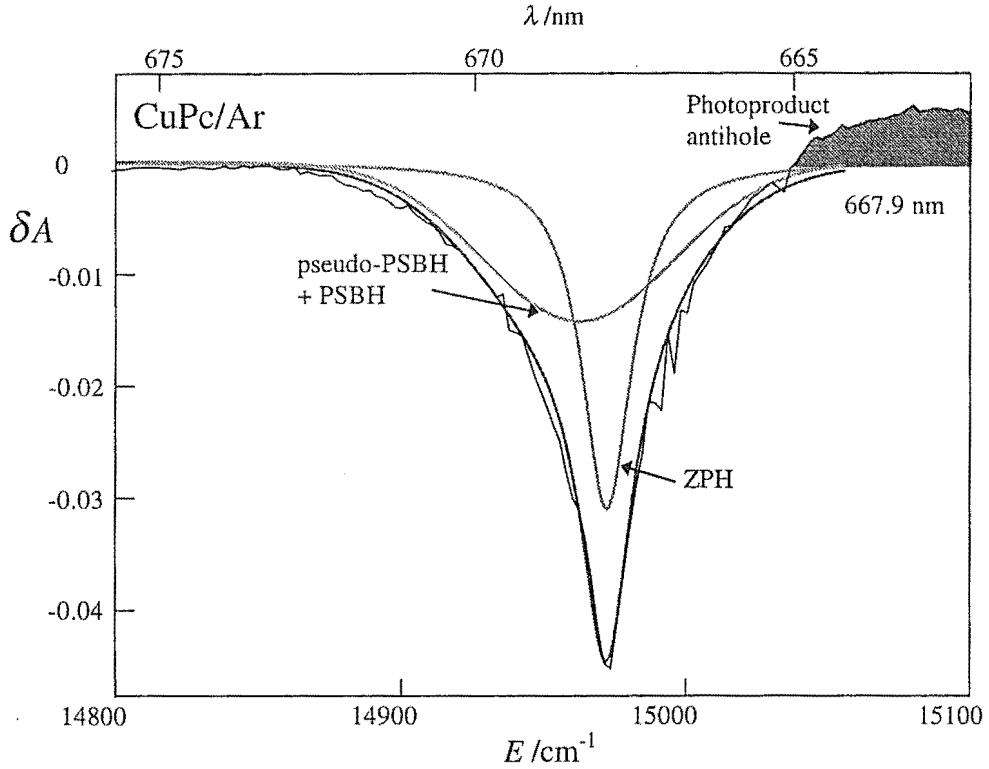

Figure 7.9. An example of the fitting of the hole-absorption spectra with two bands. The central Lorentzian has $\Delta_{\mathrm{ZPH}} = 15\ \mathrm{cm}^{-1}$.

be seen extending out to the red, overlapping with photoproduct antiholes which now appear on both sides of the hole. Strong VSBHs are seen in the Q(1,0) band region, with a number of pseudo-VSBHs to the very left of the figure. It is likely that the antihole to the blue of E_{burn} is directly related to the ZPH, while the antihole to the red is associated with the pseudo-VSBHs.

- The burn on the blue side of the Q(0,0) band (at 651.0 nm) also shows a relatively broad pseudo-PSBH which now interferes with a much stronger photoproduct band and a number of pseudo-VSBHs. A lesser amount of photoproduct antihole is seen immediately to the blue of the ZPH. VSBHs are again present.
- When the hole is burnt in the Q(1,0) band, (628.9 nm), pseudo-VSBHs in the Q(0,0) region dominate the spectrum. Note that the same general shape of pseudo-PSBH to the red, and photoproduct antihole to the blue is seen in both the Q(1,0) hole and the Q(0,0) feature. The energy shifts of the vibrational holes from the burn energy in all of the spectra shown in Figure 7.8 agree well with literature values of excited-state vibrational energies for other MPcs, as discussed in Section 7.3.4.

7.3.2.2 ZnPc/Ar

The preburn and 670.4, 633.0, 660.5 and 655.9 nm burn absorption spectra of ZnPc/Ar are shown in Figure 7.10. Holes were burnt in the order listed, and the matrix was annealed between each burn – with the exception of that at 655.6 nm, which was directly preceded by burns on the red side of the Q(0,0) band (670.0 - 670.4 nm, not shown). Note the hint of site structure in the preburn Q(0,0) absorption band. Much sharper structure has been seen by Vancott *et al.*[19] and Prince and Williamson[152] – the differences between their spectra and that shown here are due to deposition conditions.

In general, hole burning in the Q(0,0) region of ZnPc/Ar gives rise to sharp ZPHs which are not fully resolved at the band pass used in these experiments. Linewidths were determined by fitting as described in Section 7.3.2.1, the results being $\Delta_{\mathrm{ZPH}} \simeq 5$ - 8 cm^{-1}, $\Delta_{\text{pseudo-phonon}} \simeq 100$ cm^{-1}, and $E_{\text{phonon}} \simeq 200$ cm^{-1}. Note that the latter is much larger than was found for CuPc/Ar. The hole profiles are similar to the simulations shown in Figure 7.6, where the zero-phonon line is relatively narrow and E_{phonon} is large. The hole shapes rapidly become broader and more asymmetric with extended burn times, due to increasing contribution from pseudo-PSBHs and antiholes, and are also dependent on the region of the Q(0,0) band being irradiated. Details of the individual spectra are given below.

- Burning at 670.4 nm produced a sharp ZPH, with a very large pseudo-PSBH to the red. The intensity of the latter band is probably due to the length of the burn – at 300 s this was 5 times longer than the other two Q(0,0) band burns. Note that the pseudo-PSBH is not symmetrical, but rather skewed towards higher energy. This may be accounted for by the fact that the pre-burn absorption intensity decreases rapidly to the red of the burn wavelength, and so the number of molecules with phonon sideband intensity at the burn wavelength (responsible for the pseudo-PSBH) will also drop off with decreasing energy. Consequently, the band maximum for the pseudo-PSBH will be shifted closer to the ZPH. Broad VSBHs can be seen in both the Q(0,0) and the Q(1,0) band regions. To the blue of the ZPH, interference between photoproduct antiholes and the PSBH is observable. Note that this region of the spectrum has $\delta A < 0$, indicating that the antihole behaviour is substantially different to that found for other burns.

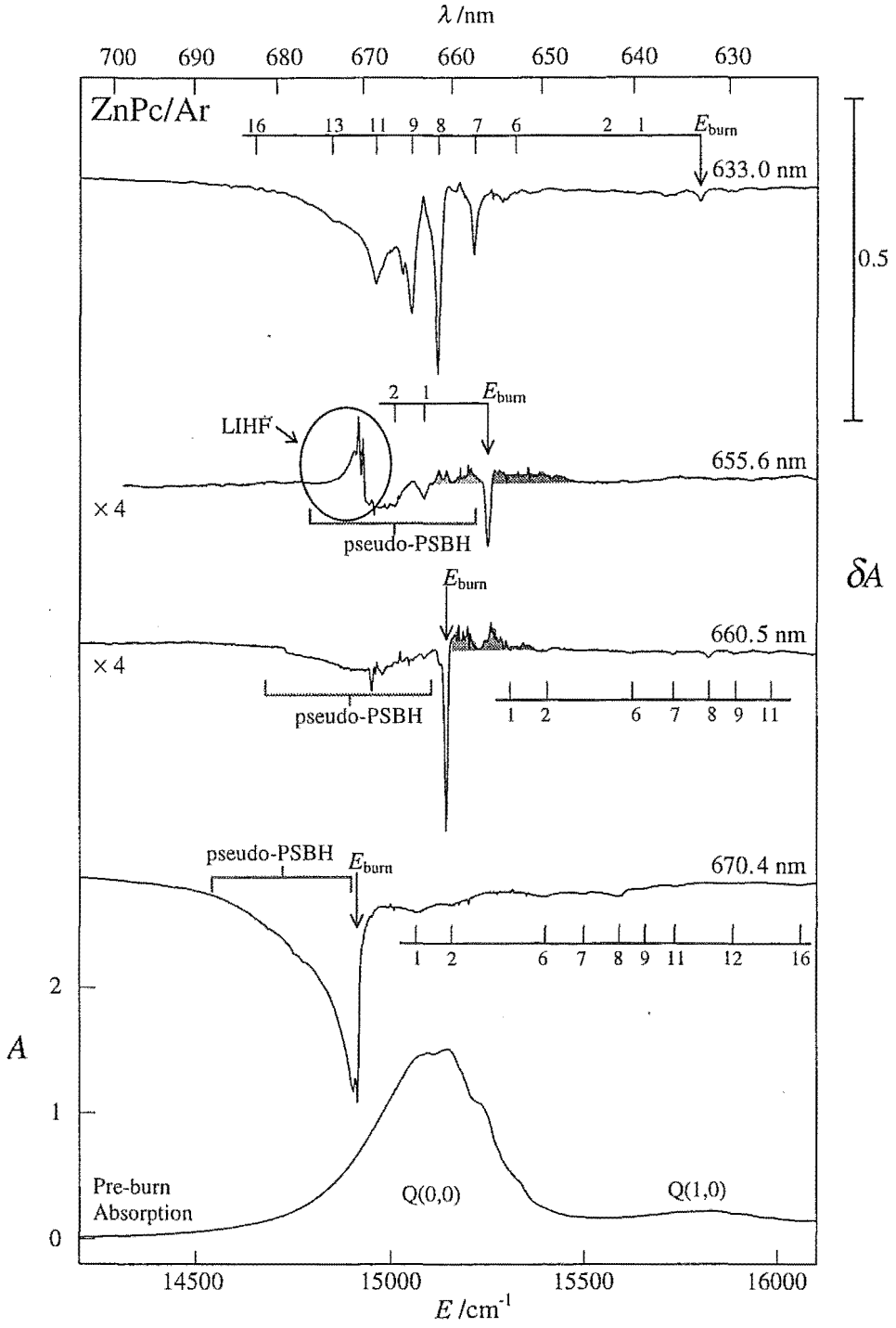

Figure 7.10. Hole-absorption spectra for ZnPc/Ar. Burn wavelengths are given on the right-hand side. The pre-burn absorption spectrum is shown for comparison. Arrows indicate the burn positions, with grids extending to the left and right showing the positions of pseudo-VSBHs and VSBHs respectively. The numbering of these holes allows cross-referencing with Table 6.2. Photoproduct antiholes are shaded.

Investigation of the spectrum over a wider region, as shown in Figure 7.11 reveals that a positive band appears far to the blue of the Q band. Such a large shift implies that the hole-burning mechanism is not purely non-photochemical, as will be discussed in Section 7.3.7.

- The spectrum of the burn in the centre of the Q(0,0) band, at 660.5 nm, has similar features to those seen for CuPc although with a much sharper ZPH. The broad negative band to the red of the ZPH can again be attributed to the pseudo-PSBH, and the positive band to the blue represents interference between the PSBH and the photoproduct antihole. Overlaying these features are a number of pseudo-VSBHs and VSBHs, with the latter extending out into the Q(1,0) region.
- The burn at 655.6 nm is similar, with the exception that photoproduct antiholes now appear on both sides of the ZPH, as was the case for the corresponding CuPc burn. This spectrum is further complicated, however, by antihole features around 670 nm, which are due to laser-induced hole filling (LIHF) of the previous, non-annealed burn. The phenomenon of LIHF is discussed in more detail in Section 7.3.6.
- The burn at 633.0 nm into the Q(1,0) band is similar to the CuPc Q(1,0) burn, but with no positive region in the Q(0,0) band which would be attributable to photoproduct antiholes. As with the 670.4 nm ZnPc burn, these antiholes have shifted outside the Q-band envelope, as seen in Figure 7.11. A beautiful set of pseudo-VSBHs is also distinguishable in this hole spectrum, as presented in Section 7.3.4.

Another ZnPc/Ar matrix was also studied, with hole burning and spectral measurement taking place at 11 K. The absorption-hole spectrum of a 660-s burn at 662.9 nm is shown at the top of Figure 7.12. A well-defined pseudo-PSBH is seen to the red of the ZPH. Directly to the blue of the ZPH some evidence of photoproduct antiholes is seen. The overlapping PSBH is much more intense than those seen in the hole-burning spectra measured at 1.6 K, as is consistent with its known dependence on temperature.[129] A series of VSBHs is seen in the Q(1,0) and Q(2,0) regions. Note that the negative hole areas are not equally matched by positive antiholes. However, unlike the ZnPc burns shown in Figure 7.11, antiholes are not seen anywhere between 230 and 730 nm. This fact appears to indicate that some type of 'photobleaching' has occurred, causing loss of intensity over the

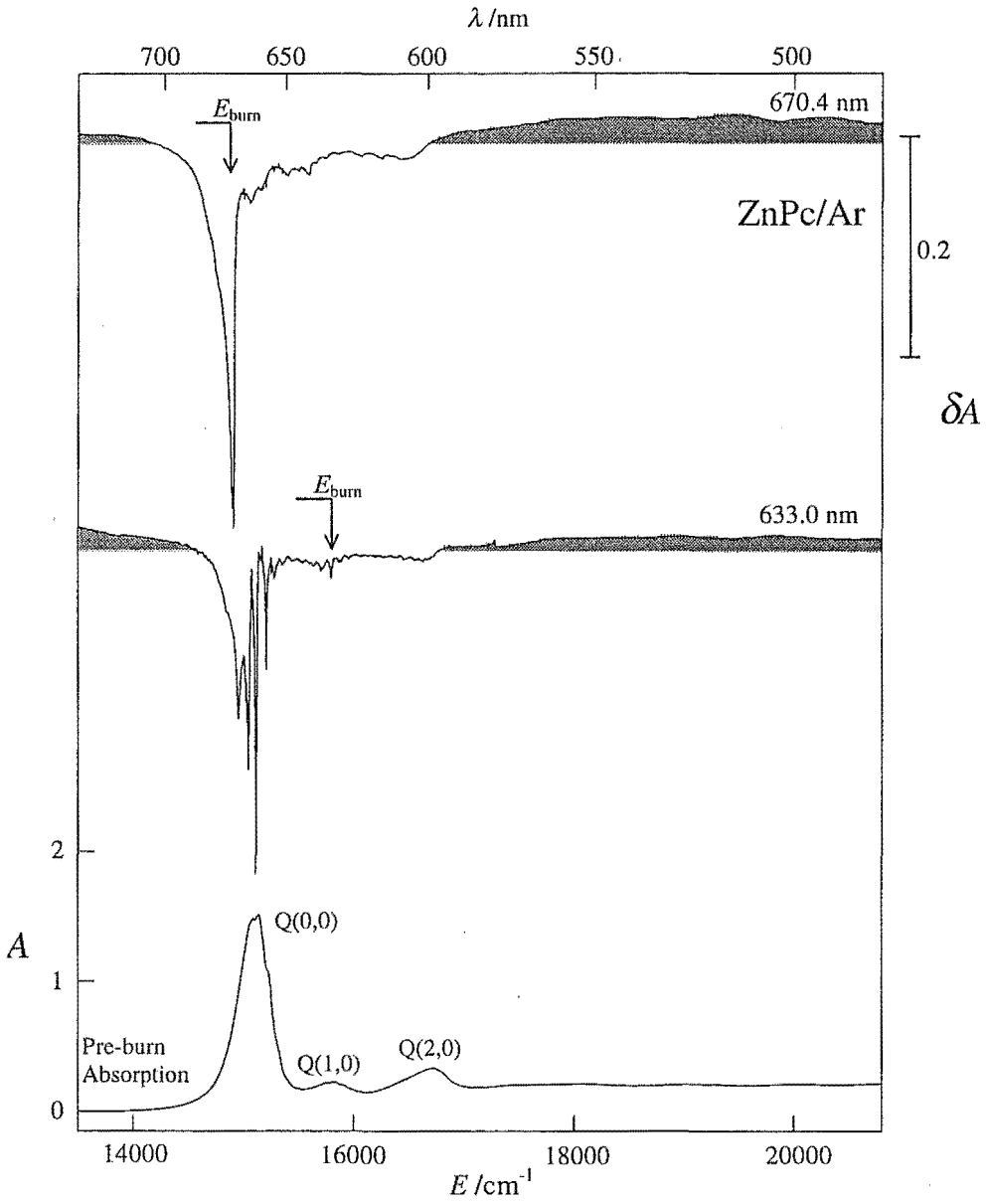

Figure 7.11. 670.4 nm and 633.0 nm hole-absorption spectra for ZnPc/Ar over an expanded region. Regions of positive δA are shaded. The pre-burn absorption spectrum is shown for comparison.

entire Q (and B) band. Such photobleaching was seen to occur consistently for high-temperature burns where the matrix was in a vacuum. It would thus seem that this process is temperature dependent, as it was not apparent in any of the 1.6 K spectra. The mechanism of such bleaching is not known, but it may be caused by loss or redistribution of matrix material due to localised heating by the laser beam. The middle spectrum in Figure 7.12 shows the result of correcting for 4% photobleaching. The Q-band positive and negative areas are now approximately equal, and the overall hole shape seems credible, with a pseudo-PSBH to the red of the burn, and overlaying PSBHs and photoproduct antiholes to the blue. The same general shape is seen in the Q(1,0) VSBH region.

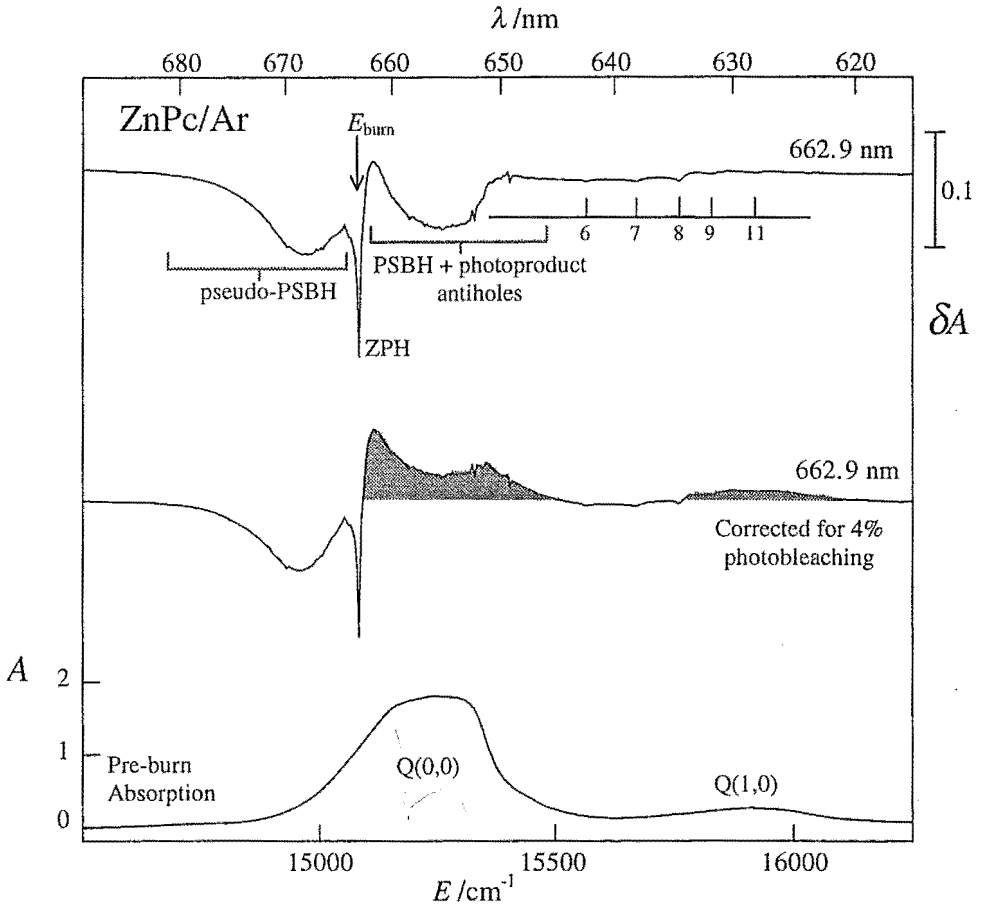

Figure 7.12. Hole-absorption spectra for ZnPc/Ar investigated at 11 K. The top plot is the 'raw' hole-absorption spectrum, while the middle plot show the spectrum corrected for 4% photobleaching (see text). Burn wavelengths are given on the right-hand side. The pre-burn absorption spectrum is shown for comparison. The burn position is indicated by an arrow, with a grid extending to the left showing the positions of VSBHs. The numbering of these holes allows cross-referencing with Table 6.2. The photoproduct antiholes are shaded.

It might be thought that the wide-range ZnPc spectra in Figure 7.11 could also be explained (with an additional shift in baseline) by photobleaching, *i.e.* that after correction for such an effect antihole bands would appear close to the hole, and those outside the Q-band region would disappear. Analysis shows, however, that even after such a correction the positive bands to the blue of the Q region remain.

7.3.2.3 $LuPc_2$/Ar

Figure 7.13 shows the results of three burns into the Q(0,0) band of $LuPc_2$/Ar, at 659.9, 650.0 and 641.0 nm, along with the pre-burn absorption spectrum. The matrix was annealed at 28 K for 10 min between each burn. Fitting of the red- and centre-burn spectra (described in Section 7.3.2.1) indicates that the ZPHs are quite broad, with $\Delta_{ZPH} \simeq 25$ cm^{-1}. This broadness may be due to rapid radiationless deactivation to lower-lying electronic states. The pseudo-PSBHs have $\Delta_{\text{pseudo-phonon}}$ = 200 - 250 cm^{-1}, and $E_{\text{phonon}} \simeq 150$ cm^{-1}. As seen for CuPc and ZnPc, the pseudo-PSBHs grow in magnitude as the burn position moves to higher energy across the Q(0,0) band, and the antiholes are primarily blue-shifted.

Hole burning to the red (659.9 nm) and centre (650.0 nm) of the band was facile, with shallow (~1% of pre-burn absorbance) holes being obtained after illumination for only 15 s at low burn power. In contrast, burning into the blue side of the Q(0,0) band was very difficult. A 150-s burn at 641.0 nm resulted in an extremely broad and shallow hole at the burn wavelength with a series of significantly stronger holes to the red.

As discussed in Chapter 6, there are three transitions making up the Q(0,0) band of $LuPc_2$. VanCott *et al.*[39] have fitted Gaussian bands in this region, which they label (from high to low energy) $Q(0,0)_A$, $Q(0,0)_B$ and $Q(0,0)_C$,with the majority of the intensity coming from the latter two bands. Since there has been shown to be significant configuration interaction between the three Q-band states,[39,107] it is possible that the red-shifted side holes of the 641.0-nm burn are of an electronic nature. However, given that their shifts from E_{burn} agree well with the excited-state vibrational frequencies of CuPc and ZnPc (Section 7.3.4) it seems more likely that the laser is burning into a vibrational side-band region, and that the red-shifted holes are pseudo-VSBHs. Burning into the blue of the CuPc/Ar and ZnPc/Ar Q(0,0) bands (Figures 7.8 and 7.10 respectively) also produced a series of pseudo-VSBHs,

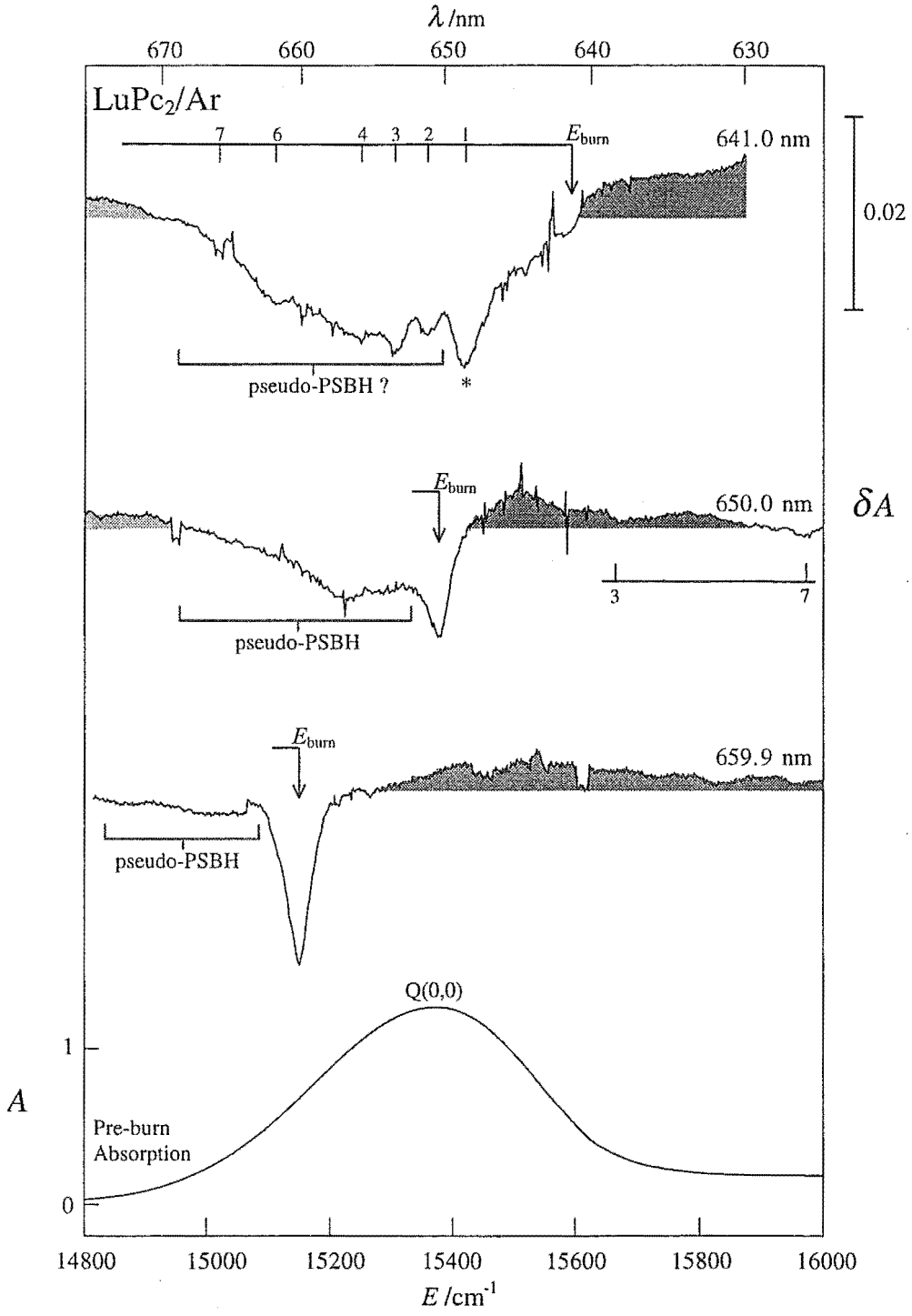

Figure 7.13. Hole-absorption spectra for $LuPc_2$/Ar. Burn wavelengths are given on the right-hand side. The pre-burn absorption spectrum is shown for comparison. Arrows indicate the burn positions, with grids extending to the left and right showing the positions of pseudo-VSBHs and VSBHs respectively. The numbering of these holes allows cross-referencing with Table 6.2. Photoproduct antiholes are shaded.

however in each instance these were not as intense as the ZPH. It thus appears that in the case of $LuPc_2$/Ar, the component band of greatest intensity at 641.0 nm (probably $Q(0,0)_A$) is not amenable to hole burning, and holes only appear through burning into a (weak) vibrational overtone of one or both of the other transitions.

This interpretation is supported by the fact that the 641.0-nm spectrum can be fitted nicely using the same parameters as for the red- and centre-burn spectra if the burn wavelength is taken to be 185 cm^{-1} to the red of the actual burn position. E_{burn} then coincides with the strongest pseudo-VSBH, marked with $*$ in Figure 7.13. In other words, the broad negative hole to the red of the burn energy appears to consist primarily of a pseudo-PSBH arising from this vibrational hole, rather than from the true ZPH.

7.3.3 Hole-MCD Spectra

In Figures 7.15, 7.16 and 7.17, hole-MCD spectra are compared with the pre-burn MCD in the Q(0,0) region for CuPc/Ar, ZnPc/Ar and $LuPc_2$/Ar respectively. $\delta\Delta A$ is the change in ΔA that occurs due to hole-burning; $\delta\Delta A = \Delta A_{post} - \Delta A_{pre}$. The holes were burnt at zero field, and the hole-MCD spectra measured at 5T.

As stated in Section 7.3.1, the excited-state terms of each of these molecules will be split, at zero magnetic field, into two components whose energy separation is designated ΔQ. The upper and lower components are designated Q_+ and Q_- respectively. Transitions terminating in Q_- are predominately rcp, and occur on the red side of the Q band, while those terminating in Q_+ (predominately lcp) are on the blue side. The MCD-hole spectra can be qualitatively rationalized as holes burnt into one of these two CF/SO states, accompanied by electronic side holes, as detailed below and shown in Figure 7.14.

When burning occurs on the red edge of the Q(0,0) band, the ZPH is mainly due to transitions to Q_-. Removal of the molecules with these transitions leaves a positive ($\delta\Delta A > 0$) 'hole' (Q_- ZPH) in the hole-MCD at the burn wavelength. For every transition to Q_-, there will be an associated Q_+ transition, appearing as an electronic side-band hole (ESBH) at higher energy. Since the correlation between the Q_+ and Q_- energies is weak, and ΔQ has a broad distribution, the ESBH is not easily observed in absorption. However in MCD, the nature of the pseudo-$\mathcal{A}$

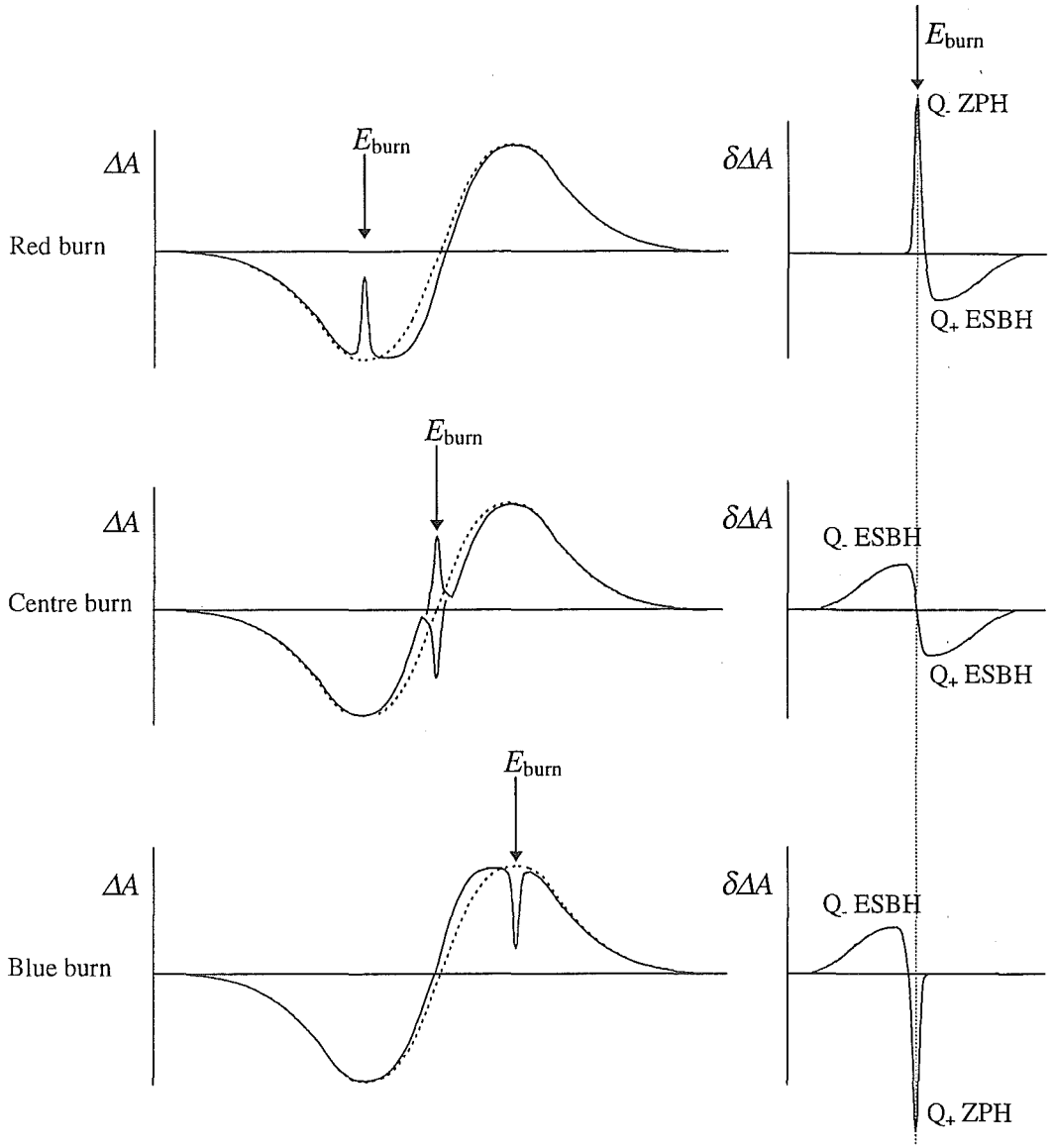

Figure 7.14. The MCD and hole-MCD spectra expected to result from burns to the red, centre and blue of an inhomogeneously broadened band. In each case, both ZPHs and ESBHs are burnt. The band shapes are explained in the text. The dotted line represents the pre-burn MCD.

terms (Section 3.4) is such that those sites with small ΔQ will give the strongest Q_+ ESBH, (proportional to $1/\Delta Q$) and hence the overall bandshape appears biased towards the burn wavelength. In the same manner, burning to the blue of the band produces a negative hole at the burn wavelength due to the Q_+ ZPH. The associated Q_- ESBH appears as a broad positive band to lower energy, skewed towards the burn wavelength.

If the burn is in the centre of the band, approximately equal numbers of Q_- and Q_+ transitions will be removed. Hence, both positive Q_- and negative Q_+ ZPHs

will be formed at the burn wavelength, which will cancel. Each of these transitions will, however, have an associated ESBH, and so a positive Q_- ESBH band would be expected to lower energy, and a negative Q_+ ESBH band to higher energy, each band again being broad and skewed towards the burn energy. (The field will actually cause Zeeman splitting of the Q_- and Q_+ ZPHs, with the former decreasing, and the latter increasing in energy. Thus, for matrices with sharp site structure and well-resolved bands, a narrow negative-$\mathcal{A}$-term shaped feature should be seen centred around the burn energy.)

An additional complication arising in the case of a NPHB mechanism is the production of antiholes in the Q(0,0) band region. Such antihole bands may obscure the ESBH features, and, in contrast to the latter, will be spread evenly over their energy range.

7.3.3.1 CuPc/Ar

The CuPc hole-MCD spectra of Figure 7.15 can be interpreted in the manner of the general discussion above.

- For the burn at 667.9 nm, on the red side of the Q(0,0) band, a relatively sharp positive band is seen at the burn wavelength (Q_- ZPH), with a broader negative band immediately to higher energy (Q_+ ESBH). The photoproduct antiholes are probably spread out over the spectrum, and so barely distinguishable above the noise level. The remainder of the spectrum, above ~15100 cm^{-1}, contains interfering contributions from remnants of the Q_+ side hole with photoproduct antiholes and underlying vibrational side holes.
- In the 651.0-nm burn spectrum, transitions at the burn wavelength terminate predominantly in Q_+, and so give a negative feature at the burn wavelength. The positive lobe immediately to the blue is associated with the Q_+ photoproduct antihole, which is, in this case, confined to a narrow range between the burn wavelength and the blue-most limit of Q(0,0). The electronic side hole is associated with Q_- and gives a positive hole-MCD band to the red, skewed towards the burn wavelength by the $1/\Delta Q$ intensity dependence.
- For the burn at 659.9 nm (corresponding to the centre of the Q band, where $\Delta A \simeq 0$) no distinct feature was seen at the burn wavelength. This is as expected, since terminations in Q_+ and Q_- are equally likely, and their contributions to $\delta\Delta A$

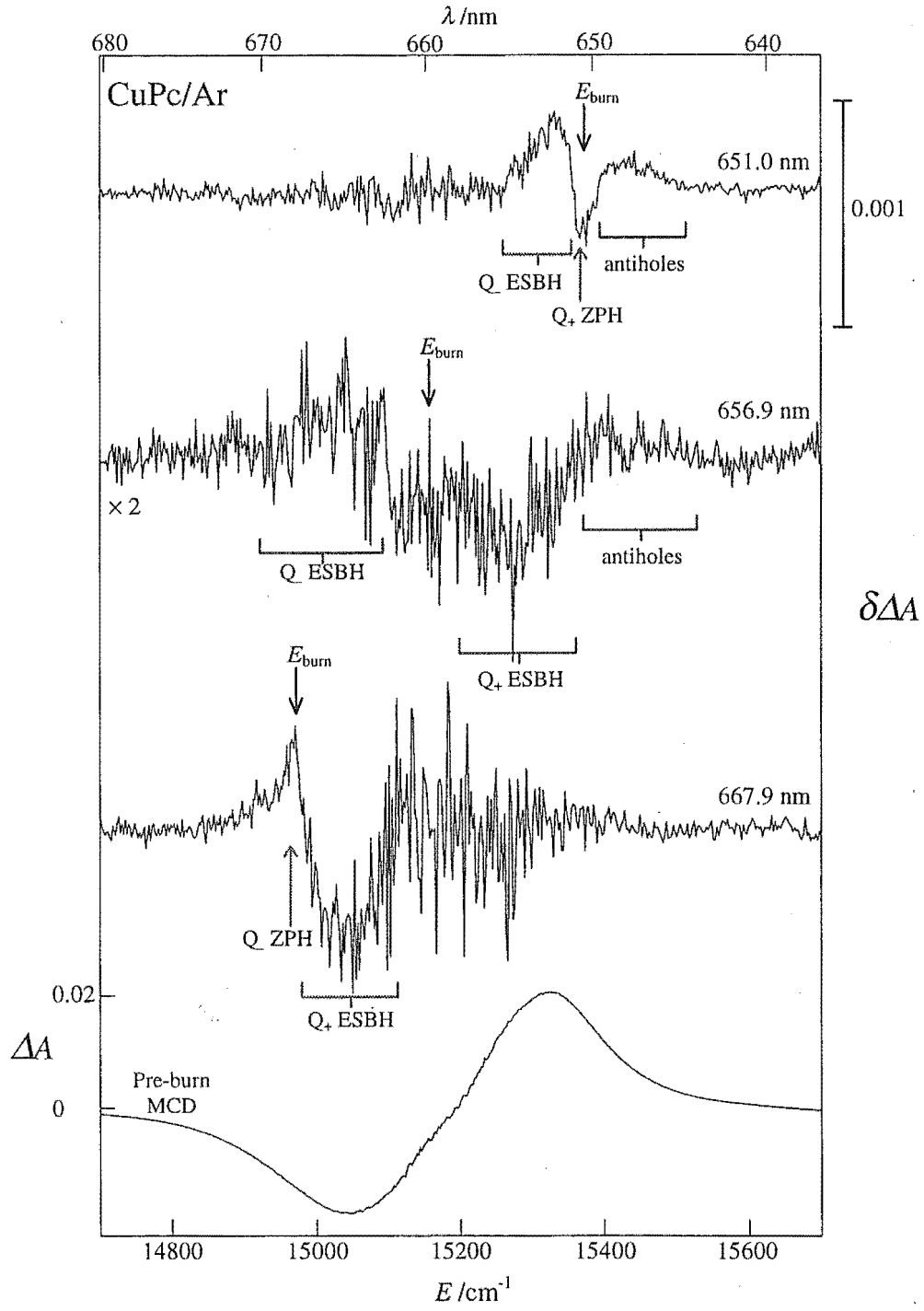

Figure 7.15. Hole-MCD spectra for burns into the Q(0,0) band of CuPc/Ar. Arrows indicate the burn wavelength. Other features are also marked. The pre-burn MCD spectrum is shown at the bottom.

will cancel. A broad positive Q_- ESBH occurs to the red. To the blue are the positive Q_+ ESBH and the photoproduct antiholes.

7.3.3.2 ZnPc/Ar

The ZnPc/Ar hole-MCD spectra are shown in Figure 7.16. Note that, as seen in absorption, the ZnPc hole features are much sharper than those of CuPc.

- Irradiation to the red of the Q(0,0) band (670.4 nm) predominately burns transitions terminating in Q_-, giving a positive feature at the burn wavelength. The strong positive feature to the red of the burn is the pseudo-PSBH, also terminating in Q_-. The Q_+ ESBH is seen as a broader negative band to the blue of the burn wavelength.
- The burn at 655.6 nm produces a negative hole at the burn wavelength, indicative of burning into transitions terminating in Q_+, as expected for a blue burn. The Q_- ESBH appears immediately to the red of this hole, but due to overlap with a negative pseudo-PSBH, there are both positive and negative features in this region. As mentioned in Section 7.3.2.2, the spectra of this burn are complicated by antiholes produced by LIHF of a previous non-annealed burn. These features, along with a number of pseudo-VSBHs are present well to the red of the burn wavelength.
- The hole-MCD spectrum for the burn at 660.5 nm looks unusual. If the positive band at the burn wavelength is real, then (unlike the CuPc and $LuPc_2$ burns into the centre of the Q(0,0) band) only Q_--terminating transitions are removed, instead of the equal mixture of Q_+ and Q_- expected. Continuing with this interpretation, the features to the blue are the Q_+ ESBH and corresponding photoproduct antiholes. Repetition of the experiment would be necessary to confirm this result, however, due to time constraints this was not possible.

7.3.3.3 $LuPc_2$/Ar

The hole-MCD spectra for $LuPc_2$/Ar are shown in Figure 7.17.

- The burn into the red side of the Q(0,0) band (659.9 nm) gives a spectrum very similar to the corresponding CuPc/Ar burn. A positive hole-MCD lobe (burning into Q_-) is seen at the burn energy, with a negative Q_+ ESBH to higher energy.

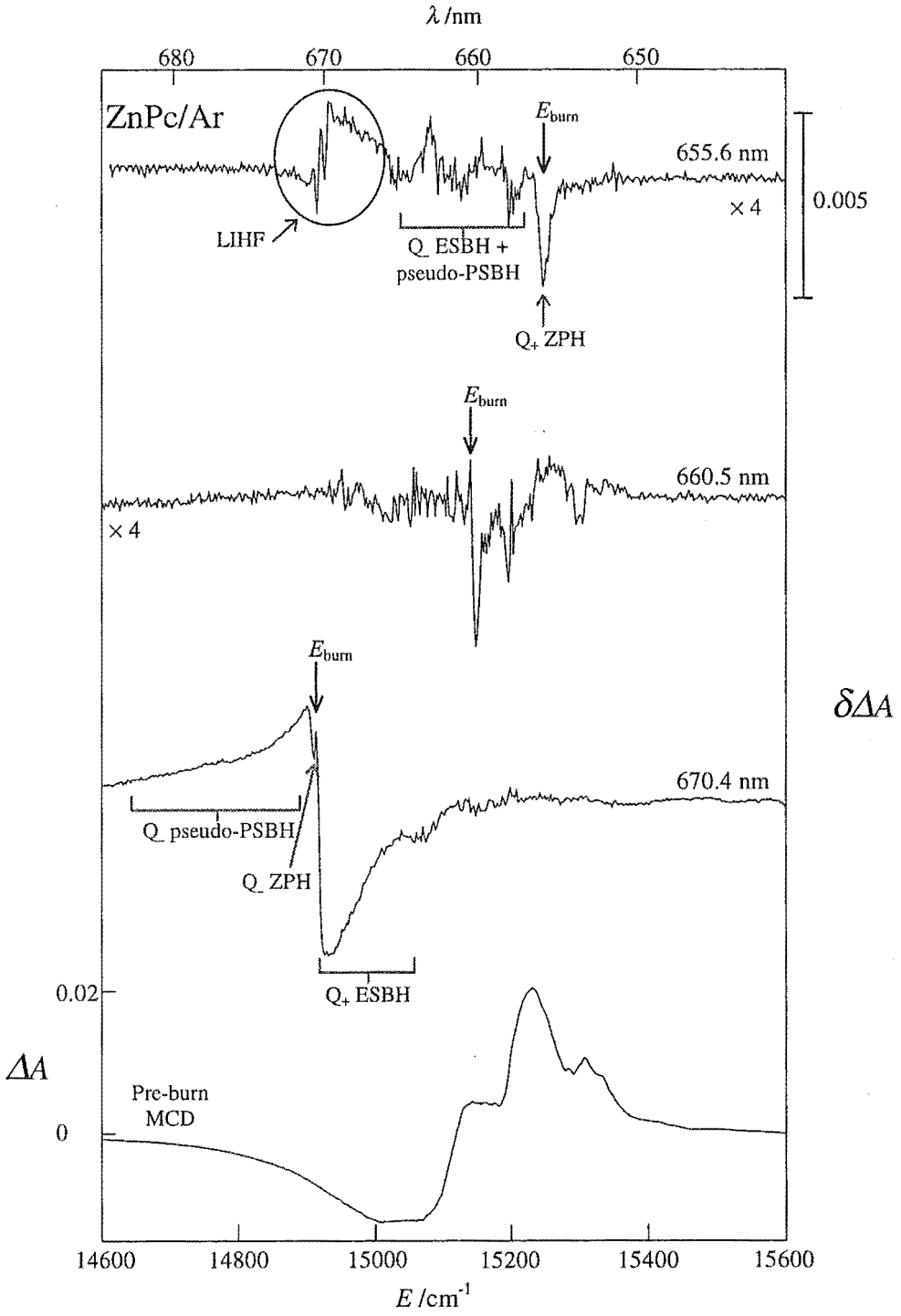

Figure 7.16. Hole-MCD spectra for burns into the Q(0,0) band of ZnPc/Ar. Arrows indicate the burn wavelength. Other features are also marked. The pre-burn MCD spectrum is shown at the bottom.

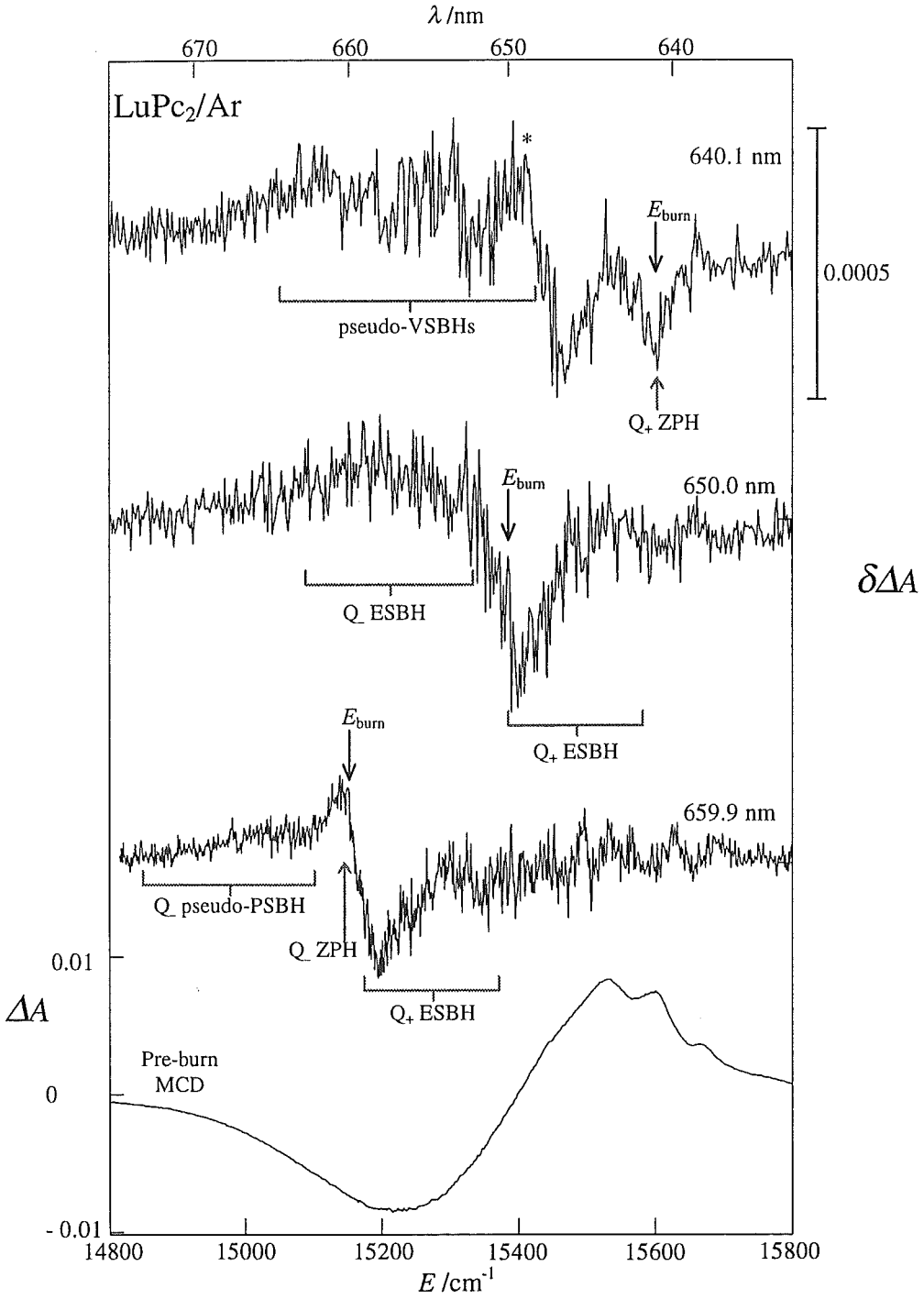

Figure 7.17. Hole-MCD spectra for burns into the Q(0,0) band of $LuPc_2$/Ar. Arrows indicate the burn wavelength. Other features are also marked. The pre-burn MCD spectrum is shown at the bottom.

Evidence of a positive pseudo-PSBH can be seen to the red.

- There is no strong feature at the burn wavelength of the 650.0-nm burn spectrum; approximately equal numbers of Q_- and Q_+ transitions are burnt, and hence their ZPHs cancel. The positive Q_- ESBH and the negative Q_+ ESBH can be seen to lower and higher energy respectively.
- Despite the shallow nature of the corresponding absorption hole, the MCD-hole spectrum of the 641.0-nm burn has a relatively intense negative band at the burn wavelength, the sign of which might seem to indicate burning into Q_+. However, since burning is primarily into a region of vibrational overtones (Section 7.3.2.3), the situation is considerably more complicated than for the other hole-MCD spectra. As stated in Section 7.3.2.3, the main feature of the absorption-hole spectrum is seen 185 cm^{-1} to the red of the burn wavelength, (marked by $*$ in Figure 7.13). This shift corresponds to a vibrational frequency seen in other MPc spectra and so the feature is probably a pseudo-VSBH. In the hole-MCD a positive band is seen at this position (marked by $*$ in Figure 7.16), with a broader negative hole to higher energy. This indicates burning into Q_-, seemingly at odds with the assignment of the ZPH. However this vibrational frequency is known to be a Jahn-Teller (JT) mode in MPcs;[19] the JT effect causes inversion of the sign of the MCD relative to a normal vibration. Hence the negative band at the burn energy corresponds primarily to burning into the JT vibrational overtone of a Q_- transition.

7.3.4 Vibrational Side-Band Holes

When burning into the vibrational side bands, pseudo-VSBHs appear, with shifts in energy from the burn wavelength corresponding to excited-state vibrational frequencies. These holes are most clearly observed by burning into the Q(1,0) band. An example of such a burn into ZnPc is shown in Figure 7.18. The spectra were obtained by burning at 633.0 nm, indicated by a shift of 0 cm^{-1} in the figure. The top plot is of the absorption-hole spectrum, *i.e.* $\delta A = A_{\text{post-burn}} - A_{\text{pre-burn}}$. The lower plot shows the corresponding 'antihole spectrum' resulting from a subsequent anneal; $\delta A = A_{\text{post-anneal}} - A_{\text{post-burn}}$. Comparison of the two spectra allows more accurate determination of which vibrational features are real.

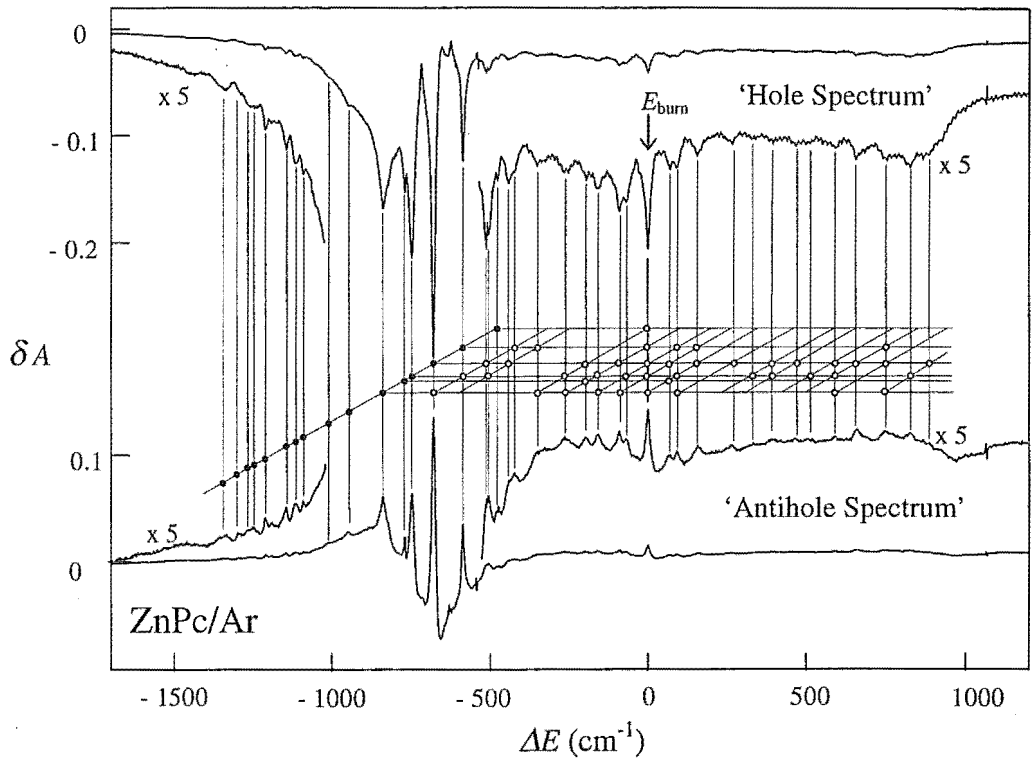

Figure 7.18. A burn into the Q(1,0) band of ZnPc/Ar at 633.0 nm. The upper plot is of the hole-absorption spectrum, and the lower plot shows the corresponding 'antihole' spectrum resulting from a subsequent anneal ($\delta A = A_{\text{post-anneal}} - A_{\text{post-burn}}$). The burn has produced a large number of pseudo-VSBHs which can be classified into two types. 'Origin' pseudo-VSBHs are shown on the grid as filled circles, and the progressions building on each of these origins are shown as open circles.

The vibrational holes can be classified into two types, with filled circles on the first (extended) diagonal of the grid pattern representing observed pseudo-VSBHs which correspond to (0,0), or origin, transitions of various sites. The rest of the grid indicates the predicted overtones and combinations built upon these 'origin' pseudo-VSBHs. Those actually observed are indicated by open circles. The pseudo-VSBHs in these spectra are much broader that those obtained by burning into Q(0,0) band. This is due to the short lifetimes of the vibronic states, caused by rapid deactivation of the vibrations.

Vibrational frequencies obtained from a series of measurements made by burning at different wavelengths within the Q(0,0) and Q(1,0) contours of ZnPc/Ar, CuPc/Ar and $LuPc_2$/Ar are included in Table 7.2. The data agree well with those obtained for ZnPc from a detailed fitting of both absorption and MCD line shapes[19] and from measurements in Shpol'skii (hydrocarbon) matrices.[149,150]

Table 7.2. Q-band excited-state vibrational energies (cm^{-1}) determined from the ZnPc/Ar, CuPc/Ar and $LuPc_2$/Ar spectra. Literature values are listed for comparison.

Mode[a]	ZnPc/Ar	CuPc/Ar	$LuPc_2$/Ar	ZnPc/Ar	ZnPc/Shpol'skii		MgPc/Shpol'skii	
	This work	This work	This work	Ref[19]	Ref[149b]	Ref [150]	Ref[149b]	Ref[150]
1	166	174	185	154				
2	239	251	244	225			247	
3		289	294	258		260	275	
4	324	335	352					355
5		413					412	
6	483	500	489	479	478	475	479	477
7	587	590	581	589	589	584	583	583
8	676	685	688	676	675	676	672,680	677
9	744	752		739	742	738	741	739
10	771		769				759	
11	834	848		840	841	832	824,835	823
12	947	959			954		935	
13	1012				1008	1006	1008	
14	1090				1093			
15	1117				1117	1116	1118	1116
16	1139	1159		1133	1143,1151		1152	
17	1209			1215	1206		1208	1212
18	1264	1269			1278			
19	1280				1291		1300	
20	1334	1341		1334	1332	1333	1339	1334
21	1423			1408	1412,1418		1415	
22	1502			1500	1492	1497		1495
23	1562	1583		1565	1531	1583		
24	1611			1600				

[a] Numbering is given to allow cross-reference with hole-absorption spectra

[b] Only the strongest vibrations given in this reference have been listed here.

7.3.5 Hole-Growth Kinetics for CuPc/Ar

A series of consecutive burns was conducted at 659.9 nm in the CuPc/Ar matrix (Figure 7.19) and the hole-growth kinetics of this series were analysed. The efficiency of hole formation clearly decreases with cumulative burn period, t_b, but the details of the kinetics are partly obscured by overlap with antiholes. Figure 7.20 shows the relationship between A^h and t_b, where A^h is the dimensionless zeroth absorption moment of the hole,

$$A^h \equiv \int \frac{\delta A}{E} dE \tag{7.5}$$

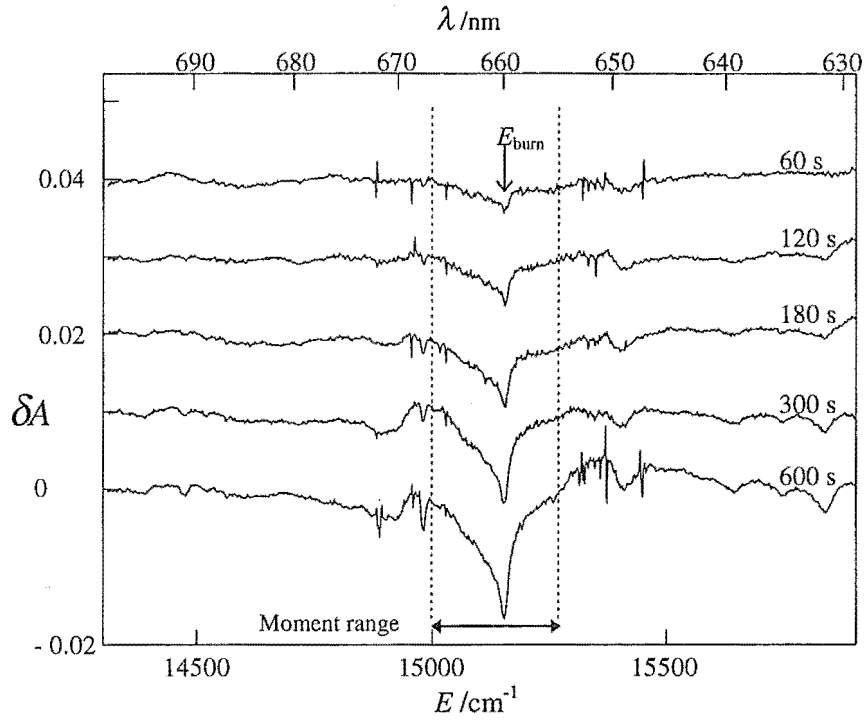

Figure 7.19. A series of holes burnt at 659.9 nm into the Q(0,0) band of CuPc/Ar using a flux of 10 mW cm^{-2}. The cumulative burn time (t_b) is indicated on the right-hand side.

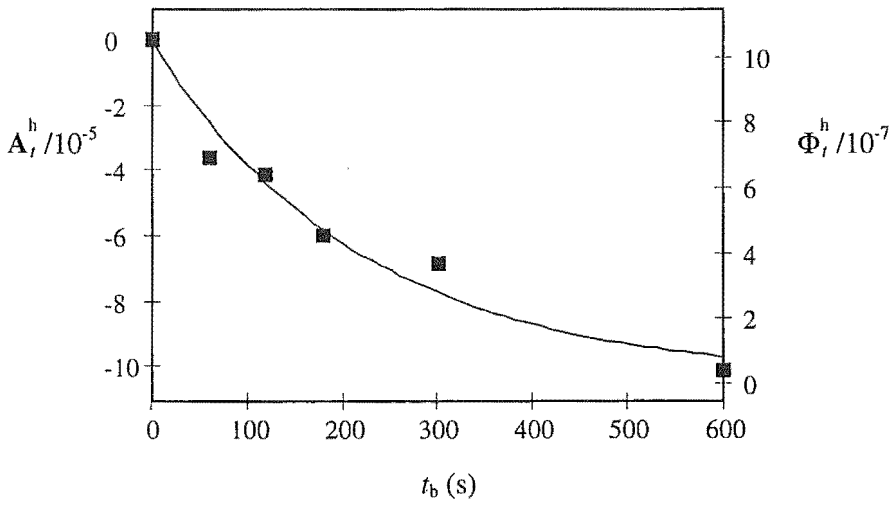

Figure 7.20. The kinetics of hole burning at 659.9 nm into CuPc/Ar. A_t^h is the zeroth absorption moment of the hole, and Φ_t^h is the transient quantum yield of hole-burning.

Moments were taken over the range shown in Figure 7.19, in an attempt to exclude contributions due to the pseudo-PSBH and photoproduct antiholes. The time dependence of A^{h} was modelled by an exponential decay,

$$\mathrm{A}_t^{\mathrm{h}} = \mathrm{A}_\infty^{\mathrm{h}}(1 - e^{-kt}) \tag{7.6}$$

where k is a rate constant and $\mathrm{A}_\infty^{\mathrm{h}}$ is the value of the zeroth moment of the hole at complete saturation, $\mathrm{A}_\infty^{\mathrm{h}} \simeq -10^{-4}$.

The transient quantum yield of hole-burning (Φ_t^{h}) is proportional to the rate of change of $\mathrm{A}_t^{\mathrm{h}}$ with time,

$$\Phi_t^{\mathrm{h}} = \left[\frac{N_{\mathrm{A}}\pi r^2 hcE_{\mathrm{burn}}}{3.266 \times 10^5 P(1 - 10^{-A})\mathcal{D}_0}\right]\frac{d\mathrm{A}_t^{\mathrm{h}}}{dt} \tag{7.7}$$

where N_{A} is Avogadro's number, r is the radius of the (circular) sample (cm), h is Planck's constant (J s), c is the concentration of the sample (mol L^{-1}) and E_{burn} is the burn energy (cm^{-1}). P is the laser power (J s^{-1}), A is the pre-burn absorbance at the burn energy, and $\mathcal{D}_0$ is the dipole strength of the Q(0,0) transition. Combining (7.6) and (7.7), and representing the term of (7.7) in square brackets as C gives

$$\begin{aligned}
\Phi_t^{\mathrm{h}} &= C\frac{d(\mathrm{A}_\infty^{\mathrm{h}}(1 - e^{-kt}))}{dt} \\
&= -Ck\mathrm{A}_\infty^{\mathrm{h}} e^{-kt} \\
&= Ck(\mathrm{A}_\infty^{\mathrm{h}} - \mathrm{A}_t^{\mathrm{h}})
\end{aligned} \tag{7.8}$$

Hence Φ_t^{h} is linearly related to $\mathrm{A}_t^{\mathrm{h}}$, and also decays exponentially. This is illustrated by the right-hand ordinate of Figure 7.20, which assumes a value for the dipole strength of $\mathcal{D}_0 = 20$ – this is similar to values found for other MPcs.[46,61,153,154] Thus an initial quantum yield of $\Phi_0^{\mathrm{h}} \simeq 10^{-6}$ is estimated, with the hole saturating after ~ 10 min irradiation at ~ 10 mW cm^{-2}, at which point the hole depth is about 2% of the optical density.

7.3.6 Hole Filling

Once a hole has been burned, its profile can change with time. The nature of such changes and the rate at which they occur can depend on temperature or laser irradiation. One form of alteration of hole profile with time (primarily seen in amorphous hosts) is due to spectral broadening, or 'dispersive kinetics'. This

is believed to arise from tunnelling-induced rearrangement of TLSs, since it occurs even at very low temperatures where barriers to rearrangement cannot be overcome thermally.[128] This process is shown as (4) in Figure 7.21. (Processes (**1**), (**2**) and (**3**) in the figure represent hole burning, as described in Section 7.1.2.1.)

A second mechanism involves annealing of a sample above a certain temperature, which, taken to the extreme, can cause complete erasure of the hole. This is due to one of two effects; either reversal of the photo-induced change which led to hole formation by thermally surmounting the ground-state barrier (process (**5**) in Figure 7.21), or relaxation of the strain defining the inhomogeneous line, *e.g.* 'melting' of an Ar matrix . High-temperature erasure of holes occurs for almost all hole-burning materials, the only known exceptions being certain rare-earth ions in crystals, which have been found to retain their spectral hole structure even after cycling to room temperature.[155]

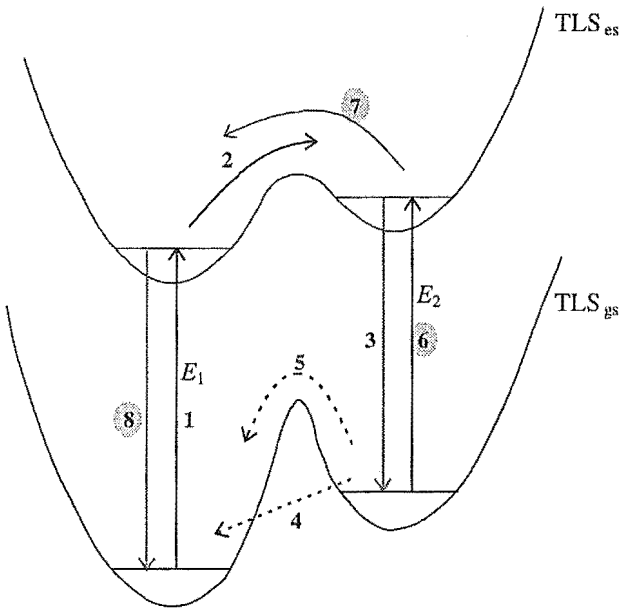

Figure 7.21. Proposed mechanisms for spontaneous hole filling (**4**), annealing (**5**), and laser-induced hole filling (**6**), (**7**), (**8**) in a guest-coupled TLS.

Laser-induced hole filling (LIHF) is a third phenomenon by which a hole burnt at a certain energy (E_1), is partially filled by subsequent burning at a secondary energy (E_2). A number of cases of LIHF were observed in the experiments discussed in this chapter, although the phenomenon was not investigated in a systematic way.

way. LIHF has been reported for both PHB and NPHB mechanisms. Despite its scientific and technological importance (it is a limiting factor in high-density optical information storage[156]) the mechanism by which LIHF operates is not well understood.

The first attempt to interpret the phenomenon of LIHF was made by Fearey *et al.*,[157] who studied holes burnt in dye- and rare-earth-ion-doped polymers. They proposed a model involving energy transfer between guest molecules by means of host TLSs. This mechanism could not, however, explain the observed dependence of the filling efficiency on the sign of $E_2 - E_1$; all investigations have noted that LIHF is significantly more efficient when the second burn is to the blue of the first, *i.e.* $E_2 > E_1$. Van der Berg and Vőlker[158]proposed that for ionic dyes in alcohol glasses, LIHF was caused by reversion of the photoproduct present at E_2 by a photochemical-type mechanism. Shu and Small[151] invoke the same antihole-reversion mechanism for cresyl violet in a polyvinyl alcohol polymer (a NPHB system which has similar characteristics to those seen in the MPc/Ar spectra), but attribute it to guest-coupled TLS interconversion. This is represented by processes (6), (7) and (8) in Figure 7.21. In this case, the general blue-shifting of the antihole seen for dyes in amorphous solids explains the relative ease of filling for $E_2 > E_1$. The weak filling observed for $E_2 < E_1$ was suggested to be due to excitation by the primary burn of high-energy vibrations of the host to the red of E_1, which would form a weak, uniform background hole. Murase and Horrie,[156,159] primarily interested in cases with $E_2 < E_1$, built on this idea. They proposed that LIHF was due to 'non-site-selective' excitations, such as those due to lattice vibrations and vibronic transitions, and that the initial hole appears to fill because of a smaller decrease in absorption in the region of the original hole than in its non-burned surroundings. The results of Pan *et al.*[160] agree with this latter explanation; they burnt a series of holes at 1.5-nm intervals from higher to lower energy, and found that hole filling at E_1 was primarily due to interaction of the pseudo-PSBH.

Of all the investigations described above, the work of Shu and Small[151] appears to be the most comprehensive, and most relevant to our experiments. Four examples of LIHF observed in our data are shown in Figures 7.22, 7.23, 7.24 and 7.25. The second hole spectrum in each figure shows the difference between the two burns, *i.e.* $\delta A_1 = A_1 - A_0$, $\delta A_2 = A_2 - A_1$, where A_0 is the absorption spectrum before the first burn. In each case, the burn fluences for E_1 and E_2 were approximately equal.

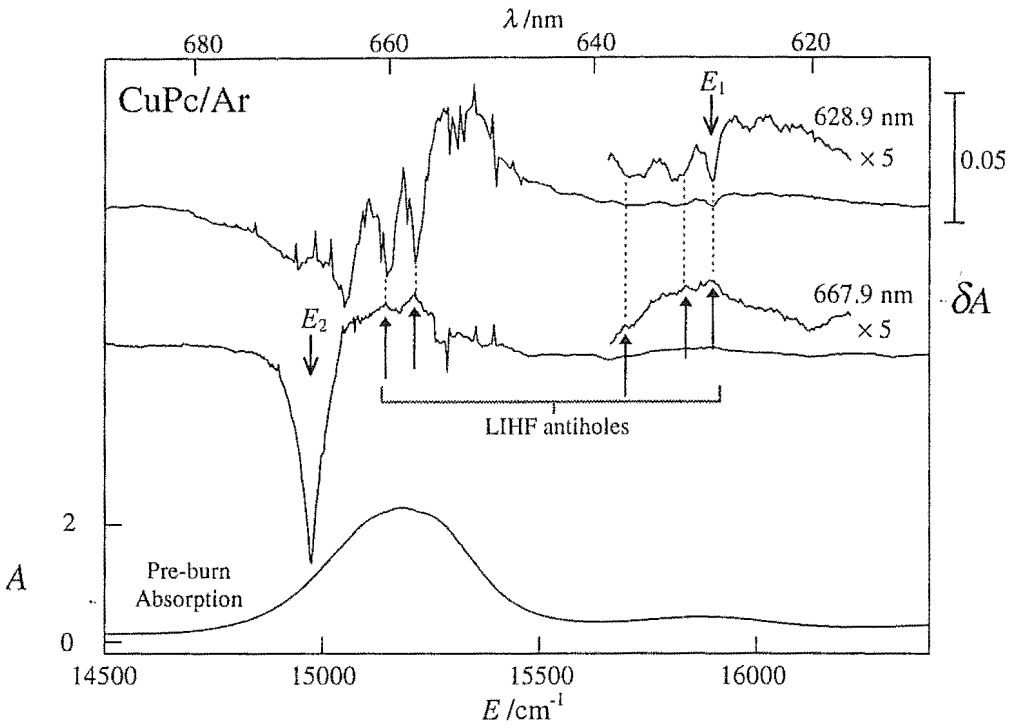

Figure 7.22. Two consecutive burns into CuPc/Ar. The first burn at 628.9.nm (top spectrum) is slightly filled by the second burn (667.9 nm, shown in the central spectrum). The clearest examples of individual LIHF antiholes are indicated by arrows.

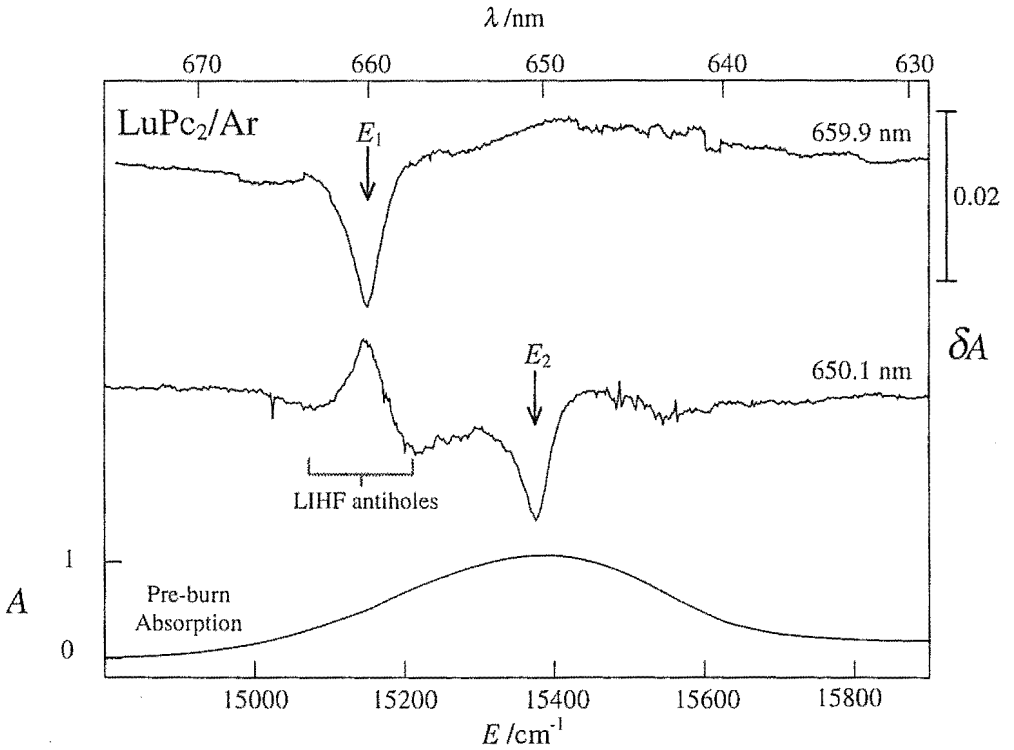

Figure 7.23. Two consecutive burns into the Q(0,0) band of $LuPc_2$/Ar at 659.9 nm (top) and 650.1 nm (centre) respectively. Substantial LIHF, seen in the second spectrum, is indicated.

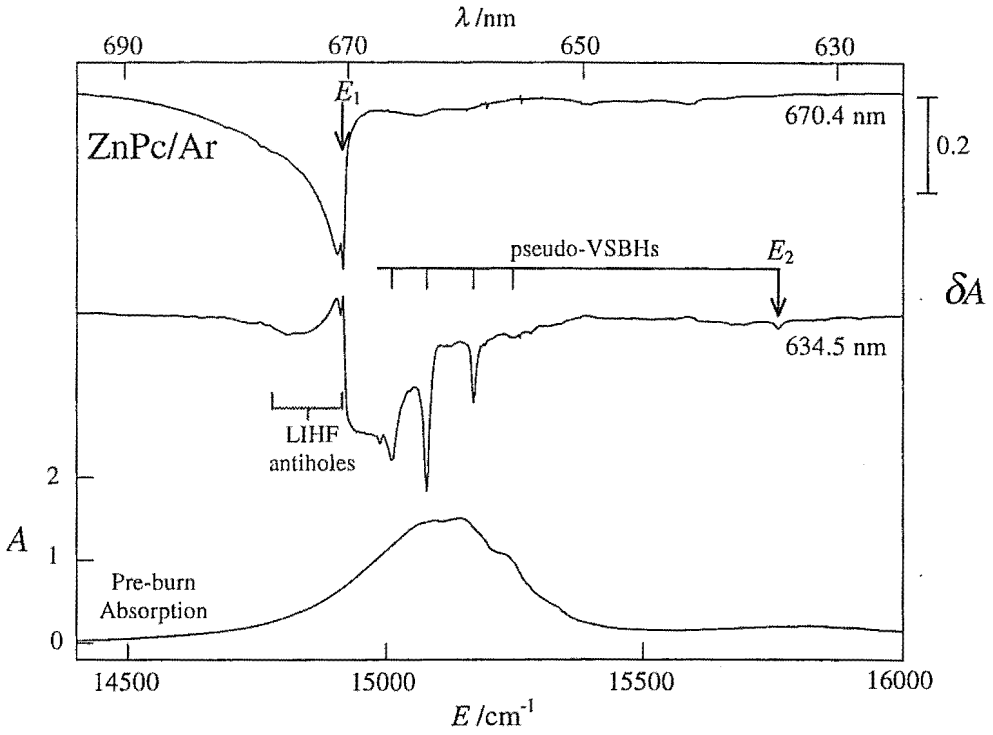

Figure 7.24. Two consecutive burns into the ZnPc/Ar matrix at 670.4 nm (top) and 634.5 nm (centre). Substantial LIHF is seen in the bottom spectrum. A number of spectral features are marked.

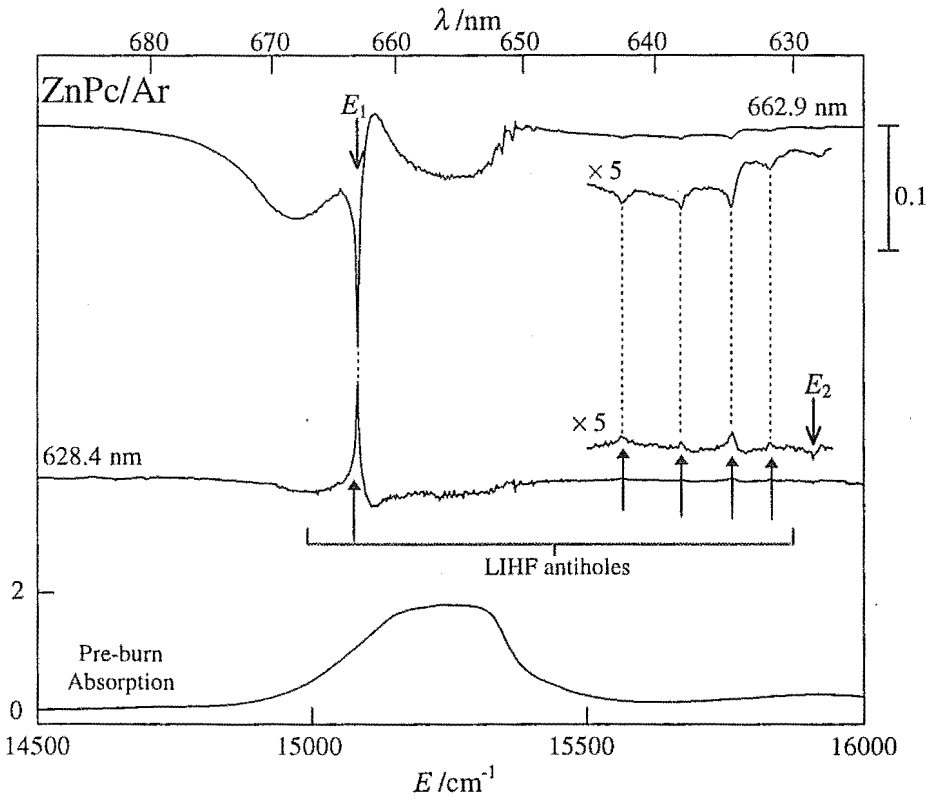

Figure 7.25. Two consecutive burns into the ZnPc/Ar matrix investigated at 11 K. Holes were burnt at 662.9 nm (top) then 628.4 nm (centre). Substantial LIHF is seen in the bottom spectrum. Evidence of photobleaching can also be seen. A number of spectral features are marked.

Figure 7.22 shows an example of LIHF with $E_2 < E_1$; a burn into the Q(1,0) band of CuPc/Ar (628.9 nm) is followed by a burn at 667.9 nm, into Q(0,0). Hole filling is weak ($\sim 10-20\%$), and in the Q(0,0) region is seen as two sharper antiholes superimposed on the broader photoproduct antihole band of the second burn. LIHF can also be seen in the Q(1,0) region. In contrast, when the order of the two burns is reversed to give $E_2 > E_1$, the extent of LIHF is substantial, as seen in the $LuPc_2$/Ar and ZnPc/Ar spectra of Figures 7.23, 7.24 and 7.25. Because of lack of knowledge about the nature of the PSBHs, pseudo-PSBHs and photoproduct antiholes of these systems, it is not possible to give accurate hole-filling percentages, but these are estimated at 70-90%.

In the $LuPc_2$/Ar spectra of Figure 7.23, both holes were burnt in the origin band, as was the case in Shu and Small's work.[151] Note that the widths of the hole and the LIHF-antihole are equal. Here, the antihole is superimposed on the pseudo-PSBH of the second burn. Figure 7.24 shows spectra of holes burnt into the Q(0,0) band of ZnPc/Ar (670.4 nm), and then the Q(1,0) band (634.5 nm). Again, the LIHF-antihole appears in the same region as a broad hole (probably due to overlapping PSBHs and pseudo-PSBHs). Correction of the E_2 burn spectrum for 90% hole filling leaves a smooth 'baseline' in the region of E_1, indicating that the pseudo-PSBH and ZPH are filling in concert. The efficiency of this LIHF process is quite remarkable, and shows not only that 90% of the molecules burnt by the first laser are altered to have some absorbance at E_2, but also that these molecules have very strong 'memory' of their initial profile, *i.e.* the TLS interchange is very specific.

LIHF was also observed in the ZnPc/Ar matrix investigated at 11 K. As shown in Figure 7.25, a hole was first burnt at 662.9 nm (red side of Q(0,0)) and then in the Q(1,0) overtone band, at 628.4 nm. From comparison of the shape of the holes and LIHF-antiholes it appears that in this case, filling of the ZPH and pseudo-PSBH does not occur in unison, with little of the original pseudo-PSBH being filled. However, this cannot be determined for certain, due to the occurrence of photobleaching (Section 7.3.2.2), which, at this temperature, occurs with each burn.

7.3.7 The Hole-Burning Mechanism

The absorption and MCD hole-burning spectra presented here appear to provide evidence both for and against a NPHB mechanism in these materials. Consider first the evidence supporting such a mechanism:

(i) The hole profiles are very similar to those observed for NPHB of dye/polymer systems.[128,147,151]

(ii) With the exception of the 670.4 nm ZnPc burn, the photoproduct antiholes associated with Q(0,0) holes are confined within the inhomogeneous envelope of Q(0,0), indicating that the molecules are chemically unchanged by the process, but that their environments and/or conformations have been altered.

(iii) The integrated intensities of the holes and antiholes approximately cancel. (Due to problems with baseline consistency, accurate determination of the zero-point of the hole spectra is difficult, and so comparison of integrated intensities can only be approximate.) This is not necessarily true for photochemical hole burning, as the oscillator strengths of the photoproducts need not be the same as that of the original material.

(iv) The decay of hole-burning efficiency seen for CuPc (as discussed in Section 7.3.5) is typical of a NPHB hole-burning mechanism; molecules residing at the most photoactive sites are rapidly converted, leaving slower-burning species and hence leading to saturation of hole growth.

(v) Evidence of LIHF is compatible with a NPHB mechanism.[151] While some photochemical processes are irreversible, NPHB is intrinsically reversible.

There are strong indications, however, that the hole-burning process in CuPc/Ar is not based on a conventional NPHB mechanism:

(vi) Despite intensive efforts, it has not proved possible to burn holes in a pentacene/Ar matrix of similar concentration prepared under the same conditions.[161] Since NPHB of pentacene is efficient in polymer films,[162] it therefore follows that Ar is not an intrinsically efficient photophysical hole-burning host medium for planar π systems.

(vii) Some holes burnt into the ZnPc/Ar matrix (Figure 7.10) have photoproduct bands that are shifted into regions well outside the Q-band envelope,

indicating a photochemical product.

(viii) Although phosphorescence has been observed for CuPc in a Shpol'skii matrix[149] and in solid CCl_4,[163] no emission was seen from CuPc/Ar down to 6250 cm^{-1} in the experiments covered here, despite the use of a high-sensitivity ADC 403L Ge detector and a much higher concentration than is possible in the above-mentioned solvents.

The last point suggests that the triplet states of the molecules studied here are deactivated by some mechanism. The matrix medium is unlikely to provide solvent-induced non-radiative deactivation pathways that are more efficient than the liquid solutions, so deactivation of ^4E_u and $^2E_u^T$ states of CuPc/Ar probably involves some other mechanism.

Debacker *et al.*[164] have studied the triplet-state deactivation of ZnPc and MgPc in DMSO. They found that the decay kinetics shift from first order in the concentration of triplet-state species to second order as the concentration is increased to $\sim 2 \times 10^{-4}$ mol L^{-1}. Clearly, a triplet-triplet annihilation process operates at higher concentrations. Furthermore, they used transient absorption spectra to detect the intermediate presence of $ZnPc^-$ ions. Hence they concluded that the deactivation process involves charge separation rapidly followed by charge recombination;

$$^3MPc^* + {}^3MPc^* \rightarrow MPc^+ + MPc^- \rightarrow {}^1MPc + {}^1MPc \qquad (7.9)$$

where $*$ indicates an electronic excited state. In solution, this process is facilitated by molecular diffusion, which allows close approach between molecules within the triplet-state lifetime. But given the very much higher concentrations found in the Ar matrices studied here (Table 7.1), an equivalent process (involving quartet states for the odd-electron CuPc and $LuPc_2$ systems) seems entirely possible in the MPcs, even in the absence of diffusion. This mechanism would explain the phosphorescence quenching of CuPc in Ar. Further empirical evidence of significant inter-chromophore interactions in concentrated Ar matrices is obtained from two sources. Firstly, the observed red shifting of emission from even-electron MPc systems[33,165] may be accounted for by inter-molecular dipole-dipole energy transfer. Secondly, a weak absorption band was observed to the red of the Q(0,0) band in the CuPc/Ar and $LuPc_2$/Ar matrices studied here at 1.6 K (at 14530 and 14230 cm^{-1} respectively). This feature has not been seen in more dilute matrices of the same

chromophores, and has a similar separation from the Q(0,0) band (although significantly less intensity) as a band observed by Lucia *et al.*,[59] which they attributed to intermolecular interactions.

It is proposed here that the process described in (7.9) could be responsible for hole-burning in the MPc/Ar matrices as follows. Charge separation will impose large physical changes on the molecules that may in turn substantially disrupt their local environment. Rapid electron back-transfer means that the overall process leaves the system chemically unchanged so that the resultant holes have the characteristics (i) to (v) typical of NPHB. Although the overall process is equivalent to NPHB, it essentially involves photochemical steps. This proposed mechanism shares similarities with one discussed by van der Berg and Volker[158] for ionic dye molecules, which involved *intramolecular* electron transfer from one side of the guest molecule to the other.

The data for the 670.4-nm and 633.0-nm burns into ZnPc/Ar in Figure 7.10 lend substantial support for this proposal. The photoproduct bands occur in regions in which $ZnPc^+$ and $ZnPc^-$ absorb,[166,167] suggesting that some of the intermediate ions of (7.9) are trapped. Why such trapping would be more likely for ZnPc/Ar than for CuPc/Ar and $LuPc_2$/Ar is debatable, but the explanation may involve the relative efficiency of intersystem crossing, excited-state lifetimes, and the effects of concentration.

The MCD-hole spectra also provide indirect support for this proposed hole-burning mechanism. The sign of each MCD hole unambiguously defines the SO-CF level (Q_+ or Q_-) into which the excitation occurs. If the hole-burning mechanism involves a single chromophore, the Q_+ holes (at the blue end of Q(0,0)) should be broader due to a shorter lifetime induced by intramolecular relaxation to Q_-. However, the hole widths seen in Figures 7.15, 7.16 and 7.17 are almost independent of the burn wavelength, suggesting that intermolecular processes play a dominant role in their determination.

7.4 Conclusion

A combination of matrix-isolation, hole-burning and magnetooptical techniques have been applied to CuPc, ZnPc and $LuPc_2$ in Ar matrices. Holes were burnt at ~1.6 K and could be filled by warming the sample to ~28 K for 10-20 min. Broad holes were observed in the Q(0,0) band of (non-fluorescent) CuPc/Ar and $LuPc_2$Ar, and instrument-limited holes in ZnPc. The hole-burning kinetics of CuPc have been analysed and the initial quantum efficiency of burning is estimated at $\sim 10^{-6}$. The presence of VSBHs and pseudo-VSBHs has allowed the determination of excited-state vibrational frequencies for all three species.

The structure of the hole-MCD spectra provide evidence that the Q states are split by crystal-field and, for CuPc and $LuPc_2$, spin-orbit interactions (qualitatively confirming the temperature-dependence analysis of Chapters 4 and 6); with transitions in the red and blue wings of the Q(0,0) envelope terminating predominantly in a lower- (Q_-) and a higher-energy (Q_+) level respectively. The complex nature of the Q-band region of the $LuPc_2$/Ar system is evident in the MCD-hole spectra, and further experiments may provide information regarding CF and SO splittings of the many states in this region.

Although the hole spectra are similar to those expected of a NPHB mechanism, more detailed observations reveal significant discrepancies. These can be rationalised in terms of an intermolecular charge-separation mechanism followed by fast charge-recombination/electron back-transfer involving the triplet states of the Pc ligands. This mechanism is consistent with previously observed triplet decay kinetics[164] and similar to an intramolecular process suggested by van der Berg and Volker[158] for ionic dye molecules.

Although it would have been informative to carry out other experiments which suggest themselves from this analysis, due to financial and temporal constraints (arising largely from the fact that the work was not carried out in our laboratory), this was not possible. Nonetheless, the preliminary data presented here give an introduction to the interesting phenomena seen in MPcs in Ar matrices, as well as providing the first report of the combination of hole-burning and MCD spectroscopies.

The results obtained show that the situation is not nearly as simple as first envisaged, and that it is not easy to get precise, unambiguous information. This is partly due to the fact that the Ar matrices studied showed broad bands in the absorption and MCD spectra, indicating a large number of sites with poor correlation of ΔQ. Other researchers[19,152] have seen sharp site structure for ZnPc/Ar, indicating a much higher degree of ΔQ correlation. It is suggested that further work in this area might involve producing matrices for which spectra are dominated by sharp bands, and burning into these sharp sites. This should be possible for ZnPc/Ar and $LuPc_2$/Ar, but might be difficult for CuPc/Ar, which seems to be intrinsically broad. Sharp site structure will also make investigation of Jahn-Teller effects viable, facilitating analysis of SO and CF splittings of the excited states.

Another area of further work would be investigation of the differences in Δ_{phonon} and E_{phonon} values observed for ZnPc/Ar, CuPc/Ar and $LuPc_2$/Ar. In particular, experiments employing a range of matrix concentrations would show whether intermolecular host-host interactions have any effect on this value.

Chapter 8

Conclusion

This thesis describes some of the types of molecular information which can be obtained from the application of absorption, MCD and hole-burning spectroscopies to a range of metallophthalocyanines (MPcs) and metalloporphyrins. Such materials were for the main part studied in Ar matrices. The technique of matrix isolation provides a number of benefits over other condensed-phase samples, in particular, the reduction of intermolecular interactions between the chromophore molecules, often leading to sharper spectral bands. The matrix host, Ar, is transparent down to vacuum-UV wavelengths, interacts only weakly with embedded molecules, and is optically isotropic; the latter point being of importance in the measurement of MCD.

One of the effects studied in this thesis requires the measurement of MCD spectra at low, accurately defined temperatures. This has been achieved by immersing samples in liquid helium, in the bore of a super-conducting magnet. Compatibility of this technique with the use of matrix-isolated samples requires that a matrix be transferred from the deposition region, where it is under vacuum, into the magnetic field and optical path, where it is bathed in liquid (or gaseous) helium. A 'matrix-injection' procedure, which accomplishes this task, has been refined.

The Q ($\pi \rightarrow \pi^*$) bands of the odd-electron CuPc, CoPc and CuTBP molecules (which have degenerate ground states) have been found to exhibit weakly temperature-dependent MCD, with the magnitude of the MCD increasing with decreasing temperature. This effect has been shown to be due to zero-field splitting ($\sim$1 - 2 cm^{-1}) of the excited-state levels, arising from the interaction of exchange and spin-orbit coupling between allowed and forbidden excited-state ^2E_u terms. The SO coupling is ascribed to a (relatively small) degree of mixing of the metal into the essentially ligand-based excited-state $e_g(\pi)$ molecular orbital. In the case of CuPc, (the only molecule for which appropriate theoretical parameters are available) the calculated splitting is within a factor of 2 of that found experimentally. It is notable that the small zero-field splittings have been obtained in the presence of absorption bandwidths of $\sim$300 cm^{-1}, indicating the utility of MCD in the extrac-

tion of information on weak perturbations not accessible by conventional absorption spectroscopy. The work pertaining to CuPc has been published in the *Journal of Physical Chemistry*.[168]

The bisphthalocyanine, $LuPc_2$, has also been observed to exhibit MCD temperature dependence of both the Q and RV bands. In the case of the Q band, this effect is weak, and has been shown to arise from a zero-field splitting ($\sim$1.5 cm^{-1}) of the excited-state levels, caused by first-order spin-orbit coupling. The strength of this coupling is ascribed to the Lu^{3+} p-orbital contribution to one of the excited-state molecular orbitals. The spin-orbit coupling constant for this metal orbital is very large ($\zeta_{5p} \gtrsim 9000$ cm^{-1}), and so only a small contribution ($\lesssim 0.05\%$) is required to explain the observed splitting. The temperature dependence of the RV band is significantly stronger, with the sign of the $\mathcal{A}$-term-shaped band changing from positive at high temperatures to negative at lower temperatures. The relative strength of this effect (equivalent to a zero-field splitting of $\sim$65 cm^{-1}) has been attributed to a larger metal contribution to the orbitally degenerate excited-state molecular orbital. The RV band has not previously been definitively assigned. From the observed temperature dependence results, either of two assignments proposed in the literature are possible. Measurement of absorption spectra over a wider temperature range and investigation of the temperature dependence of the BV band are two areas of research which might aid the assignment of the RV band - theoretical calculations which explicitly include metal contributions would also be extremely useful.

Hole-burning is a spectroscopic technique by which discrete (or a small number of) sites within an inhomogeneously broadened absorption band may be investigated. In an effort to determine site-specific information on excited-state magnetic effects in MPcs (for comparison with the site-averaged parameters obtainable by MCD), experiments in which a magnetic field was applied after holes had been burnt have been carried out on ZnPc/Ar, CuPc/Ar and $LuPc_2$/Ar, allowing the measurement of hole-MCD spectra. However, the spectra obtained were found to be significantly more complicated than first envisaged, and analysis was necessarily qualitative rather than quantitative. For each sample, evidence for crystal-field splitting and spin-orbit splitting (for CuPc and $LuPc_2$) was observed, with transitions in the red and blue wings of the Q(0,0) band terminating in lower- and higher-energy levels respectively.

A hole-burning mechanism has been proposed which involves intermolecular charge separation, followed by fast charge recombination. The observation of vibrational and pseudo-vibrational side-band holes in the hole-absorption and hole-MCD spectra has allowed determination of excited-state vibrational frequencies for all three molecules. Preliminary results have been published in the *Journal of Luminescence*,[51] and those pertaining to CuPc in *Chemical Physics Letters*.[169] Part of the problem with the complexity of the hole spectra arises from the fact that the Ar matrices studied all showed broad absorption and MCD bands, indicating a large number of poorly correlated sites. Sharp site structure has been observed by other researchers for ZnPc, and it is suggested that further work in this area might involve producing spectra with such sharp bands, and burning into these well-defined sites.

Appendix I

$2jm$s for $D_{4d} \supset D_4 \supset C_4$

The 2jms and complex conjugates of each irrep and partner (in Butler and Mulliken notation) are given. The D_4 values have not been tabulated, except in the case of the irrep 2 (E_2), where the path 2 2 2 (E_2 b_1 ε) is represented by the partner label 2/2, and the path 2 $\widetilde{2}$ 2 (E_2 b_2 ζ) by the partner label $\widetilde{2}$/2.

$\lvert a\,\alpha\rangle$	$\equiv$	$\lvert a\,a_1\rangle$	$2jm$ $\binom{a}{\alpha}$	$\lvert a^*\,\alpha^*\rangle$	$\equiv$	$\lvert a^*\,a_1^*\rangle$
A_1 a_1		0 0	+1	A_1 a_1		0 0
A_2 a_2		$\widetilde{0}$ 0	−1	A_2 a_2		$\widetilde{0}$ 0
B_1 b_1		4 0	+1	B_1 b_1		4 0
B_2 b_2		$\widetilde{4}$ 0	−1	B_2 b_2		$\widetilde{4}$ 0
E_1 1		3 1	+1	E_1 -1		3 -1
E_1 -1		3 -1	+1	E_1 1		3 1
E_2 ε		2 2/2	+1	E_2 ε		2 2/2
E_2 ζ		2 $\widetilde{2}$/2	−1	E_2 ζ		2 $\widetilde{2}$/2
E_3 1		1 1	+1	E_3 -1		1 -1
E_3 -1		1 -1	+1	E_3 1		1 1
$E_{1/2}$ $\frac{1}{2}$		$\frac{1}{2}$ $\frac{1}{2}$	+1	$E_{1/2}$ $-\frac{1}{2}$		$\frac{1}{2}$ $-\frac{1}{2}$
$E_{1/2}$ $-\frac{1}{2}$		$\frac{1}{2}$ $-\frac{1}{2}$	−1	$E_{1/2}$ $\frac{1}{2}$		$\frac{1}{2}$ $\frac{1}{2}$
$E_{3/2}$ $\frac{3}{2}$		$\frac{3}{2}$ $\frac{3}{2}$	+1	$E_{3/2}$ $-\frac{3}{2}$		$\frac{3}{2}$ $-\frac{3}{2}$
$E_{3/2}$ $-\frac{3}{2}$		$\frac{3}{2}$ $-\frac{3}{2}$	−1	$E_{3/2}$ $\frac{3}{2}$		$\frac{3}{2}$ $\frac{3}{2}$
$E_{5/2}$ $\frac{3}{2}$		$\frac{5}{2}$ $\frac{3}{2}$	+1	$E_{5/2}$ $-\frac{3}{2}$		$\frac{5}{2}$ $-\frac{3}{2}$
$E_{5/2}$ $-\frac{3}{2}$		$\frac{5}{2}$ $-\frac{3}{2}$	−1	$E_{5/2}$ $\frac{3}{2}$		$\frac{5}{2}$ $\frac{3}{2}$
$E_{7/2}$ $\frac{1}{2}$		$\frac{7}{2}$ $\frac{1}{2}$	+1	$E_{7/2}$ $-\frac{1}{2}$		$\frac{7}{2}$ $-\frac{1}{2}$
$E_{7/2}$ $-\frac{1}{2}$		$\frac{7}{2}$ $-\frac{1}{2}$	−1	$E_{7/2}$ $\frac{1}{2}$		$\frac{7}{2}$ $\frac{1}{2}$

Appendix II

$3jm$s for $D_{4d} \supset D_4 \supset C_4$

The $3jm$s listed here are given in Butler notation, the correspondence of this with Mulliken notation may be seen by inspection of Appendix I. The D_4 values have not been tabulated, except in the case of the irrep 2, where the path 2 2 2 is represented by the partner label 2/2, and the path 2 $\widetilde{2}$ 2 by the partner label $\widetilde{2}$/2. The $3jm$s are ordered by the right-hand element, the order being the one-dimensional, then two-dimensional irreps in numerical order. In each case, the right-hand element has lowest rank in this order. The superscript † indicates that the 3jm is odd (should be multiplied by -1) with respect to permutation of any two columns.

0	0	0	$3jm$
0	0	0	1

$\widetilde{0}$	$\widetilde{0}$	0	$3jm$
0	0	0	-1

4	4	0	$3jm$
0	0	0	1

$\widetilde{4}$	$\widetilde{4}$	0	$3jm$
0	0	0	-1

$\frac{1}{2}$	$\frac{1}{2}$	0	$3jm^\dagger$
$\frac{1}{2}$	$-\frac{1}{2}$	0	$\frac{1}{\sqrt{2}}$

1	1	0	$3jm$
1	-1	0	$\frac{1}{\sqrt{2}}$

$\frac{3}{2}$	$\frac{3}{2}$	0	$3jm^\dagger$
$\frac{3}{2}$	$-\frac{3}{2}$	0	$\frac{1}{\sqrt{2}}$

2	2	0	$3jm$
2/2	2/2	0	$\frac{1}{\sqrt{2}}$
$\widetilde{2}$/2	$\widetilde{2}$/2	0	$-\frac{1}{\sqrt{2}}$

$\frac{5}{2}$	$\frac{5}{2}$	0	$3jm^\dagger$
$\frac{3}{2}$	$-\frac{3}{2}$	0	$\frac{1}{\sqrt{2}}$

3	3	0	$3jm$
1	-1	0	$\frac{1}{\sqrt{2}}$

$\frac{7}{2}$	$\frac{7}{2}$	0	$3jm^\dagger$
$\frac{1}{2}$	$-\frac{1}{2}$	0	$\frac{1}{\sqrt{2}}$

4	$\widetilde{4}$	$\widetilde{0}$	$3jm^\dagger$
0	0	0	-1

$\frac{1}{2}$	$\frac{1}{2}$	$\widetilde{0}$	$3jm$
$\frac{1}{2}$	$-\frac{1}{2}$	0	$\frac{1}{\sqrt{2}}$

1	1	$\widetilde{0}$	$3jm^\dagger$
1	-1	0	$\frac{1}{\sqrt{2}}$

$\frac{3}{2}$	$\frac{3}{2}$	$\widetilde{0}$	$3jm$
$\frac{3}{2}$	$-\frac{3}{2}$	0	$\frac{1}{\sqrt{2}}$

2	2	$\widetilde{0}$	$3jm^{\dagger}$
2/2	$\tilde{2}/2$	0	$\frac{1}{\sqrt{2}}$

$\frac{5}{2}$	$\frac{5}{2}$	$\widetilde{0}$	$3jm$
$\frac{3}{2}$	$-\frac{3}{2}$	0	$-\frac{1}{\sqrt{2}}$

3	3	$\widetilde{0}$	$3jm^{\dagger}$
1	−1	0	$-\frac{1}{\sqrt{2}}$

$\frac{7}{2}$	$\frac{7}{2}$	$\widetilde{0}$	$3jm$
$\frac{1}{2}$	$-\frac{1}{2}$	0	$-\frac{1}{\sqrt{2}}$

$\frac{1}{2}$	$\frac{7}{2}$	4	$3jm$
$\frac{1}{2}$	$-\frac{1}{2}$	0	$-\frac{1}{\sqrt{2}}$
$-\frac{1}{2}$	$\frac{1}{2}$	0	$\frac{1}{\sqrt{2}}$

1	3	4	$3jm$
1	−1	0	$\frac{1}{\sqrt{2}}$
−1	1	0	$\frac{1}{\sqrt{2}}$

$\frac{3}{2}$	$\frac{5}{2}$	4	$3jm$
$\frac{3}{2}$	$-\frac{3}{2}$	0	$-\frac{1}{\sqrt{2}}$
$-\frac{3}{2}$	$\frac{3}{2}$	0	$\frac{1}{\sqrt{2}}$

2	2	4	$3jm$
2/2	2/2	0	$\frac{1}{\sqrt{2}}$
$\tilde{2}/2$	$\tilde{2}/2$	0	$\frac{1}{\sqrt{2}}$

$\frac{1}{2}$	$\frac{7}{2}$	$\widetilde{4}$	$3jm$
$\frac{1}{2}$	$-\frac{1}{2}$	0	$\frac{1}{\sqrt{2}}$
$-\frac{1}{2}$	$\frac{1}{2}$	0	$\frac{1}{\sqrt{2}}$

1	3	$\widetilde{4}$	$3jm$
1	−1	0	$-\frac{1}{\sqrt{2}}$
−1	1	0	$\frac{1}{\sqrt{2}}$

$\frac{3}{2}$	$\frac{5}{2}$	$\widetilde{4}$	$3jm$
$\frac{3}{2}$	$-\frac{3}{2}$	0	$\frac{1}{\sqrt{2}}$
$-\frac{3}{2}$	$\frac{3}{2}$	0	$\frac{1}{\sqrt{2}}$

2	2	$\widetilde{4}$	$3jm$
2/2	$\tilde{2}/2$	0	$\frac{1}{\sqrt{2}}$

$\frac{1}{2}$	1	$\frac{1}{2}$	$3jm$
$\frac{1}{2}$	−1	$\frac{1}{2}$	$\frac{1}{\sqrt{2}}$
$-\frac{1}{2}$	1	$-\frac{1}{2}$	$\frac{1}{\sqrt{2}}$

1	$\frac{3}{2}$	$\frac{1}{2}$	$3jm^{\dagger}$
1	$-\frac{3}{2}$	$\frac{1}{2}$	$\frac{1}{\sqrt{2}}$
−1	$\frac{3}{2}$	$-\frac{1}{2}$	$-\frac{1}{\sqrt{2}}$

$\frac{3}{2}$	2	$\frac{1}{2}$	$3jm$
$\frac{3}{2}$	2/2	$\frac{1}{2}$	$\frac{1}{2}$
$-\frac{3}{2}$	2/2	$-\frac{1}{2}$	$\frac{1}{2}$
$\frac{3}{2}$	$\tilde{2}/2$	$\frac{1}{2}$	$\frac{1}{2}$
$-\frac{3}{2}$	$\tilde{2}/2$	$-\frac{1}{2}$	$-\frac{1}{2}$

2	$\frac{5}{2}$	$\frac{1}{2}$	$3jm^{\dagger}$
2/2	$\frac{5}{2}$	$\frac{1}{2}$	$-\frac{1}{2}$
2/2	$-\frac{5}{2}$	$-\frac{1}{2}$	$-\frac{1}{2}$
$\tilde{2}/2$	$\frac{3}{2}$	$\frac{1}{2}$	$\frac{1}{2}$
$\tilde{2}/2$	$-\frac{3}{2}$	$-\frac{1}{2}$	$-\frac{1}{2}$

$\frac{5}{2}$	3	$\frac{1}{2}$	$3jm$
$\frac{3}{2}$	−1	$-\frac{1}{2}$	$-\frac{1}{\sqrt{2}}$
$-\frac{3}{2}$	1	$\frac{1}{2}$	$\frac{1}{\sqrt{2}}$

3	$\frac{7}{2}$	$\frac{1}{2}$	$3jm^{\dagger}$
1	$-\frac{1}{2}$	$-\frac{1}{2}$	$-\frac{1}{\sqrt{2}}$
−1	$\frac{1}{2}$	$\frac{1}{2}$	$-\frac{1}{\sqrt{2}}$

1	2	1	$3jm$
1	$2/2$	1	$\frac{1}{2}$
-1	$2/2$	-1	$-\frac{1}{2}$
1	$\tilde{2}/2$	1	$\frac{1}{2}$
-1	$\tilde{2}/2$	-1	$-\frac{1}{2}$

$\frac{3}{2}$	$\frac{5}{2}$	1	$3jm^{\dagger}$
$\frac{3}{2}$	$\frac{3}{2}$	1	$-\frac{1}{\sqrt{2}}$
$-\frac{3}{2}$	$-\frac{3}{2}$	1	$\frac{1}{\sqrt{2}}$

2	1	1	$3jm$
$2/2$	1	1	$-\frac{1}{2}$
$2/2$	-1	-1	$-\frac{1}{2}$
$\tilde{2}/2$	1	1	$-\frac{1}{2}$
$\tilde{2}/2$	-1	-1	$\frac{1}{2}$

2	3	1	$3jm$
$2/2$	1	1	$-\frac{1}{2}$
$2/2$	-1	-1	$-\frac{1}{2}$
$\tilde{2}/2$	1	1	$\frac{1}{2}$
$\tilde{2}/2$	-1	-1	$-\frac{1}{2}$

$\frac{5}{2}$	$\frac{7}{2}$	1	$3jm^{\dagger}$
$\frac{3}{2}$	$-\frac{1}{2}$	-1	$-\frac{1}{\sqrt{2}}$
$-\frac{3}{2}$	$\frac{1}{2}$	1	$\frac{1}{\sqrt{2}}$

$\frac{7}{2}$	$\frac{7}{2}$	1	$3jm$
$\frac{1}{2}$	$\frac{1}{2}$	-1	$-\frac{1}{\sqrt{2}}$
$-\frac{1}{2}$	$-\frac{1}{2}$	1	$-\frac{1}{\sqrt{2}}$

$\frac{3}{2}$	3	$\frac{3}{2}$	$3jm$
$\frac{3}{2}$	1	$\frac{3}{2}$	$\frac{1}{\sqrt{2}}$
$-\frac{3}{2}$	-1	$-\frac{3}{2}$	$\frac{1}{\sqrt{2}}$

2	$\frac{7}{2}$	$\frac{3}{2}$	$3jm^{\dagger}$
$2/2$	$\frac{1}{2}$	$\frac{3}{2}$	$\frac{1}{2}$
$2/2$	$-\frac{1}{2}$	$-\frac{3}{2}$	$\frac{1}{2}$
$\tilde{2}/2$	$\frac{1}{2}$	$\frac{3}{2}$	$\frac{1}{2}$
$\tilde{2}/2$	$-\frac{1}{2}$	$-\frac{3}{2}$	$-\frac{1}{2}$

3	$\frac{7}{2}$	$\frac{3}{2}$	$3jm$
1	$\frac{1}{2}$	$-\frac{3}{2}$	$-\frac{1}{\sqrt{2}}$
-1	$-\frac{1}{2}$	$\frac{3}{2}$	$\frac{1}{\sqrt{2}}$

$\frac{5}{2}$	$\frac{7}{2}$	2	$3jm$
$\frac{3}{2}$	$\frac{1}{2}$	$2/2$	$-\frac{1}{2}$
$-\frac{3}{2}$	$-\frac{1}{2}$	$2/2$	$-\frac{1}{2}$
$\frac{3}{2}$	$\frac{1}{2}$	$\tilde{2}/2$	$-\frac{1}{2}$
$-\frac{3}{2}$	$-\frac{1}{2}$	$\tilde{2}/2$	$\frac{1}{2}$

3	3	2	$3jm$
1	1	$2/2$	$\frac{1}{2}$
-1	-1	$2/2$	$\frac{1}{2}$
1	1	$\tilde{2}/2$	$\frac{1}{2}$
-1	-1	$\tilde{2}/2$	$-\frac{1}{2}$

$\frac{5}{2}$	3	$\frac{5}{2}$	$3jm$
$\frac{3}{2}$	1	$\frac{3}{2}$	$-\frac{1}{\sqrt{2}}$
$-\frac{3}{2}$	-1	$-\frac{3}{2}$	$-\frac{1}{\sqrt{2}}$

Appendix III

Transformation Coefficients for $|SO_3\ SO_2\rangle$ to $|D_{4d}\ C_4\rangle$

These transformation coefficients were determined by relating the chains $O_3 \supset SO_3 \supset SO_2 \supset C_4$ and $O_3 \supset D_{\infty h} \supset D_{8h} \supset D_{4d} \supset D_4 \supset C_4$ using the method of Butler.[113]

Parity (O_3)	$\lvert SO_3\ SO_2\rangle$	$\lvert D_{4d}\ C_4\rangle$
+	$\lvert 0\ \ 0\rangle$	$\lvert 0\ \ 0\rangle$
−	$\lvert 0\ \ 0\rangle$	$\lvert 4\ \ 0\rangle$
+	$\lvert \frac{1}{2}\ -\frac{1}{2}\rangle$	$\lvert \frac{1}{2}\ -\frac{1}{2}\rangle$
+	$\lvert \frac{1}{2}\ \ \frac{1}{2}\rangle$	$\lvert \frac{1}{2}\ \ \frac{1}{2}\rangle$
−	$\lvert \frac{1}{2}\ -\frac{1}{2}\rangle$	$\lvert \frac{7}{2}\ -\frac{1}{2}\rangle$
−	$\lvert \frac{1}{2}\ \ \frac{1}{2}\rangle$	$\lvert \frac{7}{2}\ \ \frac{1}{2}\rangle$
+	$\lvert 1\ \ 0\rangle$	$\lvert \widetilde{0}\ \ 0\rangle$
+	$\lvert 1\ -1\rangle$	$-\lvert 1\ -1\rangle$
+	$\lvert 1\ \ 1\rangle$	$-\lvert 1\ \ 1\rangle$
−	$\lvert 1\ \ 0\rangle$	$\lvert \widetilde{4}\ \ 0\rangle$
−	$\lvert 1\ -1\rangle$	$-\lvert 3\ -1\rangle$
−	$\lvert 1\ \ 1\rangle$	$-\lvert 3\ \ 1\rangle$
+	$\lvert \frac{3}{2}\ -\frac{1}{2}\rangle$	$\lvert \frac{1}{2}\ -\frac{1}{2}\rangle$
+	$\lvert \frac{3}{2}\ \ \frac{1}{2}\rangle$	$-\lvert \frac{1}{2}\ \ \frac{1}{2}\rangle$
+	$\lvert \frac{3}{2}\ -\frac{3}{2}\rangle$	$\lvert \frac{3}{2}\ -\frac{3}{2}\rangle$
+	$\lvert \frac{3}{2}\ \ \frac{3}{2}\rangle$	$\lvert \frac{3}{2}\ \ \frac{3}{2}\rangle$
−	$\lvert \frac{3}{2}\ -\frac{1}{2}\rangle$	$\lvert \frac{7}{2}\ -\frac{1}{2}\rangle$
−	$\lvert \frac{3}{2}\ \ \frac{1}{2}\rangle$	$-\lvert \frac{7}{2}\ \ \frac{1}{2}\rangle$
−	$\lvert \frac{3}{2}\ -\frac{3}{2}\rangle$	$\lvert \frac{5}{2}\ -\frac{3}{2}\rangle$
−	$\lvert \frac{3}{2}\ \ \frac{3}{2}\rangle$	$\lvert \frac{5}{2}\ \ \frac{3}{2}\rangle$
+	$\lvert 2\ \ 0\rangle$	$\lvert 0\ \ 0\rangle$
+	$\lvert 2\ -1\rangle$	$-\lvert 1\ -1\rangle$
+	$\lvert 2\ \ 1\rangle$	$\lvert 1\ \ 1\rangle$
−	$\lvert 2\ \ 0\rangle$	$\lvert 4\ \ 0\rangle$
−	$\lvert 2\ -1\rangle$	$-\lvert 3\ -1\rangle$
−	$\lvert 2\ \ 1\rangle$	$\lvert 3\ \ 1\rangle$

Appendix IV

HOLES.BAS

This QuickBASIC program simulates hole-absorption spectra, as discussed in Chapter 7. A number of the subroutines handling the plotting of spectra to the screen and a HPG file have been omitted. Note that due to constraints of page size, some lines of code have been wrapped to the next line. This is indicated by '...' at the point at which the line is broken.

```
'*************************************************************************
'                              HOLES.BAS
'
'          By Cara Dunford                                    1996

'  This program calculates the lineshape of spectral holes, based on
'  equations (1), (2) and (3) from Lee, Hayes and Small, J. Chem. Phys.
'  91(6), 1989, p 3463- 3469.
'
'  Subroutines from HARDPLOT and SCRNPLOT are called for plotting of
'  spectra to HPG files and the screen.
'*************************************************************************

REM $DYNAMIC

DECLARE SUB calcAo ()
DECLARE SUB ChoosePattern (HIFORE AS INTEGER, NFORE AS INTEGER, Boxfore AS INTEGER, ...
 PATTEDIT AS INTEGER, PATTLENGTH AS SINGLE, REESET AS INTEGER)
DECLARE SUB InitialValues ()
DECLARE SUB exptplot (multiple)
DECLARE SUB ReadBlk02 ()
DECLARE SUB getdata2 ()
DECLARE SUB display (multiple)
DECLARE SUB answer2 ()
DECLARE SUB BurntBandAbs ()
DECLARE SUB diffSpec ()
DECLARE SUB BandAbs ()
DECLARE SUB mcd (hardplotMCD$, Zeeman!)
DECLARE SUB BandWidth ()
DECLARE SUB gaussian (gauss!, EminusEmax!, FWHM!)
DECLARE SUB PlotInfo (info1$, info2$, info3$, info4$)
DECLARE SUB lorentzian (lorentz!, EminusEmax!, FWHM!)
DECLARE SUB FCfactor ()
DECLARE SUB integral ()
DECLARE SUB triangulation (area, integrand, oldintegrand)
DECLARE SUB scale (XMin!, XMax!, YMin!, YMax!, Xscale!, Yscale!)
DECLARE SUB PU ()
DECLARE SUB PD ()
DECLARE SUB plot (XMin AS SINGLE, XMax AS SINGLE, YMin AS SINGLE, YMax AS SINGLE)
DECLARE SUB filename (COM$, end$, ToWrite )
DECLARE SUB WIND1 (Topy AS INTEGER, LftX AS INTEGER, BOTY AS INTEGER, RTX AS INTEGER, ...
 Boxfore AS INTEGER)
DECLARE SUB plotteron (COM$)
DECLARE SUB chooseframe (NFORE)
```

```
DECLARE SUB choosepens (NUMPENS)
DECLARE SUB GetPen (IPEN AS INTEGER)
DECLARE SUB plottitle (ITITL AS STRING)
DECLARE SUB plotaxes ()
DECLARE SUB sr (WDTH AS SINGLE, HEIGHT AS SINGLE, IC AS INTEGER)
DECLARE SUB sc (XMin AS INTEGER, XMax AS INTEGER, YMin AS INTEGER, YMax AS INTEGER, ...
 IZERO AS INTEGER)
DECLARE SUB pa (X AS SINGLE, Y AS SINGLE)
DECLARE SUB lb (ITITL AS STRING)
DECLARE SUB DI (RUNN AS SINGLE, RISE AS SINGLE, ISET AS INTEGER)
DECLARE SUB Plotticks (XMin AS SINGLE, XMax AS SINGLE, YMin AS SINGLE, YMax AS SINGLE, ...
 axis AS INTEGER)
DECLARE SUB SingleSiteAbs ()
DECLARE SUB axisdraw (XMin!, YMin!, XMax!, YMax!, NFORE AS INTEGER, NBack AS INTEGER, ...
 axis AS INTEGER)

COMMON SHARED findFile COMMON SHARED XMin!, YMin!, XMax!, YMax!
COMMON SHARED NumOmegaSteps, omegamin, omegaStepSize, omegamax
COMMON SHARED nu, s, omegaM, gamma, gammaCap, pi, rmax, omegaB
COMMON SHARED speccolour
COMMON SHARED Xscale, Yscale
COMMON SHARED hardplot$, hardplotPreburn$, hardplotBurn$, hardplotDiff$
COMMON SHARED hardplotBurnInd$, hardplotMCD$
COMMON SHARED TwoExcitedStates$, BandShape$, hardplotexptal$
COMMON SHARED  hardplotPreburnInd$, hardplotDiffInd$, hardplotSingle$
COMMON SHARED nuMin, NuMax, nuM, nuStepSize, NumNuSteps, bandfwhm, bandfwhm1
COMMON SHARED constant, burntime
COMMON SHARED Ao0(), Ao1(), At0(), At1()
COMMON SHARED which
COMMON SHARED BandGorL(), BandGorL1(), bandNormal          'band shape parameters - fn of nu
COMMON SHARED SiteFWHM(), FCfac()             'single-site Lorentzian band width
COMMON SHARED AbsShift                   'energy splitting of excited states
COMMON SHARED multiple, ymaxexpt, ymaxexpt1, exptal$, specfitWidth$, TwoFiles$
COMMON SHARED YmaxCalc, YmaxCalc1

COMMON SHARED HoldBlock
COMMON SHARED LAB$(), Xexpt(), Yexpt(), FileNum AS INTEGER
COMMON SHARED numpts AS INTEGER, Kopt  AS INTEGER, BaseLined
COMMON SHARED Topy AS INTEGER, LftX AS INTEGER, BOTY AS INTEGER
COMMON SHARED RTX AS INTEGER, Boxfore AS INTEGER

'*************************************************************************
'  Setting up screen
        CLS
        SCREEN 9, , 0, 0
        COLOR 7, 0
        WIDTH 80, 43
        VIEW (640 / 11, 350 / 11)-(640 / 1.1, 350 / 1.1)

        CALL InitialValues

'*************************************************************************
'  Set up plotter file
        IF hardplot$ = "Y" THEN
           SCREEN 9, , 1, 1
           CALL plot(XMin, XMax, YMin, YMax)
           CALL scale(XMin, XMax, YMin, YMax, Xscale, Yscale)
           CALL sc(XMin * Xscale, XMax * Xscale, YMin * Yscale, YMax * Yscale, 1)
           WINDOW (XMin, YMin)-(XMax, YMax)
           SCREEN 9, , 0, 0
         END IF

'*************************************************************************
'  To get an experimental data file
```

```
        IF exptal$ = "Y" THEN
           CALL filename(COM$, ".DAT", 0, "Name of hole data file ? ")
           CALL ReadBlk02
           CALL getdata2
           CALL display(1)
           IF hardplotexptal$ = "Y" THEN
              SCREEN 9, , 1, 1
              CLS 0
              COLOR 10
              PRINT "For the plotting of the experimental hole data ...."
              CALL ChoosePattern(10, 3, 10, 7, 1, 1)       'set line pattern
              CALL exptplot(1)          ' Hard plot experimental data points
              SCREEN 9, , 0, 0
              WINDOW (XMin, YMin)-(XMax, YMax)
            END IF
           IF TwoFiles$ = "Y" THEN
              CALL filename(COM$, ".DAT", 0, "Name of Abs data file ? ")
              CALL ReadBlk02
              CALL getdata2
              CALL display(multiple)
              IF hardplotexptal$ = "Y" THEN
                 SCREEN 9, , 1, 1
                 CLS 0
                 LOCATE 6, 8
                 COLOR 10
                 PRINT "For the plotting of the experimental Abs data ...."
                 CALL ChoosePattern(10, 3, 10, 7, 1, 1)       'set line pattern
                 CALL exptplot(multiple)          ' Hard plot experimental data points
                 SCREEN 9, , 0, 0
                 WINDOW (XMin, YMin)-(XMax, YMax)
               END IF
            END IF
         ELSE                    ' Set up screen plot if no experimental data file
          CALL axisdraw(XMin!, YMin!, XMax!, YMax!, 7, 1, 1)
        END IF
        CALL FCfactor
        CALL BandWidth
        CALL SingleSiteAbs
        CALL BandAbs
        BEEP
      FOR i = 1 TO 3
        IF i = 1 THEN burntime = .000001
        IF i = 2 THEN burntime = .00001
        IF i = 3 THEN burntime = .0001
        CALL BurntBandAbs
        BEEP
        CALL diffSpec
      NEXT i

STOP
CLOSE #23                 'closes HPG file
STOP

'---------------  Error routine  -------------------------------------

nofile: IF ERR = 53 THEN
           findFile            RESUME NEXT
           'STOP
         END IF
'-------------------------------------------------------------------------

ohno:

STOP
```

```
RESUME
STOP

REM $STATIC
SUB BandAbs

REM $DYNAMIC
'*************************************************************************
'  This subroutine calculates the pre-burn absorption spectrum.
'
'  The equation for absorption is A = gamma*c*l*E*Do*f(E)
'  where Do is the dipole strength of the transition and f is the lineshape.
'  E is the energy.  The intensity at the band maximum (Io) is given by the
'  equation for A at the corresponding energy, Eo.
'  Hence, we can rearrange the eqn in Io to give Do = Io/(gamma*c*l*Eo*f(Eo)
'  and so our equation for absorbance becomes
'                        A = Io * (E/Eo) * (f(E)/f(Eo))
'  Thus we now have a band height parameter which is independent of the band
'  width.  (Otherwise, since f(E) is normalised, f(Eo) is dependent on the
'  band width, and so we cannot change the height independently.)
'*************************************************************************


REDIM BandGorL(-1 TO NumNuSteps)
REDIM Ao0(0 TO NumOmegaSteps)

'*************************************************************************
'  Calculate Band Absorption as a function of nu, and the
'  band normalising factor. (Not a function of omega)
'  ie, calculates a Gaussian or Lorentzian based on the given
'  band width, and band maximum (from this it determines the height)


        FOR j = 0 TO NumNuSteps
           nu = nuMin + j * nuStepSize
           IF BandShape$ = "G" THEN
              CALL gaussian(BandGorL(j), nu - nuM, bandfwhm)
            ELSE
              CALL lorentzian(BandGorL(j), nu - nuM, bandfwhm)
           END IF
              CALL triangulation(Normalarea, BandGorL(j), BandGorL(j - 1))
        NEXT j
       bandNormal = Normalarea        ' Normalising factor = area under curve


'*************************************************************************
'  Calculation of the y value (absorption) at the band maximum (loop
'  is outside normal omega steps, in case range used does not
'  include the band maximum (nuM)).


                                                'Point at/just below nuM
         omega = omegamin + omegaStepSize * INT((nuM - omegamin) / omegaStepSize)
         YmaxCalc = 0              'necessary for 2nd time through subroutine

'*************************************************************************
'  Calculate single-site Lorentzian (function of  omega, nu and r)
         FOR r = 0 TO rmax
           area = 0
           FOR j = 0 TO NumNuSteps
             nu = nuMin + j * nuStepSize
             CALL lorentzian(SiteLorentz, omega - nu - (r * omegaM), SiteFWHM(r))
             integrand = BandGorL(j) * SiteLorentz / bandNormal
             CALL triangulation(area, integrand, oldintegrand)
```

```
            oldintegrand = integrand
          NEXT j
          YmaxCalc = FCfac(r) * area + YmaxCalc 'sum over all values of r
        NEXT r

'*************************************************************************
'  Calculate pre-burn Absorption spectrum


      FOR i = 0 TO NumOmegaSteps
          omega = omegamin + omegaStepSize * i          'X coordinate  for A
          'PRINT omega
          FOR r = 0 TO rmax
          area = 0
          areai = 0
           FOR j = 0 TO NumNuSteps
             nu = nuMin + j * nuStepSize

'*************************************************************************
'  Calculate single-site Lorentzian (function of  omega, nu and r)

             CALL lorentzian(SiteLorentz, omega - nu - (r * omegaM), SiteFWHM(r))


             integrand = BandGorL(j) * SiteLorentz / bandNormal
             CALL triangulation(area, integrand, oldintegrand)
             oldintegrand = integrand
           NEXT j
           junk = FCfac(r) * area
           Ao0(i) = FCfac(r) * area + Ao0(i) 'sum over all values of r
         NEXT r

'*************************************************************************
' Scale calculated spectrum to peak height of exptal spectrum

         IF exptal$ = "Y" THEN
            calc = Ao0(i) * (omega / nuM) * (ymaxexpt / YmaxCalc) / multiple
            junk = calc
          ELSE
            calc = Ao0(i) * multiple
            junk = calc
         END IF
        PSET (omega, junk), 14

'*************************************************************************
' Plotting to HPG file

          IF hardplotPreburn$ = "Y" THEN
           IF hardplotPreburnInd$ = "Y" THEN
             IF omega = omegamin THEN
                SCREEN 9, , 1, 1
                CLS 0
                LOCATE 6, 8
                COLOR 10
                PRINT "For the plotting of the pre-burn absorption bands ...."
                CALL ChoosePattern(10, 3, 10, 7, 1, 1)       'set line pattern
                SCREEN 9, , 0, 0
                WINDOW (XMin, YMin)-(XMax, YMax)
              ELSE
                CALL PU
                CALL pa((omega - omegaStepSize) * Xscale, oldcalc * Yscale)
                CALL PD
                CALL pa(omega * Xscale, calc * Yscale)
                CALL PU
```

```
                CALL pa((omega - omegaStepSize) * Xscale, oldjunk * Yscale)
                CALL PD
                CALL pa(omega * Xscale, junk * Yscale)
                CALL PU
              END IF
              oldcalc = calc
              oldjunk = junk
            ELSE
             IF omega = omegamin THEN
                SCREEN 9, , 1, 1
                CLS 0
                LOCATE 6, 8
                COLOR 10
                PRINT "For the plotting of the pre-burn absorption band ...."
                CALL ChoosePattern(10, 3, 10, 7, 1, 1)       'set line pattern
                SCREEN 9, , 0, 0
                WINDOW (XMin, YMin)-(XMax, YMax)
                CALL PU
                CALL pa(omega * Xscale, junk * Yscale)
                CALL PD
              ELSE
                CALL pa(omega * Xscale, junk * Yscale)
              END IF
           END IF
          END IF
        NEXT i

END SUB

REM $STATIC
SUB BandWidth
REM $DYNAMIC


'************************************************************************
'  This subroutine determines the bandwidth (FWHM) for the
'  single-site lorentzian profile, depending on the phonon number (r)
'************************************************************************

REDIM SiteFWHM(0 TO rmax)

       FOR r = 0 TO rmax
         IF r = 0 THEN                  'FWHM for zero phonon line
             SiteFWHM(r) = gamma
           ELSEIF r = 1 THEN            'FWHM for 1-phonon line
             SiteFWHM(r) = gammaCap
           ELSE                         'FWHM for >= 2-phonon line
             SiteFWHM(r) = SQR(r) * gammaCap
          END IF
        NEXT r

END SUB

REM $STATIC
SUB BurntBandAbs

REM $DYNAMIC

'************************************************************************
'  This subroutine calculates the post-burn absorption spectrum.
'************************************************************************

REDIM At0(0 TO NumOmegaSteps)
REDIM At1(0 TO NumOmegaSteps)
```

```
REDIM BurnProfile(0 TO NumNuSteps)

'*************************************************************************
'  Calculate single-site burn profile.  This is a function of nu only, so
'  need only be determined at one value of omega.
'  The contribution to the site shape at the burn energy (omegaB) from
'  each of the single sites (with a ZPL maximum at nu) is calculated.
'  The contribution from zero, one, two etc phonon processes at each
'  value of nu + r*omegaM is summed

        FOR j = 0 TO NumNuSteps
           nu = nuMin + j * nuStepSize
           SingSite = 0
           FOR r = 0 TO rmax
              CALL lorentzian(SingSiteLorentz, omegaB - nu - (r * omegaM), SiteFWHM(r))
              SingSite = FCfac(r) * SingSiteLorentz + SingSite
            NEXT r
           BurnProfile(j) = EXP(-1 * constant * burntime * SingSite)
         NEXT j

'*************************************************************************
'  Calculate post-burn absorption spectrum

        FOR i = 0 TO NumOmegaSteps
            omega = omegamin + omegaStepSize * i    'X coordinate  for At
            FOR r = 0 TO rmax
             area = 0
             areai = 0
             FOR j = 0 TO NumNuSteps
               nu = nuMin + j * nuStepSize
               CALL lorentzian(SiteLorentz, omega - nu - (r * omegaM), SiteFWHM(r))
               integrand = BandGorL(j) * SiteLorentz * BurnProfile(j) / bandNormal
               CALL triangulation(area, integrand, oldintegrand)
               oldintegrand = integrand
            NEXT j
            At0(i) = FCfac(r) * area + At0(i) 'sum over all values of r
            NEXT r

'*************************************************************************
' Scale calculated spectrum to peak height of exptal spectrum

              IF exptal$ = "Y" THEN
                calc = At0(i) * (omega / nuM) * (ymaxexpt / YmaxCalc) / multiple
                junk = calc
               ELSE
                calc = At0(i) * multiple
                junk = calc
              END IF
              PSET (omega, junk), 13

'*************************************************************************
'  Plotting to HPG file

         IF hardplotBurn$ = "Y" THEN
            IF hardplotBurnInd$ = "Y" THEN
               IF omega = omegamin THEN
                  SCREEN 9, , 1, 1
                  CLS 0
                  LOCATE 6, 8
                  COLOR 10
                  PRINT "For the plotting of the post-burn absorption bands ...."
                  CALL ChoosePattern(10, 3, 10, 7, 1, 1)       'set line pattern
                  SCREEN 9, , 0, 0
                  WINDOW (XMin, YMin)-(XMax, YMax)
```

```
                ELSE
                  CALL PU
                  CALL pa((omega - omegaStepSize) * Xscale, oldcalc * Yscale)
                  CALL PD
                  CALL pa(omega * Xscale, calc * Yscale)
                  CALL PU
                  CALL pa((omega - omegaStepSize) * Xscale, oldjunk * Yscale)
                  CALL PD
                  CALL pa(omega * Xscale, junk * Yscale)
                  CALL PU
                END IF
                oldcalc = calc
              ELSE
                IF omega = omegamin THEN
                  SCREEN 9, , 1, 1
                  CLS 0
                  LOCATE 6, 8
                  COLOR 10
                  PRINT "For the plotting of the post-burn absorption band ...."
                  CALL ChoosePattern(10, 3, 10, 7, 1, 1)       'set line pattern
                  SCREEN 9, , 0, 0
                  WINDOW (XMin, YMin)-(XMax, YMax)
                  CALL PU
                  CALL pa(omega * Xscale, junk * Yscale)
                  CALL PD
                ELSE
                  CALL pa(omega * Xscale, junk * Yscale)
                END IF
              END IF
            END IF
          NEXT i

END SUB

REM $STATIC
SUB calcAo

        area = 0
        FOR i = 1 TO numpts
          IF Xexpt(i) >= omegamin AND Xexpt(i) <= omegamax THEN
            IF i <> 1 THEN
              area = area + Yexpt(i) * ABS(Xexpt(i) - Xexpt(i - 1)) + (Yexpt(i) ...
                - Yexpt(i - 1)) * ABS(Xexpt(i) - Xexpt(i - 1)) / 2
            END IF
          END IF
        NEXT i
        PRINT area

END SUB

SUB diffSpec

REM $DYNAMIC

'************************************************************************
'  This subroutine calculates the hole spectrum, = post burn - pre-burn
'************************************************************************

        FOR i = 0 TO NumOmegaSteps
          omega = omegamin + omegaStepSize * i          'X coordinate  for A

'*** Scale calculated spectrum to peak height of exptal spectrum

          IF exptal$ = "Y" THEN
```

```
            junk = (At0(i) - Ao0(i)) * (omega / nuM) * (ymaxexpt / YmaxCalc)
          ELSE
            junk = (At0(i) - Ao0(i)) * multiple
          END IF
          PSET (omega, junk), 14

'*************************************************************************
'  Plotting to HPG file

          IF hardplotDiff$ = "Y" THEN
             IF hardplotDiffInd$ = "Y" THEN
               IF omega = omegamin THEN
                  SCREEN 9, , 1, 1
                  CLS 0
                  LOCATE 6, 8
                  COLOR 10
                  PRINT "For the plotting of the 'hole' bands ...."
                  CALL ChoosePattern(10, 3, 10, 7, 1, 1)       'set line pattern
                  SCREEN 9, , 0, 0
                  WINDOW (XMin, YMin)-(XMax, YMax)
                ELSE
                  CALL PU
                  CALL pa((omega - omegaStepSize) * Xscale, oldcalc * Yscale)
                  CALL PD
                  CALL pa(omega * Xscale, calc * Yscale)
                  CALL PU
                  CALL pa((omega - omegaStepSize) * Xscale, oldjunk * Yscale)
                  CALL PD
                  CALL pa(omega * Xscale, junk * Yscale)
                  CALL PU
                END IF
                oldcalc = calc
                oldjunk = junk
              ELSE
               IF omega = omegamin THEN
                  SCREEN 9, , 1, 1
                  CLS 0
                  LOCATE 6, 8
                  COLOR 10
                  PRINT "For the plotting of hole spectrum ...."
                  CALL ChoosePattern(10, 3, 10, 7, 1, 1)       'set line pattern
                  SCREEN 9, , 0, 0
                  WINDOW (XMin, YMin)-(XMax, YMax)
                  CALL PU
                  CALL pa(omega * Xscale, junk * Yscale)
                  CALL PD
                ELSE
                  CALL pa(omega * Xscale, junk * Yscale)
                END IF
             END IF
          END IF
        NEXT i


END SUB

REM $STATIC
SUB display (junk)

'*************************************************************************
'  This subroutine sets up the screen for display of experimental data
'*************************************************************************

REM $DYNAMIC
```

```
'*************************************************************************
' plot axes and axis labels

        SCREEN 9, , 0, 0
        CALL axisdraw(XMin, YMin, XMax, YMax, 7, 0, 1)

'*************************************************************************
' draw experimental points

        FOR i = 1 TO numpts
          PSET (Xexpt(i), Yexpt(i) / junk), 12
        NEXT i

END SUB

REM $STATIC
SUB exptplot (junk)

'*************************************************************************
'  This subroutine sets up parameters for plotting experimental data
'  to a file
'*************************************************************************

       IF hardplotexptal$ = "Y" THEN
        CALL PU
        FOR i = 1 TO numpts
        Yexpt(i) = Yexpt(i) / junk
          IF Xexpt(i) >= XMin AND Xexpt(i) <= XMax THEN
            IF Yexpt(i) >= YMin AND Yexpt(i) <= YMax THEN
               CALL pa(Xexpt(i) * Xscale, Yexpt(i) * Yscale)
               CALL PD
             END IF
           END IF
         NEXT i
       END IF


END SUB

SUB FCfactor

'*************************************************************************
'  This subroutine calculates Franck-Condon factors for given
'  values of S (Huang-Rhys factor) and r (phonon number)
'*************************************************************************

REDIM FCfac(0 TO rmax)

'*************************************************************************
'  Create factorials

            FOR r = 0 TO rmax
                IF r = 0 THEN                       'calculate r!
                    rfactorial = 1
                 ELSE
                    rfactorial = r * oldr
                 END IF
                oldr = rfactorial

'*************************************************************************
'  Calculate the Franck-Condon factor

                FCfac(r) = (s ^ r) * EXP(-s) / rfactorial
```

```
            NEXT r
END SUB

SUB filename (COM$, end$, ToWrite
'************************************************************************
' This subroutine prompts the user for a file to read from or write to,
' depending on value of ToWrite
'************************************************************************

DEFINT A-Z

        SCREEN 9, , 1, 1
        COLOR 7, 1

        CLS 0

        Topy = 10
        BOTY = Topy + 6
        LftX = 10
        RTX = LftX + 60


        CALL WIND1(Topy, LftX, BOTY, RTX, 4)

     DO
        COLOR 10
       DO
        LOCATE Topy + 3, LftX + 2
        PRINT SPACE$(39)
        LOCATE Topy + 3, LftX + 5
        PRINT FileTitle$, :
        INPUT "", Port$
        IF Port$ = "" THEN BEEP
       LOOP WHILE Port$ = ""
        COM$ = ""
        FOR i = 1 TO 8
          IF MID$(Port$, i, 1) = "." THEN EXIT FOR
          COM$ = COM$ + MID$(Port$, i, 1)
         NEXT i
        fil$ = COM$ + end$
        findFile         ON ERROR GOTO nofile
        LOCATE 37, 1
        FILES fil$
        LOCATE 37, 1
        PRINT SPACE$(30)
        PRINT SPACE$(30)
        PRINT SPACE$(30)
        junk$ = "Y"

        IF findFile             BEEP
           LOCATE Topy + 3, LftX + 3: PRINT "                              "
           LOCATE Topy + 3, LftX + 3: PRINT "  File not found"
           SLEEP 1
           junk$ = "N"
         END IF

        IF findFile           IF ToWrite             FileNum = FREEFILE
           OPEN fil$ FOR BINARY ACCESS READ WRITE AS #FileNum
         ELSE
          BEEP
           DO
              LOCATE Topy + 3, LftX + 3: PRINT SPACE$(56)
              LOCATE Topy + 3, LftX + 3: PRINT "  Overwrite existing file ?"
```

```
            LOCATE Topy + 3, LftX + 31: INPUT "(Y/N) ", junk$
            junk$ = UCASE$(junk$)
            IF junk$ <> "N" AND junk$ <> "Y" THEN BEEP
          LOOP WHILE junk$ <> "N" AND junk$ <> "Y"
        END IF
       END IF
      LOOP WHILE junk$ <> "Y"

END SUB

DEFSNG A-Z
SUB gaussian (gauss, EminusEmax, FWHM)

'************************************************************************
'  This subroutine calculates a Gaussian bandshape, requiring values for
'  FWHM (band width), energy, (cm-1) and energyMax (energy of band maximum)
'
'  Relates Gaussian half-width-at-1/e-height (HWEH) to Gaussian full-width
'  at half maximum height (FWHM).  NB, Specfit outputs HWEH not FWHM.
'************************************************************************

       IF specfitWidth$ = "Y" THEN
          HWEH = FWHM
        ELSE
          HWEH = FWHM / (2 * SQR(LOG(2)))      'p149 Piepho and Schatz
       END IF
       gauss = 1 / (HWEH * SQR(pi)) * EXP(-1 * (EminusEmax) ^ 2 / HWEH ^ 2)

END SUB

SUB getdata2

'************************************************************************
'  Adapted from subroutine GETDATA in program SPECFIT
'  Reads in the experimental data points
'************************************************************************

DEFINT I-N

       IF HoldBlock           Text$ = "No " + LAB$(Kopt) + " data in file."
         GOSUB PrintText
         EXIT SUB
        END IF

       IF BaseLined           Text$ = "File not Baselined"
         GOSUB PrintText
         EXIT SUB
        END IF

       FSTBLK         numpts = HoldNPts
       REDIM Xexpt(numpts), Yexpt(numpts)


       NBlks = INT((numpts + 127) / 128)
       IPOS& = FSTBLK         IPOS& = IPOS& * 512 + 1

       SEEK #FileNum, IPOS&

       FOR Index = 1 TO numpts
          GET #FileNum, , Xexpt(Index)
       NEXT Index

       IPOS& = (FSTBLK         IPOS& = IPOS& * 512 + 1
       SEEK #FileNum, IPOS&
```

```
        FOR Index = 1 TO numpts
           GET #FileNum, , Yexpt(Index)
        NEXT Index

        IF BaseLined            IF ModNumber <> 4 THEN
            FOR i = 1 TO numpts
              Xexpt(i) = 1E+07 / Xexpt(i)
            NEXT i
           END IF
          IF ModNumber = 2 THEN
           IENDPT = INT(numpts / 2)
           FOR i = 0 TO IENDPT
             TEMP = Xexpt(i)
             SWAP Xexpt(1 + i), Xexpt(numpts - i)
             SWAP Yexpt(1 + i), Yexpt(numpts - i)
            NEXT i
          END IF
        END IF

        EXIT SUB

PrintText: Topy = 15: BOTY = 19: LftX = 26: RTX = 50
          CALL WIND1(Topy, LftX, BOTY, RTX, Boxfore)
          COLOR HIFORE
          BEEP: BEEP
          LOCATE Topy + 2, LftX + 2: PRINT Text$
          'CLOSE #Filenum

          Answ$ = ""
          WHILE Answ$ = ""
             Answ$ = INKEY$
          WEND

          CALL WIND1(Topy, LftX, BOTY, RTX, 0)
          RETURN

END SUB

DEFSNG I-N
SUB InitialValues

'*************************************************************************
'  This subroutine sets the values of the parameters for the calculation.
'*************************************************************************

REM $DYNAMIC
REDIM LAB$(2)
REDIM HoldBlock REDIM Xexpt(300), Yexpt(300), YCalc(300), XCalc(300)


'*************************************************************************
' Band absorption parameters

        nuMin = 14800           'wavenum min for band integration
        NuMax = 15200           'wavenum max for band integration
        nuM = 15000             'band maximum
        nuStepSize = 5          'this is the interval at which single-site
                                'Lorentzians are calculated - needs to be quite
                                'small to avoid getting ripples.
        NumNuSteps = ABS(NuMax - nuMin) / nuStepSize
        bandfwhm = 400          'Band width (FWHM) 1st excited state
        ymaxexpt = 1.55         'experimental band maximum
```

```
'************************************************************************
'  Single-site Abs parameters

        s = 1                   'Huang-Rhys factor
        omegaM = 200            'mean phonon frequency  (cm-1)
        gamma = 5               'homogeneous line width (cm-1)
                                '(=FWHM for zero phonon line)
        gammaCap = 150          'FWHM of 1-phonon line  (cm-1)
        pi = 3.1415927#         'value of pi
        rmax = 4                'number of phonons to include in stepping
        omegamin = 14800        'wavenum minimum        (cm-1)
        omegamax = 15200        'wavenum maximum        (cm-1)
        omegaStepSize = 10      'wavenum step size
        NumOmegaSteps = ABS(omegamax - omegamin) / omegaStepSize
        constant = 44000        '(burn intensity)*(abs cross section)*(HB quantum yield)
        burntime = .0001        'seconds
        omegaB = 15000          'Burn position (cm-1)
        multiple = 10

'************************************************************************
'  Axis coordinates

        XMin! = omegamin
        YMin! = -.0000025
        XMax! = omegamax
        YMax! = 0 '.022 ' .005  '.0001  '.008

        'exptal$ = "Y"              'compare with experimental file
        'TwoFiles$ ="Y"             'load both abs and hole data files
        BandShape$ = "G"            'use Gaussian for band shape
        hardplot$ = "Y"             'plot at all
        'hardplotPreburn$ = "Y"     'plot overall pre-burn
        'hardplotBurn$ = "Y"        'plot overall after-burn
        'hardplotBurnInd$ = "Y"     'plot individual after-burns
        'hardplotPreburnInd$ = "Y" 'plot individual pre-burns
        hardplotDiff$ = "Y"         'plot hole spectrum
        'hardplotDiffInd$ = "Y"     'plot individual holes
        'hardplotexptal$ = "Y"      'plot experimental curve
        'hardplotSingle$ = "Y"      'plot single site lorentzian profile
        'specfitWidth$ = "Y"        'assume the line width given is
                                    'full width at 1/e height

'************************************************************************
'  Experimental Data parameters

        LAB$(1) = "Abs"
        LAB$(2) = "MCD"
        Kopt = 1


END SUB

REM $STATIC
SUB lorentzian (lorentz, EminusEmax, FWHM)

'************************************************************************
'  This subroutine calculates a Lorentzian bandshape, requiring values
'  for FWHM (band width), and EminusEmax (energy minus energy of band maximum)
'************************************************************************

        lorentz = FWHM / (2 * pi) * 1 / ((EminusEmax) ^ 2 + (FWHM / 2) ^ 2)

 END SUB
```

```
SUB plot (XMin AS SINGLE, XMax AS SINGLE, YMin AS SINGLE, YMax AS SINGLE)

'*************************************************************************
'  This subroutine sets up frame, axis labels etc for the HPG file output
'  by calling various HARDPLOT subroutines
'*************************************************************************

DEFINT A-Z

          REDIM pentext$(1 TO 3)
          REDIM PENS(1 TO 3)
          NUMPENS = 3

          pentext$(1) = "Title"
          pentext$(2) = "X & Y axes"
          pentext$(3) = "Calculated curve"


          FOR i = 1 TO NUMPENS
            PENS(i) = 1
           NEXT i

        SCREEN 9, , 1, 1
        CLS
        COM$ = "com1:"
        CALL filename(COM$, ".HPG", 1, "Name of file to plot results to ? ")
        CLS
        CALL plotteron(COM$)

        VIEW (640 / 12, 350 / 11)-(640 / 1.1, 350 / 1.1)
        WINDOW SCREEN (7, 5)-(73, 40)
        CALL chooseframe(7, 6, 8)
        CLS
        CALL choosepens(NUMPENS, pentext$(), PENS(), 6, 7, 8)
        CLS

'*************************************************************************
'  Title

        CALL GetPen(PENS(1))

        Topy = 10                                   'draw box
        BOTY = Topy + 6
        LftX = 10
        RTX = LftX + 60

        CALL WIND1(Topy, LftX, BOTY, RTX, 4)
        COLOR 10, 1
        LOCATE Topy + 3, LftX + 2
        INPUT "Title of plot"; ITITL$
        CALL plottitle(ITITL$)

'*************************************************************************
'  Axes

        CALL GetPen(PENS(2))
        CALL plotaxes
        CALL sr(1, 2, 1)
        CALL sc(7, 73, 5, 40, 1)

'*************************************************************************
'  X axis label

        CALL pa(36, 2)
```

```
        ITITL$ = "Energy (cm-1)"
        CALL lb(ITITL$)
        'CALL DI(0!, 1!, 1!)

'************************************************************************
'   List parameters

        CALL PlotInfo(info1$, info2$, info3$, info4$)
        CALL pa(5, 0)
        CALL lb(info1$)
        CALL pa(5, -1)
        CALL lb(info2$)
        CALL pa(5, -2)
        CALL lb(info3$)
        CALL pa(5, -3)
        CALL lb(info4$)


'*************** Y axis label

        CALL DI(0!, 1!, 1!)
        CALL pa(-3, 19)
        ITITL$ = "Intensity"
        CALL lb(ITITL$)
        CALL DI(1!, 0!, 0!)
        CALL sr(1, 2, 1)
        CALL Plotticks(XMin, XMax, YMin, YMax, 3)  'X AXIS AND LEFT Y AXIS



END SUB

DEFSNG A-Z
SUB PlotInfo (info1$, info2$, info3$, info4$)
'************************************************************************
'  This subroutine sets up the information printed with each HPG file
'************************************************************************

        info1$ = "S =" + STR$(s) + ",  Num Phonons = " + STR$(rmax)
        info1$ = info1$ + ",  omegaM =" + STR$(omegaM)
        info1$ = info1$ + ",  Gamma ZPL =" + STR$(gamma)
        info1$ = info1$ + ",  Gamma Phonon = " + STR$(gammaCap)

        info2$ = info2$ + "Burn Time = " + STR$(burntime) + "s"
        info2$ = info2$ + ",  Burn Pos = " + STR$(omegaB) + "cm-1"

        info3$ = info3$ + "Integration limits = " + STR$(nuMin) + " to " + STR$(NuMax)
        info3$ = info3$ + ",  Intergration step = " + STR$(nuStepSize)
        info3$ = info3$ + ",  Energy step = " + STR$(omegaStepSize)

        info4$ = info4$ + "Band1 max = " + STR$(nuM) + "cm-1"
        info4$ = info4$ + ",  Band2 max = " + STR$(nuM + AbsShift) + "cm-1"
        info4$ = info4$ + ",  Band1 width = " + STR$(bandfwhm) + "cm-1"
        info4$ = info4$ + ",  Band2 width = " + STR$(bandfwhm1) + "cm-1"

END SUB

SUB ReadBlk02


'************************************************************************
'  Adapted from subroutine READBLK0 in program SPECFIT
'  Reads in the 'front material' of the experimental data file (number of
'  points, etc)
```

```
'*************************************************************************

        REDIM TITLE(35)

        SEEK #FileNum, 1

        FOR i = 1 TO 35
          GET #FileNum, , TITLE(i)
        NEXT i

        '1-70 CHAR Title

        DEF SEG = VARSEG(TITLE(1))
         ITITL$ = ""
        FOR i = 1 TO 70
           ITITL$ = ITITL$ + CHR$(PEEK(VARPTR(TITLE(1)) + i - 1))
        NEXT i

        ERASE TITLE

        '48 1st Abs block
        GET #FileNum, 97, HoldBlock
        '50 Num Abs points
        GET #FileNum, 101, HoldNPts
        '48 1st MCD block
        GET #FileNum, 115, HoldBlock
        '50 Num MCD points
        GET #FileNum, 119, HoldNPts
        ' 65 INPUT MOD OF SPECTROMETER
        GET #FileNum, 129, ModNumber

        '41 CHECK TO SEE IF Abs DATA PRESENT
        GET #FileNum, 81, DataPresent
        '44 CHECK TO SEE IF MCD DATA PRESENT
        GET #FileNum, 87, DataPresent
        ' 83 Check to see if Field is on
        GET #FileNum, 165, DataPresent
        ' 85 CHECK TO SEE IF DATA HAS BEEN BASELINED
        GET #FileNum, 169, BaseLined
        ' 86 CONCENTRATION
        GET #FileNum, 171, Concentration

        ' 88 PATHLENGTH
        GET #FileNum, 175, Pathlength

        ' 90 TEMPERATURE
        GET #FileNum, 179, Temperature

        ' 92 INPUT MAGNET USED FOR DATA
        GET #FileNum, 183, Magnet         IF Magnet
        ' 93 CURRENT
        GET #FileNum, 185, Current


END SUB

SUB scale (XMin, XMax, YMin, YMax, Xscale, Yscale)

'*************************************************************************
'  In the subroutine,  a scaling factor is introduced into the data
'  to be hard plotted so that the data points are not read into the
'  HPG file in exponential form.
'  ie, there are no numbers very close to zero other than zero itself
'  (HPG ignores EXX at the end of a number in exponential form)
```

```
'*************************************************************************

IF ABS(XMin) > ABS(XMax) THEN Xfactor = ABS(XMin) ELSE Xfactor = ABS(XMax)
IF ABS(YMin) > ABS(YMax) THEN Yfactor = ABS(YMin) ELSE Yfactor = ABS(YMax)
Xscale = 30000 / Xfactor
Yscale = 30000 / Yfactor

END SUB

SUB SingleSiteAbs


REM $DYNAMIC

REDIM l(0 TO NumOmegaSteps)

        FOR i = 0 TO NumOmegaSteps
            omega = omegamin + omegaStepSize * i    'X coordinate
            FOR r = 0 TO rmax
            CALL lorentzian(lorentz, omega - nu - r * omegaM, SiteFWHM(r))
               l(i) = FCfac(r) * lorentz + l(i)  'sum over all values of r
            NEXT r
           PSET (omega - nu, l(i)), 3

'*************************************************************************
'  If plotting to a file

          IF hardplotSingle$ = "Y" THEN
               IF omega = omegamin THEN
                  SCREEN 9, , 1, 1
                  CLS 0
                  LOCATE 6, 8
                  COLOR 10
                  PRINT "For the plotting of hole spectrum ...."
                  CALL ChoosePattern(10, 3, 10, 7, 1, 1)       'set line pattern
                  SCREEN 9, , 0, 0
                  WINDOW (XMin, YMin)-(XMax, YMax)
                  CALL PU
                  CALL pa((omega - nu) * Xscale, l(i) * Yscale)
                  CALL PD
                ELSE
                  CALL pa((omega - nu) * Xscale, l(i) * Yscale)
                END IF
          END IF

        NEXT i

END SUB

REM $STATIC
SUB triangulation (area, integrand, oldintegrand)

        IF nu <> nuMin THEN
            area = area + integrand * nuStepSize + (integrand - oldintegrand) * ...
              nuStepSize / 2
          END IF



END SUB
```

References

(1) Dolphin, D., Ed., *The Porphyrins*; Academic Press: New York, 1978- 1979; Vol. I to VII.

(2) Kalyanasundaram, K., *Photochemistry of Polypyridine and Porphyrin Complexes*; Academic Press: Suffolk, 1992.

(3) Moser, F. H.; Thomas, A. L., *The Phthalocyanines: Manufacture and Applications*; CRC Press: Florida, 1983; Vol. II.

(4) Moser, F. H.; Thomas, A. L., *Phthalocyanine Compounds*; American Chemical Society Monograph Series; Reinhold Publishing Corporation: New York, 1963.

(5) Moser, F. H.; Thomas, A. L., *The Phthalocyanines:Properties*; CRC Press: Florida, 1983; Vol. I.

(6) Thomas, A. L., *Phthalocyanine Research and Applications*; CRC Press: Florida, 1990.

(7) Leznoff, C. C.; Lever, A. B. P., Eds., *Phthalocyanines - Properties and Applications*; VCH Publishers: New York, 1989; Vol. I.

(8) Leznoff, C. C.; Lever, A. B. P., Eds., *Phthalocyanines - Properties and Applications*; VCH Publishers: New York, 1993; Vol. II.

(9) Leznoff, C. C.; Lever, A. B. P., Eds., *Phthalocyanines - Properties and Applications*; VCH Publishers: New York, 1993; Vol. III.

(10) Platt, J. R., In *Radiation Biology*; Hollaender, A., Ed.; McGraw- Hill Book Company: New York, 1956; Vol. III, pp. 71-123.

(11) Gouterman, M., In *Pophyrins*; Dolphin, D., Ed.; Academic Press: New York, 1978; Vol. 3, pp. 1-165.

(12) Simpson, W. T., *J. Chem. Phys.* **1949**, *17*, 1218-1221.

(13) Michl, J., *Pure & Appl. Chem.* **1980**, *52*, 1549-1563.

(14) Barth, G.; Linder, R. E.; Bunnenberg, E.; Djerassi, C., *Ann. NY Acad. Sci.* **1973**, *206*, 223.

(15) VanCott, T. C.; Koralewski, M.; Metcalf, D. H.; Schatz, P. N.; Williamson, B. E., *J. Phys. Chem.* **1993**, *97*, 7417-7426.

(16) Gasyna, Z.; Metcalf, D. H.; Schatz, P. N.; McConnell, C. L.; Williamson, B. E., *J. Phys. Chem.* **1995**, *99*, 5865-5872.

(17) Longuet-Higgins, H. C.; Rector, C. W.; Platt, J. R., *J. Chem. Phys.* **1950**, *18*, 1174-1181.

(18) Gouterman, M.; Wagniere, G. H.; Snyder, L. C., *J. Mol. Spectrosc.* **1963**, *11*, 108-127.

(19) VanCott, T. C.; Rose, J. L.; Williamson, B. E.; Boyle, M. E.; Misener, G. C.; Schrimpf, A. E.; Schatz, P. N., *J. Phys. Chem.* **1989**, *93*, 2999-3011.

(20) Ceulemans, A.; Oldenhof, W.; -Gorller-Walrand, C.; Vanquickenborne, L. G., *J. Am. Chem. Soc.* **1986**, *108*, 1155-1163.

(21) Buckingham, A. D.; Stephens, P. J., *Ann. Rev. Phys. Chem.* **1966**, *17*, 399-432.

(22) Stephens, P. J., *J. Chem. Phys.* **1970**, *52*, 3489- 3516.

(23) Stephens, P. J., In *Advances in Physical Chemistry*; Prigogine, I.; Rice, S. A., Eds.; John Wiley and Sons: New York, 1974; Vol. 35, pp. 197- 264.

(24) Stephens, P. J.; Suëtaka, W.; Schatz, P. N., *J. Chem. Phys.* **1966**, *44*(12), 4592-4602.

(25) Shashoua, V. E., *J. Am. Chem. Soc.* **1965**, *87*, 4044- 4048.

(26) Sutherland, J. C., In *Pophyrins*; Dolphin, D., Ed.; Academic Press: New York, 1978; Vol. 3, pp. 225-248.

(27) Holmquist, B., In *Pophyrins*; Dolphin, D., Ed.; Academic Press: New York, 1978; Vol. 3, pp. 249-270.

(28) Goldbeck, R. A., *Acc. Chem. Res.* **1988**, *21*(3), 95- 101.

(29) Stillman, M. J.; Nyokong, T., In *Phthalocyanines Properties and Applications*; Leznoff, C. C.; Lever, A. B. P., Eds.; VCH Publishers: New York, 1989; Vol. II, pp. 133-257.

(30) Cheeseman, M. R.; Greenwood, C.; Thompson, A. J., *Adv. Inorg. Chem.* **1991**, *36*, 201-255.

(31) Stillman, M. J., In *Phthalocyanines. Properties and Applications*; Leznoff, C. C.; Lever, A. B. P., Eds.; VCH Publishers: New York, 1993; Vol. III, pp. 227-296.

(32) Piepho, S. B.; Schatz, P. N., *Group Theory in Spectroscopy with Applications to Magnetic Circular Dichroism*; Wiley: New York, 1983.

(33) Metcalf, D. H.; VanCott, T. C.; Snyder, S. W.; Schatz, P. N.; Williamson, B. E., *J. Phys. Chem.* **1990**, *94*, 2828-2832.

(34) Misener, G. C. Ph.D. Thesis, University of Virginia, Charlottesville, Virginia, 1987.

(35) Williamson, B. E.; VanCott, T. C.; Boyle, M. E.; Misener, G. C.; Stillman, M. J.; Schatz, P. N., *J. Am. Chem. Soc.* **1992**, *114*, 2412-2419.

(36) Upton, A. H. P. M.Sc. Thesis, University of Canterbury, Christchurch, 1991.

(37) Langford, V. S. Ph.D. Thesis, University of Canterbury, Christchurch, 1997.

(38) Chen, G. C.; Yang, J. T., *Analytical Letters* **1977**, *10*, 1195-1207.

(39) VanCott, T. C.; Gasyna, Z.; Schatz, P. N., *J. Phys. Chem.* **1995**, *99*, 4820-4830.

(40) Vogler, A.; Kunkely, H., *Angew. Chem. Int. Ed. Engl.* **1978**, *17*, 760.

(41) Liou, K.; Newcomb, T. P.; Heagy, M. D.; Thompson, J. A.; Heuer, W. B.; Musselman, R. L.; Jacobsen, C. S.; Hoffman, B. M.; Ibers, J. A., *Inorg. Chem.* **1992**, *31*, 4517-4523.

(42) Whittle, E.; Dows, D. A.; Pimentel, G. C., *J. Chem. Phys.* **1954**, *22*, 1943.

(43) Clark, R. J. H.; Hester, R. E., Eds., *Spectroscopy of Matrix- Isolated Species*; John Wiley & Sons Ltd: Chichester, 1989; Vol. 17.

(44) Amey, R. L.; Cole, R. H., *J. Chem. Phys.* **1964**, *40*, 146-148.

(45) Krausz, E.; McDonald, P., *J. Phys. E: Sci. Instrum.* **1978**, *11*, 801-804.

(46) Krausz, E. R.; Mowery, R. L.; Schatz, P. N., *Ber. Bunsenges. Phys. Chem.*

1978, *82*, 134-136.

(47) Upton, A. H. P.; Williamson, B. E., *J. Phys. Chem.* **1994**, *98*, 71-76.

(48) Durieux, M.; Rusby, R. L., *Metrologia* **1983**, *19*, 67- 72.

(49) Rose-Innes, A. C.; Rhoderick, E. H., *Introduction to Superconductivity*, 2nd ed.; Permagon Press Ltd: Bath, 1978.

(50) Taylor, A. W. B., *Superconductivity*; Wykeham Publications Ltd: London, 1970.

(51) Krausz, E.; Riesen, H.; Schatz, P. N.; Gasyna, Z.; Dunford, C. L.; Williamson, B. E., *J. Lumin.* **1996**, *66&67*, 19-24.

(52) Krausz, E., *Aust. J. Chem.* **1993**, *46*, 1041-1054.

(53) Krausz, E. R.; Ludi, A., *Inorg. Chem.* **1985**, *24*, 939-943.

(54) Richtmyer, F. K.; Kennard, E. H.; Cooper, J. N., *Introduction to Modern Physics*, 6th ed.; McGraw-Hill: New York, 1969.

(55) Butler, P. H., *Point Group Symmetry Applications*; Plenum Press: New York, 1981.

(56) Butler, P. H. and associates. The program RACAH v3.1; Department of Physics and Astronomy, University of Canterbury, New Zealand.

(57) Rose, J. L.; Smith, D.; Williamson, B. E.; Schatz, P. N.; O'Brien, M. C. M., *J. Phys. Chem.* **1986**, *90*, 2608-2615.

(58) Douglas, I. N.; Grinter, R.; Thomson, A. J., *Mol. Phys.* **1974**, *28*(6), 1377-1388.

(59) Lucia, E. A.; Verderame, F. D.; Taddei, G., *J. Chem. Phys.* **1970**, *52*, 2307-2310.

(60) Huang, T. H.; Rieckhoff, K. E.; Volgt, E. M., *J. Chem. Phys.* **1981**, *85*, 3322-3326.

(61) Edwards, L.; Gouterman, M., *J. Mol. Spectrosc.* **1970**, *33*, 292-310.

(62) Brown, C. J., *J. Chem. Soc. (A)* **1968**, 2488-2493.

(63) Mason, R.; Williams, G. A.; Fielding, P., *J. Chem. Soc. Dalton Trans.* **1979**, 676-683.

(64) Williams, G. A.; Figgis, B. N.; Mason, R.; Mason, S. A.; Fielding, P. E., *J. Chem. Soc. Dalton Trans.* **1980**, 1688-1692.

(65) Ake, R. L.; Gouterman, M., *Theoret. Chim. Acta (Berl)* **1969**, *15*, 20-42.

(66) Henriksson, A.; Roos, B.; Sundbom, M., *Theoret. Chim. Acta* **1972**, *27*, 303-313.

(67) Schaffer, A. M.; Gouterman, M.; Davidson, E. R., *Theoret. Chim. Acta* **1973**, *30*, 9-30.

(68) Liang, X. L.; Flores, S.; Ellis, D. E.; Hoffman, B. M., *J. Chem. Phys.* **1991**, *95*, 403-417.

(69) Rosa, A.; Baerends, E. J., *Inorg. Chem.* **1994**, *33*, 584-595.

(70) Kashiwagi, H.; Takada, T.; Obara, S.; Miyoshi, E.; Ohno, K., *Int. J. Quantum Chem.* **1978**, *14*, 13-27.

(71) Benard, M., *Angew. Chem. Suppl.* **1982**, 1845-1852.

(72) Soares II, L. de A.; Trsic, M.; Berno, B.; Aroca, R., *Spectrochim. Acta A* **1996**,

52, 1245-1253.

(73) Gibson, J. F.; Ingram, D. J. E.; Schonland, D., *Discuss. Faraday Soc.* **1958**, *26*, 72-80.

(74) Griffith, J. S., *Discuss. Faraday Soc.* **1958**, *26*, 81-95.

(75) Assour, J. M., *J. Am. Chem. Soc.* **1965**, *87*, 4701- 4706.

(76) Ingram, D. J. E.; Bennett, J. E., *Discuss. Faraday Soc.* **1955**, *19*, 140-146.

(77) Lin, W. C., *Inorg. Chem.* **1976**, *15*, 1114-1118.

(78) Lever, A. B. P., *J. Chem. Soc.* **1965**, *2*, 1821-1829.

(79) Figgis, B. N.; Nyholm, R. S., *J. Chem. Soc.* **1959**, 338-345.

(80) Martin, R. L.; Mitra, S., *Chem. Phys. Lett.* **1969**, *3* (4), 183-184.

(81) Figgis, B. N.; Kucharski, E. S.; Reynolds, P. A., *J. Am. Chem. Soc.* **1989**, *111*, 1683-1692.

(82) Schatz, P. N.; Mowery, R. L.; Krausz, E. R., *Mol. Phys.* **1978**, *35*(6), 1537-1557.

(83) Stillman, M. J.; Thomson, A. J., *J. Chem. Soc. Faraday Trans. 2* **1974**, *70*, 805-814.

(84) Levine, I. N., *Quantum Chemistry*, 4th ed.; Prentice-Hall: New Jersey, 1991.

(85) Cory, M. G.; Zerner, M. C., *Chem. Rev.* **1991**, *91*, 813-822.

(86) McClure, D. S., *J. Chem. Phys.* **1952**, *20*, 682-686.

(87) Blume, M.; Watson, R. E., *Proc. Roy. Soc. (London)* **1963**, *271A*, 565-578.

(88) Fraga, S.; Karwowski, J.; Saxena, K. M. S., *Handbook of Atomic Data*; Elsevier Scientific Publishing Company: Amsterdam, 1976.

(89) Helberger, J. H.; Hever, D. B., *Ann.* **1938**, *536*, 173-182.

(90) Karavaeva, E. B.; Berezin, B. D.; Potapova, T. I., *Zh. Prikl. Spectrosk.* **1980**, *32*(3), 512-515.

(91) Vartanyan, A. T., *Dokl. Akad. nauk SSSR* **1983**, *270*, 115-119.

(92) Zalesskii, I. E.; Kotlo, V. N.; Sevchenko, A. N.; Solov'ev, K. N.; Shkirman, S. F., *Dokl. Akad. nauk SSSR* **1973**, *210*, 312- 315.

(93) Kobayashi, N.; Numao, M.; Kondo, R.; Nakajima, S.; Osa, T., *Inorg. Chem.* **1991**, *30*, 2241-2244.

(94) Gouterman, M., *J. Mol. Spectrosc.* **1961**, *6*, 138-163.

(95) Weiss, C.; Kobayashi, H.; Gouterman, M., *J. Mol. Spectrosc.* **1965**, *16*, 415-450.

(96) Even, U.; Magen, J.; Jortner, J.; Friedman, J., *J. Chem. Phys.* **1982**, *77*, 4384-4390.

(97) Lau, P. W.; Lin, W. C., *J. Inorg. Nucl. Chem* **1975**, *37*, 2389-2398.

(98) Zerner, M.; Gouterman, M., *Theoret. Chim. Acta (Berl)* **1966**, *4*, 44-63.

(99) McHugh, A. J.; Gouterman, M.; Weiss, C., *Theoret. Chim. Acta* **1972**, *24*, 346-368.

(100) Lee, L. K.; Sabelli, N. H.; LeBreton, P. R., *J. Phys. Chem.* **1982**, *86*(20),

3926-3931.

(101) Platenkamp, R. J.; Canters, G. W., *J. Phys. Chem.* **1981**, *85*(1), 56-63.

(102) References within VanCott, T. C.; Gasyna, Z.; Schatz, P. N.; Boyle, M. E., *J. Phys. Chem.* **1995**, *99*, 4820-4830.

(103) Gasyna, Z.; Schatz, P. N.; Boyle, M. E., *J. Phys. Chem.* **1995**, *99*, 10159-10165.

(104) Markovitsi, D.; Tran-Thi, T. H.; Even, R.; Simon, J., *Chem. Phys. Lett.* **1987**, *137*, 107-112.

(105) De Cian, A.; Moussavi, M.; Fischer, J.; Weiss, R., *Inorg. Chem.* **1985**, *24*, 3162-3167.

(106) Ostendorp, G.; Homborg, H., *Z. Anorg. Alleg. Chem* **1996**, *622*, 1222-1230.

(107) Ishikawa, N.; Ohno, O.; Kaizu, Y., *Chem. Phys. Lett.* **1991**, *180*, 51-56.

(108) Orti, E.; Bredas, J. L.; Clarisse, C., *J. Chem. Phys.* **1990**, *92*(2), 1228-1235.

(109) Ishikawa, N.; Ohno, O.; Kaizu, Y., *J. Phys. Chem.* **1993**, *97*, 1004-1010.

(110) Ishikawa, N.; Kaizu, Y., *J. Phys. Chem.* **1996**, *100*, 8722-8730.

(111) Rousseau, R.; Aroca, R.; Rodriguez-Mendez, M. L., *J. Mol. Struct.* **1995**, *356*, 49-62.

(112) Paillaud, J. L.; Drillon, M.; De Cian, A.; Fischer, J.; Weiss, R.; Villeneuve, G., *Phys. Rev. Lett.* **1991**, *67*, 244-247.

(113) Butler, P. H., *Point Group Symmetry Applications*; Plenum Press: New York, 1981; p. 67.

(114) Altmann, S. L.; Herzig, P., *Point-Group Theory Tables*; Clarendon Press: Oxford, 1994.

(115) Dieke, G. H., *Spectra and Energy Levels of Rare Earth Ions in Crystals*; Interscience Publishers: New York, 1968.

(116) Wybourne, B. G., *Spectroscopic Properties of Rare Earths*; Interscience Publishers: New York, 1965.

(117) Atkins, P. W.; Friedman, R. S., *Molecular Quantum Mechanics*, 3rd ed.; Oxford University Press: Oxford, 1997.

(118) Minor, P. C.; Gouterman, M.; Lever, A. B. P., *Inorg. Chem.* **1985**, *24*(12), 1894-1900.

(119) McClure, D. S., *Electronic Spectra of Molecules and Ions in Crystals*; Solid State Reprints; Academic Press: New York, 1959.

(120) Bloembergen, N.; Purcell, E. M.; Pound, R. V., *Phys. Rev.* **1948**, *73*, 679.

(121) Szabo, A., *Phys. Rev. B* **1975**, *11*, 4512.

(122) Kharlamov, B. M.; Personov, R. I.; Bykovskaya, L. A., *Opt. Commun.* **1974**, *12*, 191.

(123) Gorokhovskii, A. A.; Kaarli, R.; Rebane, L. A., *JETP Lett.* **1974**, *20*, 216.

(124) Friedrich, J.; Haarer, D., *Angew. Chem. Int. Ed. Engl.* **1984**, *23*, 113-140.

(125) Haarer, D.; Silbey, R., *Physics Today* **1990**(May), 58-65.

(126) Voelker, S., *Ann. Rev. Phys. Chem.* **1989**, *40*, 499- 530.

(127) Maier, M., *Appl. Phys. B* **1986**, *41*, 73-90.

(128) Jankowiak, R.; Hayes, J. M.; Small, G. J., *Chem. Rev.* **1993**, *93*, 1471-1502.

(129) Moerner, W. E., Ed., *Persistent Spectral Hole-Burning: Science and Applications*; Springer-Verlag: Berlin, 1988; Vol. 44.

(130) Voelker, S., *J. Lumin.* **1987**, *36*, 251.

(131) Macfarlane, R. M.; Vial, J. C., *Phys. Rev. B* **1986**, *34*, 1.

(132) Breinl, W.; Friedrich, J.; Haarer, D., *Phys. Rev. B* **1986**, *34*, 7271.

(133) de Vries, H.; Wiersma, D. A., *Phys. Rev. Lett.* **1976**, *36*, 91.

(134) Hochstrasser, R. M.; King, D. S., *J. Am. Chem. Soc.* **1975**, *97*, 4760.

(135) Olson, R. W.; Lee, H. W. H.; Patterson, F. G.; Fayer, M. D.; Shelby, R. M.; Burum, D. P.; Macfarlane, R. M., *J. Chem. Phys.* **1982**, *77*, 2283.

(136) Moerner, W. E.; Chraplyvy, A. R.; Sievers, A. J.; Silsbee, R. H., *Phys. Rev. B* **1983**, *28*, 7244.

(137) See, for example, the special issue 'Spectral Hole Burning and Related Spectroscopies'., *J. Lumin.* **1995**, *64*(1-6).

(138) Geissinger, P.; Haarer, D., *Chem. Phys. Lett.* **1992**, *197*(1,2), 175-180.

(139) Geissenger, P.; Richter, W.; Haarer, D., *J. Lumin.* **1993**, *56*, 109-115.

(140) Giering, T.; Geissinger, P.; Kador, L.; Haarer, D., *J. Lumin.* **1995**, *64*, 245-251.

(141) Geissinger, P.; Kador, L.; Haarer, D., *Phys. Rev. B* **1996**, *53*, 4356-4366.

(142) Radziszewski, J. G.; Waluk, J.; Michl, J., *J. Mol. Spectrosc.* **1990**, *140*, 373-389.

(143) Braun, D.; Ceulemans, A.; Dick, B.; Konami, H., *Chem. Phys. Lett.* **1994**, *225*, 398-403.

(144) Hayes, J. M.; Jankowiak, R.; Small, G. J., In *Persistent Spectral Hole-Burning: Science and Applications*; Moerner, W. E., Ed.; Springer- Verlag: Wurzburg, 1988.

(145) Rebane, K. K.; Rebane, L. A., In *Persistent Spectral Hole-Burning: Science and Applications*; Moerner, W. E., Ed.; Springer-Verlag: Wurzburg, 1988.

(146) Raja, N.; Reddy, S.; Lyle, P. A.; Small, G. J., *Photosynthesis Research* **1992**, *31*, 167-194.

(147) Shu, L.; Small, G. J., *J. Opt. Soc. Am. B* **1992**, *9* (5), 724-732.

(148) Lee, I.-J.; Hayes, J. M.; Small, G. J., *J. Chem. Phys.* **1989**, *91*, 3463-3469.

(149) Huang, T. H.; Rieckhoff, K. E.; Voigt, E. M., *J. Chem. Phys.* **1982**, *77*(7), 3424-3441.

(150) Koromaev, O. N.; Personov, R. I., *Opt. Spectrosc.* **1974**, *37*, 507-509.

(151) Shu, L.; Small, G. J., *J. Opt. Soc. Am. B* **1992**, *9* (5), 738-745.

(152) Prince, B.; Williamson, B. E. ; Unpublished data.

(153) Scheidt, W. R.; Mondal, J. U.; Eigenbrot, C. W.; Alder, A.; Radonovich, L. J.; Hoard, J. L., *Inorg. Chem.* **1986**, *25*, 795-799.

(154) Ough, E. A.; Stillman, M. J., *Inorg. Chem.* **1994**, *33* , 573-583.

(155) Winnacker, A.; Shelby, R. M.; Macfarlane, R. M., *J. de Chem. Colloq.* **1985**, *C7*, 543.

(156) Murase, N.; Horie, K., *Chem. Phys.* **1994**, *183*, 135- 146.

(157) Fearey, B. L.; Carter, T. P.; Small, G. J., *Chem. Phys.* **1986**, *101*, 279-289.

(158) van den Berg, R.; Voelker, S., *Chem. Phys.* **1988**, *128* , 257-273.

(159) Murase, N.; Horie, K., *Chem. Phys. Lett.* **1993**, *209* (1,2), 42-46.

(160) Pan, Y. L.; Zhao, Y. Y.; Chen, L. B.; Yin, Y.; Li, F. M., *Chem. Phys.* **1996**, *202*, 277-283.

(161) Reisen, H.; Krausz, E. R.; Williamson, B. E. ; unpublished results.

(162) Voelker, S., *J. Lumin.* **1987**, *36*, 251-262.

(163) Rieckhoff, K. E.; Voigt, E. M., In *Molecular Luminescence. An International Conference*; Lim, E. C., Ed.; W.A. Benjamin: New York, 1969; pp. 295-307.

(164) Debacker, M. G.; Deleplanque, O.; van Vlierberge, B.; Sauvage, F. X., *Laser Chem.* **1988**, *8*, 1-11.

(165) Bajema, L.; Gouterman, M.; Meyer, B., *J. Mol. Spectrosc.* **1968**, *27*, 225-235.

(166) Mack, J.; Stillman, M. J., *J. Am. Chem. Soc.* **1994**, *116*, 1292-1304.

(167) Nyokong, T.; Gasyna, G.; Stillman, M. J., *Inorg. Chem.* **1987**, *26*, 548-553.

(168) Dunford, C. L.; Williamson, B. E., *J. Phys. Chem. A* **1997**, *101*, 2050-2054.

(169) Dunford, C. L.; Williamson, B. E.; Schatz, P. N.; Gasyna, Z.; Krausz, E.; Reisen, H., *Chem. Phys. Lett.* **1996**, *260*, 522-528.